The Dissertation Committee for Richard K. Harrison Certifies that this is the approved version of the following dissertation:

MECHANISMS AND APPLICATIONS OF NEAR-FIELD AND FAR-FIELD ENHANCEMENT USING PLASMONIC NANOPARTICLES

Committee:

Adela Ben-Yakar, Supervisor

Arumugam Manthiram

Brian Korgel

Halil Berberoglu

Ananth Dodabalapur

Matthew Hall

MECHANISMS AND APPLICATIONS OF NEAR-FIELD AND FAR-FIELD ENHANCEMENT USING PLASMONIC NANOPARTICLES

by

Richard K. Harrison, B.S.; M.S.E.

Dissertation

Presented to the Faculty of the Graduate School of
The University of Texas at Austin
in Partial Fulfillment
of the Requirements
for the Degree of

Doctor of Philosophy

The University of Texas at Austin
December 2012

Dedication

For my wife, whose love, care and support made the completion of this dissertation possible. She has been my editor, source of inspiration, and sounding board over the course of my graduate studies, but above all else, she has been my best friend.

This dissertation is also dedicated to my family, who mean so much to me, including my sisters, cousins, grandparents, aunts, uncles, and in-laws. I want to especially thank my parents for everything: for their unwavering love, for the freedom and opportunity to pursue my goals, and for teaching me about the important things in life.

Acknowledgements

I would first like to thank my advisor, Dr. Adela Ben-Yakar, for enabling the pursuit of research that I was passionate about over the course of my doctoral studies. Her support has been integral to my success, and I admire her commitment to excellence and research vision. I have learned a great deal while I have been in the lab, both in terms of research subject matter as well as about how to be a scientist. I would also like to thank all my committee members for serving on my committee and for serving as a source of inspiration. Their scientific expertise and friendly willingness to help has been much appreciated. The lab environment of respect, open collaboration, and scientific curiosity in the Ben-Yakar group is truly exceptional, for which all the members deserve special acknowledgement. I learned a great deal from my co-workers, and they made the challenges of research easier and even fun. The experiences that we have had together and the friendships that we forged are some of the things I value most from my time as a graduate student. I look forward to maintaining these friendships in the coming years.

Many other people have positively contributed to my experience and graduate studies at UT-Austin as teachers, helpful staff members, and colleagues. I would like to specifically acknowledge the staff at the CNM and TMI, both current and past, who were a great resource in performing challenging experiments. Dr. Maxim Yurkin, who developed the open-source software package ADDA, was very helpful in discussions on the science of simulating optical responses of nanoparticles. Dr. Vahid Akhavan, Taylor Harvey and Jackson Stolle of the Korgel group were excellent teachers and collaborators. I would also like to acknowledge gratefully appreciated support from the Cockrell School of Engineering Graduate Engineering Doctoral Scholarship.

MECHANISMS AND APPLICATIONS OF NEAR-FIELD AND FAR-FIELD ENHANCEMENT USING PLASMONIC NANOPARTICLES

Richard K. Harrison, Ph.D.

The University of Texas at Austin, 2012

Supervisor: Adela Ben-Yakar

The resonant interaction of light with metal nanoparticles can result in extraordinary optical effects in both the near and far fields. Plasmonics, the study of this interaction, has the potential to enhance performance in a wide range of applications, including sensing, photovoltaics, photocatalysis, biomedical imaging, diagnostics, and treatment. However, the mechanisms of plasmonic enhancement often remain poorly understood, limiting the design and effectiveness of plasmonics for advanced applications. This dissertation focuses on evaluating the mechanisms of plasmonic enhancement and distinguishing between near and far field effects using simulations and experimental results.

Thorough characterization of metal nanoparticle colloids shows that electromagnetic simulations can be used to accurately predict the optical response of nanoparticles only if the true shapes and size distributions are taken into account. By coupling these optical interaction calculations with heat transfer models, experimental limits for the maximum optical power before nanoparticle melting can be found. These limits are important for plasmonic multiphoton luminescence imaging applications.

Subsequently, we demonstrate ultrafast laser plasmonic nanoablation of silicon substrates using gold nanorods to identify the near-field enhancement and mechanism of plasmon-assisted ablation. The experimentally observed shape of the ablation region and reduction of the ablation threshold are compared with simulations to show the importance of the enhanced electromagnetic fields in near-field nanoablation with plasmonic nanoparticles.

The targeted use of plasmonic nanoparticles requires narrow size distribution colloids, because wide size distributions result in a blurring and weakening of the optical response. A new synthesis method is presented for the seeded-growth of nearly monodisperse metal nanoparticles ranging from 10 to 100 nm in diameter, both with and without dielectric shells of controlled thickness. This method is used to acquire fine control over the position and width of the plasmonic peak response. We also demonstrate self-assembled sub-monolayers of these particles with controllable concentrations, which is ideal for looking at plasmonic effects in surface and layered geometries.

Finally, we present results for the spatial distribution of absorption around plasmonic nanoparticles. We introduce field-based definitions for distinguishing near-field and far-field regions and develop a new set of equations to determine the point-by-point enhanced absorption in a medium around a plasmonic nanoparticle. This set of equations is used to study plasmon-enhanced optical absorption for thin-film photovoltaic cells. Plasmonic nanoparticle systems are identified using simulations and proof-of-concept experiments are used to demonstrate the potential of this approach.

Table of Contents

List of Tables

List of Figures

Chapter 1: Plasmonics

1.1: MOTIVATION

Optics and photonics are rapidly advancing fields that find increasing use in sensing, biomedical diagnosis, computing, and energy applications. Plasmonics is a frontier within the field of optics, where optical effects can be dramatically enhanced through the extraordinary sub-diffraction concentration of light around metal nanoparticles. Plasmonics structures can enhance low level light to provide enhanced performance for solar applications, but plasmonics can also be used with high intensity lasers to provide nanoscale localization that cause nonlinear effects. Though the dramatic results of light interacting with metal nanoparticles have been observed for centuries, the mechanisms behind plasmonic enhancement mechanisms often remain poorly understood. In this dissertation, we study the plasmonic response of metal nanoparticles through a correlation of experimental, theoretical, and computational results to identify mechanisms and optimize plasmonic enhancement in the near- and far-fields.

In this first chapter, we introduce the background and review the literature for plasmonic effects of metal nanoparticles. We illustrate the concepts of primary interest through previously published studies from the literature and our own example calculations. Finally, we present the organization and objectives of this dissertation.

1.2: OVERVIEW OF PLASMONICS

Plasmonics is a unique field where complicated physical interactions at the nanoscale can be directly perceived. The Lycurgus Cup (*c.* 4th century AD, Roman Empire) is a famous historical example of plasmonic phenomena (Figure 1.1). The cup shows strong differences in the observed color if illuminated from the outside (scattering-dominated optical interaction) as compared to illumination from the inside (absorption-dominated optical interaction).

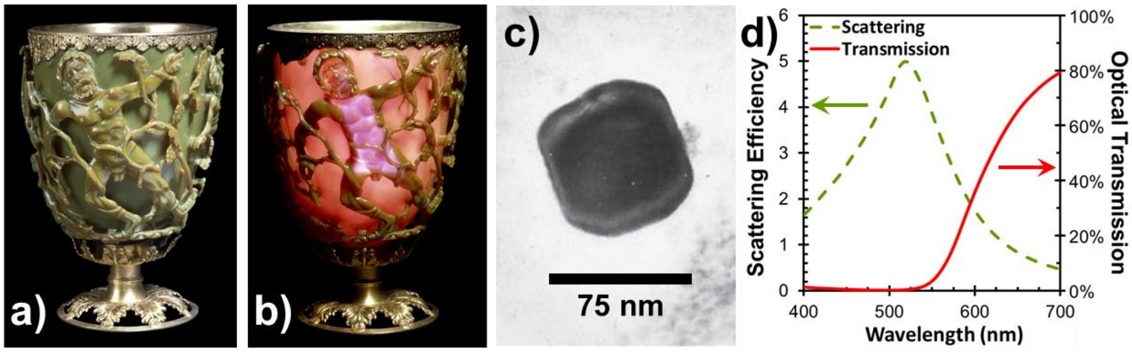

Figure 1.1: Origin of the extraordinary optical response of the Lycurgus cup. *(a)Artifact illuminated from the outside, and (b) from the inside, (c) transmission electron microscopy image of a metal nanoparticle in a glass fragment, and (d) calculated optical properties of the embedded nanoparticles in the glass composite. Images (a) and (b) are courtesy of the British Museum, and micrograph (c) is reproduced from* ***[1]****.The arrows in (d) correspond to the respective axes of the curves shown.*

The observed difference in the optical behavior of the cup by wavelength is termed ‘dichroism’ and it is a striking example of the use of plasmonics in an *objet d’art*. The fascinating changes in the coloration with lighting condition is based on the effect of 50 – 100 nm silver-gold-copper (~75:20:5) alloy nanoparticles embedded in the glass walls of the cup, shown in Figure 1.1c. To explain this phenomenon, we have calculated the differences in the transmission and scattering spectra for a glass with a dilute concentration of embedded 75 nm, gold-silver-copper alloy nanoparticles. The scattering response has a strong peak at 519 nm in the green portion of the spectrum, leading to a perceived green color when illuminated from the outside. The calculated transmission, however, shows that the particles will strongly attenuate the green light when illuminated from within, leading to a reddish color, where the optical attenuation is primarily due to absorption by the particle.

The brilliant coloration provided by plasmonic particles has been marveled at for millennia, providing intense hues and intriguing effects in colloidal solutions. Some of the brilliant coloration of stained glass windows (particularly reds and yellows) is due to plasmonic nanoparticles. Nanoparticle concentrations as low as 10^{-14} M can be readily detected by eye alone due to plasmonic phenomena [2]. Indeed, the molar absorptivity, which indicates the peak strength of a dye, is more than 66,000× greater for gold nanospheres (7.7×10^9 M^{-1} cm^{-1}) than the very strong dye Rhodamine B (1.2×10^5 M^{-1} cm^{-1}) [3]. Anisotropic gold and silver nanoparticles can have even larger molar absorptivities than gold nanospheres.

Michael Faraday first hypothesized in 1857 that the color of ‘ruby gold’ metal solutions was due to ‘finely divided’ solid gold particles [4]. Solutions of colloidal gold can be extremely stable, as some of the nanoparticles synthesized by Faraday remain in solution 150 years after their formation [5]. In the early 20th century, colloidal gold was studied in some of the most groundbreaking research, accounting for three Nobel prizes (Ostwald 1909, Zsigmondy 1925, Svedberg 1926) [4]. The mechanism of the optical effects was first understood with the seminal work of Gustav Mie in 1908 describing the optical properties of colloidal suspensions of metal nanoparticles [6]. Mie’s primary contribution was in the full expression of electromagnetic waves with a spherical object to explain the absorption and scattering interactions. Since that time, great strides have been made in correlating optical effects with shape and using mathematical and computational predictions.

As a scientific discipline, plasmonics is a rapidly growing field that enables the extraordinary manipulation of light with sub-wavelength metallic nanostructures through surface plasmons. A surface plasmon is a coherent oscillation of conduction band electrons on the surface of metal structure near a metal-dielectric interface. A dielectric surface acts as a boundary, limiting the oscillation path and confining the electron motion. The coherent oscillations occur because of attractive and repulsive forces of the optical electromagnetic fields (of which the light consists) on the quasi-free charges present in metals. Figure 1.2 shows a representation of the plasmon resonance for metal nanoparticles.

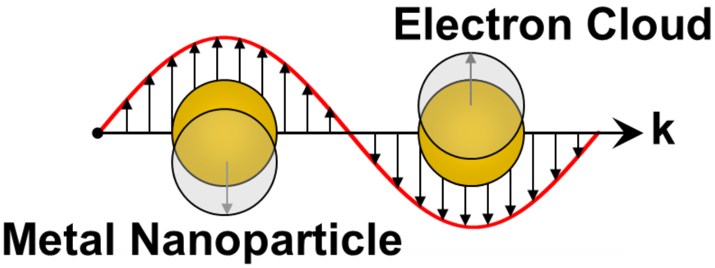

Figure 1.2: Schematic of plasmonic resonance showing the oscillatory motion of free electrons interacting with one cycle of light.

A surface plasmon exhibits a strong optical interaction between the particle and incident light when the frequency of the incident light coincides with the resonance frequency of the particle. A plasmon response is defined by the existence of a narrow frequency band over which a resonance can occur. This oscillation frequency is dependent on the size of the structure and the materials present. For most metals, this resonance occurs in the ultraviolet portion of the electromagnetic spectrum. However, for nanoscale noble metals, such as gold, silver, or copper, the resonance frequency can be shifted into the range of visible to near-infrared (NIR) light.

On account of the resonant interaction between the coherently oscillating electrons and the incident light, plasmonic structures can interact with light from an area much larger than their physical cross-section. This is analogous to the gravitational pull exerted by the Earth on passing meteorites. Based on an initial trajectory, a hypothetical meteorite could pass cleanly by the planet, but on account of the gravitational interaction force, meteorites are drawn in towards the planet, providing us with ‘shooting stars’.

Analogously, the plasmonic interaction effect draws light into the particle, providing enhanced optical interaction cross-sections. Non-plasmonic particles that are much smaller than the wavelength of the incident light will exhibit very little optical interaction. This is expected, because electromagnetic radiation interacts very weakly with objects smaller than a quarter of the wavelength ($\lambda/4$). For a plasmonic particle on resonance, however, a very different interaction pattern can be observed. In this case, the surrounding light field is significantly disrupted, as the particle draws in light from a large area around the particle.

Figure 1.3 shows the two images of the electromagnetic field lines representing the flow of optical energy around a 50 nm silver nanosphere in water. Off resonance (Figure 1.3a), the light has very little interaction with a particle much smaller than the wavelength (diameter $d \approx \lambda/10$). On resonance (Figure 1.3b), however, the plasmonic structure draws light in from area that is significantly larger than the geometrical cross-section of particle itself on account of induced electromagnetic forces.

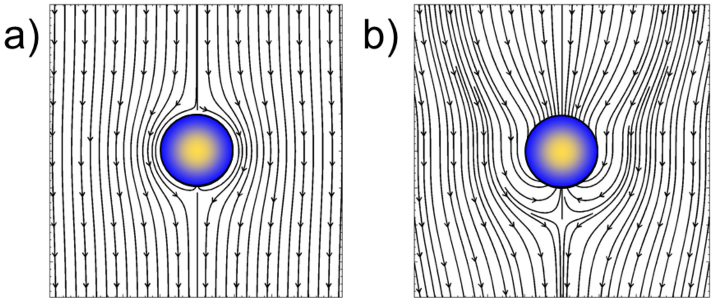

Figure 1.3: The plasmonic response of a 50 nm silver sphere in water. *a) The electromagnetic field lines for light passing around the nanosphere off the resonance wavelength. b) The field lines of on-resonance light interacting with the plasmonic particle. The interaction cross-section on resonance is more than fifty times as large as off-resonance.*

The ability of a plasmonic particle to interact with light is known as the extinction, which consists of two components: absorption of light by the particle and scattering of light away from the incident direction. These two terms represent the mechanisms by which optical intensity can be removed from an incident beam of light. The interaction (absorption and scattering) cross-sections are measures of the ability of a particle to remove light from the forward direction of propagation. The cross-section is an effective area (perpendicular to the direction of the incident light) over which the light interacts with the particle. The extinction cross-section, C_{ext}, is a sum of the scattering, C_{sca}, and absorption, C_{abs}, cross-sections (Eq. (1.1)). The strength of a plasmonic interaction is most conveniently expressed in terms of the ratio of the interaction cross-section, C, to the geometrical cross-section, A_{CS}, of the structure [7]. These terms are known as the interaction efficiencies, Q, shown in Eq. (1.2). The normalized optical interaction theorem remains valid (Eq. (1.3)).

$$C_{ext} = C_{sca} + C_{abs} \tag{1.1}$$

$$Q_{ext} = \frac{C_{ext}}{A_{CS}} \qquad Q_{sca} = \frac{C_{sca}}{A_{CS}} \qquad Q_{abs} = \frac{C_{abs}}{A_{CS}} \tag{1.2}$$

$$Q_{ext} = Q_{sca} + Q_{abs} \tag{1.3}$$

For plasmonic nanoparticles, the extinction efficiency can be much larger than 1 as the resonant interaction draws light towards the particle from a much wider area than the geometrical area. A comparison of typical non-plasmonic and plasmonic interaction spectra is shown in Figure 1.4. The non-plasmonic silica (SiO_2) particle is a pure dielectric, and thus no light is absorbed by the particle, resulting equivalent extinction and scattering cross-sections. The extinction cross-section of the silica particle is approximately four orders of magnitude smaller over the entire spectrum than the gold nanoparticle. Additionally, the trends are significantly different. The scattering cross-section scale decreases with increasing wavelength for the silica nanoparticle, while a plasmon resonance peak is seen in the gold spectrum.

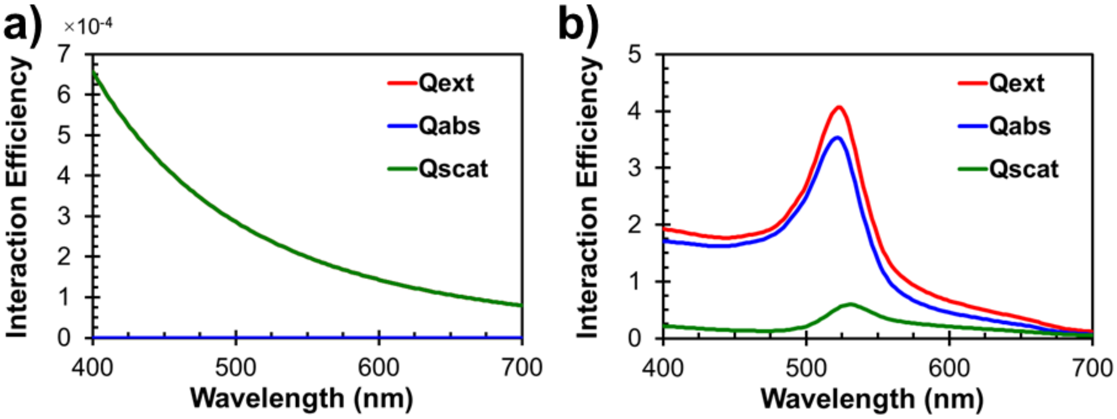

Figure 1.4: Typical plasmonic and non-plasmonic optical interaction spectra. *The interaction spectra are shown for (a) 50 nm silica (non-plasmonic) and (b) gold (plasmonic) nanoparticles, both in a water environment over the visible region of the electromagnetic spectrum. Note the difference in scale between the two plots.*

For spherical particles, the interaction is characterized by the non-dimensional size parameter *x*, shown in Eq. (1.4).

$$x = kr \tag{1.4}$$

The variables k and r in Eq. (1.4) refer to the wave number of the light, defined in Eq. (1.5), and the radius of the particle, respectively. The variables in the wave number include the wavelength of the incident light in a vacuum (λ) and the complex index of refraction of the metallic particle in the embedding medium ($\widetilde{m}$). In the general case, the complex refractive index will have a real portion η, relating to the angular refraction of the incident light, and an imaginary part κ, corresponding to absorption (Eq. (1.6)).

$$k = \frac{2\pi\widetilde{m}}{\lambda} \tag{1.5}$$

$$\widetilde{m} = \eta + \kappa i \tag{1.6}$$

For particles much smaller than the wavelength of the incident light ($x \ll 1$, $|\widetilde{m}|x \ll 1$), a simple mathematical relationship can be found for the optical interaction efficiencies. This simplification, commonly known as the Rayleigh or electrostatics approximation, is shown in Eq. (1.7) [7].

$$\begin{gathered} Q_{abs} = 4x \, Imag\left\{\frac{\varepsilon_p - \varepsilon_m}{\varepsilon_p + 2\varepsilon_m}\right\} \\ Q_{sca} = \frac{8}{3}x^4 \left|\frac{\varepsilon_p - \varepsilon_m}{\varepsilon_p + 2\varepsilon_m}\right|^2 \end{gathered} \tag{1.7}$$

In Eq. (1.7), the variables ε_p and ε_m correspond to the relative permittivities of the particle and the surrounding medium. In this approximation, it is clear that the absorption and scattering will become large when the frequency-dependent permittivity of the particle, ε_p, approaches the negative of twice the permittivity of the medium, ε_m. Interestingly, metals can support negative permittivities. The relative permittivity (also known as the complex dielectric function) is related to the components of the refractive index as shown in Eq. (1.8).

$$\varepsilon = (\eta^2 - \kappa^2) + 2\eta\kappa i \tag{1.8}$$

From the electrostatics approximation, several conclusions can be reached. First, the absorption of small particles will be much larger than the scattering, as $x \ll 1$ for very small particles and the interaction cross sections will approximately scale as a function of x for absorption and x^4 for scattering. Absorption only occurs if the particle material has a complex dielectric constant. Second, for a particle consisting of a material whose dielectric constant is weakly dependent on the wavelength (such as a dielectric material in an air environment), we can understand that both scattering and absorption will be strongest for short wavelengths because of the wavelength dependence. If we then approximate air molecules and airborne particulates as dielectric spheres (as the physics community often does), we can gain a conceptual understanding of our perception of the blue sky, as shorter wavelength light will be significantly more efficiently scattered. A convolution of the scattered light with the biological response of the color sensitive cones in our eyes will yield a peak in the blue region. We can also grasp the increased solar spectrum reddening at sunset, when light from the sun passes through an increased thickness of atmosphere (especially in the dense, particulate-rich low, near-surface layers). In this case, the extinction is significantly increased for shorter wavelength light, while longer wavelength light is transmitted.

Finally, and most relevant for our discussion of plasmonics, large (resonant) interaction efficiencies will be observed in the case of $\varepsilon_p \approx -2\varepsilon_m$. This is an especially applicable result for small metal nanoparticles because the dielectric function of metals is frequency-dependent, size-dependent, and can be negative. The electrostatics approximation can be useful for a conceptual understanding of plasmonics, but they cannot be used for the accurate calculations of realistic plasmonic nanoparticles larger than a few nanometers. For example, the electrostatics approximation has only a 0.5% error in the extinction cross-section for a 10 nm gold sphere in water for incident light of λ=500 nm, but this increases to 163% error for a 100 nm sphere under the same conditions. For this reason, we use full electromagnetic solutions and experimentally-validated dielectric constants throughout this dissertation. The mathematical basis for these calculations will be described in later chapters.

Another intriguing effect of a plasmonic resonance is a region of strongly enhanced electromagnetic fields in close vicinity to the surface of a nanostructure. This plasmonic property is known as near-field enhancement, where the electromagnetic fields are concentrated to higher levels than the incident optical fields.

We will first show and explain the effect of the four primary variables (size, material, medium, and shape) that affect the plasmonic resonance of a metallic nanoparticle.

1.3: EFFECT OF THE SIZE IN PLASMONICS

Plasmonics is a truly nanoscale scientific phenomenon on account of the physical mechanisms behind the origin of a plasmonic resonance. Plasmonic responses will occur in nanoscale features and not in bulk materials because of the limited coherence length of oscillations and the requirement that all electrons are subjected to the same optical forces. As the feature size increases, conflicting directions of electron motion will lead to plasmon dephasing (loss of coherent electron motion) and leading to bulk material behavior.

For nano-scale metallic structures supporting a plasmonic resonances, the size can have a dramatic effect on the plasmonic behavior. For example, increasing the diameter of a spherical nanoparticle leads to a corresponding red-shift in the plasmonic response, meaning that the resonance will shift to longer wavelengths (Figure 1.5). As the wavelength increases, the frequency decreases. The resonance shift can be understood in terms of the oscillation path of the electrons moving together. A larger particle will support a longer period in the collective oscillatory motion of the electrons corresponding to the increased distance of motion.

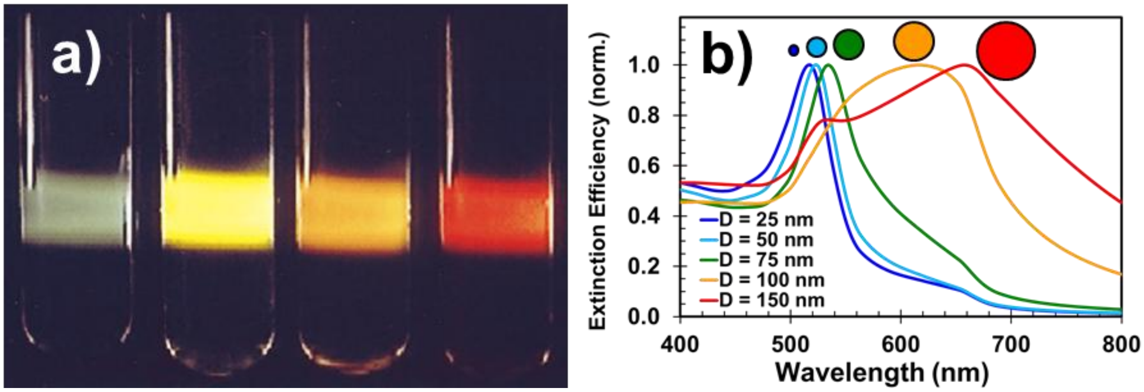

Figure 1.5: The nanoparticle size effect on plasmonic resonance. *(a) Scattered light from gold nanospheres of various sizes in water. From left to right, the* $\sim 10^{-12}$ *M solutions are colloidal particles of 40, 78, 118 and 140 nm in diameter yielding green, yellow, orange and red scattered light peaks, respectively. (b) Normalized extinction efficiencies for various sizes of gold nanospheres in water. The circles above the plot correspond to the relative cross-sectional area of the spheres simulated. Image (a) is adapted from* ***[2]***.

Figure 1.5 shows the increase in the plasmonic resonance wavelength with particle diameter. Small spheres have a narrow resonance, but the resonance broadens as the size increases. For 150 nm particles, two peaks can be observed in the spectral response: a dipolar resonance (~660 nm) and a quadrupolar resonance (~530 nm). These resonances correspond to different oscillation patterns. Small particles with diameters less than about 25 nm can only support an idealized back-and-forth linear type dipolar oscillation, but larger particles can exhibit various other oscillation patterns. Electron motion in conductors occurs on the surface, and thus for large particles with larger radii of curvature, the direction of travel deviates more strongly from the direction of excitation. Furthermore, the higher order multipoles will be characterized by shorter oscillation paths between nodes, yielding shorter wavelength resonance wavelengths. Figure 1.6 shows the electric field lines for the first few multipolar resonances.

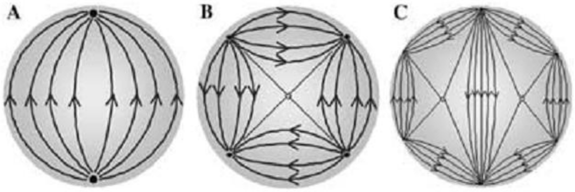

Figure 1.6: Schematic diagrams of the plasmonic modes within a metal nanosphere. *The images show the electric field lines and corresponding oscillation paths for the a) dipolar, b) quadrapolar, and c) octapolar modes. The images are taken from* ***[8]****.*

As the particle size changes, the nature of optical interaction can also change for a plasmonic nanoparticle. The two primary mechanisms of optical interaction are absorption and scattering. Figure 1.7 depicts the differences for two different sizes of gold nanoparticles in water. As shown in Figure 1.7a, absorption is the dominant mechanism of optical interaction for small particles. The ratio of absorption to extinction increases as the particle size decreases. For larger particles, however, scattering provides the primary source of extinction for large particles (Figure 1.7b). Additionally, the total extinction efficiency tends to increase as the particle size increases, which can be seen by comparing the scale of the two plots in Figure 1.7. The differences in the source of extinction can be very important for practical use of plasmonic nanoparticles. For example, absorption by the particle leads to heating of the particle, which can lead to melting and destruction of the particle at high incident optical intensities. Conversely, large scattering efficiencies will result in significant redirection of incident optical power.

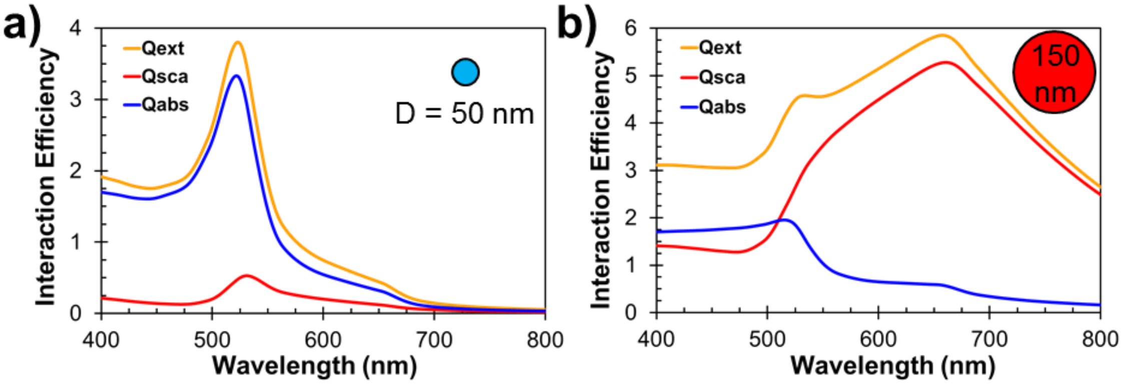

Figure 1.7: Interaction efficiencies for two different sizes of gold nanospheres in water. *a) 50 nm gold nanosphere in water, and b) 150 nm gold nanosphere in water. In addition to a substantial red-shift in the peak resonance wavelength, there is also a change in the dominant source of extinction, which is absorption for the smaller sphere and scattering for the larger sphere.*

1.4: EFFECT OF THE MATERIAL IN PLASMONICS

Noble metal nanospheres are widely studied because their plasmonic resonance occurs in the visible portion of the electromagnetic spectrum. However, other materials can have resonances across the electromagnetic spectrum, depending on the energy levels in the materials, provided that the material has quasi-free electrons. For example, nanoparticles of aluminum, potassium, and sodium all have strong resonances in the ultraviolet under vacuum conditions, while silicon carbide has a resonance in the infrared.

All of the Group 11 metals (Cu, Ag and Au) with filled *d* electron orbitals exhibit plasmonic resonances in the visible. Specifically, gold nanoparticles have been widely studied because of their early discovery and biological compatibility. Silver and copper exhibit blue- and red-shifted resonances with respect to gold, respectively, as can be seen in Figure 1.8. Silver has a particularly strong resonance and can be readily synthesized and suspended in aqueous solutions using similar reactions as for gold nanoparticles.

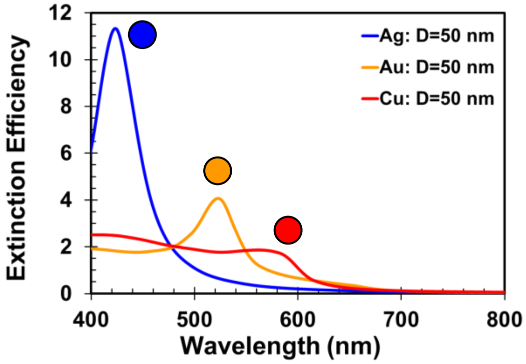

Figure 1.8: Extinction efficiencies for 50 nm noble metal nanospheres formed from the noble metals. *The spheres show the difference in optical response that is observed depending on the metal of which the sphere consists.*

1.5: EFFECT OF THE MEDIUM IN PLASMONICS

While it is clear that the specific metal supporting a plasmon will have a strong effect on the plasmonic properties of a nanostructure, it is perhaps less obvious that the surrounding dielectric material will also have a significant effect. This is indeed the case. Figure 1.9 shows the effect of varying the surrounding material on the resonant wavelength of a gold nanosphere.

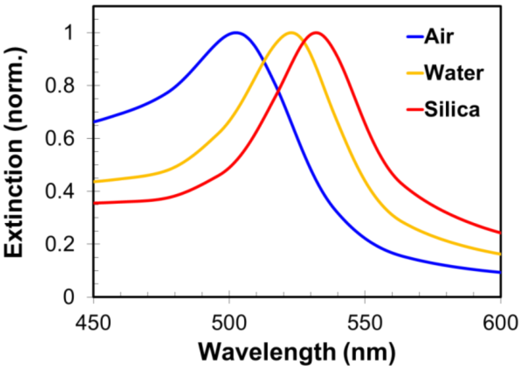

Figure 1.9: Normalized extinction efficiencies for 50 nm spheres embedded in various dielectric materials. Larger refractive indices of the medium leads to a red shift in the plasmonic response.

This effect can be considered in terms of the refractive index, n_M, of the surrounding material. A spectral shift of 30 nm is observed as the index changes from air ($n_M \approx 1$) to silica ($n_M \approx 1.5$). Using this mechanism, metal nanoparticles can be used as a refractive index sensor, as even slight changes can be detected if a plasmonic nanostructure is observed with a sensitive spectrometer. Furthermore, a pronounced increase in the strength of the resonance (as measured by the extinction) can also be seen for embedding media with higher refractive indices.

The medium has an effect on the plasmonic response because of two main factors. First, the effective wavelength (and corresponding speed) of the light in a medium is reduced by a factor of the index of refraction of the medium. Secondly, the relative difference between the material properties of the metal and the surrounding dielectric material is altered. This can be taken into account by dividing the optical properties of the metal particle by the properties of the surrounding medium to provide effective values. These changes result in different wavelength and size criteria to achieve plasmonic resonance.

1.6: EFFECT OF THE SHAPE IN PLASMONICS

The shape of a metal nanostructure can have the most dramatic effect on the plasmonic properties of a nanoparticle. The previous examples have all referred to spherical nanoparticles. As the spherical symmetry is broken, however, a whole new range of plasmonic properties can be accessed. These properties include order of magnitude increases in the optical interaction efficiency, polarization dependence, increased near-field enhancements, and independent control of the size and resonance. Various shapes, such as nanorods, triangular prisms, ellipsoids, cuboids, and cross-shaped metallic nanostructures, have been fabricated to date to examine the effect of shape on the plasmonic properties.

Figure 1.10 shows several specific experimental examples from the scientific literature demonstrating the striking effect that nanoparticle shape can have on the optical interaction. The top portion of both Figure 1.10 *a* and *b* show scanning electron microscopy (SEM) images of various particles prepared with wet-chemistry and electron beam (e-beam) lithography techniques, respectively. The color images in the middle show dark-field microscopy images of the particle, where the true colors come from the light scattered by the nanostructures of different shapes. Dark-field microscopy is a technique where the unscattered light (also known as ballistic photons) is blocked, and only light that has been scattered is detected, usually in an annular (ring-type) region. Dark-field microscopy can separate the scattering behavior from the extinction, and can thus provide specific information about the size and shape of individual particles. Plasmonic particles can be detected optically because they have scattering cross-sections much larger than the geometrical cross-sections.

Finally, the bottom images in Figure 1.10 show the spectra corresponding to the colors observed. These examples show how small differences in the nanoparticle shape can have a large effect on the plasmonic response.

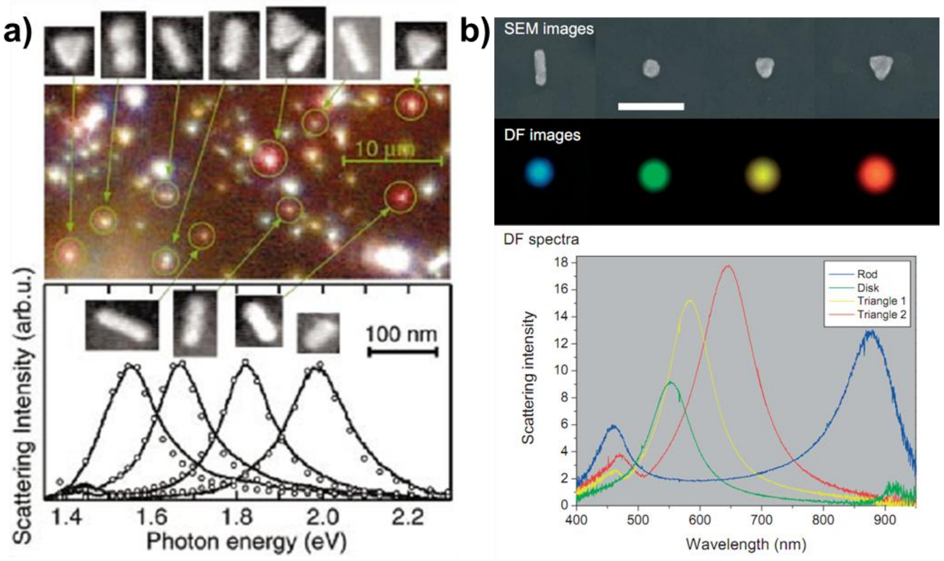

Figure 1.10: Correlation of the scattering spectrum of individual nanoparticles with their shape. *The scattering response is shown for (a) colloidal nanoparticles and (b) nanostructures fabricated using e-beam lithography. The actual nanoparticle shape from SEM and optical response spectra are shown for each particle size and shape. The colors of the curves in the bottom half of (b) correspond to the color of the scattered light shown in the top part. The scale bar in (b) is 300 nm. The images are taken from* ***[9]*** *for (a) and* ***[10]*** *for (b).*

Metal nanorods are one particularly interesting shape owing to their strong plasmonic resonance and tunability over a wide range of visible to NIR wavelengths. Nanorods can be colloidally synthesized using soft-templated growth methods for a wide range of length-to-width aspect ratios. The shift in the resonance with aspect ratio is shown in Figure 1.11. As the aspect ratio increases, two peaks become evident in the extinction spectra. The peak at 525 nm is due to a transverse surface plasmon resonance (TSPR) across the width of the nanorod. The TSPR peak is similar to the peak for a spherical nanoparticle with a diameter equal to the width of the nanorod. The TSPR peak is efficiently excited for light polarized along the short axis.

The long wavelength peak is due to an oscillation of electrons along the length of the rod, known as the longitudinal resonance. The longitudinal surface plasmon resonance (LSPR) is very strong, but it can only be excited by incident light polarized along the long axis of the nanorod. A simplified schematic of the plasmonic response is shown in Figure 1.11a. A longer oscillation path will generally give rise to a red-shifted plasmonic response.

Figure 1.11b shows an averaged response over all incident polarizations, demonstrating the dominance of the longitudinal peak. Though the optical condition where the polarization of the incident light matches with the nanorod long axis represents only a small fraction of the total configurations, the longitudinal peak is still the strongest feature in the spectral response.

It is important to note that, in contrast to spherical particle shapes, the spectral response is decoupled from the overall nanoparticle size or volume. In fact, the aspect ratio becomes a much better indicator of the nanoparticle response, but it is not the only important factor. For example, a ‘large’ nanorod with a diameter of 50 nm will have a resonance at around 780 nm with an aspect ratio of 2.75 (length of 137.5 nm), but a ‘small’ nanorod with a diameter of 10 nm needs an aspect ratio of 4 to achieve the same resonance (length of 40 nm). This intriguing separation of effects can allow for the tuning of other plasmonic properties, such as the scattering to absorption ratio, while maintaining the same longitudinal plasmonic resonance wavelength. At the resonance wavelength, a larger 50×137.5 nm diameter nanorod will have a scattering to absorption ratio of 315.7% (scattering dominated), but the 10×40 nm diameter nanorod has a scattering to absorption ratio of only 3.6% on resonance (absorption dominated).

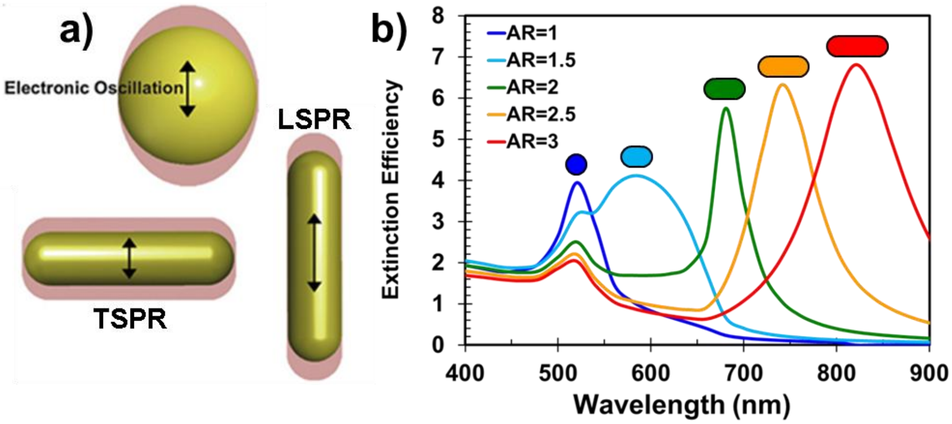

Figure 1.11: Plasmonic response of gold nanorods. *a) Schematic representation of the electron oscillation that gives rise to transverse and longitudinal plasmonic responses in nanorods* ***[11]****. b) Extinction efficiencies for gold nanorods with a diameter of 50 nm. The aspect ratio (AR) is the ratio of the length to the diameter. The nanorods are spherically-capped cylinders, where AR=1 corresponds to a sphere. The cartoons show the relative scale and length of the nanoparticles.*

1.7: ORGANIZATION OF THIS DISSERTATION AND OBJECTIVES

In this dissertation, we present a study of the mechanisms and applications of near-field and far-field enhancement of plasmonic metal nanoparticles. Our focus in this work is examining and resolving the distinctions and possible effects that can be accomplished on a nanometer length scale using plasmonic nanoparticles.

Our first objective is developing simulation techniques for predicting the optical response of plasmonic nanoparticles. We will discuss the usage of different types of computational tools and then identify how they can be used for calculating the plasmonic response for different nanoparticle shapes and configurations. We then develop computational tools and validate their usage in calculating optical properties through a comparison with experimental results including a characterization of nanoparticle samples and heat transfer studies. These results can be used to provide information that suggests limits for experimental optical intensities when using plasmonic nanoparticles.

The second goal of this dissertation is in the application of near-field enhancement to the creation of nanoscale ablation features on a substrate using ultrafast lasers. First, we will review various methods by which lasers can be used to achieve controlled nanofabrication, and introduce plasmonic near-field nanoablation. We will then simulate near-field enhancement around plasmonic nanoparticles, with a goal of investigating near-field intensity enhancement around nanoparticles to predict surface ablation. Subsequently, we will present experimental results for ultrafast laser plasmonic nanoablation, including the polarization dependence of asymmetric nanoparticles, the threshold for ablation, and effective plasmonic enhancement. This information is used to correlate simulated near-field enhancement effects with experimental observations to evaluate mechanisms behind plasmonic near-field nanoablation.

Third, we develop of experimental procedures for synthesizing high quality nanoparticles of various materials, shapes, and configurations including shell structures and self-assembly on a substrate. Synthesis efforts are necessary to obtain custom particles for use in experimental applications. Synthesizing nanoparticles with narrow size distributions is also vital for identifying plasmonic effects, as small deviations in the nanoparticle size and shape can have a large effect on the plasmonic response. We will present protocols and characterization results for synthesized gold and silver nanoparticles, as well as silica spheres and shell structures. Evenly distributed two-dimensional arrangements of plasmonic nanoparticles can be useful for a range of applications, so we also present the fabrication and characterization of self-assembled monolayers of plasmonic nanoparticles.

The fourth objective of this dissertation is to find a theoretical basis and spatial distribution for the near-field absorption enhancement in the material surrounding plasmonic nanoparticles in an absorbing medium. This analysis can be useful for nonlinear absorption, thin film solar cells, and in other applications where the absorption density (light absorbed per unit volume) is important. We will examine the effect of absorption by the medium on the plasmonic response of a metal nanoparticle and look at the far-field effect of a particle on absorption by the medium. New descriptions of the near-field enhanced volume, magnitude of enhanced absorption by the medium, and near-field absorption efficiency will be presented using a point-by-point method for calculating the local absorption of optical energy in the medium surrounding a spherical plasmonic nanoparticle. The utility of this new calculation framework will be demonstrated in a calculation of nonlinear absorption around a gold sphere

We will apply the lessons of the previous chapters to a promising application for plasmonics: the enhancement of optical absorption in thin film solar cells. In this application, the efficiency of thin film solar cells can be enhanced if the optical absorption can be improved. We will consider various mechanisms of enhancement, including direct near-field absorption and high-angle scattering, and multiple locations of locating the plasmonic nanoparticle within the solar cell. We will develop and implement simulations to identify strong candidates for enhancing absorption. Finally, we present proof-of-concept experiments showing the benefit of plasmonics for thin film solar applications. This dissertation seeks to address these five objectives.

Chapter 2: Theory and Simulation of Plasmonics

In this chapter, we present the theory and techniques used for the simulation of the plasmonic properties of metal nanoparticles. The simulation of plasmonic properties is vital for the applied use of plasmonics, as it enables an understanding of physical mechanisms behind experimental observations. First, we introduce the topic of electromagnetic simulation for optical properties, including a comparison of the various techniques. We then present how the material properties influence the optical response, followed by a section on how energy conservation can be used to evaluate plasmonic effects. The following sections discuss the two primary computational methods that we use for simulating the plasmonic properties of metal nanoparticles, including analytic methods for spheres and discrete approximations for asymmetric nanoparticles, and evaluate the error associated with these methods. Finally, we link the calculated properties with experimental observable phenomena to verify accuracy and make predictions, including the characterization of sets of colloidal nanoparticles and an evaluation of nanoparticle heating.

2.1: INTRODUCTION

Understanding the origins and controlling factors of the plasmonic response of metal nanostructures is crucial for their practical use. There are four variables that contribute most strongly to the optical response of a plasmonic object: the material, surrounding medium, size, and shape. These variables will lead to wavelength-dependent spectral effects in the optical response of a plasmonic structure that also depend on the parameters of the incident light such as incidence direction, polarization state, and intensity. The vast number of possibilities and the strong dependence of the plasmonic response on each variable leads to an enormous range of potential optical interactions. There is an expansive range of plasmonic effects that can be used for scientific purposes, including: spectral effects that can be used for index of refraction sensing, localized enhancement of absorption for imaging or photodynamic therapy, angular-dependent scattering, near-field enhancement for nanoablation, ultrafast mechanisms, nonlinear microscopy, optical emission, and chemical effects. These effects can be difficult to directly measure, and experimental evidence can be ambiguous because of the short time scale and nanometer length scale. However, if the size and shape of the plasmonic nanostructure is known, electromagnetic calculations can provide field enhancements, the extent and magnitude of optical energy deposition, and can yield information that can be correlated with experiments to identify the mechanisms behind the plasmonic enhancement. Thus, it is advantageous to simulate plasmonic structures when designing plasmonic experiments.

The field of computational electromagnetic is broad, but all methods solve or approximate the Maxwell equations of electromagnetism from various directions. There are three major categories of techniques for simulating the optical interaction of electromagnetic radiation with structures: analytical techniques, surface discretization models, and volume discretization models. An extensive list of different light scattering codes has recently become available on the website of Dr. Thomas Wriedt [12].

Analytical techniques are generally based on solutions of the electromagnetic wave equations for the shape and properties of the simulated structure. This technique is the fastest and most accurate, but the shapes that have been determined analytically is limited to spheres, inifinite cylinders, ellipsoids, and cubes. Extensions to analytical techniques, such as spheres on a surface [13], concentric coated spheres[14] and the T-Matrix approach [15] have also been developed. The T-Matrix (transition-matrix) approach and multiple multipole (MMP) are hybridized solution methods where, similar to the solution for a sphere, the incident and scattered fields from each constituent portion of a structure are expressed in terms of spherical harmonic wave functions.

Non-analytical techniques break up the structure into small pieces where the electromagnetic field properties can be solved. These techniques are necessary for the vast range of electromagnetic interactions beyond the limited geometries with available analytical solutions. Surface discretization techniques, including both finite element and boundary element methods, account for the optical energy crossing a boundary and the fields at each location in space on a surface. This technique can also be relatively fast, but care must be taken in meshing the objects to ensure accuracy. The most well-known commercial implementations of this technique are the Ansys and COMSOL code packages, which are implemented into multiphysics code suites.

The final category of electromagnetic wave solution methods is volume discretization. This category can be broken up into two distinct approaches. Finite difference (especially in the time domain) techniques are often used for the simulation of electromagnetic radiation with structures. This technique directly solves for the electric and magnetic fields at every point in a structure. The advantages of this technique are numerous. First, the approach is very conceptually easy to understand and simulations are straightforward to set up. The structure is broken up into small discretized elements over which the field is assumed to be constant. The technique can provide near-exact field solutions for the discretized structure simulated. Additionally, periodic structures and plasmonic features on substrates can be readily solved in some implementations. There are a few commercially available finite-difference time-domain (FDTD) solution packages. Among those, Vancouver-based Lumerical is most readily used FDTD package for plasmonic simulations [16]. In addition, several open-source implementations of FDTD exist as well. However, there are a few disadvantages to finite difference methods. First, FDTD typically requires simulating the whole computational domain, including a substantial region outside the particle. Few FDTD codes have implemented variable size cells, so the same discretization level must be used both near and far from the particle. Special care must also be taken at the domain boundaries to avoid artificial reflections, which is usually overcome using perfectly matched layers. Furthermore, restrictions on the material properties can be onerous, as the entire spectral response should ideally be known for any metals simulated, as opposed only to the material properties at a wavelength of interest. Finally, this approach is the most computationally intensive of all the approaches described thus far, leading to long simulation times and increased granularity for simulated structures.

Another subset of volume discretization methods includes the discrete dipole approximation. In the discrete dipole technique, the structure is broken up into small regions that are assumed to have constant material properties and a single polarization response. An initial estimate of the total structure is first found from the incident light, and then the initial guess for the element polarizations are iteratively refined. A final solution is reached when the change from one iteration to the next falls below a pre-defined level, at which point the induced fields and polarizations have converged. The electromagnetic fields can be found at any point in space by determining the summed response of all dipoles on that point. The primary disadvantage of this technique is the approximation of a constant dipole polarization over a finite volumetric region of space. The technique becomes exact as the discrete dipoles become vanishingly small. For many optical situations, however, very accurate results can be found with even a relatively small number of dipoles. This technique can be very rapid and the calculations can be parallelized over a number of computer processors. Extremely large numbers ($>10^8$) of elements over a range of wavelengths can be solved for in reasonable time frames on desktop computers, in contrast with the more computationally-intensive FDTD approach. This technique is nearly ideal for the solution of isolated asymmetric plasmonic nanoparticles in a homogenous medium, as only the particle must be discretized and simulated to obtain a complete picture of the optical response. Experimentally relevant values such as the absorption, scattering, extinction cross-sections, and angular scattering intensity can be readily obtained from the summed response of all dipoles. Additionally, only the conditions at a single wavelength must be known to simulate that wavelength. DDSCAT, originally developed by Draine and Flatau, is the most popular DDA code package, but several other open source or academic use versions also exist. This technique becomes more cumbersome for particles on a surface, or for materials that approach perfect conductors, but accurate solutions can be reached in both cases if care is taken in the simulation setup.

In this dissertation, we focus on analytical methods for the solutions of spherical geometries and discrete dipole approximation for non-spherical geometries. The theoretical underpinnings of the specific methods are described in the following sections.

2.2: OPTICAL PROPERTIES OF MATERIALS

The optical response of a material is dictated by its characteristic optical properties over the spectrum. To simulate the optical properties of any material, the dielectric function, or corresponding complex refractive indices, must be known. The complex refractive index $\widetilde{m}$ is defined in terms of a real part η and an imaginary coefficient κ (Eq. (2.1)). The real refractive index η is related to the phase velocity in the material, while the imaginary refractive index κ expresses the optical absorptivity of the material.

$$\widetilde{m} = \eta + i\kappa \tag{2.1}$$

The dielectric function (or relative permittivity) can be expressed in terms of the complex refractive index, shown in Eq. (2.2), where the tilde indicates a complex value. The dielectric function can be divided into a real part, ε', and an imaginary component, ε'', given by the first and second terms in Eq. (2.2). Both the refractive indices and the related dielectric function are wavelength-dependent.

$$\tilde{\varepsilon} = (\eta^2 - \kappa^2) + 2\eta\kappa i \tag{2.2}$$

A qualitative understanding of the optical properties for a dielectric material can be understood using the Lorentz model. The Lorentz model approximates an electron bound to an ion core as a simple harmonic oscillator system, analogous to a mass attached to a spring. In this case, incident electromagnetic fields lead to harmonic oscillations of the electron cloud, similar to the stretching modes of a spring. This model can be used to connect the displacement of the electron cloud and the associated restoring force with the optical properties, specifically the dipole polarizations, such that the dielectric function can be identified. Damping in this system is provided by electron collisions (electron-electron or electron-phonon). Multiple electron states can be considered by summing the effect of several different oscillation conditions to account for higher order effects. This approach can provide insight on optical behavior of many materials. For example, at frequencies far from the resonance conditions, most materials will exhibit ‘normal’ dispersion, where the real part of the refractive index decreases with increasing wavelength. The Lorentz model can be also used to understand the frequency and size dependence of the dielectric function. Fundamental equations exist which restrict the possible values of a material’s optical properties to purely physical values with causality restraints, known as the Kramers-Kronig relations.

For transparent, purely dielectric materials, the relatively smooth curve of experimental data for refractive index can usually be approximated with a high degree of accuracy using the Sellmeier equation. The Sellmeier equation, shown in Eq. (2.3), is a simplification of the multiple-oscillator Lorentz model at wavelengths far from resonance conditions that satisfies the Kramers-Kronig relations. This semi-empirical equation was originally proposed to model the dispersion effects of glasses [17].

$$\eta = \left(1 + \sum_{i=1}^{N} \frac{B_i \lambda^2}{\lambda^2 - C_i^2}\right)^{1/2} \tag{2.3}$$

The refractive index of many transparent dielectric materials can be accurately determined using the Sellmeier equation once the coefficients have been determined. Table 2.1 presents the four term Sellmeier coefficients for water [18] and amorphous silicon dioxide (SiO_2, fused silica) [19].

Table 2.1: Four term Sellmeier coefficients for water and amorphous silica in the transparent region from [18] and [19], respectively.

Material	B_1	C_1	B_2	C_2	B_3	C_3	B_4	C_4
Water	0.568909	0.071486	0.171971	0.135099	0.020625	0.161993	0.112397	3.267270
Fused Silica	0.547885	0.058409	0.556304	0.111188	0.475273	8.596471	6.702533	49.173434

The fit for water agrees very well with independent experimental measurements from the National Institute for Standards and Technology [20], with a relative error < 0.1% for wavelengths between 300 – 1000 nm. The data for silica also matches published data [21] using independent experimental techniques to within 0.4% for over the same range, but even this small discrepancy could be accounted with slight differences in the sample preparation. The predicted real refractive indices (curves) of these materials are shown in Figure 2.1 compared the experimental measurements (symbols). We used Sellmeier expressions to quickly and accurately determine the optical constants for water and silica dielectric media throughout our studies.

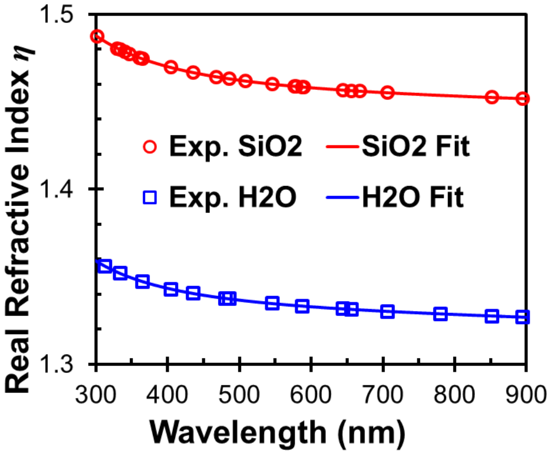

Figure 2.1: Comparsion of experimentally determined and predicted data for the real refractive index of water and fused silica. *The data points show experimental values from **[20,21]**and the lines show the Sellmeier equation fits **[18,19]** for water and silica, respectively.*

Metals are characterized by significantly more complicated refractive index behavior as a function of wavelength. Metals exhibit complex refractive indices, including both a real (η) and imaginary component (κ). The imaginary component cause a dramatic effect on the optical properties, including increased reflectivity and a corresponding optical absorption according to Eq. (2.4), where α is the absorption coefficient.

$$\alpha = \frac{4\pi\kappa}{\lambda} \tag{2.4}$$

A non-zero absorption coefficient means that light within this material will be attenuated as a function of path length within the material. This attenuation is often given according to Beer's law, which is applicable for a light travelling within a slab of material. Equation (2.5) shows Beer's law, which states that the intensity I will fall exponentially from an initial value I_0 as a function of the absorption coefficient and distance travelled L within the material.

$$I = I_0 e^{-\alpha L} \tag{2.5}$$

The absorption coefficient and Beer's law are simplifications of the expression for the intensity of a wave of light travelling in a material, where the intensity passing a point is given by the Poynting vector and harmonic expressions are used to describe the electric field and magnetic fields.

The quasi-free electrons in metals can provide the most important contribution to their optical response. The optical properties of a metal can be idealized with the Drude model, shown in Eq. (2.6), which is the specific case of a Lorentz harmonic oscillator with zero restoring force (or 'spring constant') for quasi-free electrons. The plasma frequency ω_p and damping constant γ are material-dependent terms which depend on the number density of quasi-free electrons, electron velocity, and electron collision time in a given material. The frequency of light ω is given in Eq. (2.7), where c is the speed of light in a vacuum.

$$\varepsilon = 1 - \frac{\omega_p^2}{\omega^2 + i\gamma\omega} \tag{2.6}$$

$$\omega = \frac{2\pi c}{\lambda} \tag{2.7}$$

For aluminum, the free electron contribution dominates the optical properties of the material in the visible region, primarily because resonance conditions lie well in the ultraviolet, and the Drude model alone can approximate the optical properties of aluminum with a reasonable degree of accuracy from 2 – 10 eV (124 – 620 nm).

Unfortunately, the Drude model does not provide accurate values for the noble metals in the visible region on account of interband transitions. Modifying the Drude equation to account for the interband transistions of bound electrons can yield a more accurate expression. This can be accomplished by summing the contributions of free electrons and bound electrons using the Drude and Lorentz models together (Eq. (2.8)).

$$\varepsilon_{bulk} = \varepsilon_{bound} + \varepsilon_{free} \tag{2.8}$$

Notably, Etchegoin *et al.* followed this approach to predict the optical properties of gold, obtaining a maximum error of 14% for η and 6% for κ when compared with experimental values [22]. While this study presents an interesting approach, the error in this semi-empirical model is still sufficient to cause significant uncertainty in simulated plasmonic optical properties. Thus, we obtain metal dielectric function values from an interpolated curve fit to experimentally determined dielectric function values for all wavelengths to ensure accuracy. Various experimental values have been presented in the literature, but the two most commonly used for the simulation of plasmonic nanoparticles are those presented by Johnson and Christy [23] and the data set tabulated by Palik [24]. We evaluated the plasmonic response of materials using the optical properties presented in these two data sets and found small but consequential differences in the predicted plasmonic peak position and enhancement magnitude. We chose to use the data published by Palik throughout this dissertation, as special care was taken to ensure the purity and cleanliness of the surfaces evaluated in these experimental data. The experimental measurements and cubic spline fits are shown for the complex refractive indices and reflectivity of the noble metals in Figure 2.2.

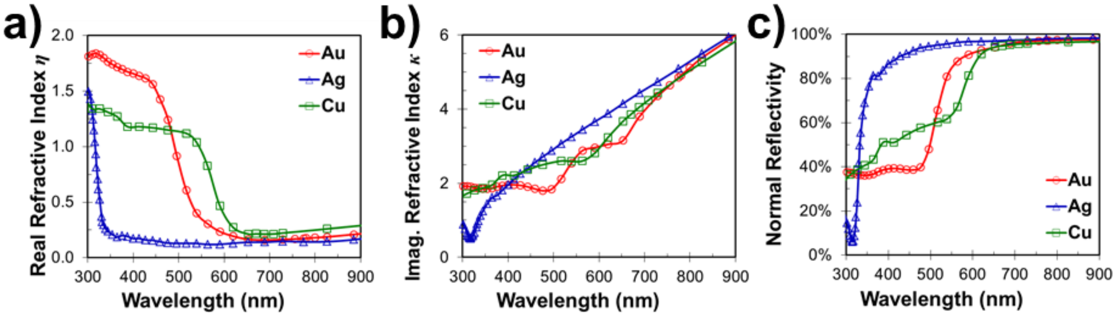

Figure 2.2: Experimentally determined optical properties of gold, silver and copper (symbols), with interpolated fits (lines). *a) Real refractive index, b) imaginary refractive index, and c) normal incidence reflectivity for a flat, thick substrate. The data points in a) and b) are taken from* ***[24]****, and the lines and c) are our calculations based on this data.*

Care must be taken when using bulk values for nanoscale phenomena. For very small nanoparticles, the oscillation path of electrons can be constrained by the particle boundary. Specifically, the collision of free electrons with the metal surface, which acts as a limit on electron motion, provides a damping source not included in the bulk optical properties of a material. Size-induced surface damping only becomes an appreciable effect for particles smaller than ~10 nm. Equation (2.9) shows the free electron portion of the dielectric function, ε_{free}, from the Drude model. Here, ω is the frequency of the light and ω_p is the plasma frequency of the metal defined in Eq. (2.10), and γ is the electron collision frequency in the metal.

$$\varepsilon_{free} = 1 - \frac{\omega_p^2}{\omega^2 + i\omega\gamma_{bulk}} \tag{2.9}$$

$$\omega_p = \left(\frac{4\pi N_e e^2}{m_e}\right)^{1/2} \tag{2.10}$$

In the preceding equations, e represents the charge of an electron, m_e is the mass of an electron, N_e is the number density of free electrons, c is the speed of light in a vacuum and λ is the wavelength of the light.

As shown by Scaffardi and Tocho [25], metal surface damping can be accounted for by replacing the bulk value of the collision frequency γ_{bulk} in with a size-dependent collision frequency γ_{mod}. This includes the effect of a particle surface by constraining the electron motion and increasing the collision frequency as the size of the particle decreases. Equation (2.11) shows how the collision frequency can be modified, where v_F is the Fermi velocity of electrons in the metal and L_{eff} is the effective path length. The L_{eff} term is sometimes given simply as the particle radius, but this is not applicable for asymmetric particle shapes. A more rigorous approach by Coronado and Schatz proposes to use the expression shown in Eq. (2.12) for the effective path length [26]. In this equation, the ratio of the volume V to the surface area of a particle S can be used to determine the effective electron path length for any arbitrary closed surface volume.

$$\gamma_{mod} = \gamma_{bulk} + \frac{\nu_F}{L_{eff}} \tag{2.11}$$

$$L_{eff} = \frac{4V}{S} \tag{2.12}$$

Scaffardi and Tocho evaluated the predicted and experimentally observed plasmonic response of extremely small gold nanoparticles in water and found that the predictions fit best with experiments if only the imaginary component of the dielectric function was modified in size damping [25]. Mathematically, any adjustment of the collision frequency will necessarily have an effect on both the real and imaginary parts of ε_{free}. However, we treat this as an empirical observation and following this procedure to correct the dielectric function values for size-related surface damping for very small particles (*D*<10 nm) according to the Drude model with a modified damping constant. In our calculations, the unmodified free electron portion was subtracted from the bulk experimentally determined dielectric function to identify the bound electron contribution. Subsequently, the free electron portion was modified using Eqs. (2.9)-(2.12) to yield a final size-corrected complex dielectric function.

2.3: FUNDAMENTAL OPTICAL INTERACTION THEORY

The conservation of energy for electromagnetic fields is given by the Poynting theorem [27]:

$$\oint_A \boldsymbol{S} \cdot \hat{n}\, dA = -½ \int_V \boldsymbol{J}^* \cdot \boldsymbol{E}\, dV - ½ \int_V \left(\boldsymbol{E} \cdot \frac{d\boldsymbol{D}}{dt} + \boldsymbol{H} \cdot \frac{d\boldsymbol{B}}{dt} \right) dV \tag{2.13}$$

The Poynting theorem states that the flow of energy across a control boundary (left hand side) is equivalent to the amount of energy consumed within the control volume as a result of the electromagnetic interactions (right hand side). The flow of energy across the boundary is given by the normal component of the Poynting vector integrated across the control volume surface. The terms on the right side refer to the conduction heating and energy stored in the electromagnetic fields within the volume, respectively. Here, asterisks indicate the complex conjugate of the value, and bold typeface indicates vectors. The Poynting vector, S, describes the magnitude and direction of electromagnetic flow at a specific location and is given by the cross product of the electric and magnetic fields (Eq. (2.14)).

$$\boldsymbol{S} = ½(\boldsymbol{E} \times \boldsymbol{H}^*) = ½(\boldsymbol{E}_{inc} + \boldsymbol{E}_{sca}) \times (\boldsymbol{H}_{inc}^* + \boldsymbol{H}_{sca}^*) \tag{2.14}$$

The optical electric and magnetic fields present around any arbitrary scatterer consist of a superposition of the electromagnetic fields present due to the incident (*inc*) and scattered (*sca*) light at each point in space. Equation (2.15) shows the Poynting vector components that can be identified to describe the total Poynting vector, $\boldsymbol{S}$, in terms of the scattered fields, $\boldsymbol{S}_{sca}$, the incident fields, $\boldsymbol{S}_{inc}$, and the interaction between these fields, $\boldsymbol{S}_{ext}$.

$$\begin{gathered}\boldsymbol{S} = \boldsymbol{S}_{sca} + \boldsymbol{S}_{inc} + \boldsymbol{S}_{ext} \\ \boldsymbol{S}_{sca} = ½(\boldsymbol{E}_{sca} \times \boldsymbol{H}_{sca}^*) \\ \boldsymbol{S}_{inc} = ½(\boldsymbol{E}_{inc} \times \boldsymbol{H}_{inc}^*) \\ \boldsymbol{S}_{ext} = ½(\boldsymbol{E}_{inc} \times \boldsymbol{H}_{sca}^* + \boldsymbol{E}_{sca} \times \boldsymbol{H}_{inc}^*)\end{gathered} \tag{2.15}$$

Equation (2.16) shows the integration of the scalar product of the Poynting vector with a unit vector surface normal $\hat{n}$ over a closed surface surrounding the particle. This term provides the total energy flow across the boundary, namely the absorbed energy by the nanoparticle (*NP*).

$$Q_{abs} = \frac{-1}{I_0 A_{CS}} \oint_{NP} \boldsymbol{S} \cdot \hat{n}\, dA \tag{2.16}$$

Each component of the Poynting vector can similarly be integrated over the area of the control surface to determine the constituent optical interactions:

$$\begin{aligned} Q_{ext} &= \frac{-1}{I_0 A_{CS}} \oint_{\mathrm{NP}} \boldsymbol{S}_{ext} \cdot \hat{n} dA \\ Q_{sca} &= \frac{1}{I_0 A_{CS}} \oint_{\mathrm{NP}} \boldsymbol{S}_{sca} \cdot \hat{n} dA \\ Q_{inc} &= \frac{-1}{I_0 A_{CS}} \oint_{\mathrm{NP}} \boldsymbol{S}_{inc} \cdot \hat{n} dA \end{aligned} \tag{2.17}$$

Unitless interaction efficiencies, Q, are obtained if the interaction is normalized by the amount of optical energy incident on the area 'shadowed' by the particle, $I_0 A_{CS}$, where in I_0 is the uniform incoming intensity and A_{CS} is the geometrical cross-section of the particle. These efficiencies are useful when comparing the optical response of plasmonic particles of different sizes and shapes. They can be much larger than 1, indicating that the particle draws in light from an area significantly larger than the particle itself, on account of the resonant interaction between the collective oscillations of electrons in the particle and the incident light. The sum of these four positive efficiency terms provides the fundamental optical interaction expression:

$$Q_{ext} = Q_{sca} + Q_{abs} - Q_{inc} \tag{2.18}$$

The Q_{inc} efficiency term represents the amount of energy that would be consumed by the medium in the absence of the particle. The term Q_{inc} vanishes for non-absorbing media because the same amount of energy leaves the control volume as enters and is thus not included in the standard expression of the optical interaction theorem.

The expressions shown in this section are generally valid for all particle shapes, as they are based only on an expression of energy conservation for optical electromagnetic energy flow. Arriving at useful solutions for these equations, however, requires the calculation of the fields around a scattering object, which can be challenging and approximations or numerical methods are often used to reach estimated solutions.

2.4: ANALYTICAL METHODS FOR SPHERICAL NANOPARTICLES (MIE THEORY)

An exact analytical solution can be obtained for the special case of a plane wave light interacting with a sphere in a non-absorbing medium ($Q_{inc} = 0$). The groundbreaking work of Gustav Mie included the exact analytical description of electromagnetic waves interacting with a sphere [6]. Mie theory provides this solution by expressing the incident and scattered electric and magnetic fields inside and outside of the sphere through a series expansion in vector spherical harmonics [7]. The electric and magnetic fields at each point can then be determined by summing the contributions of each order n in the series expansion. Assuming that the electromagnetic fields are finite at the center of the sphere, the continuity of the tangential components at the sphere surface boundary, we can arrive at a system of linear equations. We can then solve these equations to determine the harmonic coefficients of the system for each order n of the expansion: a_n and b_n for the fields outside the particle, shown in Eq. (2.19), and c_n and d_n within the particle, shown in Eq. (2.20).

$$a_n = \frac{m\psi_n(mx)\psi_n'(x) - \psi_n(x)\psi_n'(mx)}{m\psi_n(mx)\xi_n'(x) - \xi_n(x)\psi_n'(mx)}$$

$$b_n = \frac{\psi_n(mx)\psi_n'(x) - m\psi_n(x)\psi_n'(mx)}{\psi_n(mx)\xi_n'(x) - m\xi_n(x)\psi_n'(mx)} \tag{2.19}$$

$$c_n = \frac{m\psi_n(x)\xi_n'(x) - m\xi_n(x)\psi_n'(x)}{\psi_n(mx)\xi_n'(x) - m\xi_n(x)\psi_n'(mx)}$$

$$d_n = \frac{m\psi_n(x)\xi_n'(x) - m\xi_n(x)\psi_n'(mx)}{m\psi_n(mx)\xi_n'(x) - \xi_n(x)\psi_n'(mx)} \tag{2.20}$$

The Riccati-Bessel functions, ψ_n and ξ_n, and their derivatives present in Eqs. (2.19) and (2.20) can be numerically determined using either upward or downward regression [7]. For very large spheres, downward regression should be used, but a comparison of both methods showed that upward regression was sufficient for all nanospheres studied.

The fields at each point can be used to determine the Poynting vector components. The integral over a spherical surface surrounding the scatterer can subsequently be found using orthogonality and term-by-term integration. Finally, compact, elegant expressions for the interaction efficiencies can be found by eliminating the purely real Riccati-Bessel functions to yield equations that depend only on the harmonic coefficients of the particle in the medium [7].

$$\begin{gathered}
Q_{ext} = \frac{2}{k^2r^2}\sum_{n=1}^{\infty}(2n+1)Re\{a_n + b_n\} \\
Q_{sca} = \frac{2}{k^2r^2}\sum_{n=1}^{\infty}(2n+1)(|a_n|^2 - |b_n|^2) \\
Q_{inc} = 0 \\
Q_{ext} = Q_{abs} + Q_{sca}
\end{gathered} \tag{2.21}$$

The variable r in Eq. (2.21) is the radius of the sphere, and k is the wave number of light in the medium surrounding the particle. For a given wavelength of light in a vacuum, λ, and refractive index of the surrounding medium, m, the wave number can be expressed as shown in (2.22).

$$k = \frac{2\pi m}{\lambda} \tag{2.22}$$

We developed our own codes for all calculations based on Mie theory for optical efficiencies, electromagnetic fields inside and outside the particle, and angular-dependent scattering amplitudes, asymmetry parameter, and phase-functions. We developed these codes to be valid for particles embedded in either dielectric (non-absorbing) or absorptive media. We extensively validated our code against previously published values for the harmonic coefficients, optical interaction efficiencies, scattering amplitudes, and electromagnetic fields inside and outside the sphere.

2.5: DISCRETE DIPOLE APPROXIMATION

We use the Discrete Dipole Approximation (DDA) method for electromagnetic calculations of non-spherical shapes throughout this dissertation [28,29]. In DDA simulations, the simulated geometry is divided into small cubic regions, within which the induced dipole polarization is assumed to be uniform. The sum interaction of the dipole polarizations can be used to determine the total interaction of light with the entire structure. DDA only simulates the structures of interest, and does not need to explicitly compute the boundary conditions and external regions. This difference in calculation technique makes DDA computationally efficient, but DDA is an approximation. The approximation becomes exact as the dipole size becomes infinitely small. Researchers have implemented DDA successfully for many different applications in simulating light interactions with particles, including interstellar dust, blood cells, and colloidal nanoparticles [30,31,3]. The discrete dipole approximation method has been extensively reviewed in the literature [32,33,34].

In short, the DDA method is based on solving the complex polarization, $\widetilde{\boldsymbol{P}}$, at a given location f induced by the direct interaction with the incident field, $\widetilde{\boldsymbol{E}}_{inc}$, plus the summed effect of all other dipoles in the structure on the given dipole. The fundamental equation of the discrete dipole approximation describes how a set of dipolar regions respond to an incident electromagnetic field as given by:

$$\widetilde{\boldsymbol{P}}_{\boldsymbol{f}} = \alpha_f \widetilde{\boldsymbol{E}}_{inc,f} + \sum_{\boldsymbol{f \neq h}}^{\boldsymbol{N}} \overline{\boldsymbol{G}}_{f,h} \widetilde{\boldsymbol{P}}_h \tag{2.23}$$

Here, the Green's function $\overline{\boldsymbol{G}}_{f,h}$ can be used to determine the effect of a dipole in the system at position h on another dipole at position f. This effect is considered for all dipoles in the system, where the total number of dipoles in the simulated region is denoted N. Boldface type with an tilde indicates a complex vector value, while the bar indicates a matrix. The term α_f represents the polarizability at a given dipole location f, which can be related to the optical properties of the material. Various polarizability definitions have been proposed and developed including the promising filtered-coupled dipole (FCD) approach, but we focus on the lattice dispersion relation (LDR) for most simulations, as explained in [35]. The expression in Eq. (2.23) yields a set of linear equations where the total polarization response of each dipole can be iterated until no further change is observed. Very complicated electromagnetic interactions, including higher order responses, can be observed from the interaction of many small dipole elements.

A plane wave propagating in a direction specified by the wave vector $\boldsymbol{k}$ at a location m given by a vector $\boldsymbol{r}$ can be expressed as shown in Eq. (2.24). As all fields are linearly dependent on the initial field strength E_0, the final fields can be normalized by the initial intensity to provide enhancement values.

$$\vec{\mathbf{E}}_{inc,f}\left(\vec{\mathbf{r}}_f\right) = \mathrm{E}_0 e^{i\vec{\mathbf{k}}\cdot\vec{\mathbf{r}}_f} \tag{2.24}$$

The Green's function operator, shown in Eq. (2.25), can be used to calculate the effect of each dipole on another.

$$\bar{\mathbf{G}}_{f,h}\left(\vec{\boldsymbol{r}}_{f,h}\right) = \frac{e^{ik|\mathrm{r}|}}{|\mathrm{r}|^3}\left[k^2|\mathrm{r}|^2\left((\hat{r}\times\bar{\boldsymbol{I}})\times\hat{r}\right) + (1-ik|\mathrm{r}|)(3\hat{r}(\hat{r}\cdot\bar{\boldsymbol{I}})-\bar{\boldsymbol{I}})\right] \tag{2.25}$$

Here, the vector $\vec{\boldsymbol{r}}_{m,n}$ corresponds to the direction and distance between dipoles f and h, while the magnitude is given by $|\underline{r}|$ and the direction is given by unit vector $\hat{r}$. The term $\bar{\boldsymbol{I}}$ represents an identity matrix (diagonal matrix of ones) for the operation of the Green's function on the polarization vector.

Once the polarizations are found using the Green's function, incident field, and polarizability, the electric field at that location can also be found in a direct expression from the material properties, shown in Eq. (2.26). In this equation, the variable d is size of the cubic dipole unit (d^3 is the volume), and ε_m is the relative permittivity (or complex dielectric function) of the material at that location.

$$\vec{\mathbf{E}}_m = \frac{4\pi}{d^3(1-\varepsilon_m)}\vec{\mathbf{P}}_m \tag{2.26}$$

Equations (2.27), (2.28), and (2.29) show how the standard optical interaction efficiencies can be obtained from the computed polarizations, $\boldsymbol{P}$, and fields, $\boldsymbol{E}$, at each dipole location m. To account for the different physical cross-sections 'seen' by the light for different orientations of a non-spherical particle, the area in the denominator is usually replaced with an effective area, A_{eff}, given by the cross-sectional area of a volume-equivalent sphere.

$$Q_{ext} = \frac{4\pi k}{A_{eff}} \sum_{i=1}^{N} Im\{\vec{\boldsymbol{P}}_i \cdot \vec{\boldsymbol{E}}^*_{i,inc}\} \tag{2.27}$$

$$Q_{abs} = \frac{4\pi k}{A_{eff}} \sum_{i=1}^{N} Im\{\vec{\boldsymbol{P}}_i \cdot \vec{\boldsymbol{E}}^*_{i,total}\} \tag{2.28}$$

$$Q_{sca} = Q_{ext} - Q_{abs} \tag{2.29}$$

There are several different open source implementations of the discrete dipole method. The relative advantages and disadvantages of each have been recently reviewed [29] . The most well-known DDA package is DDSCAT by Draine and Flatau, which was the first widely available DDA code. After early experiments with the DDSCAT, we chose the DDA computation package ADDA, developed by Yurkin and Hoekstra at the University of Amsterdam, for our calculations because of demonstrated speed and efficiency, and access to parallel processing capabilities [34,36]. Parallel computing is necessary for the simulation of large computational domains. ADDA also allows easy access to dipole polarization vector data at each volume element (voxel), which is important for our calculations of electromagnetic fields at arbitrary locations. We rely extensively on auxiliary Matlab programs that we developed to enhance the capabilities of ADDA for material properties, geometry generation, batch and shell file processing, spectra generation, and near-field calculations.

2.6: BENCHMARKING DDA CALCULATIONS WITH MIE THEORY

Before using DDA for optical simulations of non-spherical plasmonic particles, we initially verified the accuracy of the method through comparison with Mie theory calculations for spherical geometries. The discrete dipole approximation method was initially developed for the simulation of interstellar dust in a vacuum medium [32,28], but the method should theoretically be extensible for any material in an arbitrary embedding media. The accuracy of DDA for the calculation of interaction cross-sections has been investigated for general cases [29,37], but the outset of our simulation efforts, no quantitative evaluations of the accuracy of DDA for plasmonic metal nanoparticles at near-infrared wavelengths were available. Near-infrared wavelengths are interesting because it corresponds to the center wavelength of Titanium:Sapphire (Ti:Sa) ultrafast lasers, which are often used for nanostructuring and biomedical studies. It was thus necessary for us to test the performance of the method for relevant particle sizes, materials, and incident wavelengths.

Early efforts in the development of DDA provided several convergence criteria that would imply accuracy if they were satisfied, each based on the assumptions made in the approximation. The first proposed criterion for the accuracy of the DDA method is that the lattice spacing, or dipole cube size, is small compared to the wavelength of light inside the scattering material, which can be expressed mathematically as shown in Eq. (2.30) [33].

$$|\tilde{m}|kd < 1 \tag{2.30}$$

In this non-dimensional figure of merit, $|\tilde{m}|$ is the magnitude of the complex index of refraction, k is the wave vector and d is the side length of a single dipole cube. In this work, we typically refer to the number of dipoles *ND* across the characteristic dimension *D* of a particle, where *ND* = *D/d*.

It was originally suggested that if the inequality in Eq. (2.30) was satisfied, then the DDA method should yield accurate results [33]. This first criterion is related to the fundamental approximation of the discrete dipole approximation, which is that the polarization can be approximated as constant over some small but finite region. The second criterion for DDA accuracy is that the lattice spacing is small relative to the radius of curvature of the particle, which relates primarily to the discretization and accurate simulation of the shape. While these criteria can be readily satisfied with the modern computational capabilities, no indication of the error on the optical interaction terms (extinction, absorption and scattering cross-sections) can be easily determined with these 'rules of thumb'.

We also consider another for evaluating the accuracy of DDA calculations. First, we recognize that DDA accuracy will be lowest for shapes with a large radius of curvature and large surface area relative to the volume. Cubic domains are generally poor approximation for curved particle shapes at the surface. Therefore, simulating spheres using DDA and comparing the results to the exact values obtained from Mie theory will provide a good estimate of the maximum error expected for a given particle volume. This approach can also be used to understand the effect of the refractive index on accuracy by isolating that effect.

First, we evaluate the effect of the number of unit dipoles for a sphere of specific sizes and material properties. The discretization of a scattering object can have a strong effect on the calculated properties if done improperly. The shape approximation becomes more accurate as the size of the cubic dipole unit decreases relative to the total particle size, shown in Figure 2.3.

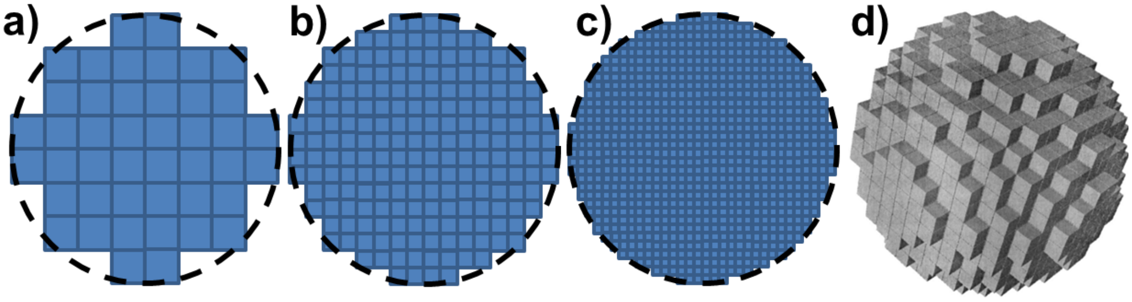

Figure 2.3: Representations of the shape accuracy in DDA simulations. *The cross section of a sphere is shown with a) 8, b) 16 or c) 32 dipoles across the diameter. d) A three-dimensional representation of a sphere consisting of cubic dipoles* ***[38]****. Increasing the number of dipoles for a curved particle generally leads to a more accurate approximation of the particle shape.*

The second major effect of simulating a three-dimensional object by the summed response of a set of small cubes has to do with the fundamental approximation of the DDA method. As mentioned previously, the discrete dipole approximation becomes an exact solution as the dipole size becomes infinitely small. As the size of the dipole is finite, this implies that the approximation of a constant dipolar response over a discrete volume can lead to inaccuracies. The accuracy of the calculated optical interaction cross-sections can be improved by decreasing the size of the cubic dipoles which make up the simulated nanoparticle, on account of two separate effects: better resolution of curvature as well as improving the fundamental accuracy of DDA. As the size of the dipoles decreases, corresponding to an increase in the number of dipoles across a given sphere diameter, the calculated cross-sections converge towards the exact value.

We first tested DDA for the calculation of purely dielectric spheres to isolate and evaluate the shape effect of discretizing a curved surface with a set of cubic domains. A very limited number of dipoles can be used to accurately approximate the particle optical response across the visible and near-infrared spectrum. For example, our DDA calculations for a 150 nm silica sphere in the wavelength range of 400 to 900 nm have a maximum relative error of only 1.9% in the scattering cross section with a very small $ND = 8$ (total number of dipoles = 210). This was simulated across the whole spectrum at 10 nm intervals in about 3 seconds on a personal computer. We also find that the accuracy increases with wavelength for a given discretization level because of the decreasing refractive index and wave number. These results imply that, at least for the interaction cross-sections, the shape error is a minor effect. These simulations had a maximum $|\tilde{m}|kd$ of 0.43, showing that the inequality provides a reasonable degree of accuracy in this case.

We find that a much lower non-dimensional convergence parameter is required to achieve similar accuracy for metal nanoparticles. The large imaginary component of the refractive index in the long wavelength region causes a significant error unless a large number of dipoles are used to reduce the error due to finite dipole size. Figure 2.4 presents the optical interaction efficiency spectra of three sizes of gold nanospheres in water calculated with DDA and compared with the exact Mie theory values. For the same discretization, the accuracy of the absorption efficiency degrades at long wavelengths and for larger particles, although the overall trends, scattering and extinction efficiencies all remain similar.

For an isolated 50 nm gold nanospheres at the plasmon resonance condition (λ = 532 nm, in water), the errors in the absorption and scattering cross-sections were 4.5% and 2.4%, respectively, for a DDA simulation with 64 dipoles across the sphere diameter (1.4×10^5 total dipole elements) as compared with the exact Mie solution. For the same size sphere simulated at near-infrared wavelengths (λ = 780 nm) in an air environment with the same discretization, the error for DDA calculations in the scattering cross-section remains relatively small (3.6 %), indicating that low dipole DDA simulations are useful for scattering calculations even for large refractive indices.

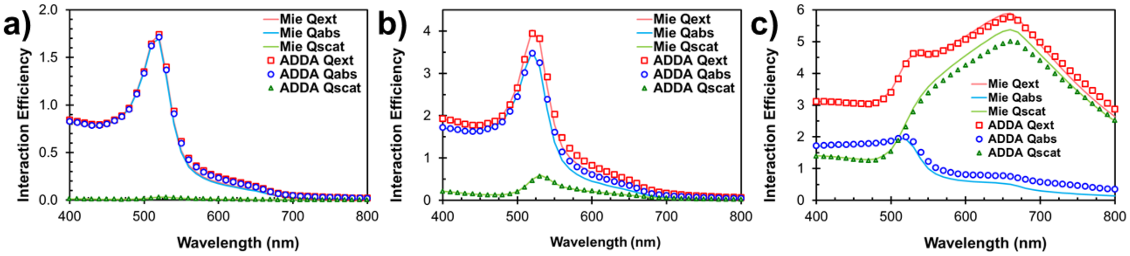

Figure 2.4: Comparison of DDA results with exact values from Mie theory. *The interaction efficiencies are shown for a) 25 nm, b) 50 nm, and c) 150 nm gold spheres in an aqueous environment. The accuracy degrades for larger particles in the red-NIR portion of the spectrum. All DDA simulations are discretized with 48 dipoles across the sphere diameter.*

However, DDA tends to overestimate the absorption cross-section for large refractive indices. We observe large relative errors in the absorption (67%) compared with the exact Mie solution, even though the $|\tilde{m}|kd$ parameter is only 0.03 under these conditions. This suggests that a much more stringent requirement than the conventional Eq. (2.30) should be observed for DDA calculations in the near-infrared region. Part of the reduced accuracy at long wavelengths is due to the low value for the absorption efficiency: $Q_{abs} = 0.0151$ according to Mie theory. We attribute this inaccuracy to the larger absolute magnitude of the index of refraction present at longer wavelengths and increased relative index of refraction at the interface.

If the number of dipoles across the sphere diameter is increased to 256 (8.8×10^6 dipoles in total), the error in the scattering cross-section almost vanishes (0.9%), while the relative error in the absorption cross-section improves to 17.9% for a 50 nm sphere at

780 nm in an air environment, although improved calculation accuracy comes at the cost of increased convergence time for near-infrared wavelengths. In all cases, the predicted absorption cross-section is larger than the Mie solution, and thus can be viewed as a 'worst case' limiting estimate. The convergence of the interaction efficiency with increasing number of dipoles is shown in Figure 2.5 for three different sizes of gold nanoparticle at a single wavelength (λ=780 nm) in water.

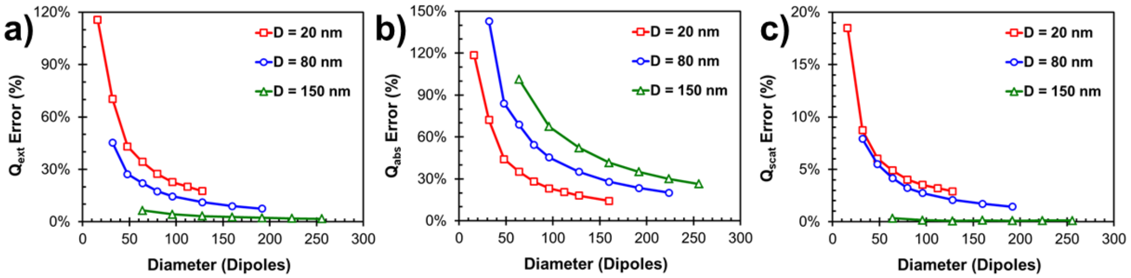

Figure 2.5: Convergence of DDA calculations compared with Mie theory. *The error is presented for three sizes of gold spheres in water at a vacuum wavelength of 780 nm as a function of increasing number of dipoles across the diameter. Percent errors in the optical interaction efficiencies are shown for a) extinction efficiency, b) absorption efficiency, and c) scattering efficiency.*

As described above, the error in the calculated absorption cross-section can be a concern for DDA calculations for gold nanoparticles at near-infrared wavelengths. However, judicious use of large numbers of dipoles can be used to improve the accuracy to acceptable levels. The number of dipoles across the diameter presented in Figure 2.3 should be taken for illustration purposes only. When possible, we kept DDA dipole cell sizes below 1 nm to resolve particle curvature and to promote simulation accuracy. In our simulations, the $|\tilde{m}|kd$ non-dimensional parameter was set as low as possible, typically less than 0.01, by increasing the dipole number as far as available computational resources allowed.

A recent and specifically relevant paper [39], which acknowledges our input, studied the use of DDA for the simulation of gold nanoparticles in the near-infrared. Similar to our findings, they observed similar trends and found that the error in absorption cross-section could be large for gold nanoparticles at near-infrared wavelengths. In addition, the authors also found that the filtered coupled dipole (FCD) DDA solution method could provide more accurate results for interaction cross-sections. Our own calculations had previously shown that the FCD polarization prescription is superior for the calculation of interaction cross-sections for large refractive indices [39], but complications when using the FCD interaction method for near-field calculations led us to use LDR for all presented DDA results.

2.7: NANOPARTICLE SAMPLE CHARACTERIZATION AND MODELING

Numerical simulations must be able to simulate and provide accurate information about real, physical plasmonic nanoparticles or they are of no practical use, whatever the mathematical theory. Various research groups have published electromagnetic simulation studies without any comparison to any experimental data, which increases the uncertainty on their use and conclusions. Throughout our studies, we compare experimental and simulated optical properties of plasmonic nanoparticles to provide information on:

- Similarities and differences between experiments and simulations
- Ratio of scattering to absorption in optical extinction
- Effect of varying different parameters on the optical properties

For example, experimentally determined extinction spectra will almost always have a much broader plasmon peak than a simulation that uses an average nanoparticle size and shape. This difference occurs because an experimental measurement of a colloid will measure the summed response of millions of nanoparticles, all of which are slightly different sizes, and the overlap of the different plasmon peak positions results in a broadening of the peak. However, we can account for this difference by explicitly simulating a range of particle sizes and shapes, or we can perform single nanoparticle spectroscopy. It is time-consuming to synthesize and characterize a set of nanoparticles, and thus it is preferable to rapidly simulate a range of parameters to determine optimal conditions and the most important contributors to a plasmonic response. Finally, if the experimentally measured optical properties can be successfully matched using simulations, then the simulations could also provide information about more difficult to measure properties, such as the near-field enhancement and corresponding nonlinear optical response.

Ultraviolet-visible-near infrared (UV-Vis-NIR) spectrometry is a common method that can be used to rapidly measure the attenuation of light as a function of wavelength. Typical measurements using this technique take less than a minute and can be measured in a colloidal solution or on a surface. UV-Vis-NIR spectrometry can readily determine the plasmon peak for an ensemble of nanoparticles. Provided that the nanoparticles in solution are sufficiently dilute, the optical response can be extrapolated using the simulations of a single particle. It can be difficult to experimentally determine the exact concentration of gold nanoparticles in solution, so UV-Vis-NIR spectrometry data is usually normalized to a peak value of one for comparison purposes. The plasmonic peak position and width found from experimental absorbance values can then be compared to normalized simulated extinction calculations.

For spherical particles, simulations can be used to determine the nanoparticle size and polydispersity from the observed peak wavelength and width, respectively. However, nanorods and other asymmetrical particle shapes can lead to ambiguity in the optical response as the peak position is no longer directly correlated with the nanoparticle size. As mentioned previously, a nanorod with a diameter of 10 nm and aspect ratio 4 of will have the same longitudinal peak position (λ=780 nm) as a nanorod with a diameter of 50 nm and aspect ratio of 2.75. Only limited differences in the transverse resonance peak position can be observed. The ratio of the volumes of these two nanoparticles is more than 80, but the optical absorbance is very similar in the visible and near-infrared spectrum.

An alternate method of measuring a sample of nanoparticles must be employed to distinguish between these samples. An integrating sphere can be used to determine the ratio of scattering to absorption, which can be related to the volume of the nanoparticle [40]. However, this approach can not necessarily distinguish between the optical response of two different asymmetric particle shapes of similar volume, such as a nanorod and a triangular prism. These particle shapes can have very different near-field properties, so a technique for directly imaging the nanoparticle size and shape should be used. Electron microscopy techniques are particularly well suited to this task. Sub-nanometer resolution can be obtained with modern electron microscopy instruments, which can be used to fully characterize the nanoparticle size and shape. Electron microscope modalities include scanning electron microscopy (SEM), where scattered electrons are detected as an electron beam is scanned across the particle surface, transmission electron microscopy (TEM), where the spatial absorption of electrons is detected behind the sample, and a hybrid scanning transmission microscopy (STEM) method. A droplet of colloidal plasmonic nanoparticle solution is typically dried on a flat silicon substrate or an ultrathin grid-supported membrane for electron microscopy imaging. We use this technique to measure hundreds of nanoparticles to directly determine the size and shape dispersity of a set of nanoparticles.

2.7.1: Characterization of Nanoparticle Samples

We characterized colloidal gold nanoparticle samples to provide input on the effect of nanoparticle geometry using the previously described electromagnetic simulation methods. Results for four sets of nanoparticles are presented, including two spherical particles (AuNS) and two nanorods (AuNR) of various sizes. Three of the samples were purchased from commercial sources, including 150 nm spheres (AuNS2, British Biocell International, BBI) and the nanorod colloidal nanorod solutions (Nanopartz, abbreviated as NPTZ). UV-Vis-NIR spectrometry was performed on each of the samples by Ben-Yakar group member Nick Durr. The final spherical nanoparticle solution was synthesized by our group with a nominal diameter of 50 nm (AuNS1). The nanoparticles were very stable, with no appreciable shifts observed in the experimental measurements over a one year period. Figure 2.6 shows the experimental spectra for the measured particles.

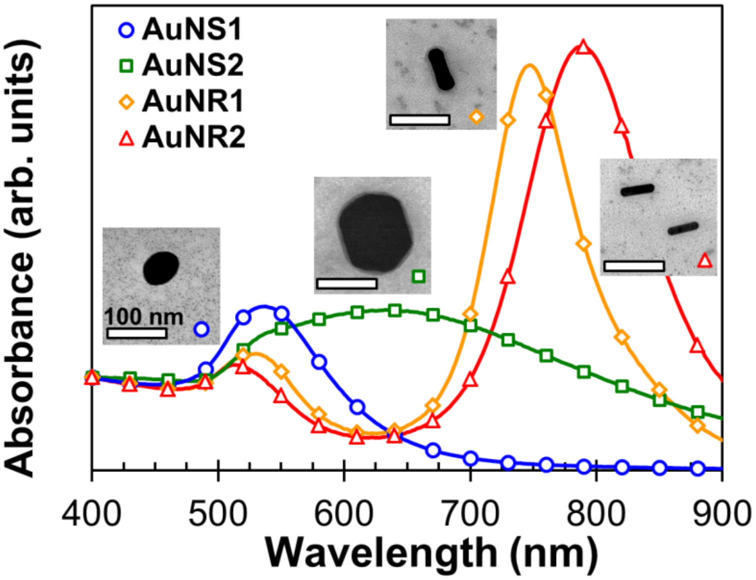

Figure 2.6: Absorbance spectra and sample images of nanoparticle test samples. *The inset STEM images are all 200 nm square, showing representative nanoparticles for each of the measured colloidal nanoparticle sets.*

Table 2.2 presents the measurements and nominal values for the nanoparticle samples considered in this study. We characterized the physical dimensions of each nanoparticle sample with high- resolution field-emission scanning transmission electron microscopy (STEM). A 2 μL aliquot of each nanoparticle solution of each sample was air dried with heating at ~70 °C on a carbon film-on-copper grid (Cu-400CN, Grid Tech). Imaging was performed on Hitachi S-5500 STEM in transmission mode at greater than 100,000× magnification. We imaged all samples using STEM to obtain nanoparticle sizes, shapes and size distributions by measuring particles for each colloidal solution using the line function in the ImageJ software package.

Table 2.2: Nanoparticle Characterization Summary and Results

Sample	**AuNS1**	**AuNS2**	**AuNR1**	**AuNR4**
Supplier	In House	BBI	NPTZ	NPTZ
Nom. Width (nm)	50	150±12	10	25
Nom. Length (nm)	50	150±12	38.5	85.9
Nom. Aspect Ratio	1	1	3.85	3.44
Nom. Peak λ (nm)	-	-	780	750
Exp. Peak λ (nm)	537 ± 2	633 ± 2	788 ± 2	754 ± 3
STEM Width (nm)	49 ± 7	163 ± 9	14 ± 4	27.6 ± 2.0
STEM Length (nm)	63 ± 11	176 ± 14	54 ± 9	76.5 ± 4.4
STEM Aspect Ratio	1.27±0.14	1.07±0.05	3.95±0.91	2.77 ± 0.21

It is worth noting that the nanoparticles all deviate from the nominal values, indicating some variance in the fabrication process, even for commercially-sourced nanoparticles. This analysis provided a range in size and aspect ratio for the nanoparticle samples. We also found several points of interest regarding the nanoparticle samples. First, the AuNS1 sample had some ellipticity, while the larger AuNS2 particles were quasi-spherical with faceted surfaces. The AuNR1 nanoparticles revealed a bone-like shape, as has been commonly reported in the scientific literature on gold nanorod synthesis. The AuNR2 sample, on the other hand, was characterized by very uniform cross-sectional diameters along the length of the nanorods.

2.7.2: Reproduction of Experimental Spectra

We simulated the absorbance spectrum for each particle, based on the size and shape measurements found in the previous section. These simulations were important for two reasons: (1) the knowledge of the extinction coefficient allows for accurate determination of particle concentration, and (2) simulating the absorbance allows us to understand the relative roles of scattering and absorption that contribute to the total extinction coefficient of the particle.

The simulated normalized extinction cross-sections for the average nanoparticle size and shape are here compared with the experimental nanoparticle absorbance spectra with a focus on reproducing the plasmonic peak position and absorbance spectral features. For all nanoparticle samples, the colloidal solutions were simulated at evenly spaced intervals across a range of wavelengths from 400 to 900 nm in a water environment using the measured average nanoparticle size and shape as found in the previous section. We assumed the particles were far enough apart to be simulated as isolated particles in all cases. The complex gold refractive index at the irradiation wavelength was obtained from a curve fit to experimentally-determined refractive index values for bulk gold. We calculated the absorption and scattering cross sections of all non-spherical shapes using DDA accounting for the size distribution and orientation of the nanoparticles. Here we apply the DDA method using a minimum of 48 dipoles across the diameter of the nanorod to minimize shape discrepancy and improve the cross-sectional accuracy of the results.

As the AuNS1 sample consisted of elliptical particles, and they thus had to be simulated as spheroids with a short axis diameter of 49 nm and an aspect ratio of 1.27. The slight ellipticity in the small-diameter nanospheres must be taken in to account to properly model the absorbance spectrum. The AuNS2 sample was modeled as a sphere using Mie theory. The AuNR2 could be simulated as hemispherically-capped cylinders with an aspect ratio of 3.95. Careful analysis of the STEM images indicated that sample AuNR1 had an hourglass-like shape with flattened ends and a tapered midsection. We simulated this nanorod sample as an elliptically-capped rotationally-symmetric shape with a sinusoidally-varying midsection. This rod had an aspect ratio of 2.77 with a maximum diameter of 27.6 nm and a minimum diameter of 23.9 nm.

To reproduce the features observed in the experimental absorbance spectra, we simulate the asymmetric samples at different orientations of the nanoparticle long axis with respect to the incident light polarization and propagation directions. Specifically, we simulate the long axis along the *x* and *y* directions for light propagating in the *z* direction with linear polarization along the *x* axis to characterize the optical response for averaged orientation as in Eq. (2.33).

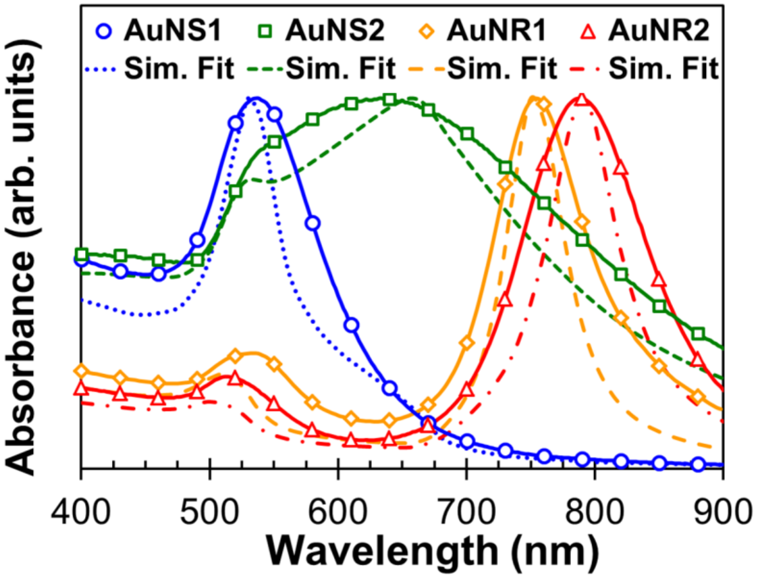

Figure 2.7: Comparison of measured and simulated absorbance for average nanoparticle sizes and shapes.

Figure 2.7 shows that the peak positions and spectral features for real nanoparticle samples can be qualitatively well fit with the computational tools available if the true shapes are simulated. The ellipsoid simulation produces the correct peak position (537 nm) for the AuNS1 nanoparticles, where a spherical approximation results in a peak well outside the experimental error (532 nm). The agreement for the AuNS2 sample is relatively poor due to the wide polydispersity of the nanoparticle sample and the faceted faces of the nanoparticles. The qualitative features of the extinction spectra, such as the short wavelength plateau and broad peak ranging from ~500 – 800 nm, are present, but the peak position is slightly separated. The shape of the AuNR2 nanorods was observed to closely match the ideal spherically-capped cylinder nanorod shape, but there were important differences for the AuNR1 nano-bone shape. The agreement in the peak position is quite satisfactory for the nanorod samples if the nanoparticle shape is accurately measured and taken into account in the DDA simulations. In all cases, the simulated spectra predict significantly narrower peaks than experimental observations show. This discrepancy occurs because the colloidal samples contain a distribution of nanoparticle sizes and shapes, as found with the STEM measurements revealed. A detailed evaluation of the simulation of the nanoparticle polydispersity is presented in the next section.

2.7.3: Detailed Simulation of One Nanorod Sample

We used the gold nanorod sample AuNR1 (Nanopartz) for our plasmon-enhanced ultrafast laser nanoablation (PLN) experiments, and therefore an extended effort was exerted to accurately simulate this nanoparticle sample. We characterized the nanorods using high-resolution SEM and scanning transmission electron microscopy (STEM) imaging (Hitachi S-5500). More than 200 individual particles were analyzed and the widths, lengths, shapes, and aspect ratios for each rod were compiled. The rods were slightly bone-shaped, had a maximum width near the ends, and had a minimum width at the waist. The average ratio of rod waist to maximum width was 0.87. From this data set, we found that the average length was 76.5 ± 4 nm, with an average width of 27.6 ± 2 nm, and a corresponding average aspect ratio of 2.8 ± 0.2, using the averaged ratios of length and maximum nanorod diameters for each rod. The uncertainties given represent one standard deviation in the measured nanorods.

Simulations were performed to develop an understanding of the effects of nanoparticle shape on the plasmonic response. By carefully imaging hundreds of nanoparticles with high resolution scanning electron microscopy (SEM), we created a more realistic model of the actual particle shape and showed that it was necessary to accurately simulate the particle shape to correctly predict the plasmonic response. It is important to characterize the size of a sample of nanoparticles, but we determined that it is also important to characterize the shape. The aspect ratio has long been known to be the dominant term in controlling the peak position of the LSPR. It has been previously shown that the shape of the endcap [41] can also play an important role in the LSPR position. We found that the tapering in the center of the rod can also significantly shift the LSPR position and must be taken into account to accurately simulate nanorods. Both the flattening of the endcap and the center tapering redshift the plasmonic resonance.

Figure 2.8 shows the simulated and experimental extinction spectra of the isolated nanorods. We directed significant effort towards obtaining accurate simulations of our gold nanorods, as was also determined necessary by Ungureanu *et al*. [42]. We investigated various sets of dielectric constants and nanorod dimensions and shapes, including flat-ended cylindrical, spherically-capped nanorods, and experimentally observed shapes. The red curve shown in Fig. 1 shows the simulated spectra using the commonly assumed spherically-capped cylinder, while the blue curve shows the more experimentally representative bone shape. The bone shape and size of the rods in the simulations were modeled after the experimentally observed shapes from a set of high-resolution SEM images, as described in the previous section. Specifically, we modeled the rods as ellipsoidally-capped (e=0.6), cylindrically-symmetric shapes with a sinusoidally-varying hourglass-like tapered midsection (D_{min} = 0.87*D_{max}). We also simulated the random orientation of nanorods in a colloidal solution by averaging the extinction at four different orientations (along *x*,*y*,*z* axes and along [1,1,1]) for each of the simulated shapes.

Figure 2.8 shows that the simulations using the more realistic bone shape match experiment much better than the commonly used spherically-capped cylindrical shape. Using the Palik dielectric constants and representative bone shape, we found excellent agreement between the calculated peak position of the longitudinal resonance and the experimentally measured peak extinction. The overall spectrum shape also followed expected trends, with a peak at ~510 nm due to the transverse plasmon resonance. All subsequent simulations were done using the bone shape for the nanorods.

To take into account the effect of the observed size distribution of our nanorods in our calculations for the bone-shaped rods, we used a weighted average of the average nanorod with plus and minus two standard deviations in measured diameter and nanorod length. We found that modeling the size distribution resulted in the broadening and slight red-shifting of the longitudinal plasmon resonance, in agreement with Prescott *et al*. [41]. The nanorod extinction peak redshifts when the size distribution is modeled because larger particles have larger absolute cross-sections, slightly skewing the peak towards longer wavelengths. The additional experimentally observed peak near 530 nm is due to cuboidal shapes observed in the SEM images but not explicitly simulated.

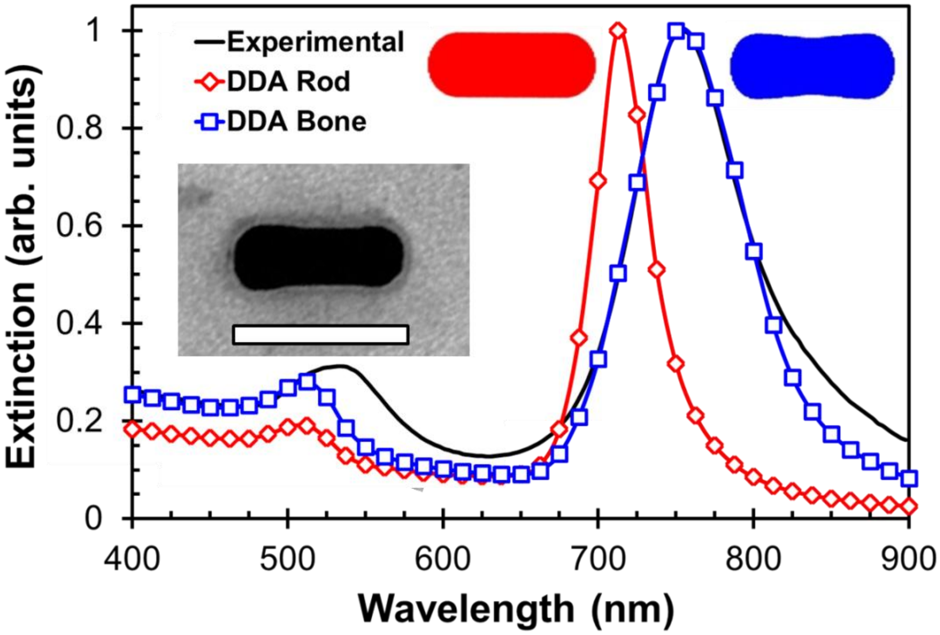

Figure 2.8: Calculated and experimental UV-Vis-NIR extinction spectra of gold nanorods. *The simulation results include two different cases: the red curve, which represents a spherically-capped cylinder and the blue curve, which represents an elliptically-capped bone. The inset shows a high-resolution SEM image of a single rod with a 75 nm scale bar. Both sets of simulations were completed with the same length, maximum width, and overall aspect ratio as the measured average values of the nanorods (28 x 77, AR = 2.8), but the bone-shaped rod simulation also includes the broadening effect of the observed nanorod size distribution (28±4 × 77±9 nm, AR = 2.8±0.3), where given ranges represent two standard deviations in nanorod size.*

It is clear that the bone shape reproduces both the extinction spectra and SEM appearance more accurately. The exceptional agreement of the simulated results with experimental observations shows that DDA can be used to accurately simulate the plasmonic behavior of gold nanorods. Our agreement between simulations and experimental results was the best shown for nanorods at the time of publication [43], and was unique in using experimentally determined values for the particle shape for a specific nanorod solution. It is important to note that only with the accurate modeling of the nanoparticle shape and size distributions do the extinction spectra match.

Simulating the scattering and extinction of realistic colloidal nanoparticle samples are important in predicting the effect of actual plasmonic particle ensembles and for designing nanoparticles for use in all further plasmonic studies, including near-field and enhancement and plasmonic solar enhancement. The computational techniques that we have developed are necessary for rapidly simulating the plasmonic properties across the entire optical spectrum, which includes hundreds of individual simulations across visible to NIR wavelengths.

2.8: OPTICAL ABSORPTION AND HEATING OF PLASMONIC NANOPARTICLES

Our initial use for the optical interaction simulations was for examining the flow of optical energy into and around the nanoparticles. Absorption is a key property in the practical application of plasmonic nanoparticles. For high intensity lasers for imaging or targeted cell destruction, absorption by the particle can lead to particle melting, and/or tissue heating. Furthermore, an understanding of the absorption properties of plasmonic particles is important for solar applications because light absorbed by plasmonic particles will serve as a loss mechanism, counteracting other gains, and should be minimized. Towards this goal, we developed numerical simulations to calculate the absorption properties of nanospheres using Mie theory and non-spherical particles using the discrete dipole method (DDA).

2.8.1 Nanoparticle Heat Transfer Model Validation

Previously published lattice expansion measurements of spherical gold nanoparticles in water by Kotaidis *et al*. [44] were first used to validate the theoretical model and the computational tools developed for this study. The calculation of the energy absorbed for spheres was performed using our Mie theory Matlab code derived from the equations given in Bohren and Huffman [7]. Our heat transfer simulations used the calculated optical absorption cross-sections (with units of area) multiplied by an incident optical fluence (units of energy per area) to determine a total amount of absorbed energy per pulse. All absorbed energy was assumed to be converted to heat, which led to an expansion of the lattice. The heat transfer model used for the following simulations was developed by previous Ben-Yakar group member Dr. Ozgur Ekici [45]. The optical energy is initially absorbed by the electrons within the nanoparticle during the pulse length of the incident laser, and the energy from the electrons is then coupled into the lattice through a two-temperature model and also coupled to a surrounding infinite water medium. We used the calculated lattice temperature change to predict the thermal expansion according to Eq. (2.31), where change in particle radius Δa is proportional to the change in temperature ΔT and the coefficient of linear expansion for gold, α_L [44].

$$\frac{\Delta a}{a} = \alpha_L(T)\Delta T \tag{2.31}$$

Using these methods, our calculation of the absorption of optical energy and conversion to heat for spherical nanoparticles showed a good agreement with previously published experimental results (Figure 2.9).

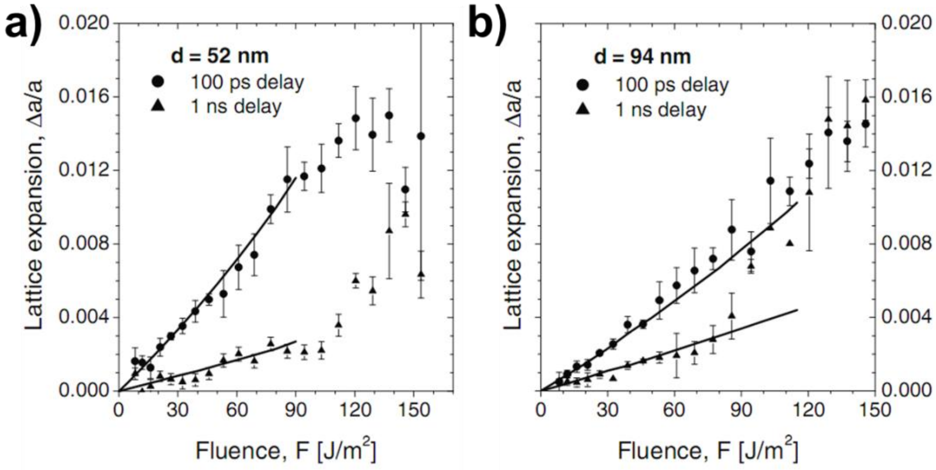

Figure 2.9: Calculations of the absorption and laser-induced heating of gold nanoparticles using extinction properties as calculated using Mie theory. *The lattice expansion of spherical gold nanoparticles of a) 52 nm and b) 94 nm diameters as a function of peak laser fluence. Lines are our calculated lattice expansion values using plasmonic simulations up to the fluence at which 90% critical temperature of water is reached, while the symbols are experimental data provided by the authors of* ***[44]****.*

Figure 2.9 shows the calculated values of the lattice expansion measurements of 52 nm and 94 nm gold particles at 100 ps and 1 ns after irradiation by a 400 nm, 100 *fs* laser pulse along with data provided by Kotaidis *et al*. [44] as a function of laser fluence. The agreement of the model predictions with the experimental data is quite satisfactory especially for the low fluence values where the measured lattice expansion increases linearly with the applied fluence for both particle sizes. It is seen that the nonlinear changes, which cannot be predicted with the presented model, are observed at earlier fluence values for the measurements with 1 ns delay compared to those with 100 ps delay. As has been discussed in detail by Kotaidis *et al*. [44], the mismatch at relatively high fluences can be attributed to the breakdown of the assumptions made in the heat transfer model due to high temperatures (close to the critical value) of surrounding water.

Therefore, it is concluded that the model and the solver employed in this study can be used to describe the heat transfer processes for the nanoparticles as long as the model assumptions are not violated.

2.8.2 Ultrafast Laser Heat Transfer in Gold Nanorods

Our primary interest in simulating the heat transfer properties of gold nanoparticles heated with ultrafast laser pulses was for determining the optical intensity limits for multiphoton imaging. Previous efforts in the Ben-Yakar group had identified gold nanorods as excellent contrast agents for deep multiphoton imaging of biological materials [46]. As described in Section 1.6: Effect of the Shape, the optical response of gold nanorods is dominated by a strong longitudinal plasmon peak in the near-infrared. The plasmonic resonance leads to significant multiphoton emission when irradiated with ultrafast laser pulses, which can then be used to create three-dimensional, optically-sectioned images by scanning the laser focus. The intense laser pulses can also lead to heating of nanoparticle, potentially leading to reshaping or destruction of the nanoparticle. It is crucial to determine the magnitude of the heating effect. Melting will result in a reshaping of the nanorod towards a sphere to minimize surface energy, which will decrease the strength of the near-infrared longitudinal plasmon resonance and weaken the multiphoton emission mechanism. Furthermore, even at reduced powers, nanoparticle heating could potentially result in explosive boiling, cavitation bubbles, or thermal damage to the surrounding biological tissues. Nanorods have also used with ultrafast lasers for localized selective hyperthermia, in which case it is important to know the localization of the temperature gradients. Thus, calculation of the fluence limits and heating behavior is necessary for effective use of these particles.

The symmetry of spherical particles precludes orientation effects; *ie*. all angular dispositions of a particle will yield identical results. However, for asymmetric particles, significant differences in the optical interaction will be observed for various orientations. For nanorods, especially in the near-infrared region, the behavior is dictated by the angle between the nanorod long-axis and the polarization of the incident beam.

We use the DDA method to simulate the optical properties of gold nanorods irradiated by near-infrared ultrafast laser pulses. At the plasmonic resonance frequency, the effective absorption efficiency can be much larger than 1, indicating that the optical cross-section is much larger than the geometrical cross-section. The absorption efficiency Q_{abs} was calculated using the computationally efficient ADDA code package. The nanorods were modeled as spherically-capped cylinders with a diameter of 14 nm and a tip-to-tip length of 48 nm, similar to typical experimental conditions. The simulation geometry was made with 128 dipoles across the nanorod diameter, and consisted of approximately 5 million dipoles. The large number of dipoles per wavelength was used to reduce the error due to the large indices of refraction of gold at these wavelengths [47]. The water environment surrounding the nanoparticles was assumed to have a uniform index of refraction of 1.333 and the complex refractive index for gold was obtained from Palik [24].

We first consider the heating of a single gold nanorod and its surrounding exposed to a single, linearly-polarized femtosecond laser pulse with a nominal fluence value of 4.70 J/m^2. At this value, the particle temperature is slightly lower than the bulk melting temperature of gold and the surrounding water temperature is near 90% of the critical temperature for water. Figure 2.10a shows the temperature profile in the water 70 *ps* after irradiation, at which point the local water temperature reaches its maximum value. Figure 2.10b shows the electron and lattice temperatures of the particle and the water temperature near the particle surface as a function of time after irradiation with a single laser pulse. The electron temperature rises during the pulse duration (250 *fs*) and reaches its maximum value at the end of the pulse. This quick electron temperature rise can be seen as an instantaneous process compared with the time scales of the subsequent electron-phonon and phonon-phonon coupling processes. Thermal equilibrium between the electrons and the lattice occurs approximately 50 *ps* after the pulse. The temperature difference at the interface between the particle surface and the adjacent water becomes negligible at around 500 *ps* after the pulse. Complete melting of the particle is observed for a fluence of 7.2 J/m^2, corresponding to an absorbed fluence of 36 fJ.

We also investigated the influences of multiple pulse irradiations on the heating of gold nanorods (Figure 2.10c). Figure 2.10c shows that the particle sheds almost all heat absorbed during one pulse by the time the next pulse arrives, even for high fluences from an oscillator-type high repetition rate of 80 MHz, where the time between pulses is only 12.5 *ns*. This result is important for two-photon luminescence imaging using the gold nanoparticles, as particles will not accumulate heat during imaging and the particles will melt only during the initial laser pulses when the laser fluence is larger than the melting threshold for a single laser pulse. This result means that particle melting or bubble formation will primarily be a single-pulse effect.

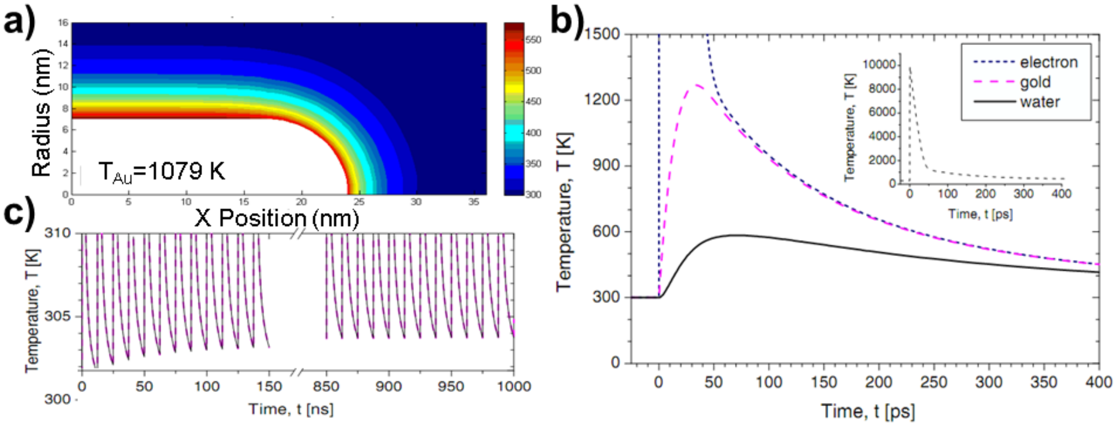

Figure 2.10: Heat transfer around a gold nanorod after the plasmonic-enhanced absorption of ultrafast laser pulses. *a) Temperature profile around the gold nanorod showing the thermal penetration distance, b) Temporal evolution of temperature profiles of the water and the electrons and lattice of a gold nanorod. In the inset, the electron temperature as a function of time is shown. c) The temperature evolution of the gold nanoparticle and water for multiple pulses at a 80 MHz repetition rate* ***[45]****.*

Nanorods in a colloidal solution will not all be aligned with the incident polarization, but will instead be randomly distributed. All three-dimensional nanorod axial configurations need to be considered to evaluate the different angular relationships between the nanorod axes and the incident polarization of the light. A nanorod perfectly aligned with the polarization of the incident light represents an extreme case for the absorption efficiency. Indeed, the absorption efficiency at 780 nm varies from $Q_{abs,max}$=11.07 to $Q_{abs,min}$=0.02 a factor of more than 500×, for this nanorod geometry for the perfectly aligned and perpendicular orientation of nanorod long axis the incident light, respectively. The nanorod long axis along the *y* and *z* axes yield nearly identical values, and can be approximated as equal. Through calculations at a sampling of data points across azimuthal and polar angles between the nanorod long axis and the polarization, we observed that the absorption efficiency varies as the square of a sinusoidal function in each angular dimension. We derived a closed-form approximation of this data, shown in Eq. (2.32).

$$Q_{abs}(\theta,\phi) = Q_{abs,max}(\sin^2\theta\cos^2\phi) + Q_{abs,min} \tag{2.32}$$

This approximation yields an error of less than 1.5% error for all calculated angle pairs. Integrating Eq. (2.32) over all angles in three dimensional space provides a simple expression, Eq. (2.33), for the average absorption cross section.

$$\bar{Q}_{abs,avg} = \frac{Q_{abs,max}}{3} + Q_{abs,min} \tag{2.33}$$

This result is applicable for an isotropic distribution of nanorods, where a nanorod is equally likely to be found at any angle, as is expected in a colloidal solution of suspended nanorods. Equation (2.33) can be used to quickly obtain an idea of the averaged properties for a nanorod sample. Furthermore, this simple formula means that the averaged response for a collection of particles can be determined with only two simulated nanorod orientations.

The absorption cross-section, and corresponding absorbed energy, of any individual gold nanorod can be significantly higher or lower than the average, because it depends strongly on the angle of the longitudinal axis with respect to the polarization of the incident light. A reduced absorption cross section implies an increase in the average fluence necessary to melt a nanorod. The difference between the fluences needed for melting between an aligned nanorod, ‘average’ nanorod, and a perpendicular nanorod are striking. Given these variations, a statistical approach is a better approach for understanding the melting of an isotropic distribution of gold nanorods in a colloidal solution.

To show the effects of orientation for isotropically distributed nanorods, we plot the percentage of nanorods that would be completely melted as a function of the incident fluence in Figure 2.11. For both sets of nanorods presented, it is observed that an increase of one order of magnitude in fluence is required to melt 65% of isotropically arranged nanorods compared with nanorods aligned perfectly parallel to the polarization of the incident light. We observe that the difference between melting fluences for the two sets of nanorods presented in Figure 2.11 becomes less significant as a higher percentage of nanorods are melted.

Our estimate of the threshold melting fluence can be compared with previously published experimental data using similar nanorod sizes from the El-Sayed group. The estimated average threshold fluence for melting all of the randomly oriented nanorods was experimentally determined by Link *et al.* [48] and found to be approximately 100 J/m^2 for an irradiation time of about 1 minute at a repetition rate of 1 kHz in a rotating cuvette. The fluence corresponds to a melted fraction of 75% of isotropically distributed nanorods in our computational model. We find this melted fraction to be in good agreement with their experimental fluence given that the nanorods in their experiment should be irradiated ~15 times during the 1 minute irradiation, which we estimate based on their stated focal volume of 0.1 μL in a 400 μL total sample size [49]. The calculations shown in Figure 2.11 are presented for a single shot laser pulses. It is clear that a larger fraction of the nanorods can be melted at a lower fluence if nanorods are exposed to multiple pulses, as the chances increase that the nanorod will be aligned with the incident pulse polarization.

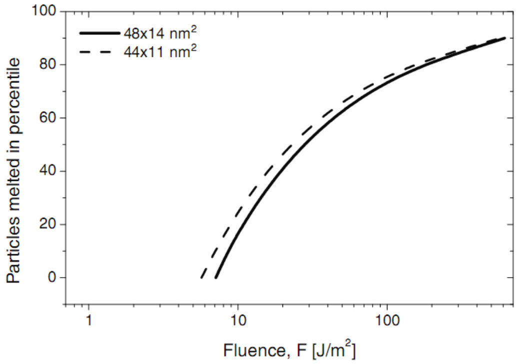

Figure 2.11: Calculations of the absorption and laser-induced heating of gold nanorods using extinction properties calculated using DDA. *The fraction of nanorods melted in a colloidal solution as a function of fluence* ***[45]****.*

As previously noted, recently, there has been much interest in the use of gold nanoparticles in biomedical applications. These simulations provide fundamental fluence limits for the usage of gold nanorods for practical ultrafast laser imaging and treatment applications. This work is described in more detail in a published manuscript [45].

2.9: CONCLUSION

In this chapter, we have identified and implemented computational techniques for simulating the optical response of plasmonic response of spherical and asymmetric plasmonic nanoparticles. First, we discussed the origin of material optical properties, then used those properties to simulate the far-field optical response of plasmonic nanoparticles. We then introduced the computational tools that we use throughout this dissertation, which could be shown to provide accurate information on real nanoparticle samples through a comparison of simulations with experimental results. Finally, this analysis was used to provide insight and thermal limits for the use of plasmonic nanoparticles with ultrafast laser irradiation.

Chapter 3: Review of Ultrafast Laser Nanoablation

Ultrafast lasers represent a nearly ideal tool for studying the plasmonic response of metal nanostructures. This is because energy can be transferred from the laser pulse to the plasmonic system with virtually no change to the particle or surroundings during the laser pulse duration. Using ultrafast lasers, many different aspects of the plasmonic behavior can be evaluated, most commonly using optical extinction, spectral effects and near-field enhancement. The plasmonic resonance can be probed using modes such as heating through vibrational analysis [50], enhanced electron emission from the surface [51], multiphoton emission from the particle [52], ablation of surrounding material [53], and reshaping of the particle [48].

In this dissertation, we use ultrafast laser nanoablation as a technique for evaluating the plasmonic resonance of asymmetrical nanoparticles while also studying the limits and mechanisms behind plasmon-mediated ultrafast laser nanoablation. To demonstrate the capability of this technique, we here review the mechanisms and techniques whereby ultrafast lasers can be used to cause material ablation, with a focus on nanoscale localization of damage effects. Understanding of how ablation occurs can be used to evaluate the near-field concentration of optical energy using plasmonic nanoparticles. Subsequently, we review four different modalities for creating laser nanoablation. Finally, we review recent applications and future prospects of near-field ablation and its current limits for the near-field confinement of *fs* laser light. The approaches outlined in this review offer several methods for opening the doors to near-field confinement and nanoablation beyond the diffraction limit. Two of the most promising applications of near-field nanoablation are nanolithography and nanosurgery.

3.1: GENERATION OF ULTRAFAST LASER PULSES

A laser operated under repetitive pulsing conditions can have much higher peak powers than continuous-wave (CW) lasers. Laser pulses with high peak intensities can be achieved in two ways: Q-switching, which is a control of the output coupling, and mode-locking, which is control of interfering laser modes within the cavity. Both methods for generating short pulses operate by building up the power circulating within the cavity and then dumping this power in intense bursts confined in time. The optical intensity present within the laser cavity can be much larger than the amount ‘lost’ from the laser cavity due to output coupling.

Pulsed lasers are often fabricated with Q-switching achieved by the controlling the optical losses in the cavity. By maintaining the laser cavity in a high-loss configuration until the gain medium reaches saturation and the highest level of population inversion, and then rapidly decreasing the cavity loss, a powerful (‘giant’) pulse can be generated. By changing the laser back to a high internal loss condition with efficient output coupling, a large amount of the energy circulating in the cavity can be dumped as a short laser pulse in the nanosecond time scale. One commonly used technique for Q-switching is acousto-optic modulation. In this case, an electrical pulse is sent to a piezo-electric device to compress a material, which will result in a change in the local index of refraction due to the mechanical strain (or pressure wave) through photoelasticity. The control of an acousto-optic modulator is limited by the speed of sound in the optical medium. If light is incident on a crystal at an angle relative to the pressure waves, Bragg scattering of the light (analogous to x-ray diffraction) can occur. The angle and the intensity of the diffracted beam can be controlled with the frequency and amplitude of the piezoelectric driver, respectively. Electro-optic modulation (active) and saturable absorbers (passive) can also be used to control the cavity losses. Q-switching techniques can be used to generate high intensity nanosecond pulses at up to megahertz repetition rates, primarily limited by the optical cavity length.

Ultrafast laser pulses, characterized by a pulse length of less than 1 picosecond (ps), can only be generated from wide bandwidth laser media. Nanosecond lasers can be used to drill and cut solid materials, but the mechanism of damage is typically heating due to the shorter time scale for heat transfer. Thus, to probe electromagnetic field-based mechanisms, shorter pulses are required. Titanium-doped sapphire crystals ($Ti:Al_2O_3$, Ti:Sapphire) are one of the most commonly used lasing media for generating ultrafast pulses. Titanium:Sapphire crystals have a stimulated emission gain peak at 780 nm and a gain bandwidth from 650 – 1100 nm. A wide gain spectrum is necessary for generating ultrafast pulses as a consequence of time-bandwidth product form of the uncertainty principle. This principle can be written in terms of the laser wavelength bandwidth $\Delta\lambda$, the minimum pulse length $\Delta\tau$, and Planck's constant, h (Eq. (3.1)).

$$\Delta\lambda\Delta\tau \geq h \tag{3.1}$$

A wide bandwidth gain medium is a fundamental requirement for ultrafast laser pulse generation, but sub-picosecond pulses cannot be generated without mode-locking. Mode-locking is the process whereby all the modes supported by the cavity are synchronized in time and phase such that the beam energy is confined to a single packet in time and space. Modes in a laser cavity are analogous to standing waves on a string, where various frequencies and numbers of nodes are supported in the cavity based on the boundary conditions. In a stable laser resonator, the cavity modes correspond to interference patterns of the laser light. Because the cavity is typically tens of thousands of wavelengths long, many different modes can be supported, but low-loss modes will typically dominate laser output. Increasing the bandwidth of the gain medium results in a strong increase in the number of modes supported by a given mode cavity. This feature is vital for the formation of ultrafast laser pulses, as the length of the pulse is inversely proportional to the mode density. With the superposition of many modes, constructive and destructive interference can be used to create a delta function-like pulse of high energy. Mode-locking can be accomplished by temporally varying the attenuation within the cavity to selectively pass only the highest intensity pulses. This attenuation can be accomplished with active mode-locking, where a modulator is oscillated at a frequency similar to the single trip cavity oscillation time, or passively, using a saturable absorber. In this manner, a set of modes can be brought into phase with a central mode, leading to cancellation of the field intensity before and after a pulse and intensification of the peak. Both mode-locking and Q-switching are used together to generate the highest peak power pulses available in the Ben-Yakar lab with the Spectra-Physics Spitfire *fs*-laser amplifier system, which can produce peak powers approaching 10 GW (10^{10} W).

The primary advantage of intense ultrafast laser pulses is the ability to induce nonlinear absorption effects. Focusing the laser can yield extremely high local electromagnetic field intensities that can be sufficient to stimulate nonlinear second, third and higher order effects, leading to multiphoton absorption and even plasma breakdown.

3.2: MECHANISMS OF ULTRAFAST LASER ABLATION

The selective laser ablation of material using the near-field confinement of light has the potential to achieve fabrication on the nanometer scale. The use of laser light for the modification of materials on the micrometer scale has been shown for many years

[54,55], but the advent of high peak intensity ultrafast lasers in the femtosecond (*fs*) regime has enabled the direct laser ablation of smaller nanoscale features with less damage to the surrounding material [56].

The extremely high laser peak intensity (>10^{12} W peak power) available with focused ultrafast lasers is an important advantage for nanostructuring. Laser-induced ionization occurs when the local electromagnetic field intensity is high enough to strip electrons from ions. At the critical free electron density, the material becomes both strongly reflective and absorbing, indicating optical breakdown, resulting in an expanding plasma that directly results in the removal of material without depending on a thermally-mediated phase change from heating. The deposition of energy on an ultrafast time scale can result in efficient material removal using low pulse energies, yielding minimal heating of the surrounding material. The resultant small heat-affected zone (HAZ) is of great interest for many applications requiring nanoscale precision, including nanofabrication and nanosurgery. The high peak intensities that can be achieved with ultrafast pulses decrease the size of the HAZ by reducing the time available for heat diffusion during the pulse, ultimately resulting in an overall decrease in the size of the affected region. Femtosecond laser pulses have been used for the modification of a variety of materials and have demonstrated advantages in industries as widely diverse as LASIK surgery and laser drilling of and cooling holes in superalloy turbine blades [57]. The effects of pulse length on ablation topography have been well studied and are clear from a comparison of the features (smaller HAZ, sharper contours) observed in the Figure 3.1 [56]. These images show the holes drilled in a 100 µm steel foil using a fluence of 4.2 J/cm^2 for the nanosecond pulse (Figure 3.1a) and only 0.5 J/cm^2 for the

200 fs pulse (Figure 3.1b). The nanosecond laser ablation shows clear evidence of melting and recast material partially ejected from the site, but the femtosecond ablation shows smooth features and minimally affected surrounding region. This is partially due to the significantly reduced fluence (8.4× less) required for laser ablation.

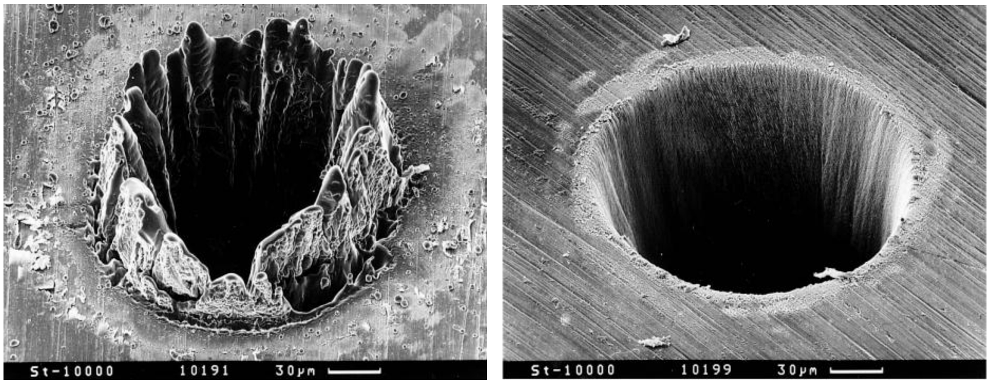

Figure 3.1: Comparison of ablation of a metal film using nanosecond and femtosecond near-infrared laser pulses. *The SEM images show multishot ablation resulting from (a) 3.3 ns and (b) 200 fs pulses. Significant melting and resolidification of the surrounding material is observed for the nanosecond pulses, while clean ablation and smooth margins are seen when using fs pulses. The images are adapted from* ***[56]****.*

As the pulse length drops from nanoseconds or picoseconds to femtoseconds, the features become more uniform and bulk heating plays a small to negligible role in the ablation process. Indeed, sub-picosecond pulses can even be used to ablate materials which are transparent to the laser wavelength through the mechanism of nonlinear absorption at high intensities coupled with avalanche ionization. Due to the capability of *fs*-lasers to ablate material regardless of optical absorption properties, ultrafast lasers have been used for the processing of such wide ranging materials as ceramics, semiconductors, metals, plastics, transparent glasses, single crystals, and biological materials such as tissue, bone, tooth, cells and subcellular organelles [58,59]. Femtosecond lasers can be used to ablate any material in principle, but the mechanisms of ablation depend on the electronic structure of the material.

In a conductive metal, the conduction band electrons can directly absorb energy from the exciting laser electromagnetic fields. Laser–metal interactions can be well described using the two-temperature model [60]. The energy in conduction band electrons equilibriate on the single femtosecond time scale and can be approximated with an average electron temperature. The electrons subsequently transfer their energy to the ions of the metal, which can be measured as the lattice temperature. The two coupled equations of the two-temperature model are shown in Eq. (3.2) and (3.3) [56].

$$C_e \frac{\partial T_e}{\partial t} = \frac{\partial}{\partial x} k_e \frac{\partial T_e}{\partial x} - \alpha(T_e - T_l) + Q \tag{3.2}$$

$$C_l \frac{\partial T_l}{\partial t} = \alpha(T_l - T_e) \tag{3.3}$$

In Eq. (3.2) and (3.3), Q is the laser source term, C is the heat capacity, k is the thermal conductivity, α is the electron-phonon coupling term, and the subscripts 'e' and 'l' represent quantities of the electrons and the lattice, respectively. These equations represent a diffusion process that is used to describe the energy transfer between electrons and phonons in the material lattice. Electrons gain kinetic energy directly from the oscillating electromagnetic fields of the incident laser light. The metal lattice heats up as the excited electrons transfer their energy through electron-phonon scattering. Electron-phonon coupling results in an equilibrium occurring on a 10's of picosecond time scale. As the lattice gains energy from the 'hot' electrons, dramatic phase changes such as explosive boiling can occur.

The primary difference between the ablation pathways of metals and dielectrics is that dielectrics must first absorb laser energy to generate free electrons. For metals, laser light energy can be directly absorbed by free electrons, but in the case of a dielectric material, 'seed' free electrons must first be generated before further ionization can occur.

For nanosecond laser ablation of dielectric materials, there is a strong dependence on the initial free electron density and local conditions, which leads to large experimentally observed uncertainty in the critical fluence for breakdown, especially in amorphous materials such as glass [61]. As the pulse becomes shorter than 5-10 ps, however, the intensity of the initial part of the pulse becomes high enough to generate sufficient 'seed' electrons. At this point, the steady-state free electron concentration becomes unimportant, and leads to the non-stochastic nature of breakdown achieved with *fs* pulses [61].

When enough of the electrons in the focal region are liberated, the dielectric can act 'metallic' through a change in the material dielectric constant, at which point further energy is absorbed through the inverse bremsstrahlung pathway. Optical breakdown, which signals material ablation, is observed when the free electron density reaches a critical level, usually defined as when the plasma frequency ω_p, defined in Eq. (2.10), equals the laser frequency ω, previously defined in Eq. **Error! Reference source not found.**. Figure 3.2 shows a diagram of the ionization process in dielectric materials.

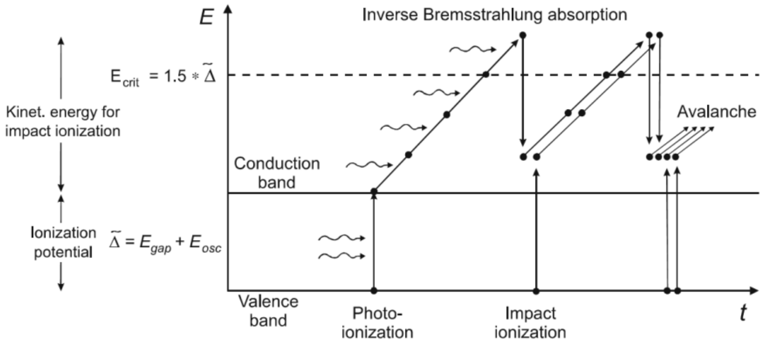

***Figure 3.2: Mechanisms of free electron generation in dielectric materials using ultrafast lasers.** Free electrons generated with photoionization gain energy from the laser fields. This energy can be transferred to free bound electrons, resulting in an exponential increase in generated electrons. The image is taken from Vogel et al. **[62]**.*

Equation (3.4) shows the rate equation approximation for free electron generation in dielectric materials [62].

$$\frac{\partial \rho}{\partial t} = \eta_{pi} + \eta_{casc} - \eta_{diff}\rho - \eta_{rec}\rho^2 \tag{3.4}$$

In Eq. (3.4), ρ is the free electron density and the η terms represent each of the source and sink rate terms for free electron generation. Photo-ionization, η_{pi}, and cascade ionization, η_{casc}, act as free electron sources, while recombination, η_{rec}, and the diffusion of electrons out of the focal region, η_{diff}, act as free electron sinks. Depending on the laser conditions, photo-ionization can be caused by multi-photon ionization (MPI) or tunneling. For ultrafast lasers, photo-ionization is the strongest initiator for the generation of free electrons, but cascade ionization is the strongest overall source of the free electrons which lead to the optical breakdown of a material. Diffusion and recombination of free electrons are minor effects for ultrashort pulses. MPI occurs when two or more photons with a sum of energies greater than the material bandgap are absorbed simultaneously. The probability of MPI scales as a function of the intensity to the power of the number of photons involved in a process. In cascade ionization, free electrons absorb energy from the laser electromagnetic fields and liberate other electrons through impact collisions that transfer kinetic energy.

At optical breakdown, the generated plasma becomes strongly reflective and absorbing. Typical free electron densities at breakdown are in the range of 10^{20}–10^{22} e^- cm^{-3}, depending on the criterion used (material modification or plasma formation). The physical mechanism of material removal from a surface for dielectrics is conversion from solid to high pressure plasma and subsequent expansion away from the substrate [63]. Figure 3.3 is a diagram of the processes by which material is removed from a dielectric material surface by *fs*-laser ablation.

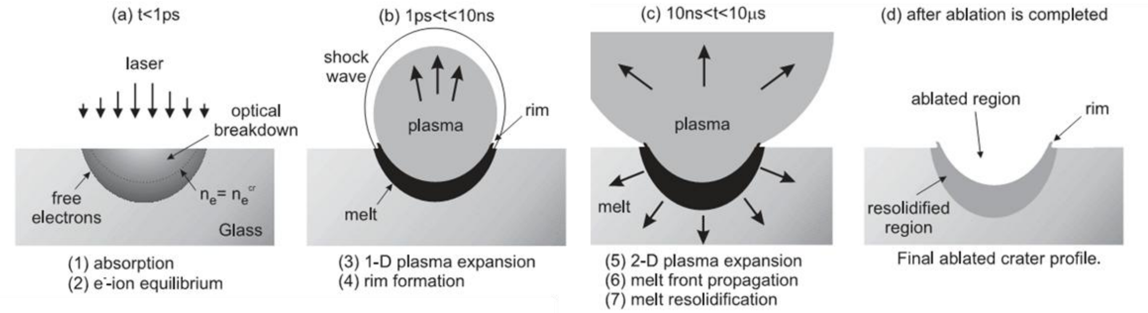

Figure 3.3: Schematic of fs laser-induced material removal for a dielectric material at different times during ablation. *Initially, free electrons are generated through multiphoton absorption, followed by cascade ionization and culminating in optical breakdown (a). Subsequently, the high-pressure plasma expands out from the material surface, leaving a crater (b). During plasma expansion, some energy is transferred to the surrounding material, leading to a thin melt region around the crater (c). Finally, the melt region resolidifies, along with a rim around the crater caused by the plasma pressure forcing melted material out of the ablation crater (d). The image is adapted from* ***[63]****.*

These differences, together with the differences in the bandgap energy, result in an order of magnitude larger breakdown fluences for dielectrics than for metals. Surface laser ablation in dielectric materials with NIR ultrafast laser pulses is a highly nonlinear process, where small increases in intensity can lead to large difference in the ablation results.

3.3: DIRECT-WRITE ULTRAFAST LASER NANOABLATION

Direct laser processing is limited by the diffraction of the beam when the focus reaches dimensions on the order of the wavelength of the laser light. Abbe's diffraction limit states that the light cannot be concentrated to a spot size smaller in diameter than half of the laser wavelength. This fundamental limit has pushed many lithographical approaches to use shorter and shorter illumination wavelengths, extending down into the ultraviolet (UV) and extreme ultraviolet (EUV) spectral regions. In these wavelengths, problems with the available light sources, sensitive photoresist and effective focusing optics arise. Due to the additional challenges facing short wavelength ablation, there is substantial interest towards using established optical components with focused visible and near-infrared (NIR) light for nanostructuring. Though effective focusing cannot be employed to create sub-100 nm spot sizes, several techniques exploiting the nonlinear properties of ultrafast lasers can be used to create nanoscale features.

Direct-write methods using advanced optical setups and an understanding of *fs*-laser interaction mechanisms have recently been used to create surface features with sub-diffraction limited dimensions. The advantages of direct-write methods are primarily in the ability to ablate nanostructures using far-field laser exposure. Sub-diffraction direct write ablation is possible by creating spatially small regions of intensity above the ablation threshold.

One method for direct write nanoablation makes use of Gaussian beam profiles and laser intensities very close to the ablation threshold of the substrate material. The concept of ablation at critical intensity is illustrated in Figure 3.4, where only the above-threshold fluence region will be ablated. Theoretically, this method could be used to reduce the ablation region to an arbitrarily small diameter, but in practice this approach is limited by the pulse–to–pulse stability of the laser and the extent of photodamage, namely HAZ. The limited thermal diffusion length that can be achieved using ultrashort laser pulses has recently enabled confining the ablation region to a region smaller than the diffraction-limited spot size. Using this method, researchers have succeeded in ablating sub–100 nm features on a glass substrate using laser pulses at NIR wavelengths [61]. Joglekar *et al*. used a stabilized sub-picosecond pulse laser (τ_p = 800 *fs*) to create rough channels of less than 40 nm across, with clean features in the 100 nm range [61].

Multi-photon absorption is another mechanism that can be exploited with Gaussian beams to create sub-diffraction limited ablation spots. This is achieved through the mechanism of absorption and the band structure of the material of interest. In high intensity, short pulse interaction regimes, the spot size can be related to the power of the intensity corresponding to the number of photons necessary to overcome the bandgap of the material. This relationship leads to a narrower distribution of deposited energy, such that the effective spot size is inversely related to the ratio of material bandgap to photon energy. This mechanism has been used to create sub-micron scale features in high bandgap dielectric materials with high intensity *fs*-laser pulses [64]. It is also the mechanism for two-photon processes such as multi-photon polymerization that can achieve smaller features than its single photon absorption counterparts. Figure 3.4 shows a schematic of the achievable ablation diameter for high-intensity laser ablation using fine control of the fluence and number of photons interacting to overcome the bandgap.

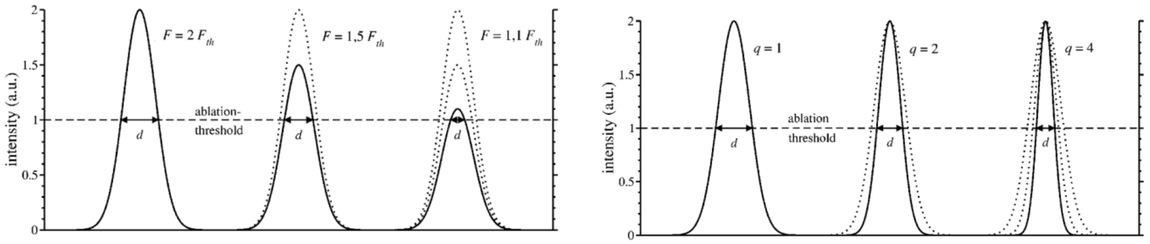

Figure 3.4: Mechanisms for creating sub-diffraction spots using ultrafast lasers. *a) Ablation spot diameter as function of the peak intensity of a Gaussian beam approaches the critical ablation threshold of the substrate material. b) Diameter of the ablation region as the number of photons necessary to overcome the material band-gap increases. The illustrations are from* ***[64]****.*

Laser Interference Lithography (LIL) can also be used for direct-write surface nanostructuring. LIL is a multi-beam process whereby the interference pattern between multiple coherent beams is used to generate differences in the intensity at specific locations in a plane. Patterns can be created with different features depending on the number and orientation of beams relative to one another. Sub-micron features over several square centimeter regions have been crafted with this technique, which has been industrially used for fabricating interference gratings [65]. Interference ablation using LIL has been used for the fabrication for surface and internal gratings in a variety of transparent dielectrics, creating nanoline features with a micron-scale period [66]. LIL is limited in the shape of structures and patterns that can be created by the complexity of the optical setup and alignment of multiple beams relative to each other. Several recent techniques have been developed to bypass the complexity of multiple independently directed interfering beams by using spatially separated beams focused through a single focusing element, but it is challenging to obtain nanometer-scale resolution with this approach [67].

LIL is best suited to the creation of wide field repeating patterns of nanoscale features. LIL can be competitive with lithographic techniques for sufficiently large scale nanostructure fabrication applications. Some examples of the patterns that can be formed with LIL are shown in Figure 3.5. The linear grating pattern can be formed with the intersection of two planar beams (Figure 3.5a), while a more complicated hexagonal close packed array of ablation sites can be formed with an intersection of three evenly spaced beams (Figure 3.5b). We calculate these interference patterns using complex beam propagation and interference of electromagnetic fields. The incident beam intensity can be tuned such that the areas of highest intensity will be ablated while the low intensity areas will be unaffected.

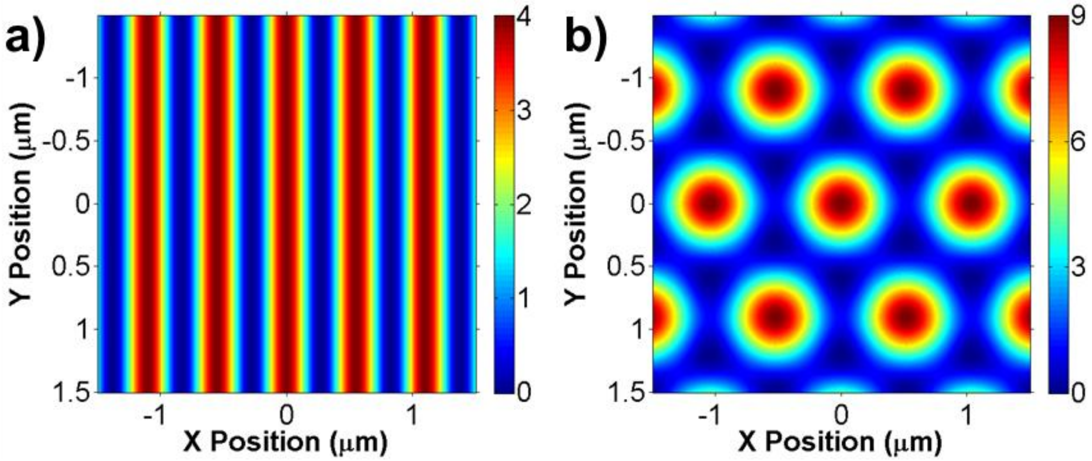

Figure 3.5: Laser interference lithography (LIL) patterns using multiple beams. *The intensity profile on a surface can be used for creating periodic features on a substrate using ultrafast laser ablation. a) Pattern generated with two beams. b) Pattern generated with three beams. Note the difference in intensity scale. The patterns are calculated with complex beam propagation. The beam intensity can be tuned such that the regions of high intensity will be ablated while low intensity areas will be unaffected.*

3.4: OVERVIEW OF NEAR-FIELD CONFINEMENT FOR ULTRAFAST LASER ABLATION

As part of the quest to create smaller and smaller features in a variety of substrates, it is necessary to obtain localization in the deposition of energy in space as well as time. As previously described, laser-based techniques have proven their ability to work on the sub-wavelength scale beyond the diffraction limit using interference and nonlinear optical techniques such as Gaussian beam thresholding, interference lithography, and two-photon polymerization [68,69,70]. However, limits on the ablation size, fabricated patterns and applicable materials mean that alternative methods must also be sought. Near-field confinement represents one of the most promising methods for creating near-field ablation regions. Near-field ablation employs small structures as 'nano-lenses' to provide electromagnetic field intensification at precise locations beyond the diffraction limit down to a few nanometer scale. Near-field focusing coupled with *fs*-pulses is a powerful strategy for obtaining fine features in substrates because the energy is focused to the nanometer scale with a focusing structure, while the fast delivery of laser energy ensures athermal ablation results.

Near-field ablation represents a frontier for the optical creation of nanometer-scale features in a variety of substrates. Near-field ablation involves a localized enhancement of the below-threshold incident light to create localized nanoscale regions above the ablation threshold intensity such that only material in the near-field 'focus' will be ablated. The advantage of this technique is that the near-field region can be much smaller than the diffraction-limited spot size, depending on the focusing structure. Near-field enhancement of electromagnetic fields typically decays exponentially as the distance from the confinement structure increases.

Several different near-field strategies have recently been pursued to find a method for spatial confinement of the laser energy to extremely small length scales – ideally on the order of nanometers. To this end, we review some recent advances in the use of near-field confinement for the localization of laser pulses for material ablation using *fs* pulses. Lithographical methods, while quite powerful, are not included within this review, as we focus on ultrafast laser-based methods that can be used for various substrates and do not require clean room facilities or photosensitive mask technology.

This review will address three of the most common approaches for coupling ultrafast light into sub-diffraction limited regions for ablation: tapered scanning probes, dielectric spherical lenses, and plasmonic metal nanostructures. Bottom-up approaches such as these involve the creation of single features are time consuming, but using these methods for mask creation could render these methods very useful. All of these methods push the current boundaries of nanoparticle positioning for potential future nanomanufacturing goals.

3.5: NANOABLATION WITH SCANNING NEAR-FIELD OPTICAL MICROSCOPY

Scanning Near-Field Optical Microscopy (SNOM) has long been used as an imaging method to resolve features below the diffraction limit for high resolution imaging, but has recently also been demonstrated as a viable technique for the nanoablation of solid materials. SNOM is a scanning probe technique in which a laser beam incident on a sharp sub-wavelength tip is intensified in the near-field through tapered tip guidance. A typical SNOM setup is incorporated into a modified atomic force microscope with a laser directed to the probe tip at a shallow angle relative to a substrate. In the imaging modality, the scattered signal is collected as the tip is scanned across a region to be imaged. SNOM can be used for imaging biological materials (coupled with fluorescence) and for capturing the plasmonic enhancements around metal nanostructures.

The SNOM technique can also be used to create localized ablation near the tip when irradiated at high optical intensity. Metallic shapes that taper to a sharp point lead to sub-diffraction focusing of light through the ‘lightning-rod effect’ [71]. Focusing can be accomplished through the tendency of light to be guided along a metallic surface. Through gradual tapering of the tip, light over a large region can be focused down to the tip, multiplicatively increasing the intensity per area. In this case, light can be focused down to the dimensions of the tip and ablated features can be even smaller due to non-uniform intensity distributions. This method of enhancement can be used for light coupled within a tapered metal-coated hollow fiber or for light directed at a sharp metallic tip.

Aperture SNOM was the first type of near-field optical probe theoretically proposed by Synge in 1928 [72], but it was not experimentally demonstrated in the visible regime until 1984 [73]. In its simplest form, this method exploits the confinement of electromagnetic fields directly behind a sub-wavelength hole in the ‘super-resolution’ near-field region. Typical setups make use of a drawn hollow dielectric tube typically coated with a metal film (generally aluminum, gold or silver). Recent studies have used aperture SNOM to create nanoscale ablation features. Fiber-coupled ultrashort pulses have been used to create nanocraters as small as 200 nm in diameter and 20 nm in depth in metal films [74]. Compared with nanosecond pulses, ultrafast laser pulses ($\tau_p \approx 100$ *fs*) yield higher aspect ratios, greater localization of deposited energy, and significantly sharper ablated features, as expected. It has also been shown, however, that the *fs*-laser light coupled into the fiber and tip is subject to modal and group velocity dispersion, resulting in *ps* time scale pulse lengths at the sample unless dispersion compensation is used. Experiments using a metal-coated tapered optical fiber with a 300 – 500 nm inner diameter final opening were able to create 200 nm width features through metal films of up to 100 nm depth [75]. Calculations show that the peak enhancement at the substrate surface is 5 times greater than the electromagnetic fields experienced at the surface coating of the probe. This enhancement allows for metal-coated SNOM tips to be used to ablate metal surfaces. Aperture SNOM probes can create features slightly smaller than the dimensions of the probe aperture when irradiated with *fs* pulses. As the aperture size falls, however, so does the laser coupling efficiency, which can limit the size of ablated features.

Apertureless probes are another common approach employed in SNOM facilities. Apertureless SNOM probes consist of sharp cantilever-mounted, metal or semiconductor cones with radii that can approach the 10 nm scale. In this case, the laser light is incident from the side rather than through the tip itself (Figure 3.6a). This type of tip can have finer resolution, but one of the negative aspects to this approach is that there is a higher concentration of light at the probe tip itself. This enhancement can be mitigated by placing the tip in near proximity to a surface, which tends to draw the maximum intensity away from the tip through gap-like tip-substrate electromagnetic field interactions [76]. However, the relative magnitude of metal and high-band gap dielectric ablation thresholds has limited this method to metal and semiconductor ablation to date. This method has been used with success with ablative spectrometry techniques for the sampling of very small volumes [77].

Ablation with an apertureless SNOM tip has the advantage that ablated regions can immediately be scanned in AFM mode to obtain a high resolution image of the surface topography. In a pioneering work with an apertureless SNOM tip and an 83 *fs* NIR laser focused at the tip-surface interface from a grazing incidence angle, Chimmalgi *et al*. [76] ablated and imaged 14 nm width lines with depths of approximately 4 nm in gold films and similar features on a silicon surface (Figure 3.6b and c). Interestingly, in this study no damage was observed to the probe tip, which was proven by first ablating using scanning probe near-field enhanced electromagnetic fields, and subsequently imaging the surface with high-resolution AFM with the same tip. If damage to the tip occurred, then there should be substantial degradation of the AFM image quality after the ablation was performed.

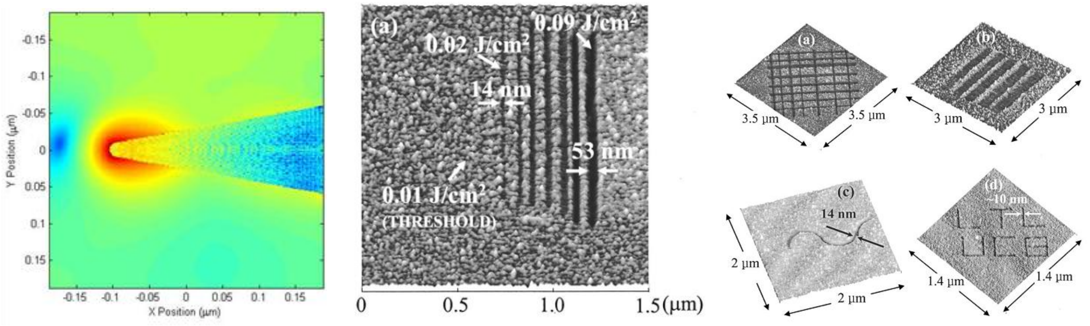

Figure 3.6: Mechanism and experimental demonstrations of nanoablation with SNOM. *a) Enhancement around a conical metallic tip irradiated by λ = 780 nm light determined with a discrete dipole approximation (DDA) simulation of the enhancement around a gold tip in a vacuum. b) Threshold measurement with a SNOM probe, and c) Fine resolution nanostructuring on a metal film with an apertureless SNOM setup. Images b) and c) are from* ***[76]****.*

At the outset of SNOM nanoablation, there was some controversy over the mechanism of apertureless SNOM nanoprobe tips in the literature. In relatively long pulse (*ns*) laser excitation, the mechanism for SNOM laser-assisted structure formation can be physical contact resulting from thermal expansion of the tip leading to the displacement of substrate material. Laser-induced heating, due to electron-phonon energy transfer, occurs on a *ps* time scale, which is much longer than the time scale of an ultrafast pulse. Through extremely precise control of the height of the probe above the surface, Milner *et al*. [78] conclusively showed that *fs* pulsed laser SNOM operation results in smaller width features when the probe tip does not contact the substrate. The study concluded that the mechanism of surface modification was either localized heat transfer from the tip or material removal through amplification of electromagnetic fields. SNOM with *ns* pulses generate significantly larger ablation regions than *fs* pulses, just as in direct–write laser processing. Furthermore, tips heated through resistive heating cannot create features of such fine resolution as those created with ultrafast laser irradiation. Thus, experimental evidence indicates an enhanced electromagnetic field mediated mechanism for SNOM nanofabrication.

For all SNOM applications, the effectiveness of the technique is largely tied to the shape of the probe. The enhanced volume of the electromagnetic fields resultant from laser-SNOM tip interactions, and thus the affected region processed by SNOM, is strongly related to the tip geometry. Specially shaped tips can thus be used to improve the shape and enhancement factor of the near-field enhancement characteristics, which can potentially lead to gains in terms of substrate nanoablation. Shaped probe tips can also increase the transmission efficiency while decreasing the effective spot size for SNOM imaging applications. Murphy-Dubay *et al*. created a bowtie aperture through a uniform metallic coating on the tip of a SiN SNOM probe using focused ion beam (FIB) milling after an efficient design optimized for using finite difference time domain (FDTD) simulations [79] (Figure 3.7c). These probes create an interesting hybrid approach between aperture and apertureless SNOM. Bowtie apertures are of great interest because of the optical concentration observed between the tips of the bowtie arms, in this case predicted by simulation to result in an enhancement of 40 times over the incident fluence. Using a bowtie aperture with a 30 nm gap, the group was able to focus light to a width of 25 nm. This approach holds promise for developing higher aspect ratio features with finer resolution through a careful electromagnetic design. Another shaped tip that has promise is the tip-on-tip geometry [80]. In this case, the end of a typical aperture SNOM tip is milled with a FIB such that only a very small resonant antenna tip is left on the surface directly adjacent to the aperture (Figure 3.7d). Shaped probe SNOM has shown promise for imaging applications, but has yet to be applied to nanoscale ablation. Scanning electron microscope images of various probe types are shown in Figure 3.7. The fabrication of extremely sharp tips and ensuring tip quality without direct observation in an electron microscope remains a challenge for SNOM nanoablation applications, especially for shaped tips.

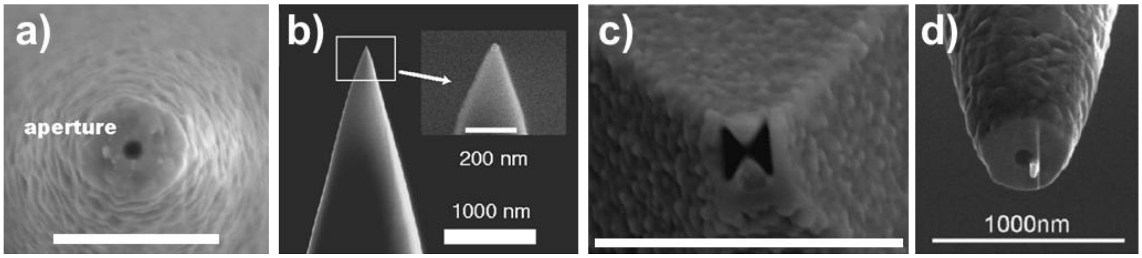

Figure 3.7: SEM Images of several different SNOM tip geometries. *a) Drawn glass fiber aperture SNOM tip, b) apertureless acid-etched gold tip* ***[81]****, c)FIB-shaped aluminum on silicon nitride pyramidal SNOM tip* ***[79]****, and d) FIB-shaped aluminum on drawn glass monopole antenna SNOM tip* ***[80]****.*

Additionally, while very attractive for surface processing in terms of arbitrary positioning capability and the creation of extremely fine features, ablation speed remains a challenge with SNOM probes, as the probe tip must be scanned over each site of interest for creating features. A parallel approach using an array of independent SNOM probes could have potential for rapidly creating small features on a large scale. Recent development of the ‘SNOMipede’, which makes use of an array of apertureless SNOM tips [82] has shown the promise of parallel SNOM control. Though SNOM tip arrays have only been demonstrated for imaging applications thus far, the potential for increasing SNOM nanofabrication throughput with this method seems strong.

3.6: NANOSPHERE LITHOGRAPHY

Near-field confinement of laser light for nanoablation can also be accomplished by focusing light using sub-micron dielectric particles in close proximity with a substrate Micro- and nanoscale dielectric spheres act as spherical microlenses, focusing the light to create intensities large enough to ablate the surface beneath the spheres. The focusing effect of small dielectric spheres can be determined with Mie theory, yielding localized regions of high electromagnetic field intensity behind the spheres. Figure 3.8 shows the near-field enhancement magnitude surrounding silica spheres. Larger spheres will exhibit much higher enhancement magnitudes (up to ~100×), but the confinement of light in terms of the 'focal' spot size decreases with the particle size, ranging from a $1/e^2$ spot radius of ~69 nm for the 250 nm sphere (Figure 3.8a) to ~166 nm for the 2.5 μm sphere (Figure 3.8c). Some enhancement occurs within the sphere for all simulated particle sizes, leading to removal of the particle in most cases. The interference patterns for the incident and scattered waves around the particle are apparent for the near-field patterns.

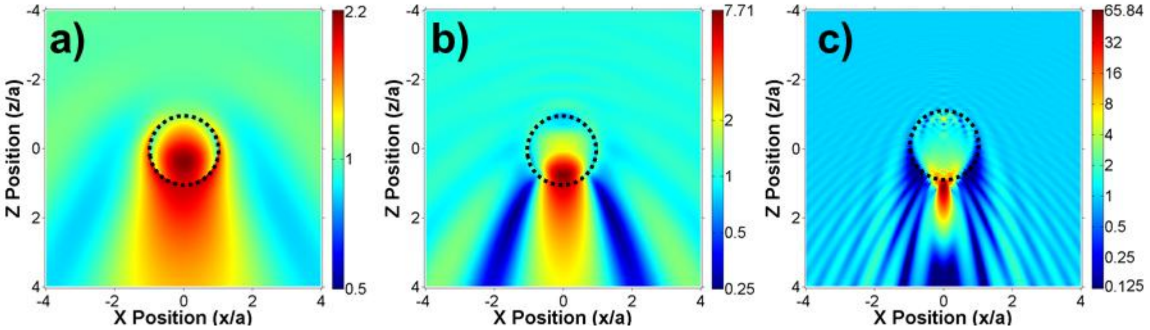

Figure 3.8: Near-field enhancement around dielectric particles for nanosphere lithography. *Simulation of the intensity enhancement (|S|) due to near-field focusing for silica spheres with a diameter of a) 250 nm, b) 500 nm and c) 2500 nm. The fields are simulated for an air environment at a wavelength of 500 nm and presented on a logarithmic scale (base 2).*

Depending on the substrate optical properties, light can be reflected back towards the sphere by the substrate and increase the effective optical sphere enhancement [53]. The 'particle-on-a-surface' problem can be solved using Weyl-type integrals and spherical harmonics expansions to obtain the field enhancements for a sphere on an infinite substrate [13]. These solutions yield several results of interest. First, it has been found that the enhancement around a dielectric particle above a silicon surface can be 50% greater than the predicted Mie theory enhancement for an isolated sphere [83]. Simulations including this effect have been able to accurately simulate ablation morphologies on substrate surfaces [53]. The substrate enhancement effect increases with the reflectivity of the substrate and as the distance between the particle and the substrate surface decreases.

Wide-field, near-field patterning can be accomplished using self-assembled monolayers (SAMs) of nanospheres in a process known as nanosphere lithography. Using surface functionalization or surfactants, dielectric spheres can be assembled on a surface into 'crystalline' monolayers on a substrate using colloidal self-organization. The spheres form into hexagonal close packed 2D arrays, with an array size that can be tuned with varying the size of the colloidal spheres. SAMs are typically fabricated using suspended dielectric sphere colloids, typically silica (SiO_2) or polymers such as polystyrene (PS), can be obtained with diameters ranging from the micron down to 50 nanometer scale with very fine size distributions with deviations as low as 1%. If these spheres are then subjected to large-beam ultrafast laser exposure, arrays of localized ablation sites can be created [53,84].

Nanosphere lithography has been demonstrated in the *fs* laser regime. Femtosecond laser pulses yield smaller diameter, deeper, and higher aspect ratio ablation craters when compared with the shallower ablation craters observed with *ps* and *ns* pulses using the same technique [85]. The diameter of the pits manufactured on silicon with this method decrease with irradiation wavelength due to increased focusing for a smaller size parameter. Brodoceanu *et al.* compared the pits generated by the frequency doubled and tripled harmonics of NIR *fs* laser pulses [84]. Figure 3.9a shows craters formed using a single 300 *fs* shot of frequency-tripled 266 nm laser light to produce craters with a diameter of 57 ± 7 nm and a depth of 6 nm on a silicon substrate. In another interesting exploration of colloidal sphere microfocusing, Cai and Piestun used tightly focused ultrashort (τ_p = 60 *fs*) pulses to examine the effects of focus position on glass surface ablation and removal of a single 1 μm sphere at a time, shown in Figure 3.9b [86]. By focusing on a single sphere at a time, arbitrary patterns of ~300 nm deep ablation sites could be created, though the spots cannot be closer than the diameter of the initial dielectric spheres with this method.

The near-field focusing of dielectric sphere micro- and nano-lenses can be effectively used to create nanocraters on semiconductors, metals, and high band gap dielectric surfaces. The dielectric sphere near-field lensing process becomes less efficient as the dielectric spheres decrease in size, and limited enhancement in the focal region reduces the usefulness of this technique for the creation of ultrasmall features. Figure 3.9 shows a comparison of several experimental implementations of the nanosphere near-field focusing method.

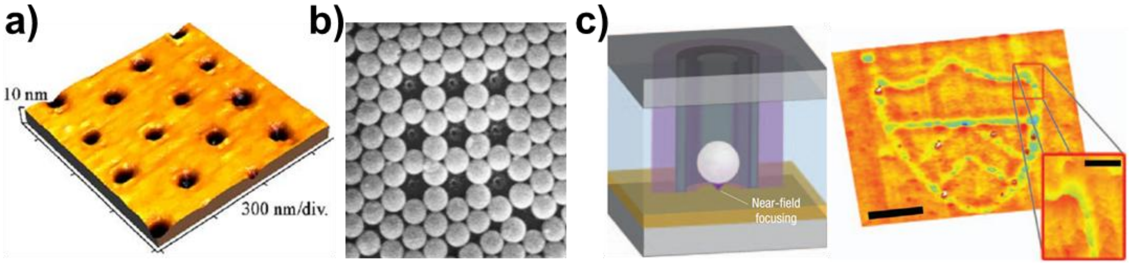

Figure 3.9: Pulsed laser near-field ablation of substrates achieved with colloidal sphere monolayers. *a) Simultaneous nanoablation with large area nanosphere lithography on silicon* ***[84]****. b) Point-by-point ablation of glass using individually targeted nanospheres* ***[86]****. c) Diagram of the trapping and focusing geometry and a representative AFM image showing a fabricated pattern on a polymer surface with 130 nm resolution* ***[87]****.*

A final method of interest for this discussion is the optical trapping of individual dielectric microspheres, which can be irradiated with a processing beam and translated to create features in a substrate (Figure 3.9c). Optical trapping is the use of spatially shaped CW beams (such as Gaussian, Laguerre-Gaussian, or Bessel beams) to stably hold a particle in place using electromagnetic forces from a laser on a particle [88]. In one recent experiment, a CW Bessel beam was used to stably trap a polystyrene particle in a lateral position while a second pulsed laser was used to ablate the substrate surface [87]. Using this technique, 130 nm ablation features were obtained on polyimide surfaces. The feature size was found to decreases with the size of the trapped focusing particle, but as a tradeoff the positional uncertainty increases with decreasing sphere size due to the Brownian motion of the sphere within the optical trap. The laser pulse length in this experiment was in the *ns* regime, but the same technique could be used with even tighter ablation features with ultrafast lasers. The authors subsequently demonstrated the parallelization of this method with multiplexed Bessel beams and captured dielectric spheres while retaining the illumination of only a single pulsed laser, which could allow for high-throughput nanostructure processing [89].

3.7: ULTRAFAST LASER NANOABLATION USING PLASMONIC METAL NANOPARTICLES

Plasmonic metal nanostructures are another method by which near-field enhancements can be used for ultrafast laser nanofabrication. The resonant interaction between light and the collective oscillations (plasmons) of conduction band electrons on the surface of the metal particle generates large electromagnetic field enhancements in close proximity to the metal surface. The resonant interaction draws the field lines of the incident radiation towards the particle over an area that can be significantly larger than the geometrical cross-section. Figure 3.10 shows the difference in mechanism with the field lines for a lens-like dielectric sphere (Figure 3.10a) and a plasmonic metal nanoparticle (Figure 3.10b). The mechanism of near-field enhancement for a dielectric sphere is primarily a concentration of light incident on the particle into a small focal region behind the particle. On the other hand, a plasmonic nanoparticle the mechanism is a focusing of energy from an area much larger than the particle itself.

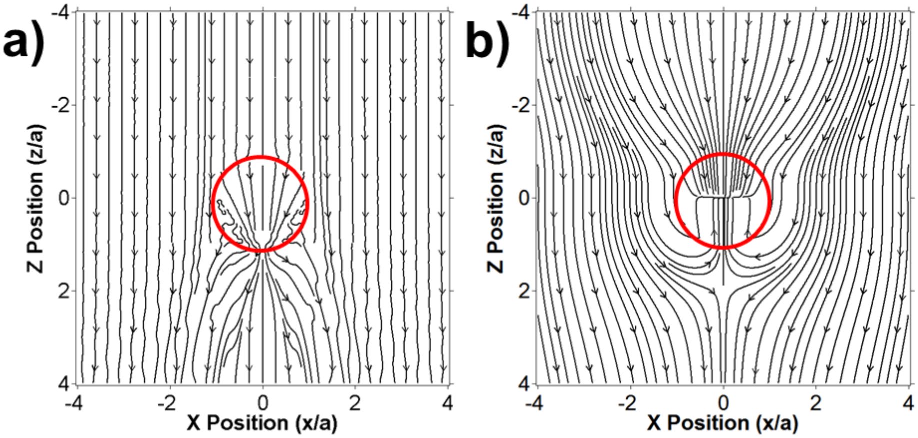

Figure 3.10: Streamline profiles showing the different mechanisms of enhancement for a dielectric sphere and plasmonic metal nanoparticle. *The direction of energy propagation, namely* $\vec{\boldsymbol{S}}$*, is shown with white lines and arrows, while the sphere location is shown with a solid red circle.*

A hallmark of plasmonic effects is the strongly wavelength-dependent nature of the enhancement. The enhanced interaction effect at the plasmonic resonance peak can lead to order of magnitude increases in the electromagnetic fields around a metal nanostructure over an area that is similar in extent to the size of the particle [90,91]. The resonance occurs in the visible range for noble metal (Au, Ag and Cu) particles on the nanometer scale, which has made these nanostructures the subject of intense scientific interest. The field enhancement of resonant gold nanospheres calculated with Mie theory is shown in Figure 3.11. The enhancement pattern changes from a dipolar response for a 25 nm sphere (a) to a multipolar enhancement pattern for a 150 nm sphere (c).

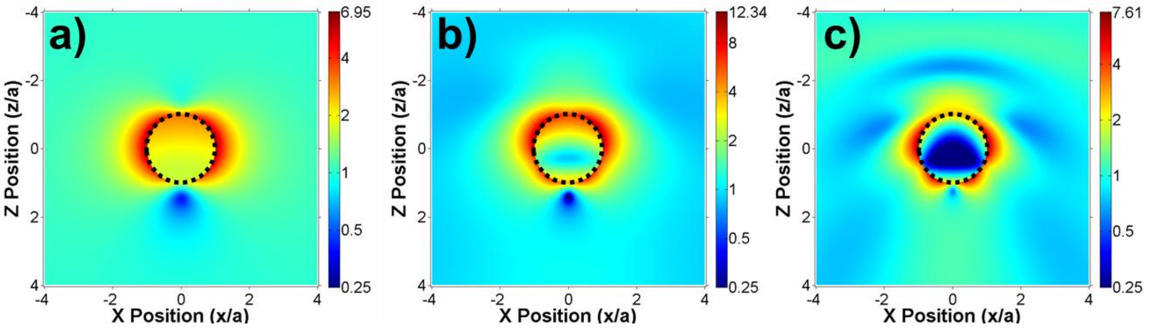

Figure 3.11: Intensity enhancement (|S|) at the plasmonic near-field resonance for gold spheres in water. *The presented plots show the enhancement for diameters of a) 25 nm, b) 75 nm, and c) 150 nm.*

The near-field enhancement around plasmonic metal nanoparticles can result in either ablation of material surrounding the particle and/or direct ablation of the particle itself. The quest to determine the physical mechanism behind plasmon-mediated ultrafast laser nanoablation is hindered by the difficulty of distinguishing effects at ultrafast time and nanometer length scales. Plech *et al*. examined the near-field ablation of gold nanoparticles through the use of *fs*-laser pump-*ps* x-ray probe measurement [92]. In this study, 38 nm gold spheres, which are characterized by a dipolar near-field enhancement pattern, were excited off-resonance at a frequency-doubled wavelength of 400 nm with 100 *fs*-laser pulses while 100 *ps*, 16.7 keV synchrotron-generated x-ray pulses were used to observe the ablation process. Ablation was observed at the tips of the nanoparticles at laser fluences between 9 and 12 mJ/cm^2, whereas at fluences above 15.5 mJ/cm^2, complete destruction of the crystalline order of the nanoparticle was observed. It was determined that field emission of electrons and ions was responsible for material removal, rather than thermal processes, because the material ablation was anisotropic *while* the particle maintained crystalline order and occurred in less than 100 *ps*. The anisotropy of the SAXS signal was consistent with a modification of the gold spheres to ellipsoids with a short axis reduced by 21% for a laser fluence of 13.5 mJ/cm^2. Intriguingly, material ablation and mass removal occurred near the poles of nanospheres, along the polarization axis, where electromagnetic field enhancement occurs. By changing the pulse duration, it was also found that the material ablation is a nonlinear effect. As the pulse is stretched from 100 *fs* to 970 *fs*, the ablation effect and observed shape anisotropy decrease and disappear, thus further confirming field emission of material, as thermal effects should be only weakly affected by pulse duration changes much shorter than the electron-phonon coupling time (~10's of *ps*) for the same pulse energy. Estimates of the particle temperature calculated from the lattice expansion confirmed this observation. The experimental results presented by Plech *et al.* support a field emission mechanism for plasmonic near-field enhanced ablation.

Plasmonic near-field enhancement can be used to create nanoablation sites when the optical fluence applied to the plasmonic structure is greater than the quotient of the ablation threshold and the enhancement factor. Plasmonic enhancement is an ultrafast phenomenon, so near-field ablation of material around a plasmonic nanoparticle can be achieved even in the case of the destruction of the localizing particle. Depending on the relative ablation thresholds of substrate and particle, this effect can limit this method to single-shot ablation. Plasmonic enhancements are strongly localized to the structure that creates them, and the highest enhancement of a plasmonic structure is typically at the surface of the nanoparticle, allowing for plasmonic ablation on the order of the size of the nanoparticle down to the few nm scale. Nanoparticle plasmonic enhancement has been demonstrated for the ablation of metals, semiconductors, dielectrics and biological materials.

The plasmonic near-field enhancement of gold nanospheres has been used to enhance the localized electromagnetic fields from *fs*-laser light for sub-diffraction limited ablation of a supporting substrate. Previous studies by the Ben-Yakar group demonstrated the fabrication of nanocraters on a silicon surface of less than 100 nm diameter and 50 nm depth using gold nanoparticles with an initial diameter of 150 nm with single pulse *fs* Ti:Sapphire laser light at a wavelength of 780 nm [93]. Through a comparison of the minimum fluence necessary to ablate the substrate with and without the gold nanoparticles, an effective enhancement of the laser fluence due to the plasmonic interaction was found for several laser polarization and incidence angle configurations, including perpendicular incident, and also for 45 degree angle of incidence for both *s* and *p* polarizations. They observed a linear relationship between the single shot ablation fluence used and the crater depth. These experiments also showed that the theoretically predicted near-field pattern was imprinted on the surface, and the morphology of the ablation patterns is shown in Figure 3.12. The confinement was found to be comparable to the metal nanoparticle radius.

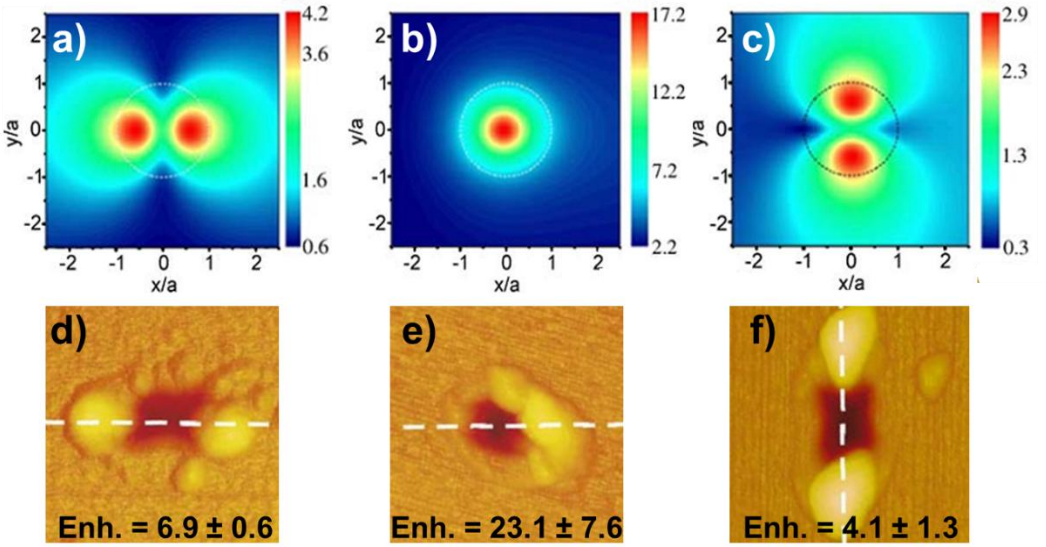

Figure 3.12: Ultrafast laser plasmonic near-field ablation with 150 nm gold spheres on a silicon surface. *The field enhancement (|S|) is calculated for normal incidence (a), p-polarization at a 45° angle of incidence (b), and s-polarization at a 45° angle of incidence (c). Characteristic ablation sites for the same conditions are shown in d), e) and f), respectively, with the experimentally determined enhancement found using the ablation threshold reduction. The images all represent a region of 300 × 300 nm and are adapted from* ***[93]****.*

Asymmetric metal nanoparticle shapes can have much larger near-field enhancements than nanospheres, meaning that they are attractive for use as nano-focusing elements for near-field ablation. The large near-field enhancement of non-spherical shapes is complicated by the polarization-dependence of the enhancement magnitude. Because of this limitation, it is easier to study large patterns of repeated structures with a defined orientation than isolated particles. One such pattern that can be experimentally fabricated are triangular metal nanoplates. Triangle nanoprism structures can exhibit very large enhancements at the triangle tips when their plasmonic resonance is coupled with the ‘lightning rod’ effect.

To create this unique nanostructure, a dielectric microsphere monolayer can be created and dried in the same manner as if they were being used for direct surface ablation. Subsequently, a noble metal is deposited (sputtered) over the sphere array template onto the substrate in high vacuum conditions. The spheres are then removed with a dissolving agent and the rounded triangular prism shapes are left behind in the spaces between the intersection of three microspheres. The prisms are formed in two perpendicular orientations whose polarization dependence can be readily studied. The planar size of these triangles is related to the original size of the sphere monolayer, with the maximum tip to tip distance and triangular height related to sphere diameter, while the thickness can be easily controlled by metal deposition rate and duration.

Boneberg *et al*. explored the optical near field of triangular nanostructures through the ablation of the substrate material by creating a *fs* 'photograph' of the field enhancement around the nanostructure. The ablation pattern was created by using a single 2 mJ pulse from a λ=800 nm Ti:Sapphire with a 150 *fs* pulse duration. This group also showed the near-field enhancement below a dielectric sphere with simulations that matched experiments and then expanded this method to explore the triangular nanostructures. The interaction between the laser light and the triangles was simulated with the discrete dipole approximation method, in which the nanostructure is broken into small cubic dipole elements and the induced polarization, and corresponding electric field, due to the incident light is calculated iteratively and numerically. In this case, enhancements on the order of 103 at the substrate surface were found for two sets of triangles with side lengths of 240 and 480 nm, respectively, both with a height of 30 nm. Experimentally, triangles with a height of 30 nm and side length of approximately 480 nm were created with a microsphere particle mask with spheres of 800 nm diameter. These triangles resulted in sharp spatially confined features beneath the tips of the triangles, where the ablation structures had features approaching the radius of curvature of the original triangles and depths of approximately 20 - 30 nm. This study also found a strong coupling effect between the repeated pattern of triangles that resulted in a different ablation pattern than for an isolated triangle. In a previous study with FDTD and experimental work, Crozier *et al*. found that the enhancement of a triangular-type structure increased with decreasing tip radius and tip angle [94]. As the gold triangles can be very sharp, similarly sharp structures can be fabricated in the substrate surface. The weakness of nanolithography methods is that only limited shapes can be fabricated using gold films applied over colloidal spheres and that several steps are required to create nano-features of interest. Through either direct or indirect laser processing methods, plasmonic nanostructures can be a powerful tool for the nanofabrication of surfaces.

The limits for plasmonic laser nanostructuring for lithography applications largely hinge on the precise positioning of the sub-wavelength confinement method, specifically for bottom-up nanoprobe or nanoparticle placement approaches. Other concerns involve the scalability of the process to industrial levels. Nanoparticle placement also has the potential for wide area nanofabrication through the parallel near-field enhancement of large spot size illumination for material ablation at many sites at once, but the precise placement of particles is one area that remains a challenge. One method for overcoming this difficulty is known as dip-pen nanolithography, where particles in solution are deposited on a surface using capillary forces from an AFM tip [95]. Another method is the direct ink-jet style printing of nanoparticles in solution onto a substrate [96]. Finally, the pre-patterning of a substrate material can be used for the creation of nanoparticle printing plates, which can be used to transfer and print nanoparticles onto surfaces [97]. While potentially very powerful, these methods are limited by the requisite colloidal solutions, rendering the accurate placement of single nanoparticles challenging. A different approach is the direct optical deposition of nanoparticles to a substrate using a process called laser-induced forward transfer (LIFT). In this method, a laser impulse is delivered to a thin polymer film directly below a target. The impulse provides the momentum for a trajectory across a narrow gap to another substrate. The method is gentle enough for the transfer of living cells [98]. The precision of this method is limited by the possibility of radial velocity components away from the desired target site, but using specially shaped beams and limiting the distance between donor and acceptor substrates can diminish this effect. This method has been used to create metal nanoparticles as small as 320 nm formed from a sacrificial metal layer [99].

Finally, the trapping method employed for dielectric particles could also be used for plasmonic near-field ablation. In this application, metal nanoparticles could be brought close to a surface at a defined location by a CW trapping beam, then irradiated with an ultrafast pulse to create localized nanoablation sites. This has yet to be demonstrated, but could have great promise for nanoablation applications.

3.8: BIOMEDICAL APPLICATIONS OF LASER NANOABLATION

The most common usage of ultrafast lasers is in the biomedical community, where they have found use in cutting flaps for LASIK surgery and for various nonlinear biomedical imaging modalities. Precise ablation on the nanometer scale (nanosurgery) for the selective laser damage to single cells and even specific organelles has become a research area of intense interest. For example, the Ben-Yakar group has demonstrated the targeted ablation of individual neurons in the model organism *Caenorhibditis elegans* to study neural regeneration [100]. Nanoaxotomy experiments have been further extended to a microfluidic lab-on-a-chip platform enabling drug discovery and the study of genetic expression and pathways [101].

The challenges to using *fs* lasers for near-field ablation in biological systems are analogous to those facing the field of nanolithography: delivery of laser light and targeting of structures of interest. For biological systems, however, fewer options are available for inducing laser damage. The SNOM and nanosphere lithography approaches are primarily applicable to flat surface geometries. Additionally, the use of micro/nanoparticles for field-intensifying effects is further limited to biologically compatible materials. Successful nanosurgery should be characterized by a high degree of specificity such that only specific cells or targets of interest are affected by the surgery. *In vivo* experiments pose a further set of challenges that must be overcome in targeting and laser delivery. Promising advanced techniques, such as the molecular targeting of nanoparticles to specific cells and the delivery of ultrafast lasers using flexible nanosurgery-enabled endoscopes, are active topics of current research.

Several different pathways for using lasers to create localized damage in biological tissue have been pursued. The most straightforward approach is the direct laser disruption of biological structures of interest. One important damage phenomenon is optoporation, which can be used for both the killing of cells as well as the transfection of material across a living cell membrane. Recent efforts using direct laser ablation incorporate high NA microscope objectives to tightly focus NIR *fs* laser light while avoiding the self-focusing due to high intensities.

The mechanism of *fs* laser nanosurgery depends on the repetition rate of the system. Ultrafast laser-induced cavitation bubbles can be used to cause nanoablation due to mechanical disruption of a structure of interest when using amplified, high energy pulses. These systems are typically characterized by repetition rates of $\sim 10^3$ Hz and corresponding time between pulses on the order of micro to milliseconds. A gas phase bubble can form when the tensile strength of the liquid is exceeded due to rapid energy deposition, resulting in a pressure wave that can disrupt the target of interest. In this regime, individual axons and single mitochondria have been severed [100,58,102]. For MHz repetition rates, a different ablation pathway is observed. An accumulation of free-electron-mediated chemical effects from *fs* laser formed low-density plasmas can result in nanodissection (photodisruption) or nanocavitation. This method has been demonstrated with the cutting of chromosomes and mitochondria [103], with sub-200 nm cuts achieved by tuning the laser power near the intensity threshold for damage effects. Alternatively, this method can be used for the optoporation for the transfection of material across the cell membrane.

While fine biological structures can be ablated using conventionally focused pulses, the advantage to near-field focusing is that less emphasis is placed on the time-consuming optical targeting of the individual biological nanostructures. Some research has been done in the field of imaging of biological structures with the SNOM technique [104,105], but most of the interest in this area has been on the molecular targeting of optical agents to cells followed by the destruction of those cells with incident laser light.

In this case, a weakly focused beam can be used to disrupt many labeled cells simultaneously without damaging unlabeled cells. In this method, the optical properties of specific cells are altered to create enhanced optical interaction. Pioneering early studies used either a stain or naturally occurring pigments, but these approaches lack flexibility for performing surgery on arbitrary cellular structures[106,107,108,109]. A more recent, efficient, and effective approach involves the use of plasmonic nanoparticles. Plasmonic nanoparticles have significant advantages over conventional dyes in terms of interaction cross-sections, absorption efficiencies, narrow tunable resonances, and spatial localization. Gold nanoparticles have been a focus for these studies due to the low biotoxicity of the metal [110].

Non-toxic gold nanoparticles can be molecularly targeted to selectively bind to certain sites or structures of interest. There are two aspects to successful targeting: using good contrast agents and attachment of the agent to a target of interest. Cells can be targeted through the use of antibodies designed to interact with receptors that are overexpressed in cancer cells. *In vivo* labeling using EGFR antibodies has been successfully applied by several research groups, with reported affinities for labeled to unlabeled cells of 6:1 [111]. New approaches of even greater selectivity, such as targeted nucleic acid ligands (aptamers) with order of magnitude better selectivity are also being pursued [112]. Recent developments in molecular targeting for cancer cells have been reviewed elsewhere [113].

Various approaches to tuning the plasmonic resonance with shape have also been pursued, with gold nanospheres, nanorods and nanoshells all having been used to selectively kill cells. The ability to create nanoparticles with resonances in the NIR has proven important for obtaining effects deep in tissue through the NIR tissue window. While gold nanospheres must be as large as 200 nm in diameter to have an extinction resonance in the NIR, nanoshells and nanorods can yield enhanced performance in the NIR region with substantially smaller dimensions [3], which can also be important for nanoparticle delivery. Studies have shown that melting and particle reshaping can be induced for non-spherical plasmonic particles during irradiation [48]. Particle reshaping has been proposed as a therapy endpoint, in which case cellular effects cease as the absorption resonance shifts away from the laser wavelength due to melting [114]. Our computational heat transfer studies using *fs* lasers showed that nanoparticles approach maximal temperatures within a few pulses [45,115], indicating that energy is not accumulated within the particles but dissipates to the surroundings between laser pulses. This result is especially important for multiphoton imaging using asymmetrical particles, as it implies that nanoparticle reshaping and elimination of the NIR resonance will occur during a single pulse or not at all.

Selective laser-induced hyperthermia is one method by which certain cells can be rendered non-viable through increased temperatures. Maintaining elevated temperatures of 41 – 47 °C for a period of several minutes can be sufficient to kill most cells. In this technique, cells are first labeled with a contrast agent and subsequently irradiated with laser light and maintained at high temperature until dead from irreversible membrane disruption and protein denaturation. Several groups have shown the use of gold nanoparticles for the selective targeting of cells with the photothermal destruction mechanism. Uses have ranged from the elimination of parasitic protozoa and murine macrophage cells with gold nanospheres to targeting human cancer cells with Au NR [116,117,118,119].

Pulsed lasers require less loading of gold nanoparticles, lower fluences for desired damage results, and can result in finer damage resolution than CW lasers. The decrease in loading and lower requisite fluences for a desired damage level is due to more efficient energy transfer to the particles and less heat transfer during the pulse. Heat transfer to the surroundings is on the time scale of tens of *ps* for phonon-phonon coupling. The increase in resolution is due to the fact that the region heated is dependent on the limited time for heat diffusion during the pulse and tighter deposition of laser energy due to nonlinear absorption. These mechanisms for more efficient and localized energy deposition are improved with a decrease in the pulse length.

For ultrashort pulses, thermoelastic and free electron-mediated chemical effects can also occur [62]. As in the direct laser ablation of biological structures, these higher fluence pathways can lead to more precise and targeted ablation results when used with plasmonic nanoparticles. Several research groups have exploited the enhanced cavitation bubble formation around nanoparticles for creating cellular-scale effects [120,121]. Ultrafast laser light interaction with conjugated gold nanospheres has been used to create optoporation of cell membranes, with both cell killing and membrane transfection as goals [122,123]. Previous studies in the Ben-Yakar group have recently shown the possibility for using enhanced near-fields around nanoparticles for membrane optoporation as well [124]. A current hypothesis is that damage can be caused by the formation of reactive oxygen species in the medium caused through plasmonic enhancement. Ultrafast laser plasmonic nanoparticle nanosurgery offers a cutting edge approach to nanoablation of biological systems and structures.

Additionally, research by our group has been ongoing into the development of *fs* endoscopic probes that promise to bring pulsed laser imaging capabilities to *in vivo* internal human surgery applications [125,126]. Our group has found that *fs* laser light can be guided with an air-core photonic crystal fiber and carefully designed micro-packaged scanning mechanisms can be combined to yield high enough fluences for cell and tissue ablation with a miniaturized endoscope. This tool has been demonstrated with plasmonic nanoparticles for enhanced imaging and ablation performance to further extend nanoparticle ablation to *in vivo* applications.

In conclusion, metal nanoparticle near-field ablation can lead to great advances in the field of nanosurgery. This technique has advantages in precision, with nanometer scale precision (beyond the diffraction limit) with minimal heating of surrounding tissue. Molecularly specific targeting can be used to target multiple cells using inexpensive, wide-field lenses without the precise application of an optical focal point on the target for rapid treatment. Single cell precision is possible with wide-field irradiation because of large enhancements for laser light can be achieved at the position of the individually targeted nanoparticles. This technique also has great potential clinical relevance, as NIR-tuned nanoparticles can lead to deep tissue ablation, as well as connections with imaging techniques such as multiphoton plasmonic imaging and endoscope applications. Molecularly targeted plasmonic metal nanoparticles coupled with *fs* laser pulses for cell ablation is at the forefront of nanosurgery.

Chapter 4: Near-Field Enhancement with Ultrafast Laser Ablation

In this chapter, we present work that explores the real, useful magnitude of plasmonic enhancement and investigate the mechanism behind plasmon-enhanced ultrafast laser nanoablation. We first review the literature that has investigated near-field enhancement. We follow up with simulation results for near-field enhancement around plasmonic metal nanoparticles. Next, we present experimental results determining the magnitude of enhancement through ablation threshold reduction. We finish with a discussion of what these results mean for plasmonic near-field enhancement.

4.1: INTRODUCTION

Near-field enhancement is a fundamental aspect of plasmonic optical interaction and must be understood for effective design and use of plasmonics for advanced applications. Surface-enhanced Raman scattering (SERS), multi-photon luminescence, near-field enhanced ablation, electron ejection and plasma formation, and nonlinear dye enhancement all depend strongly on the near-field for the transfer of optical energy from an incident beam to the surrounding material mediated by a plasmonic metal nanoparticle. Furthermore, the near-field enhancement can be the dominant mechanism for optical energy deposition around a metal nanoparticle in an absorbing medium. Near-field enhancement around plasmonic metal nanoparticles is only weakly understood. Most work thus far has been devoted to metal nanospheres for simplicity. Limited work has been done with non-spherical nanoparticles, and the primary focus of many works has been on empirical presentation of results without a clear understanding of the near-field enhancement volume size, shape or even the primary mechanisms by which enhanced near-fields interact with the surrounding regions. For these reasons, it is vital to create a new theoretical and experimental framework for the near-field enhancement around metal nanoparticles.

As plasmonic near-field enhancement volumes are very small, exploring this enhanced region experimentally can be very challenging. Some research groups have found success using scanning near-field optical microscopes to probe near-field regions, but resolution boundaries, potential effects of the probe on the plasmonic response of the particle and the possibility of collecting light that lacks real energy flow (evanescent waves) all indicate that this method could be limited in use. Another technique that has gained recent use is photoelectron emission spectroscopy. This technique uses the excitation of ultrafast lasers to promote the emission of electrons from the plasmonic nanostructure. By evaluating the structure and the enhancement factor comparing emission, an estimate of the near-field enhancement can be obtained .

Finally, small angle x-ray scattering (SAXS) coupled with ultrafast lasers has been used to conclusively demonstrate the ultrafast nature of plasmonic energy transfer [Plech]. These latter two approaches can provide insight into near-field enhancement around plasmonic metal nanoparticles, but the experimental setups for these techniques are extremely complicated and no durable picture of the near-field enhancement is created. We thus choose the femtosecond near-field nanoablation ‘photo-imprint’ technique to probe the plasmonic near-field region.

Femtosecond laser plasmonic-enhanced nanoablation can provide an enduring ablation site in the surface that follows the near-field enhancement pattern. This ablation site can then be measured in detail with existing nanometrology techniques such as SEM or AFM. Ultrafast laser nanoablation will occur on a faster time scale than heat-transfer mediated effects, so the near-field enhancement ablation mechanism can be isolated from other effects. Furthermore, the threshold for this optical interaction can be used to find the magnitude of the optical intensity enhancement. Using this method, many measurements can be taken at once for a beam much larger than the nanoparticles, yielding a snapshot of the optical fields induced around the nanoparticles.

Several recent studies by our group and others have shown the use of plasmonic enhancement of spherical gold nanoparticles with ultrafast lasers to create sub-diffraction limited features on glass and silicon surfaces [85,93]. In this method, the plasmonic focusing properties of nanoparticles provide localized, highly enhanced near-field intensities strong enough to lead to nanoscale ablation for femtosecond (*fs*) pulses. The near-field enhancement region and corresponding possible feature size scale with the size of the nanoparticle, and there are no fundamental physical limits to prevent even smaller features from being created with this technique. Plasmonic nanoparticles are of great interest because of their strong interaction with light, resulting in uses ranging from biological contrast agents to solar concentrators.

Recent studies have focused significant effort towards understanding the plasmonic properties of non-spherical 'broken symmetry' nanoparticles [127,128,129,30]. Asymmetrical nanostructures are interesting mainly because they can provide large near-field enhancements and access to polarization and orientation effects not available in spherical particles. Gold nanorods have been used extensively in recent years for photonic and biomedical studies [46,130,131]. Unlike spheres, nanorods exhibit two resonances: a transverse and larger longitudinal resonance at longer wavelengths, depending strongly on both the diameter and the aspect ratio. By changing the geometry of the rods, the central wavelength of their longitudinal resonances can be tuned from visible to near-infrared wavelengths. Both photonics and biomedical communities have proposed to use these interesting tunability properties of gold nanorods in recent years for applications ranging from two-photon luminescence imaging to optical data storage [46,131]. Few studies, however, have examined the strong electromagnetic near-field enhancement also present for plasmonic nanoparticles.

The direct cause for plasmon-assisted near-field ablation is poorly understood, though the phenomenon has been demonstrated by several groups. Ablation can occur in the near-field of plasmonic nanoparticles when coupled with high-intensity ultrafast laser pulses. In this case, localized, sub-diffraction limited features can be created on a surface due to enhanced near-fields around a plasmonic nanoparticle. The near-field enhancement is the ratio of the near-field strength to the incident laser intensity. Since there is a constant relationship between the electric and magnetic fields for a plane wave of light, the intensity is often given as proportional to the square of the electric field – $|E|^2$. Another metric of the field strength is the Poynting vector, which is the cross-product of the electric and magnetic fields and provides the magnitude and direction of the local electromagnetic energy flow. Both the electric field ($|E|^2$) enhancement and the Poynting vector magnitude have been identified as the dominant term for ablation. Several studies have evaluated the Poynting vector and electric field enhancement for near-field ablation in the case of colloidal monolayers of dielectric spheres on a substrate [132,133].

For example, Luk'yanchuk *et al*. hypothesized that the Poynting vector travelling into the surface could be the dominant term for surface ablation for dielectric spheres on a surface subjected to ultrafast laser pulses [134]. On the other hand, Plech *et al*. showed ablation near the poles of gold spheres with *fs* laser pulses using in situ SAXS measurements and the authors proposed the E-field enhancement as the reason for ablation [92]. Several other groups have also used the $|E|^2$ enhancement as a predictor of ablation [85]. In a previous work, we investigated plasmonic laser nanoablation (PLN) using gold nanospheres on a silicon surface and found that the reduction in threshold followed the Poynting vector magnitude on the surface [93]. However, the maxima in the Poynting vector and E-field enhancement occur in the same location for all of these studies using spheres, and therefore the effects of the Poynting vector and E-field cannot be distinguished from each other as a predictor of ablation, except in the magnitude. Polarization effects can be easily determined using non-spherical particles. While all of these studies provided useful information on PLN, the use of nanorods can provide a more complete picture. By taking advantage of the 'broken symmetry' of gold nanorods, where the Poynting vector and E-field enhancement patterns are displaced from one another, we can determine the dominant term for ablation by looking at the morphology of the ablation pattern in addition to comparing the reduction in the ablation threshold with the near-field enhancement terms. Studying the plasmonic near-field enhancement of gold nanorods is also of special interest because of the strong resonance in the NIR, where *fs*-lasers are readily available (Ti:Sapphire) and which is in the 'therapeutic window' of biomedical interest.

To experimentally test the dominant term for ablation, we have chosen to use non-spherical nanoparticles where the magnitude and co-location of the $|E|^2$ and Poynting vector maxima are substantially different. The $|E|^2$ enhancement that overlaps $|S|$ for spheres can be displaced for asymmetrical geometries. The near-field properties of gold nanorods are calculated using the DDA technique. Initial results showed that gold nanorods indeed exhibited a displacement in position of the $|E|^2$ and $|S|$ maxima and, most importantly, order of magnitude differences in enhancement. To compare these simulations with our experiments, we subsequently included the effect of a silicon substrate on the plasmonic near-field response of gold nanorods. Though the relative refractive index of a particle embedded in a uniform medium can easily be accounted for, the effect of a substrate in close proximity on the plasmonic response of a nanoparticle must be explicitly modeled to understand the electromagnetic effects at the interface. We find that the Poynting vector magnitude on the surface results in a significantly different enhancement magnitude and distribution around the particle than the $|E|^2$ term. This result gave us a clear path to evaluate the mechanism of ultrafast laser plasmonic near-field ablation by evaluating which term is a better predictor of ablation [43].

In this chapter, we present the PLN of silicon with enhanced femtosecond laser pulses in the near-field of gold nanorods. The surface enhancement and corresponding ablation is strongly dependent on the beam polarization, nanorod orientation, and local environment near the nanoparticle. We measure nanoparticle near-field enhancements through a reduction in the threshold energy to create surface ablation and compare the results with our simulations.

4.2: SIMULATIONS

In the second part of our efforts towards developing a comprehensive understanding of plasmonic properties of nanoparticles, we expanded our simulations to understand the interesting near-field enhancement effects around plasmonic nanoparticles. These simulations included developing near-field enhancement plots for spheres as well as the verification of DDA technique for near-field enhancement magnitude calculations for non-spherical particles. As part of this research, we studied the effect of the magnetic field and Poynting vector enhancement in addition to the more commonly studied electric field. By comparing the field enhancement around plasmonic particles with the near-field focusing observed for small dielectric spheres, shown in Figure 4.1, we showed that the plane-wave approximation is invalid in the near-field region of plasmonic nanoparticles. The plane-wave approximation is commonly used to correlate the optical intensity in terms of the squared electric field ($|E|^2$). The inaccuracy of this approximation in the near-field of a plasmonic nanoparticle indicates that the Poynting vector, |S|, is a better measure of electromagnetic enhancement in this region [43].

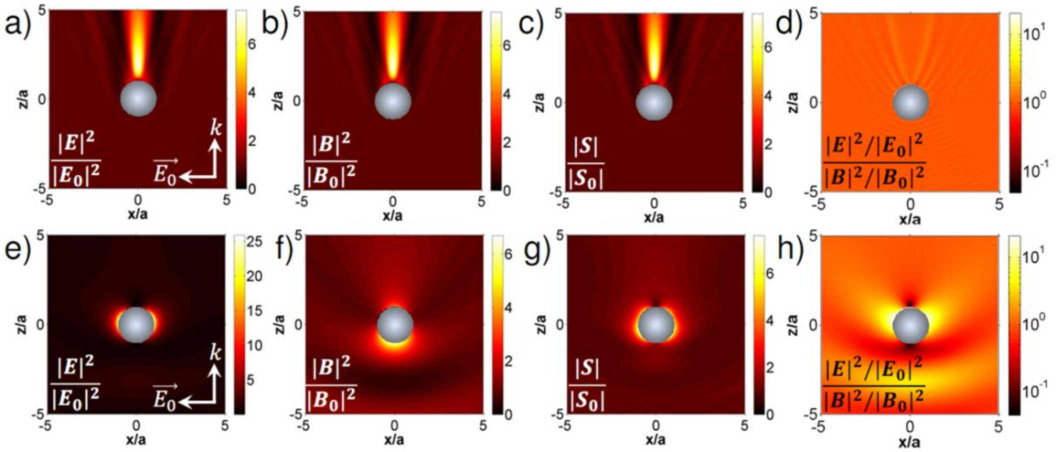

Figure 4.1: The enhanced values of electromagnetic fields around metal and dielectric nanospheres. *The calculations are for a 2 µm* SiO_2 *sphere (a – d) and a 150 nm gold sphere (e – h) in a water environment at a wavelength of 780 nm. The polarization of incident light is in the x direction and the light is propagating in the positive z direction. Note that the axes have been scaled by the radius "a" for each sphere. As can be seen in (h), the plane-wave approximation, in which the |E|/|B| ratio is constant, is invalid around the plasmonic nanoparticle.*

4.3: DISCRETE DIPOLE APPROXIMATION IN THE NEAR-FIELD

In addition to an accurate simulation of the far-field optical properties of plasmonic nanoparticles, the discrete dipole approximation can be used to determine the enhanced near-field response. We calculate the electric field and derive new equations for determining the magnetic near-field surrounding the nanoparticles from the superposition of the scattered and incident fields. Near-field enhancement magnitudes are important for understanding near-field ablation because of their effect on decreasing the ablation threshold and controlling the ablation patterns and expected size scales. We compute the scattered fields resulting from the complex dipole polarizations using Green's tensor formulation for the interaction of point dipoles with Eqs. (4.1)–(4.2) [31,27].

$$\vec{E}_{scat,m} = \sum_{n \neq m}^{N} \frac{e^{ikR_{mn}}}{R_{mn}^{3}} \left\{ \left(3\hat{r}_{mn}(\hat{r}_{mn} \cdot \vec{P}_{n}) - \vec{P}_{n}\right)\left(1 - ikR_{mn}\right) + k^{2}R_{mn}^{2}\left(\left(\hat{r}_{mn} \times \vec{P}_{n}\right) \times \hat{r}_{mn}\right) \right\} \tag{4.1}$$

$$\vec{H}_{scat,m} = \sum_{n \neq m}^{N} \frac{e^{ikR_{mn}}}{R_{mn}^{3}} \left(\hat{r}_{mn} \times \vec{P}_{n}\right)\left\{k^{2}R_{mn}^{2} + ikR_{mn}\right\} \tag{4.2}$$

We use these equations to calculate the sum electromagnetic (E and H) field strength enhancement at point m for each dipole n, having a complex polarization P_n at a distance of R_{mn} in the direction from the dipole to the field point, r_{mn}, in incident light with a wave number k. We calculate near-field enhancements from dipole polarizations using a home-written program for Eqs. (4.1)–(4.2). The Poynting vector represents the direction of light propagation, and has the magnitude of the electromagnetic energy density at a given position. To our knowledge, the calculation of magnetic fields and the Poynting vector from dipole polarizations in DDA has not been presented before our studies. Previous research in the Ben-Yakar group has identified the Poynting vector magnitude as an accurate predictor for the PLN ablation threshold [93], thus we calculate this term in our current simulations from the electric and magnetic fields at each location.

4.3.1: Benchmarking with Spheres

After developing the mathematical capability to find the ***E*****,** ***B*****,** and ***S*** from a set of dipole polarizations for any arbitrary position in space, we subsequently compared the near-field enhancement patterns obtained by DDA to those predicted using Mie theory. The accuracy of near-fields calculated using DDA has not been well-studied. Specifically, no published studies have examined the magnetic fields and the Poynting vector values calculated from DDA dipole polarizations. The results matched well both qualitatively and quantitatively. The error in fields ($|E|^2$, $|B|^2$, and $|S|$), calculated using DDA and compared with Mie theory, were confined primarily to the surface of the sphere. We compared the fields on a square grid of 150×150 nm^2 (3 diameters square) in the central vertical cross-section, including both internal and external fields. The region calculated corresponds to plus and minus one diameter in the horizontal and vertical directions from the sphere surface, which is the region that near-fields enhancements are concentrated. We divided the difference in the calculated fields from DDA and Mie theory by the Mie theory values to obtain a relative error for each point. By adding up these values and dividing by the number of points, we obtain an average relative error for the region studied. Using this method, we found an average relative error of 16%, 1% and 6% for the $|E|^2$, $|B|^2$, and $|S|$ field magnitudes, respectively, for a sphere composed of 32 cubic dipoles across the diameter at the plasmonic resonance. These errors also decreased with decreases in the dipole cube size, to only 3%, 0.4% and 1.6% for the $|E|^2$, $|B|^2$, and |S| field magnitudes, respectively, for a sphere composed of 192 dipoles across the diameter. Using these simulations, we conclude that DDA can provide accurate field enhancement values for near-field calculations. Lastly, we expanded these validation studies to qualitatively compare DDA results with published studies on the interaction of light with particles on a surface. Specifically, we compared DDA particle-on-a-surface simulations to expanded Mie theory results from the literature [134,135,13]. Our studies showed morphological agreement with published enhancement patterns and scattering distributions for spheres on a surface.

4.3.2: Near-Field around a Gold Nanorod on a Silicon Surface

DDA simulations were expanded to simulate a nanorod on a silicon substrate in an air environment to study the near-field enhancement for plasmonic laser nanoablation. These simulations automatically take into account multiple reflections between a particle and surface, a critical aspect for particle on surface simulations [134]. The dimensions of the silicon substrate were 240 x 190 x 140 nm^3, centered beneath the particle (~10 million total dipoles). The computational simulations for nanorods on a silicon substrate included the presence of a 2 nm native oxide layer. We modeled the native oxide with the optical properties of silicon dioxide, as shown in Kim *et al*. [136], using tabulated data [24]. The cross-sectional area of the domain was large enough such that edge effects did not affect the near-fields around the particle. Adjusting the planar expanse or depth of the simulated substrate beyond this level changed the peak near-field enhancements by less than 10%.

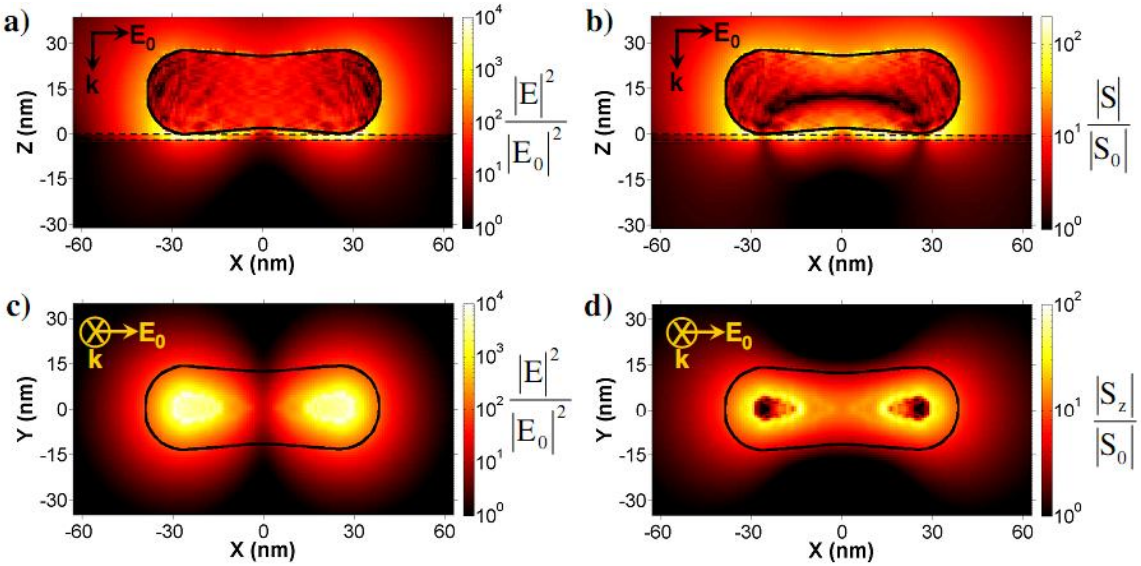

Figure 4.2: Calculated near-field enhancement around a gold nanorod (28 x 77 nm^2) on a silicon substrate. *Images a) and c) show the $|E|^2$ enhancement, while b) and d) show the enhancement in the Poynting vector magnitude |S|. The incident light has λ = 780 nm and its polarization is parallel to long axis of the nanorod. The images a) and b) show the enhancement in the central cross-section of the rod. Images c) and d) show the field enhancements in the top layer of the substrate. The black outline shows the initial position of the nanorod. Note that the substrate simulated is much larger than the expanse shown in (a – d).*

Figure 4.2 shows the electromagnetic enhancement patterns around a nanorod on a silicon surface. The curved black solid lines show the outline of the particle, and the upper and lower dashed black dotted lines show the top of the substrate surface (2 nm thick layer of SiO_2) and the top of the silicon surface, respectively. In comparing the subplots *a* – *d* in Figure 4.2, it is important to notice the differences between the $|E|^2$ and |S| plots. The $|E|^2$ – field enhancements are two orders of magnitude larger than the |S| for both the cross-sectional plots as well as for the enhancements on the top surface. The enhancement patterns are also clearly different. For the $|E|^2$ enhancement, there are two strong regions of enhancement near the end of the rod, while due to the effect of the magnetic field on the Poynting vector enhancement pattern, the |S| enhancement is more distributed beneath the nanorod. The component of the Poynting vector normal to the surface has previously been identified as responsible for surface ablation [93,134]. We show the magnitude of the *z*-component of the Poynting vector, $|S_z|$, on the silicon surface in Figure 4.2d, but show the total magnitude of the Poynting vector, |S|, in Figure 4.2b because the normal component cannot be resolved in the perpendicular cross-section.

As the nanorods are randomly distributed on the surface, it is important to understand the interaction efficiency and near-field enhancement of isolated rods as a function of the angle between the nanorod long axis and the polarization of the incident light. We therefore performed a numerical study of the enhancement and interaction efficiency compared with the polarization alignment angle for isolated particles and for particles on a surface. The results revealed a $\cos^2\theta$ dependence on interaction efficiency and peak enhancement with angle θ in both cases. It should also be noted that the skin depth, or characteristic penetration length, of near-infrared light in gold at this wavelength is on the same length scale as the diameter of the nanorods in this study.

4.4: FEMTOSECOND LASER CHARACTERIZATION

Significant characterization efforts were exerted to ensure the validity of experimental results before nanoablation studies were carried out. Ultrafast laser pulses were generated from an amplified Ti:Sapphire laser system (Spitfire, Spectra Physics) with a central wavelength at 784 nm and a measured pulse length of 184 *fs*. We first checked the beam quality at the laser system using a focusing lens and beam profiler (Spiricon LBA-PC software). The characterized beam quality revealed an initial beam diameter of 5.4 mm and a Gaussian spatial beam profile. The beam quality was excellent with M_x^2=1.09 and M_y^2 = 1.17 determined using a 1000 mm focal length lens and beam profiler system following the procedure described in [137]. The beam profile and three dimensional plot of the intensity peak as a function of position are shown in Figure 4.3.

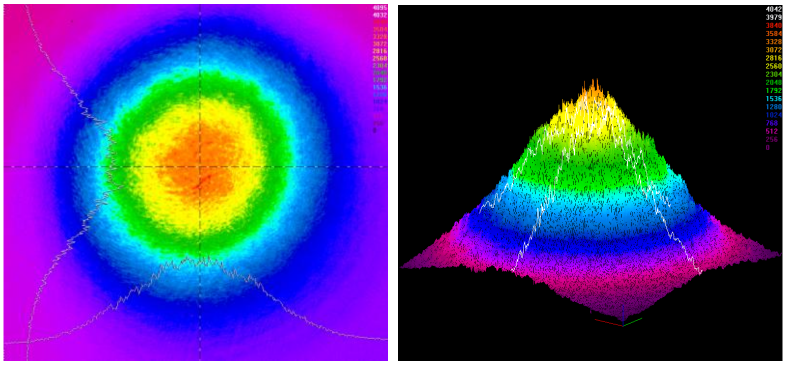

Figure 4.3: Profile of the beam from the Spitfire ultrafast laser amplifier system showing high beam quality.

4.5: ULTRAFAST ABLATION THRESHOLDS

Table 4.1 presents a summary of the *f*s-laser ablation thresholds for silicon (100), fused silica, and gold films of two different thicknesses obtained in our experiments and compared with data tabulated from other published studies. The thin gold films were fabricated through thermal evaporation onto a glass substrate, using a thin intermediary chromium layer to promote adhesion. We estimated the thresholds for single shot ablation according to the D^2 method [138]. In this method, the logarithmic dependence of the ablation diameter and fluence provide both the spot radius on the sample and threshold energy, thus a good estimate for the real threshold fluence. Using a minimum of 10 different pulse energies in all cases with the beam at normal incidence to the sample, we estimated the peak fluences at the ablation threshold. The fabricated ablation craters were evaluated using both SEM and AFM to determine the crater diameters.

Furthermore, the AFM topographical data could also be analyzed using the depth method for obtaining single shot ablation thresholds for silicon. The depth technique, which was presented in previous work of the Ben-Yakar group [93], yielded similar results to the D^2 ablation threshold method. In addition, these values agree with other reported values from the literature, as shown in Table 4.1. Our spot size and threshold uncertainties were determined from the linear regression analysis of all the spots measured for a sample.

All measurements presented in Table 4.1 use single ultrafast laser pulses with wavelengths between 775–800 nm and pulse lengths from 90–300 *fs* [93,139,140,141,142,143,144,145,146]. This is an important point, as the ablation threshold will vary significantly as a strong function of the number of applied pulses and also changes with wavelength and pulse duration. We use average fluences for the ablation thresholds shown in Table 4.1 for easy comparison with literature values. However, peak values, which provide the true local fluence at a point and are given as two times the energy divided by the spot area, are used for all local ablation measurements throughout the paper.

To measure the reduction in the ablation threshold, we needed to know the ablation threshold of the materials used without near-field enhancement effects. We investigated the *fs*–laser ablation threshold for gold films of a variety of thicknesses. One would expect that the ablation threshold for a thin film would differ from the bulk material threshold due to physical interactions with underlying layers in the thin film case. For example, other studies have observed an increase in ablation threshold with film thickness up to an effective penetration depth [147]. Since the effective penetration depth is expected to be smaller than 100 nm for near-infrared light, the 500 nm thick film is expected to have similar ablation characteristics to a bulk sample, as we observed. Due to the similarities in values and overlapping uncertainties in the threshold measurements of the gold samples, we decided to use our threshold measurement for the 500 nm gold film as the ablation threshold of gold nanoparticles, while not neglecting the possibility that the size scale of the gold nanorod might have an effect on the ablation behavior.

Table 4.1: Single-shot ultrafast laser ablation thresholds of various materials.

Material	***Thickness***	***Ablation Threshold***	***Source***
Silicon (100)	Bulk	0.21 ± 0.03 J/cm^2	**This work**
Silicon (100)	Bulk	0.19 ± 0.02 J/cm^2	[93]
Silicon (100)	Bulk	≈ 0.2 J/cm^2	[139]
Silicon (100)	Bulk	0.21 ± 0.02 J/cm^2	[140]
Fused Silica	Bulk	2.29 ± 0.27 J/cm^2	**This work**
Fused Silica	Bulk	2.1 ± 0.2 J/cm^2	[141]
Fused Silica	Bulk	≈ 2.48 J/cm^2	[142]
Fused Silica†	Bulk	2.07 J/cm^2	[143]
Gold Film on Glass	25 nm	0.40 ± 0.13 J/cm^2	**This work**
Gold Film on Glass	30 nm	0.56 ± 0.05 J/cm^2	[144]
Gold Film on Glass	300 nm	~0.6 J/cm^2	[145]
Gold Film on Glass	500 nm	0.54 ± 0.8 J/cm^2	**This work**
Gold	Bulk	0.46 ± 0.05 J/cm^2	[140]
Gold	Bulk	0.46 ± 0.05 J/cm^2	[146]

4.6: EXPERIMENTAL METHODS

A diagram of our experimental setup is shown in Figure 4.4. In this experimental setup, pulses from the Ti:Sapphire laser system are focused onto a substrate using a microscope objective lens. The objective lenses used were a air-immersion objective with a numerical aperture (NA) of 0.28 (10× magnification, Mitutoyo) or high NA water-immersion lens (NA = 0.95, 20× magnification, Olympus).

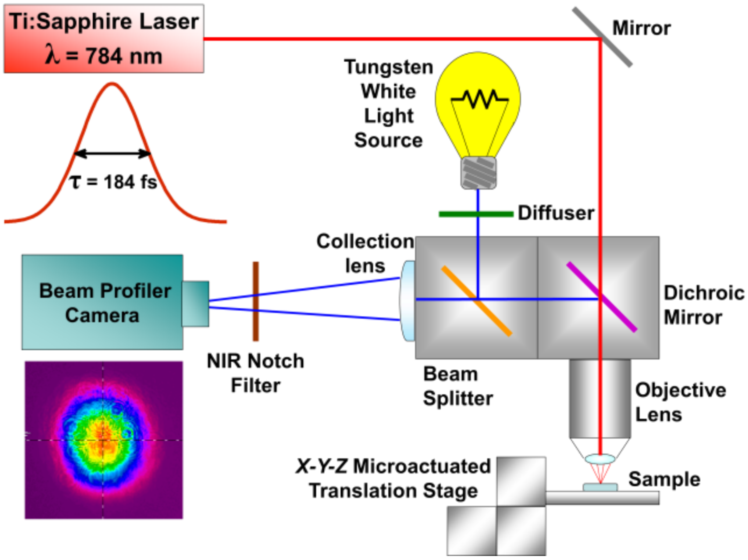

Figure 4.4: Schematic of optical setup for ultrafast laser ablation studies.

We focused the laser beam on the sample using the air-immersion objective. To characterize the spot size on the sample, we measured the diameters of craters ablated with single laser pulses on silicon in the absence of nanoparticles as a function of laser fluence. Taking advantage of the logarithmic dependence of the square of the ablation crater diameter with the fluence for a Gaussian beam, we estimated the spot size on the sample in each experiment [138]. From this data, we measured a laser beam spot size radius at the focal plane of 2.57 ± 0.15 µm. This value can be compared with a theoretical minimum spot radius of 2.23 µm for a truncated Gaussian beam using the experimental back aperture of the lens (12.5 mm) and the fill factor [148]. The beam profile at the sample was found to have a Gaussian distribution using the integrated beam profiler. Great care was employed to align the beam to achieve the best results. The surface flatness was found to vary by less than 0.01° in the *x* and *y* directions by measuring the optical focus as the substrate was translated using the microactuators.

We diced silicon (100) wafers into 5 x 5 mm^2 sections with a diamond cutter and ultrasonically cleaned them using sulfuric acid and methanol. To identify individual ablation sites, we fabricated microscale grids on the silicon surface using a focused *fs*-laser beam and deposited a 10 µL aliquot of the AuNR1 colloidal nanorod solution on this region of the silicon surface. The droplet of gold nanorods was subsequently left to dry at room temperature, leaving a relatively uniform distribution of nanorods across the surface. The samples were washed with ultrapure water after the deposition of particles to remove unattached nanorods and any other contaminants from the surface. After deposition and the initial washing, the nanorods were firmly attached to the surface, and further immersion in water or handling of the wafer had no effect on the nanorod positions or orientation. This was confirmed with before and after analysis of SEM images where the location and orientation of each nanorod in a defined region was evaluated.

After deposition and washing, the nanorods on the substrate were imaged using high resolution field emission scanning electron microscopy (SEM). Composite image of the entire 10 µm × 10 µm grid sites were created by stitching together many smaller high magnification images to yield a mosaic showing the entire grid. This process was repeated after *fs*-laser irradiation to evaluate the fate of each nanorod in the grid. More than 20 separate grids on 4 separate substrates were tested using these techniques, but the final values presented here are from a single substrate and ablation session to minimize potential errors in angle and fluences, but all obtained data were comparable. After ablation, atomic force microscopy (AFM) techniques were also employed to determine the depth of the nanoablation sites.

To minimize the effects of heating so that we could isolate the near-field effects for plasmonic ablation, we studied nanorods off-resonance in an air environment. In air, the resonance wavelength of nanorods is blue-shifted as compared with nanorods in an aqueous medium. The absorption efficiency of isolated rods is more than 20 times greater in water than in air at 780 nm.

4.7: ULTRAFAST LASER PLASMONIC LASER NANOABLATION ON A SURFACE

The silicon substrates were imaged before and after *fs*-laser irradiation using high resolution field emission scanning electron microscopy (SEM) and atomic force microscopy (AFM) techniques. Several sites on the silicon surface were targeted to observe a significant nanorod population. We irradiated the silicon at the center of each grid with a single laser pulse slightly above the silicon ablation threshold (550 - 700 mJ/cm^2). We then calculated the fluence at the position of each uniquely identifiable nanorod using the distance from the center of the single shot ablation crater and the Gaussian beam profile. By identifying the angle of each rod relative to the laser polarization, we determined the effective fluence along the long axis of the rods at each individual rod locations. Our goal was to study the effective fluence for nanorod survival, nanorod removal, and plasmonic ablation of the silicon surface. Using this data, we found ablation thresholds and corresponding enhancements for PLN using gold nanorods on silicon. Figure 4.5 shows an angled SEM view of the near-threshold ablation site and the grid. The divots within the ablation crater are the result of enhancement from nanorod assemblies within the focal region.

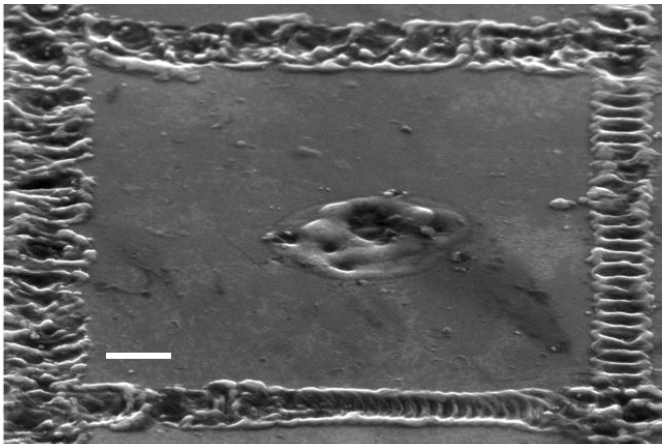

Figure 4.5: Angled SEM image showing morphology of an ablation site and the registration marks.

4.7.1: Polarization Effects

Figure 4.6 presents the percentage of nanorod removal as a function of the effective fluence. We examined over 200 nanorod sites to check if each rod was removed or remained in place after laser exposure. Each result was placed into logarithmically spaced fluence bins, containing at least 10 nanorods. Each data point in Figure 4.6 represents the percentage of rods removed in the fluence bin, and the fluence is given as the average of the rods within that bin. Unlike for spheres, the energy coupling of laser light with the rods is polarization-dependent. As discussed above, the near-field enhancement and absorption and scattering cross-sections scale as $\cos^2\theta$ multiplied by the maximum values for an aligned nanorod. By applying a $\cos^2\theta$ multiplier on the fluence, we estimated the effective fluence that each rod actually contributed to the longitudinal resonance. This correction collapsed the randomly scattered data into a single trend. The errors shown for each data point correspond to the size of each bin for the x axis and the standard deviation of the number of nanorods in each fluence bin for the y axis.

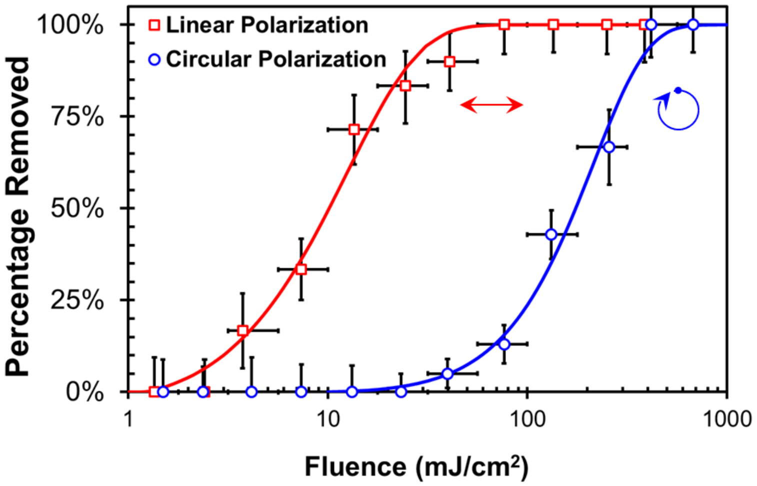

Figure 4.6: Percentage of nanorods removed from a silicon surface as a function of fluence*. The nanorods removed following single-shot irradiation are presented as a function of the effective local fluence (peak fluence) for linearly and circularly polarized laser light with cumulative Weibull fits. The data points present nanorod outcomes grouped into logarithmic fluence bins. We calculated the effective peak fluence by multiplying the local fluence by the* $\cos^2\theta$ *of the angle between the polarization and nanorod long axis.*

Due to statistical variations in rod size, aspect ratio, and shape, the thresholds for rod removal and ablation are statistical estimates. To model the statistical trend of our results, we fit the nanoparticle removal data using a Weibull cumulative damage equation [149]. The Weibull damage equation, more commonly used in materials failure analysis, fits the failure probability of inhomogeneous samples to a given load according to Eq. 5.

$$P_R = 1 - e^{-\left(\frac{F - F_{th}}{F_0}\right)^{\beta}} \tag{4.3}$$

Here, the nanoparticle removal probability, P_R, gives the percentage of rods removed for a given fluence value. The exponent, β, is a measure of the sample homogeneity and increasing β results in a narrower transition width. In our application of this equation, the applied stress is given by the laser fluence, F. The parameters for fitting include a nanorod removal threshold of $F_{th} = 1.2$ mJ/cm^2, a characteristic removal value of $F_0 = 12.2$ mJ/cm^2, when 63% rods (1 – 1/*e*) have been removed, and a β value of 1.2. The width of the transition from no removal to the removal of all nanorods can be explained by the differences in enhancement for various size nanorods. The same experiment was also performed using circularly polarized light. In this experiment, we did not observe any angular dependence with the orientation of nanorods (as expected), and found that the plasmon resonance coupling was much less efficient as a result of the continuously shifting polarization direction. For circularly polarized light, the Weibull coefficients were $F_{th} = 8.9$ mJ/cm^2 and $F_0 = 210$ mJ/cm^2 with a β value of 1.6. The β value is increased for the circularly polarized case because a degree of freedom has been removed, leading to an effectively more homogenous sample.

We attribute the nanorod removal to the ablation of the gold rod itself as a result of the enhanced intensities in its surface. To find the observed enhancement with these experiments, we compare the characteristic removal value ($F_0 = 0.012$ J/cm^2) for the gold nanorods with the ablation threshold observed for the 500 nm thick gold thin film (1.08 ± 0.15 J/cm^2). Assuming that the characteristic removal value is representative of an average rod on the surface, we obtain an enhancement of ~89 ± 13. The ablation threshold for gold nanoparticles may be lower than the threshold for bulk gold considering of size confinement and electrical isolation. Nevertheless, the enhancement value agrees within the margin of error with the peak enhancement in the Poynting vector magnitude within the nanoparticle on a silicon surface, which has a peak value of ~100.

In addition to this agreement, the removal of many nanorods outside the direct silicon modification region implies that near-field effects were responsible for their complete removal.

Other possible mechanisms for the nanoparticle removal include heating-related effects such as nanoparticle melting and its complete evaporation, explosive boiling, or surface heating/expansion resulting in nanoparticle ejection. In the case of nanoparticle ejection, however, we would expect to observe displaced nanoparticles somewhere on the silicon substrate, none of which were ever observed in our experiments. Assuming no heat transfer out of the particle during the laser pulse and using the absorption cross-section for an isolated nanorod of 28 x 76 nm^2 simulated with 192 dipoles across the nanorod diameter, the threshold for the complete particle melting would be ~37 mJ/cm^2, which is more than three times greater than the experimental characteristic removal threshold. We hypothesize that the time scale for PLN is much shorter than for a heat transfer-mediated nanorod removal. Plasma formation can occur within ~1 ps for ultrafast pulses [150], while melting does not occur until the electrons transfer absorbed energy to phonons, which occurs ~30 ps after the laser pulse for a gold nanorod [151]. If the rods are ablated by PLN, they will be removed through plasma expansion. We also note that if the heating was responsible for nanoparticle removal, there should be a fluence zone where nanorods become spherical due to melting. We therefore reason that nanoparticle ablation will occur prior to and at lower fluences to melting, boiling, or surface expansion and ejection, even if the threshold is reached for nanoparticles on a surface. We thus conclude that complete ablation of the nanorods is the cause of removal.

To test our hypothesis, we applied a single femtosecond laser pulse to create plasmonic laser nanoablation (PLN) sites in the near-field of gold nanorods deposited on a silicon surface. Prior research proved that the PLN technique could provide nano-scale 'photo-imprints' of the enhanced near-field intensity of gold nanospheres on silicon surface [93,152]. Using a similar method, we determined the enhancement magnitude through a comparison of the fluence necessary to create nanoscale ablation features with the unenhanced ablation threshold. We fabricated and measured nanoablation sites as small as 22 × 66 nm using femtosecond 780 nm light ($\lambda/35$ in the short dimension). To measure the depth of these small ablation pits, an inverse 'nano-mold' technique was developed to obtain more easily measured bumps.

We observed nanoscale laser modification and ablation of the silicon surface at local fluences significantly lower than the direct *fs*-laser ablation region of silicon ($10\ \text{mJ/cm}^2 < F < 420\ \text{mJ/cm}^2$). The efficiency of the ablation in this regime depended on the orientation of the rod relative to the incident laser polarization. We studied the nanoablation sites using high-resolution SEM to determine the nanocrater lateral dimensions and AFM to measure the nanocrater depth profiles.

Figure 4.7 shows SEM images of nanoscale ablation sites. Within the direct *fs*-laser modification region of silicon (at $F > 420\ \text{mJ/cm}^2$), the nanorod ablation sites were local semispherical craters. Outside the silicon ablation threshold, we found that the nanorod ablation sites were photo-imprints of the nanorod, very similar in size to the nanorod. This is an interesting result, because the ablation sites did not consist of two separate craters for any of the plasmonic ablation sites, even for sites very close to the ablation threshold. We interpreted this result as evidence that the Poynting vector magnitude dominated the ablation morphology. We created nanoablation feature widths as small as 22 nm (Figure 4.7a), representing the creation of λ/35 features using plasmonic near-field enhancement. Near the plasmonically-enhanced threshold, the ablation is confined to a very small and shallow region beneath the nanoparticle, as expected from DDA simulations.

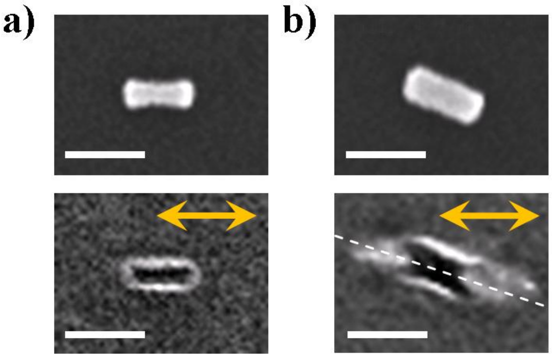

Figure 4.7: Plasmonic laser nanoablation (PLN) studies of nanorods deposited on silicon surface, including before and after images of nanoscale ablation sites. *SEM images of the nanorods before and after laser irradiation at a local effective fluence of a) 54 mJ/cm^2, right at the ablation threshold, and b) 218 mJ/cm^2. The scale bars correspond to 75 nm and the yellow arrows indicate the incident polarization.*

4.7.2: Depth Measurements

We developed a new method to measure the ablation depth profile for individual nanoablation sites by creating an inverse nanoscale mold of the ablation features on the silicon surface. We first thermally deposited an Au layer on the silicon surface at a rate of 0.5 nm/s to a final thickness of 25 nm. We then deposited a layer of chromium (Cr) on top of Au for adhesion without exposing the sample to air. By adhering a backing layer of glass to the Cr layer, we could peel the gold nanomold from the silicon surface. No release layer was necessary as the adhesion between Au and silicon is very weak. The inverse mold of the silicon surface topography thereby allowed us to measure ablation craters as raised protrusions rather than concave nanopits. A schematic of this process is shown in Figure 4.8a. Standard sharp AFM tips could then easily provide the profile of the raised protrusions, eliminating the need for fragile and costly ultrahigh resolution probes (e.g. carbon nanotube-tipped probes). Imaging raised protrusions also eliminated the difficulties associated with AFM imaging within nanoscale surface indentations. This inverse nanoscale mold method could serve as a reliable metrology technique for various nanoscale studies.

We validated the results by comparing a set of known feature sizes from the spot size crater measurements in the original and molded surfaces, and observing that fidelity was preserved. In particular, the spot size craters, which were extensively characterized with both SEM and AFM and ranged in size from greater than 10 μm to 500 nm in diameter, could be used as an on surface calibration standard to ensure that molded copies accurately reproduced surface features in the original silicon wafer.

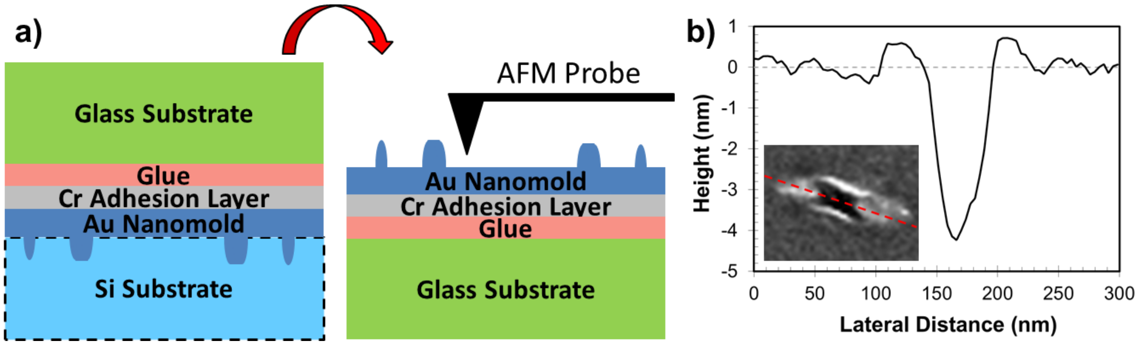

Figure 4.8: Plasmonic laser nanoablation with gold nanorods deposited on silicon surface. *a) Nanoscale ablation site measurement method and b) depth profile plot, with an inset showing the ablation site and measurement path.*

As can be seen in Figure 4.8b, a small rim was present at the edges of the nanoablation sites. This rim, previously described for the direct laser ablation of dielectrics [63], is caused by the melting of a thin surface layer beneath the surface volume at a fluence below the ablation threshold, which then is pushed to the edges of the ablation crater due to the high-pressure expanding plasma within the crater. We examined several nanoablation sites with ultrahigh resolution SEM and energy dispersive X-ray spectroscopy (EDS) for traces of gold in the crater. The results showed no gold at the crater rim or ablation sites within the limits of the system sensitivity, implying that the nanoparticle was completely removed from the ablation site.

4.7.3: Reduced Ablation Thresholds

To estimate the threshold for PLN of silicon by a gold nanorod, we plot the depths (h_a) of nanorod ablation sites as a function of the effective local fluence, shown in Figure 4.9, for a region outside of the direct *fs*-laser ablation of silicon. The effective fluence represents the portion of the incoming laser field aligned with the long axis of the gold nanorods. The results show a linear relationship between the depth of the nanoablation sites and the logarithm of the effective fluence, shown in Eq. (4.4) [93].

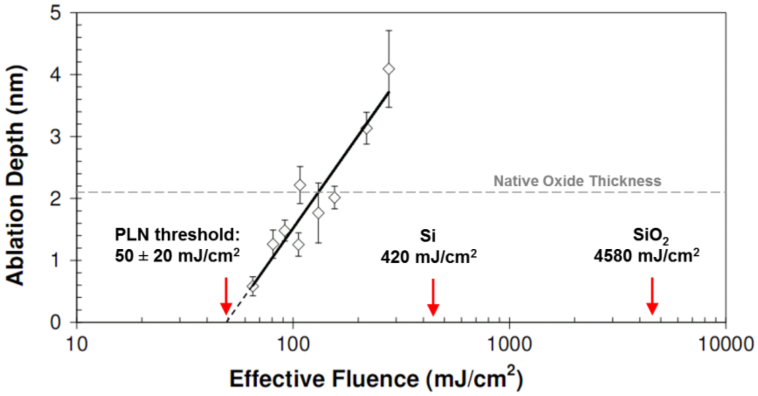

Figure 4.9: Plasmonic laser nanoablation (PLN) threshold of silicon. *A logarithmic dependence of ablation depth as a function of peak fluence is found for various sites where nanorods were present before the irradiation. Extrapolation of the linear fit to zero provides the single-shot ablation threshold (50 ± 20 mJ/cm*^{2}*) for nanorod-enhanced PLN (92× enhancement). The direct femtosecond laser ablation thresholds of silicon and silica are also given for comparison with the PLN threshold. The dashed gray line describes the thickness of the native oxide layer on silicon.*

$$h_a = \alpha_{eff}^{-1} \ln\left(\frac{F}{F_{th}}\right) \tag{4.4}$$

Using this data and Equation (4.4), we find an effective optical penetration depth, α_{eff}^{-1}, of 2.2 nm, as compared to a α_{eff}^{-1}= 129 nm for ultrafast laser ablation of silicon without plasmonic enhancement, which was found from our direct *fs*-laser experiments on silicon (Table 4.1). This difference shows the localization of plasmonically-enhanced fields around the nanoparticle and that the ablation is mainly confined to the thin oxide layer. The linear fit gives an ablation threshold, F_{th}, estimate of 50 ± 20 mJ/cm^2, where the error is calculated from linear regression analysis. This reduction in the ablation threshold reveals a plasmonic enhancement of ~8 times when compared to the direct *fs*-laser ablation of silicon. This experimental enhancement is much lower than expected from our simulation results. A significant proportion of the ablation, however, occurs within the top native oxide layer, shown with the dashed gray line in Figure 4.9, for the sites studied here. If we model the native oxide as pure SiO_2, the calculated enhancement is much more substantial for the surface ablation, which is found to be ~92 using our experimental direct *fs*-laser ablation threshold for fused silica. This magnitude of enhancement matches the Poynting vector enhancement of ~100 (Figure 4.2d) much better than the $|E|^2$ enhancement of ~10,000 (Figure 4.2c).

In addition, we observe the better match of the ablation shape with the distribution of the Poynting vector, and we thus conclude that the Poynting vector magnitude is a better predictor of ablation behavior for PLN. This conclusion is in opposed to previous work that has taken the $|E|^2$ – field as the identifier for ablation [85,92], but is in agreement with our previous study using gold nanospheres on a silicon surface [93]. In that work, we also showed that the ablation enhancement matched the magnitude of the Poynting vector on the surface. By using asymmetric gold nanorods here, we can conclusively show that the ablation pattern and enhancement match the Poynting vector magnitude better than the $|E|^2$ – field enhancement.

4.8: CONCLUSION

In this chapter, we have investigated the origin of the near-field enhancement for plasmonic laser nanoablation (PLN) using gold nanorods on a silicon surface. By using realistic shapes for our nanoparticle model, we were able to effectively simulate the near-field plasmonic enhancement behavior. From a comparison of experimentally observed nanorod nanoablation sites with simulations, we determined several parameters of importance. First, PLN with nanorods is orientation dependent and interaction scales as

$\cos^2\theta$, where θ is the angle between the nanorod long axis and the direction of polarization for nanorods on a surface. Second, we observed nanorod removal due to ablation following a statistical trend based on the nanorod size distribution and associated variation in the plasmonic enhancement. PLN with nanorods was demonstrated capable of creating nanoscale features as small as 22 nm in width on a silicon surface. The minimum feature size was found to be a photo-imprint of the nanorod, and no physical limitations should prevent the creation of even smaller features using smaller nanorods. Indeed, initial experiments were performed using the AuNR2 nanorod sample (14×54 nm^2), and ablation was observed, but the experiments were limited by the resolution of available microscopy equipment. Third, PLN with nanorods can be achieved with a laser fluence threshold of ~8 times less than the silicon ablation threshold, and ~92 times less than the silicon dioxide threshold. Finally, we conclude that the Poynting vector enhancement more accurately predicts plasmonic laser ablation than the $|E|^2$ enhancement pattern, both in terms of ablation morphology and the magnitude of enhancement. This research can be useful for predicting damage to structures and biological materials in the vicinity of nanoparticles.

In addition to developing valuable understanding of the plasmonic properties of non-spherical nanoparticles, these research efforts explored the plasmon-mediated transfer of optical energy to a semiconductor surface, which is of crucial importance for solar cells. In the course of this research, we also gained useful experience in depositing gold nanoparticles on a semiconductor surface. These studies will aid in determining the magnitude of potential near-field effects for future studies, such as in plasmonic solar enhancement.

Chapter 5: Nanoparticle Synthesis

In this chapter, we present new and adapted synthesis procedures for producing a diverse range of high quality nanoparticles using wet chemistry procedures. We also present the characterization of the synthesized nanoparticles, including UV-Vis-NIR spectroscopy, scanning transmission electron microscopy (STEM), and energy-dispersive x-ray spectroscopy (EDS). To identify plasmonic causes and effects, it is very important to have uniform samples of size-controlled nanoparticles. Furthermore, the detection of a plasmonic effect can be much improved if the polydispersity of a nanoparticle sample is reduced. While some sizes and shapes of plasmonic nanoparticles have recently become commercially available, cost and consistency can be an issue, and many different nanoparticle shapes and sizes cannot be obtained. To probe specific plasmonic effects, custom designed nanoparticles should be synthesized in-house. With this in mind, we began a significant effort towards synthesizing various types and sizes of nanoparticles for use in a range of Ben-Yakar lab experiments. In the course of these efforts, previously reported techniques were optimized, applied to new synthesis procedures and new ideas were evaluated for the fabrication of monodisperse nanoparticles of designed shapes and sizes. We conclude with a discussion of how these developed methods are useful for our experimental goals.

5.1: BACKGROUND

The colloidal synthesis of metallic nanoparticles has a wide range of advantages for the creation of plasmonic nanostructures. Metal nanoparticle synthesis is inexpensive, achievable with common laboratory equipment and chemicals, and can be used to fabricate a wide range of metal nanostructures. These particles can be stabilized in aqueous or organic solvents for time periods measured in centuries. Various reducing agents can be used to synthesize metal nanoparticles, including environmentally-friendly, biologically-derived reducing agents. Furthermore, unlike metal particles deposited by sputtering, the energy requirements are very low, as no vacuum conditions or high temperature annealing is necessary to achieve desired nanoparticle sizes. Nanoparticles can be applied on solid substrates using spray techniques, drop-casting or self-assembly, although obtaining uniform, evenly spaced nanoparticle depositions can be challenging. Lithographic approaches, such as electron-beam (e-beam) deposition, are the gold standard methods for creating designed nanostructures. Unfortunately, however, the cost and time constraints on lithography are fundamentally limiting, meaning that lithographic nanostructure nanoparticle fabrication cannot be currently be accomplished on wide enough scale for medical or solar applications.

One of the primary advantages of colloidally synthesized metal nanoparticles is the degree of control that can be obtained over the size and shape of the particle. Nanorods, branched structures, discs, triangular prisms, wires, spheres, and ovoids are among the many types of plasmonic metal nanoparticles synthesized to date. The size of particles synthesized using wet-chemistry methods can range from a nanometer to several hundred nanometers. Furthermore, shell coatings with homogenous thicknesses can be grown on top of the nanoparticle, even leading to three layer structures and more. The shell materials can be metal or dielectric materials.

Finally, colloidal nanoparticles can be functionalized for targeted medicine. In this case, ligands can be attached onto the particle surface, either electrostatically or with targeted chemical bonds, such as thiol (sulfur) groupings with gold nanoparticles. The other end of these ligands can be designed with antibodies or aptamers that will selectively attach to specific biological cells or receptors.

5.2 METHODS

Nanoparticle synthesis efforts require great attention to detail. The glassware must be exceedingly clean, as we found that even trace contamination can significantly affect nanoparticle synthesis reaction results. Therefore, we cleaned all glassware with powerful cleaning agents before use. Briefly, beakers were washed with soap and water, then soaked in *aqua regia* to remove metal ions and other contaminants and residues. Finally, the beakers were triple-rinsed with distilled water, and then again triple-rinsed with ultrapure water. Our ultrapure water system (Elga Option-Q 15) produced water with a resistivity of 18.2 MΩ·cm. Ultrapure water was used as a solvent for all aqueous reactions, while absolute ethanol (Fisher) was used for various other reactions such as the Stöber process for growing silica particles and shells.

All chemicals were used without further purification. Silver nitrate ($AgNO_3$), which has a molecular weight (MW) of 169.87 g/mol, was purchased from Acros (99%, Reagent grade). Chloroauric acid ($HAuCl_4 \times 3H_2O$) was used a gold ion source. The chloroauric acid was sourced from Acros (Reagent Grade, 99%). Trisodium citrate dihydrate ($Na_3C_6H_5O_7$, MW = 294.1) was purchased from Sigma-Aldrich (ACS Reagent Grade, >99%). Cetyl trimethyl ammonium bromide (CTAB, Fluka, 96%), tetraethylorthosilicate (TEOS, TCI, >96%), and aminopropyltriethoxysilane (APTES, Sigma-Aldrich, >98%). Sodium borohydride (Fisher Scientific) was stored in a dessicator to minimize water absorption.

5.3: SPHERE SYNTHESIS

Research by Turkevich *et al*. in 1951 (fittingly published in the Discussions of the Faraday Society) identified the citrate reduction synthesis method for creating gold nanoparticles. This reaction remains one of the simplest and most straightforward methods for synthesizing metal nanoparticles [153], but various other advances, such as the reverse micelle method, have also been used to synthesize gold particles in highly monodispersed solutions [154]. Here we present new extended results and characterization of noble metal spheres synthesized using a modified Turkevich process. We focus on reducing the size distribution of nanoparticle samples, which we evaluate through plasmonic peak full-width half-max measurements and electron microscopy.

5.3.1: Size Control with Gold Nanospheres

A recently published kinetic nanoparticle size control offers unprecedented control over nanoparticle size in a one-pot synthesis technique using sodium citrate as a reducing agent [155]. The method relies on controlling the competitive mechanisms associated with polydispersity in nanoparticle growth. One of the largest sources of different nanoparticle sizes in solution occurs due to the continuing reduction of gold ions in solution to nanoparticles, which creates a variation in nanoparticle size because the growth on each nanoparticle in solution will be similar, so nanoseeds that form later will result in smaller final nanoparticles. By controlling the energy available to the reaction processes through a slight reduction of the synthesis temperature, the creation of new seeds can be rendered energetically unfavorable. If new seed formation can be reduced, then holding the colloidal synthesis solution at temperature can result in nanoparticle size focusing through Ostwald ripening, where larger nanoparticles will approach monodispersity as the smaller particles dissolve and their constituent gold ions are integrated into larger particles. To evaluate the potential of this technique for nanoparticle growth, we synthesized a range of particle sizes using a kinetic size control approach.

Figure 5.1 shows the absorbance spectra for a set of gold nanospheres synthesized using the seeded growth method. The seeded growth technique yields repeatable gold nanoparticles with a relatively narrow size distribution. These results were obtained using a process similar to that described in [155]. For each incremental growth step, the plasmonic resonance peak, represented here as a maximum in the absorbance, red-shifts, indicating a larger nanoparticle than the previous growth stage. The only exception to this trend is in the first step of growth from the seeds, where a significant narrowing in the resonance peak is also observed. From this result, we observed that the size focusing is especially pronounced in this first growth stage

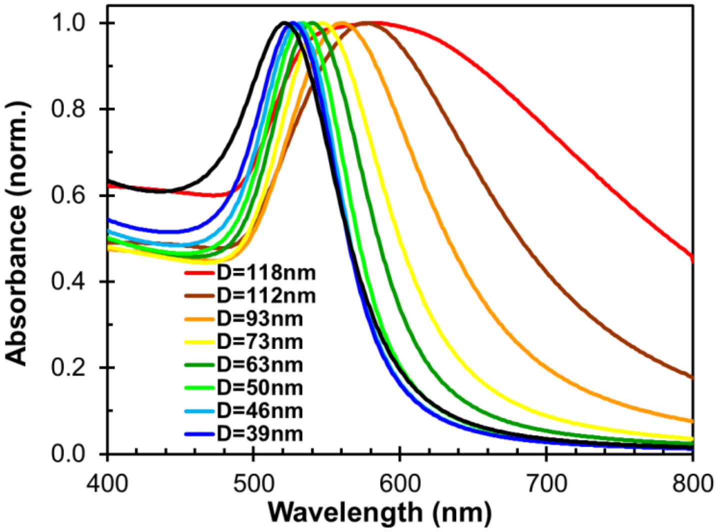

Figure 5.1: Absorbance spectra of gold nanoparticles synthesized using a kinetic ripening approach. *All nanoparticles were measured as synthesized without any purification processes. The black curve represents the initially synthesized seeds, while the colored lines show the samples taken at various growth stages. The legend shows the growth step (GS) number with the predicted size from Eq. (5.1) shown in parentheses.*

Figure 5.2 shows representative images and histograms of the measured particles for four of the nanoparticle samples synthesized with kinetic control. The synthesized nanoparticles were characterized with a field-emission scanning transmission electron microscope (Hitachi S-5500). The particles were analyzed using particle measurement tools in the microscopy software suite ImageJ. Briefly, the intensity of the particles was adjusted with a thresholding technique, and then the image was transformed into binary bit-depth. Care was taken to only count isolated particles that were well-resolved in the images.

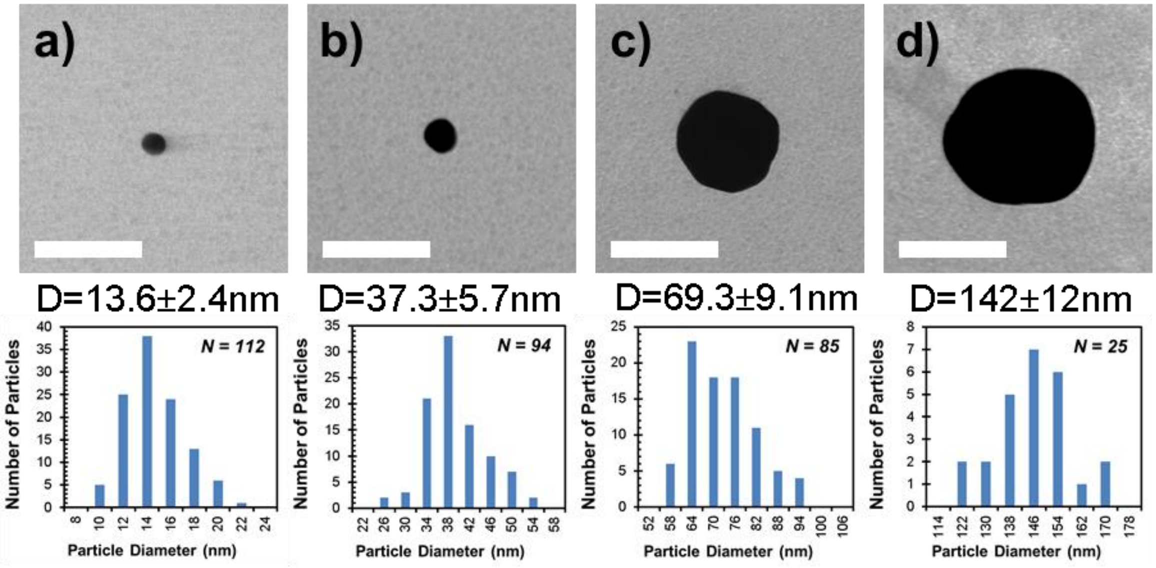

Figure 5.2: Gold nanoparticles of various sizes synthesized with kinetic control. *The top images for all nanoparticles are transmission-mode STEM micrographs of representative nanoparticles for samples prepared using a) 1, b)3, c), 6, and d) 9 growth steps. The scale bars are 100 nm. The histograms below show the distribution of measured particles, along with the number of measurements, N.*

The results for each of the syntheses are tabulated in Table 5.1. The empirically calculated gold nanoparticle diameters were found according to Equation (5.1), which was found from a numerical fit of ten separate nanoparticle synthesis, growth and characterization studies. The equation used for the empirical fit is taken from [156].

$$D = \begin{cases} 3 + (7.5 \times 10^{-5})(\lambda_{max} - 500)^4, for\ \lambda_{max} < 523 \\ 16.67\left(\sqrt{\lambda_{max} - 40} - 1\right), for\ \lambda_{max} \geq 523 \end{cases} \tag{5.1}$$

Equation (5.1) is a fit of the relationship between the nanoparticle size and plasmon resonance peak, where the nanoparticle size was measured with electron microscopy and the plasmon peak was determined using a spectrometer. The nanoparticle size can also be iteratively predicted from the plasmon peak using Mie theory by varying the diameter until the correct resonance peak value is found. The Mie theory size estimates are calculated using the constants of Johnson and Christy and fit to the peak position of the experimental spectra.

Table 5.1: Synthesized gold nanoparticle properties

Growth Step	1	2	3	4	5	6	7	8	9
Resonance Peak (nm)	521	530	530	530	530	530	530	530	530
Empirical Diameter (nm)	16	36	46	50	64	74	92	112	118
Mie Diameter (nm)	14	40	50	54	68	76	90	108	112
Measured Diameter (nm)	13.6 ±2.4	-	37.2 ±5.7	-	-	70 ±9.1	-	-	142 ±12

Both the empirical size and Mie theory yield larger predicted diameters than the measured values. A distribution of sizes in a colloidal sample results in a redshift of the peak from the ensemble average size. This occurs because larger particles have stronger optical interactions, even when normalized by size, leading to a disproportionate effect on the spectral response. Thus, it is expected that Mie theory calculations will predict a larger size than what is actually observed. The only exception to this trend is the final particle growth step, which is actually larger than prediction. For particles this large, the peak is broad and flat, meaning that any prediction based solely on a peak position will be subject to large errors. Measuring spectra and trying to determine particle size is an example of the inverse problem, which can be difficult to determine unambiguously.

5.3.2: Improved Monodispersity with Gold Nanospheres

As can be seen from the widths of the peaks in Figure 5.3, the new method approaches the narrow size distribution of commercially purchased gold nanoparticles. The peak will shift slightly for every different particle size around the median, so the presence of multiple particle sizes in a nanoparticle sample will result in a broadening of the plasmon peak.

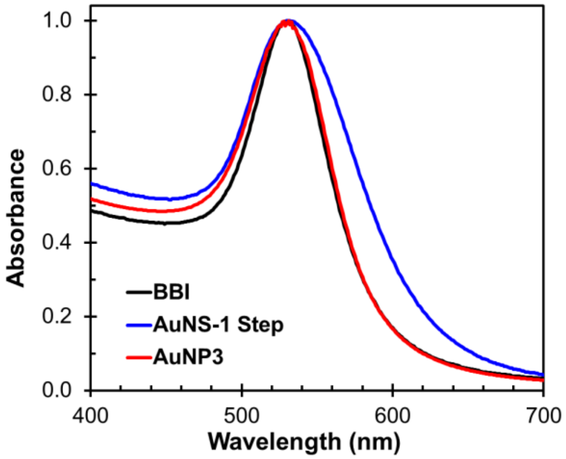

Figure 5.3: Comparison of absorbance spectra of 50 nm gold nanoparticles. *The BBI nanoparticles were purchased from a commercially available source. The other particles were fabricated in house using one-step and kinetic ripening synthesis protocols.*

Table 5.2 shows the measured and predicted properties for each of the nanoparticles shown in Figure 5.3. We also found that the stepped growth particles had improved shape and reduced ellipticity in comparison with the nanoparticles directly formed in one step.

Table 5.2: A comparison of synthesized gold nanoparticle properties. The nanospheres denoted BBI are purchased from a commercial source. The other nanoparticles are synthesized in-house with either a 1 or 3 step process.

Nanoparticles	BBI	1-Step	3-Step
Resonance (nm)	530	532	531
FWHM (nm)	70	108	70
Diameter (nm, Emp.)	43	48	46
Diameter (nm, MieJC)	48	52	50

5.3.3: Synthesis and Size Control with Silver Nanospheres

We adapted the seeded growth technique demonstrated for gold for the synthesis of silver metal nanoparticles with a range of sizes. The synthesis of silver nanoparticles has been studied in some detail, although comprehensive studies of synthesis of various sizes are unavailable. We hypothesized that the mechanisms of growth and size control should be the similar for gold and silver, although specific kinetics may be slightly different. We synthesized a range of silver nanospheres, shown in Figure 5.4a. To our knowledge, this was the first demonstration of the seeded growth of silver nanoparticles across a wide range of silver nanoparticle sizes.

Unfortunately, the silver nanoparticles synthesized in this fashion had a wider size distribution than the gold nanoparticles, resulting in broad plasmonic resonance peaks. The magnitude of the plasmonic effect will typically depend on the number of particles that respond strongly at the peak wavelength. Therefore, to obtain the best results for practical applications using plasmonic nanoparticles, additional efforts were expended to try to achieve narrower size distributions.

Initial efforts showed that the first ‘seed’ phase had significantly larger polydispersity than observed for nanoseeds prepared for gold. We also found that gold ions in solution were reduced more rapidly by sodium citrate than silver ions. It is possible that the experimentally observed wider size distribution for silver nanoparticles could be a result of early-forming nanoparticles growing more than later seeds. We note that the difference in the reduction potential, which is +1.5 V for gold and +0.8 V for silver in an aqueous environment versus hydrogen, may be at least partially responsible for these results. We hypothesized that a stronger reducing agent, such as sodium borohydride, could potentially mitigate these effects. We found that the much smaller nanoseeds prepared using the borohydride reduction method had significantly reduced polydispersity than the first ‘seed’ phase prepared using the sodium citrate reaction, leading for potential improvements in nanoparticle homogeneity using this method.

5.3.4: Advanced Methods for Size Control of Silver Nanospheres

Building on previous efforts for controlled growth of silver nanoparticles, we developed a new method for extremely fine control of the nanoparticle size. By applying the size-focusing approach to extremely fine nanoparticle seeds generated using the strong reducing agent sodium borohydride, we were able to create extremely narrow size distribution sets of nanoparticles. These particles could then be grown while maintaining the narrow size distribution properties (Figure 5.4b).

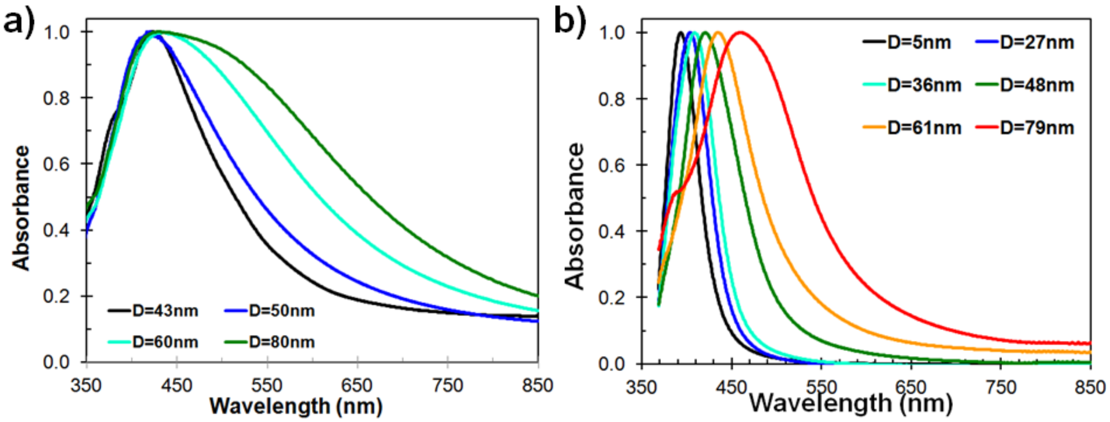

Figure 5.4: Seeded growth synthesis of silver nanoparticles of various sizes using kinetic control. *a) The citrate-only seeded growth synthesis procedure yields relatively wide size distribution plasmonic peaks. b) Small seeds initially synthesized with sodium borohydride can be grown while maintaining the initial small distribution in nanoparticle size.*

The UV-Vis-NIR spectra are shown in Figure 5.5 for two narrow size distribution nanoparticle colloids synthesized with the seeded growth method. The simulations are shown for comparison for a single nanoparticle size, revealing the near-monodispersity of samples prepared using this method.

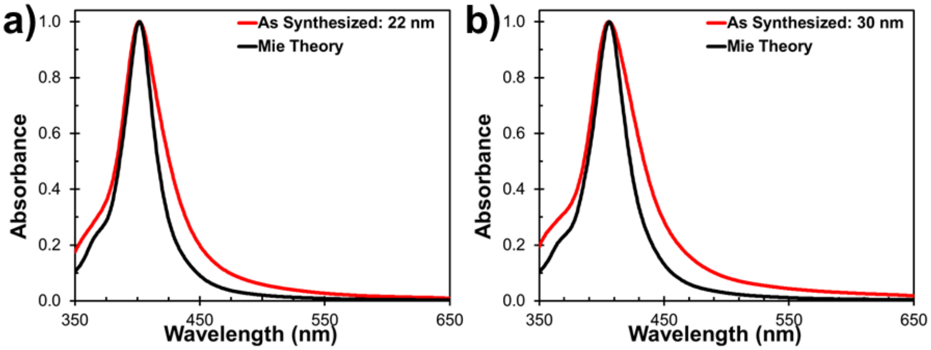

Figure 5.5: The peak position and width of narrowly distributed particles can be accurately simulated with only a single particle size. *Comparisons of experimental and simulated data for a) 22 nm and b) 30 nm spheres in an aqueous medium.*

Another interesting feature of the nanoparticle growth process was the significant narrowing in the plasmon peak during the first growth stage. This can be seen for nanoparticles prepared using both sodium citrate and sodium borohydride as an initial reducing agent. This reduction in the peak width corresponds to a ripening process where smaller nanoparticles dissolve and the added silver in solution evens out the nanoparticle sizes. A protocol for obtaining high quality silver nanoparticles through seeded growth is provided in Appendix A1.

5.4: NANOROD SYNTHESIS

With recent developments in non-spherical gold nanoparticle synthesis, the optical and plasmonic properties of a variety of new asymmetrical 'broken symmetry' geometries, such as nanorods, prisms, and stars, have been investigated [30,127]. Asymmetrical nanostructures typically can provide much larger extinctions and near-field enhancements than spherical nanoparticles for comparable resonance frequencies and volumes. In addition, non-spherical particles can also provide access to polarization and orientation effects not available in spherical particles. Gold nanorods have attracted growing interest because of their especially intense interaction with NIR light. Unlike spheres, nanorods exhibit two resonances: a transverse and larger longitudinal resonance at longer wavelengths, depending strongly on both the diameter and the aspect ratio. By changing the geometry of the rods, the central wavelength of their longitudinal resonances can be tuned from visible to near-infrared wavelengths. Furthermore, by controlling the nanorod diameter and geometry, the scattering to absorption ratio and angular distribution of scattering can be adjusted at a given plasmonic resonance wavelength. The photonics and biomedical communities have extensively studied the tunability of gold nanorods in recent years for applications ranging from two-photon luminescence imaging to optical data storage [46,131].

5.4.1: Gold Nanorod Synthesis Protocol

Gold nanorods are attractive for use in many plasmonic applications because of their stability, strong optical response, and biological compatibility. The procedure to fabricate gold nanorods (AuNRs) is straightforward (Appendix A2), but there are several pitfalls to be avoided. There are several different procedures for fabricating AuNRs, but we primarily use the two-step process, as this technique provides more consistent and successful results. The first step involves the reduction of gold in solution into small gold 'seeds', while the second step consists of the soft template-directed growth of a nanorod from the seeds. It has previously been shown that AuNR fabricated in this manner are single-crystal domains. The size, aspect ratio and longitudinal plasmon resonance peak can all be tuned during the growth stage by adjusting the ratios of the constituent chemical solutions.

There are a few issues to be aware of when synthesizing nanorods with a two-step technique. First, the brand and even batch of CTAB can be extremely important in obtaining nanorods. Prior efforts in the Ben-Yakar lab to synthesize gold nanorods were unsuccessful, most likely due to impurities in the CTAB originally used. This difficulty inspired two of the four studies that have since been published on the issues with obtaining nanorods using CTAB from different manufacturers. We have used Fluka brand CTAB successfully, but seem to have a more difficult time dissolving the CTAB powder in ultrapure water than other groups seem to have. We could not form nanorods with CTAB from at least one other manufacturer (Acros, >99%), although this CTAB was an old sample and other groups have reported successful synthesis with that brand. Furthermore, it should be noted CTAB concentrations below 60 mM resulted in no nanorod formation.

A few hours after synthesis, it may be advantageous to spin down the particles in a centrifuge (~10000 rpm) and resuspend/wash in water (3 times). This can help to avoid CTAB crystallization, which typically occurs after 24 hours. The particles can be remixed or filtered, but it can be troublesome to go through this process so it is best to resuspend in ultrapure water after synthesis. New nanoseeds should be prepared for each synthesis, as results tend to be less consistent as the seeds age. This problem can be mitigated by stabilizing the seeds with sodium citrate. The silver nitrate and gold solutions seem to have excellent shelf lives, but the other chemicals need to be mixed before gold nanorod growth.

Another interesting point is that the peak positions obtained with absorption spectrometry can give a rough idea of the aspect ratio, but the information is ambiguous, because very different nanorod geometries can yield the same longitudinal peak position. Field-emission scanning electron microscopy should be used to determine actual fabricated nanorod shape and size.

There are several key ‘rules of thumb’ for synthesizing gold nanorods. First, the nanorod aspect ratio is dependent on the $AgNO_3$ concentration. A lower concentration of silver nitrate ($AgNO_3$) will lead to shorter rods. Secondly, the total nanorod volume is strongly dependent on the amount of seeds added to the growth solution. Reducing the seed concentration will lead to fewer, larger rods as the gold in solution will be exhausted in the nanorod growth phase. The nanorod shape is weakly dependent on ascorbic acid concentration. The presented nanorod synthesis procedure will give small, primarily absorbing nanorods (roughly 13×43 nm), with a 87% yield of nanorods with a longitudinal resonance at ~800 nm. Silver nanorods can also be obtained using a similar procedure.

5.5: SILICA SHELL SYNTHESIS

Concentric nanoshell structures can be extremely interesting for plasmonic study. Silica-core, gold shell particles were one of the first structures designed with a peak in the near-infrared. Silica particles can be synthesized with a Stöber process, while a modified Stöber process can be used to grow silica shells on metal cores.

We have recently hypothesized that metal surfaces within solar absorber materials can act as electron trapping sites. If this is indeed the case, then a method for electrically insulating the particles would be necessary. To accomplish this goal, silica shells can be formed onto metal nanoparticles. Silica shells can have a profound impact on the plasmon resonance condition, which can be profitably used for photovoltaic applications. A silica shell on a metal nanoparticle changes the local environment. For a metal nanoparticle in water ($n \approx 1.33$), the presence of a silica shell ($n \approx 1.5$) will result in a weak red-shift in the plasmonic response. A silica shell on a metal nanoparticle embedded in a microcrystalline silicon medium ($n \approx 4$), however, has a very strong blue-shift effect on the plasmon resonance. Simulated spectral results are shown in Figure 5.6 illustrating these two cases. A blue shifted response can be used to employ larger particles at the same resonance wavelength, leading to larger scattering efficiencies and lower absorption losses.

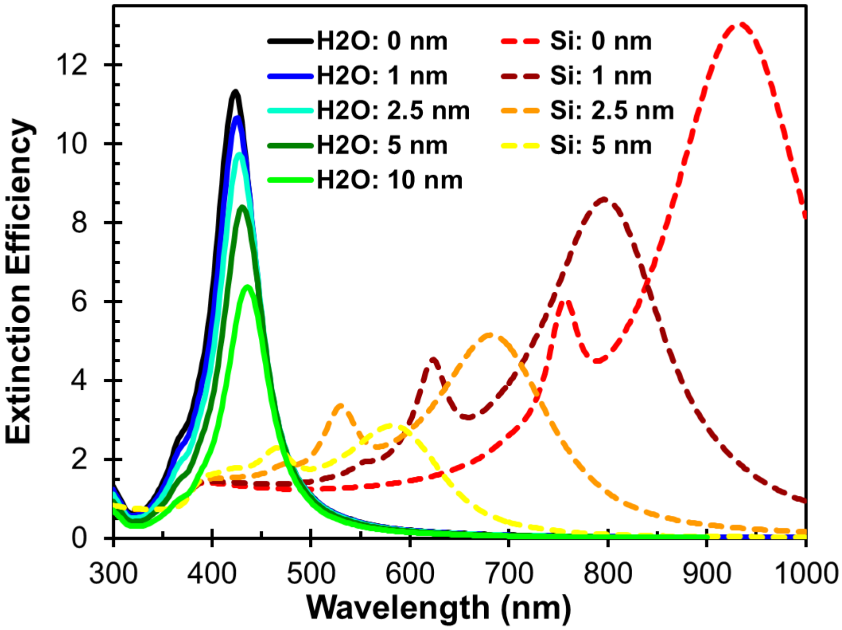

Figure 5.6: Simulations of 50 nm silver nanoparticles coated with silica shells in water and microcrystalline silicon environments. *The curves are named according to the surrounding environment and the silica shell thickness.*

Several different methods were evaluated for silica shell growth. Procedures for coating metal nanoparticles with a silica shell generally consist of two primary processes. First, there must be a replacement of the existing surfactant or stabilization ions or molecules. For citrate-stabilized nanoparticles, this can be easily accomplished, as the citrate is only weakly bound to the metal surface. For CTAB-stabilized particles, however, this can be more challenging. In this first step, a silicon-containing material should be attached to the surface. Chemically, this can be accomplished using aminopropyltriethylsilane (APTES) or tetraetylorthosilicate (TEOS). When using APS, only a monolayer can be grown effectively without causing aggregation, so extended intermediate growth must be taken with activated silica. The next step involves the growth of the silica shell in a Stöber process, typically in an ethanol-based solution using TEOS. Our initial experiments with both techniques found that the TEOS-based initial coating with subsequent growth to provide the most consistent and useful results with a rapid and simple process, so all further silica shell growth procedures were completed in this manner.

However, the TEOS growth process proceeds very slowly at room temperature, taking up to a week of growth to obtain shells of reasonable thickness. Furthermore, this process can be influenced by the surrounding temperature and environment. For this reason, we investigated catalysts to increase reaction speed. While both acidic and basic environments can aid in silica-shell deposition, challenges can arise in the form of silica particle precipitation. Ammonium (NH_4) has been used to catalyze the silica coating of gold nanoparticles, but silver nanoparticles are unstable in the presence of ammonium.

We use dimethylamine (DMA) to aid in the relatively rapid formation of silica shells on silver nanoparticles, as suggested by Kobayashi *et al.* [157]. This procedure results in coated nanospheres within five hours [158]. Figure 5.7 shows a 75 nm silver particle with a silica shell fabricated with this procedure.

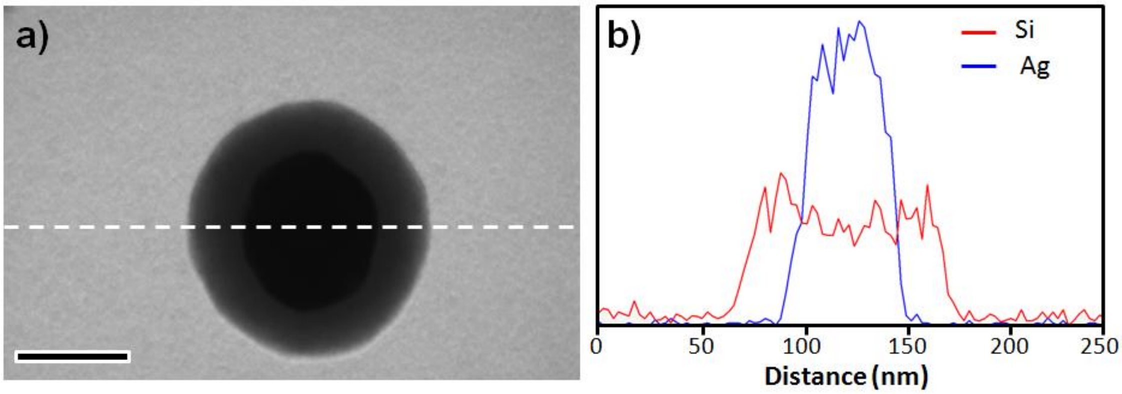

Figure 5.7: Electron microscopy results for a silica shell grown on a silver core. *a) STEM micrograph of an isolated particle, where the scale bar is 50 nm. b) Energy dispersive x-ray spectroscopy (EDS) line scan showing the locations of signal corresponding to silver and silicon in the nanoparticle. The white dashed line in a) is the scan path. Note: oxygen is undetectable with EDS, so only silver and silicon signals are shown.*

Figure 5.8 shows several representative STEM images of silica shells on silver cores. For this characterized sample, the shell thickness was found to be extremely consistent across various particles with a thickness of 19.5 ± 1.2 nm, despite a relatively wide distribution of metal core sizes.

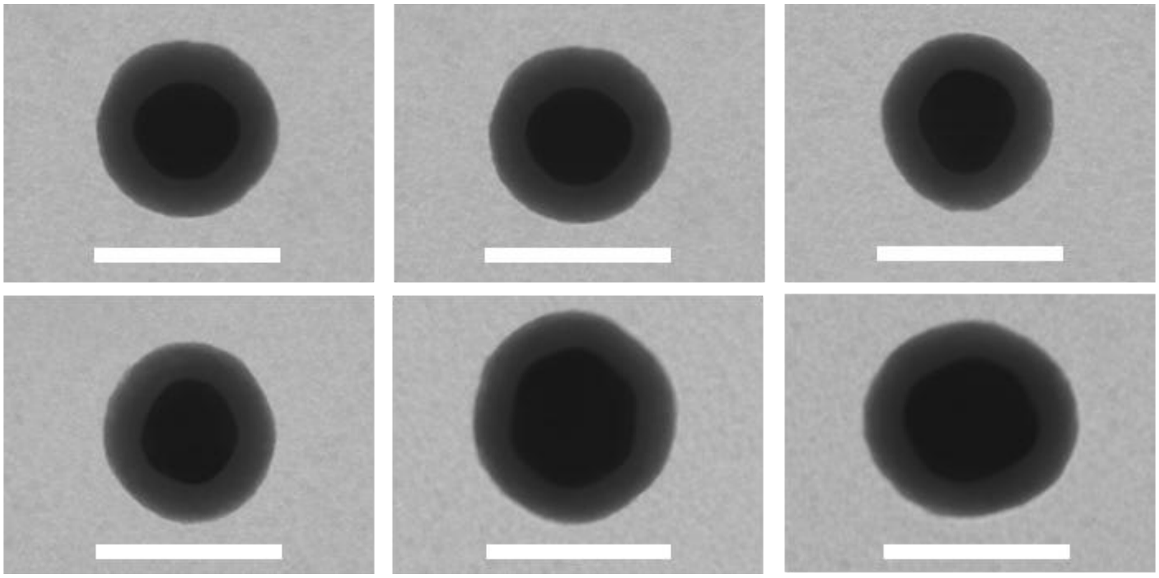

Figure 5.8: Electron microscopy images of Ag@SiO$_2$ nanoparticles showing the homogeneity of the shell thickness. *The scale bar is 100 nm. For this sample, the silica thickness was 19.5 ± 1.2 nm.*

It is necessary to control the thickness of the shell to obtain shell behaviors while maintaining enhanced near-field properties. Increased concentrations of either TEOS or DMA led to thicker coatings, but the thickness could also be effectively controlled by adjusting the initial concentration of nanoparticles. Prior results in the literature indicate that 2 nm thickness of SiO$_2$ is sufficient to greatly reduce conductivity or electron interaction with metal surfaces. Silica coatings as thin as 2 nm have previously been fabricated on gold nanoparticles [159]. However, we found that an increase in nanoparticle concentration was necessary to repeatably synthesize thin shells on silver cores. Small silver nanoparticles with thin shell structures were unstable in an 80% ethanol solution. We grow thin shells using a modified procedure with an increased concentration of up to 40% nanoparticle solution in ethanol, compared with only 20% in the previously published procedure. The rapid formation of a thick silica shell stabilizes the nanoparticles, but higher aqueous nanoparticle colloid concentrations lead to improved stability. We synthesized a range of thicknesses on silver spheres to demonstrate control of the thickness. A small set of the nanoparticles synthesized are compared in Figure 5.9.

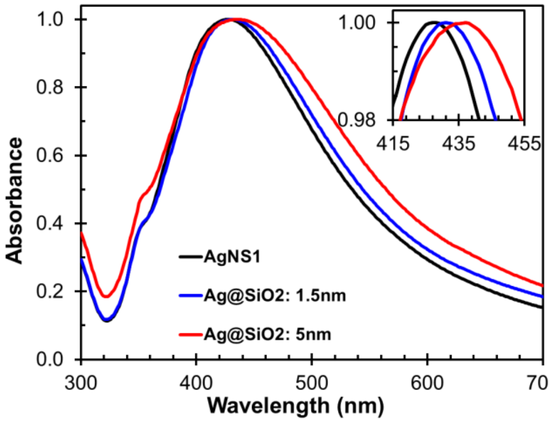

Figure 5.9: Experimental spectral shift observed for different thicknesses of silica shells on silver cores. *The inset shows the peak shift due to the presence of the thin silica shells. The values indicated are determined from the simulated thickness that provides an equivalent shift in the plasmon peak in a water medium.*

5.6: SELF-ASSEMBLED MONOLAYERS OF METAL NANOPARTICLES

To fully utilize nanoparticles in planar configurations, it is of value to assemble nanoparticles in a uniform layer on the surface with uniform spacing between the particles. Evenly distributed two-dimensional arrays of nanoparticles on a surface could be useful for refractive index sensing, plasmonic nanoablation, and photovoltaic applications. The self-assembly of nanoparticles can be accomplished by functionalizing the surface such that the nanoparticles are electrostatically bound to the surface. The procedure for self-assembly thus depends on the charge of the nanoparticles. Sodium citrate ions induce a negative charge on the surface of the nanoparticles and are often used to stabilize colloidal solutions of nanoparticles through electrostatic repulsion. Monolayers of polyvinylpyridine (PVP) and aminopropyltriethoxysilane (APTES), among others, can be used to generate a positively charged 'functionalized' surface. Nanoparticles stabilized with CTAB, on the other hand, are positively charged, meaning that a negatively charged surface functionalizing agent must be used. The mechanism for the creation of self-assembled monolayers (SAMs) is the creation of a charged monolayer surface coating, followed by the immersion of stabilized nanoparticles with the opposite charge. The nanoparticles will stick to the surface, but there is an energy barrier to agglomeration because of the like charges on the nanoparticles. The particles will self-organize on the surface according to these influences.

Initially, we followed the work of the Chumanov group for the initial development of these procedures [160,161]. Many different tests were performed to identify conditions by which homogeneous monolayers of various nanoparticle sizes in both gold and silver could be formed across a 1" × 1" area. These conditions are found to be general for substrate materials including silicon and glass, and previous research has described the method as universal. Figure 5.10 shows the regularity of spacing and high nanoparticle densities that can be achieved with surface functionalization. We found that the most important variables for effective SAM growth are surface cleanliness, nanoparticle concentration and timing. The procedure for creating SAMs is provided in Appendix A3.

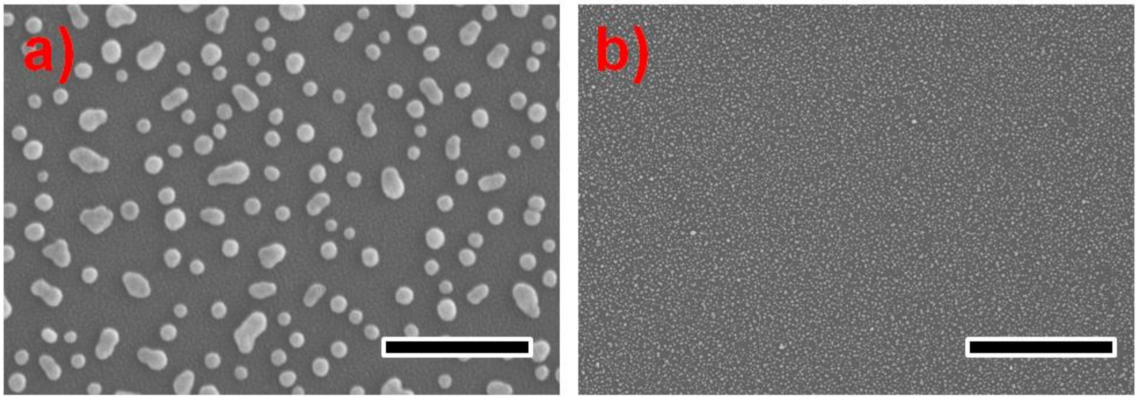

Figure 5.10: Scanning electron micrographs of self assembled monolayers of silver nanoparticles on a glass substrate. *a) High resolution zoom of the sub-monolayer of deposited silver nanoparticles. The scale bar is 250 nm. b) Wide-field view of the assembled particles showing the regularity in the deposited pattern over a large area. The scale bar is 2.5 µm.*

5.7: OTHER PARTICLES AND MATERIALS

5.7.1: Silica Spheres

Silica spheres were synthesized with a modified Stöber process [162]. Briefly, TEOS was added to a mixture of ethanol and water under stirring. Subsequently, ammonia was added to this mixture to catalyze the formation of silica nanoparticles in solution. Over a period of several hours, the reaction gradually became pearlescent, and then finally a milky white. We fabricated silica nanoparticles that were ~100 nm in diameter, but the overall size could be adjusted by varying the ratio of the reagents. These particles were synthesized to provide a non-plasmonic source of scattering and roughness for comparison with plasmonic particles for solar applications.

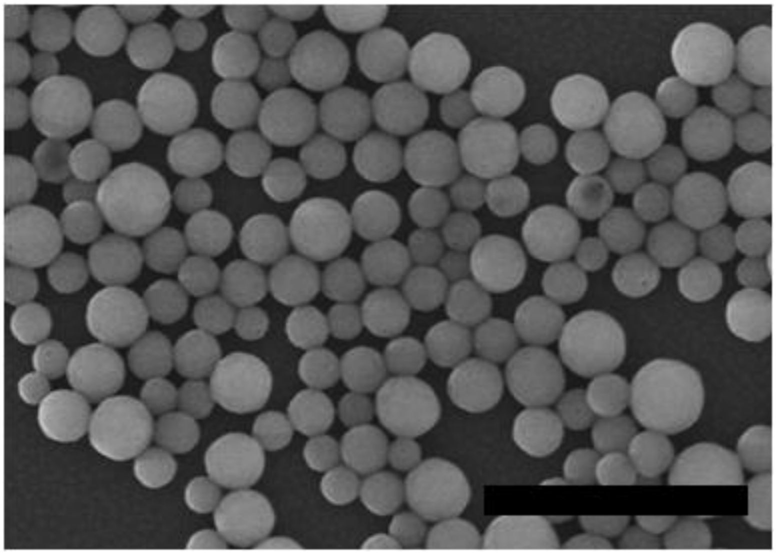

Figure 5.11: SEM image of silica nanospheres synthesized with the Stöber process. The scale bar is 1 µm in length.

5.7.2: Silver Triangles

Triangular prism nanoparticles are very attractive because of thickness, strong plasmonic response, strong near-field response, insensitivity to incident polarization, and tunability. First efforts were made towards the synthesis and characterization of silver nanoprisms following a previously presented procedure [163]. The particles were synthesized using a modified procedure from the literature according to the protocol listed below. Investigations into the sensitivity of the reactions towards various chemical reagents were carried out, showing that the reaction was strongly dependent on the concentration of silver seeds. Reduced amounts of silver seeds led to larger prisms.

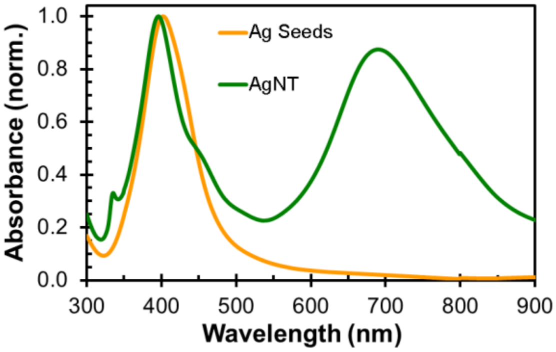

Figure 5.12: UV-Vis-NIR Spectrum of triangular silver nanoprisms synthesized in solution.

5.8: SPECTROMETER SYSTEM DEVELOPMENT AND CALIBRATION

Significant efforts in nanoparticle synthesis require a great deal of characterization analysis. The quickest and easiest way to evaluate nanoparticles during and after synthesis is through the use of UV-Vis-NIR Spectrophotometry. Spectrophotometry is a very straight-forward technique: collimated light is sent through a sample, transmission at a range of wavelengths is evaluated and finally the differences between a test sample and a control are determined. The strong optical properties of plasmonic metal nanoparticles can lead to pronounced spectral peaks even at low concentrations when measured with spectrometric methods. This technique is extremely useful for rapidly measuring plasmonic extinction spectra using the absorbance peak positions, and can also be used to evaluate nanoparticle polydispersity through absorption peak widths.

To enable testing in our lab during synthesis and to allow for vastly increased testing of various synthesis samples, a home-built nanoparticle absorbance measurement system was developed in our lab using available components, including a grating-based wavelength splitter (Andor 163), Peltier-cooled semiconductor camera, tungsten lamp, collimation optics, neutral density filters, and various optical mounting components. The spectrometer is equipped with a 100 µm × 3 mm slit that acts as a spatial filter, rejecting stray scattered light. The light from the light source was collimated with either a 50 mm lens (with a focal length of 40 mm), or a set of two glass diffusers.

As a tungsten-halogen lamp can be approximated as a blackbody source, the red and near-infrared light will dominate shorter wavelengths. A tungsten-halogen lamp has a blackbody-like emission spectrum, so the blue portion of the spectrum is reduced in comparison to the red and near-infrared regions. First, a metallic neutral density (OD = 1) filter was used to strongly attenuate near-infrared light. By adding a blue light balancing filters (Hoya Optics, LB120), the red light could be reduced, the peaking was reduced ad shifted from a maximum at 647 to 565 nm. Figure 5.13 shows results obtained using our system in comparison with results obtained two commercial systems (Cary 5000 and Shimadzu UV-3600) for the same sample of gold nanospheres.

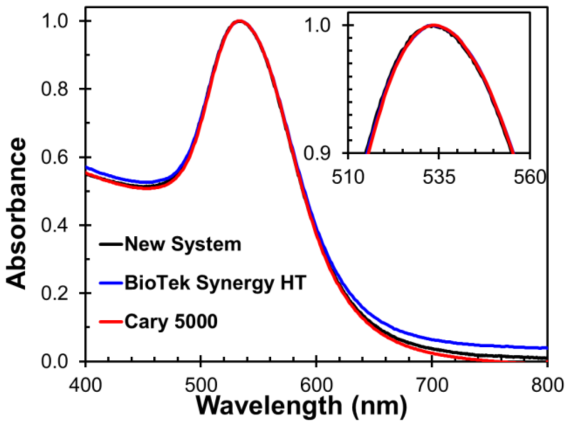

Figure 5.13: Experimental measurements of 50 nm gold nanoparticles measured on three different spectrometer systems.

Initial calibration of the peak positions was performed using four different laser systems, including a frequency-doubled diode laser at 405 nm (with a ‘leakage’ peak at 810 nm), frequency-doubled diode laser at 532 nm, helium-neon (HeNe) laser at 632.8 nm, non-mode-locked Ti:Sapphire laser operated at 760 nm, and an argon ion laser with a primary peak at 488 nm. However, this calibration method was extremely time-consuming and subject to error based on the incident direction of the attenuated laser beams. While this source of error could be mitigated, subsequent calibrations could be more rapidly achieved by using some of the high quality calibrated fluorescence filters in the lab. All acquisitions were taken with a 0.019 s exposure times and averaged over 500 exposures for a total acquisition time of 9.5 s.

5.9: CONCLUSIONS

In this chapter, we have presented synthesis methods and characterization for a wide range of nanoparticle types. An effort was made to produce high quality nanoparticle samples with narrow size distributions. We developed a new method to synthesize nearly monodisperse colloidal silver nanospheres through a controlled seeded growth method. We provide procedures for synthesizing nanoparticles. We also present a method for creating homogenous, evenly distributed arrays of nanoparticles on a surface using surface functionalization. The nanoparticles synthesized here can be directly used for plasmonic experiments.

Chapter 6: Near-Field Absorption around Plasmonic Nanoparticles

Here we present theoretical studies of the absorption in the near-field around plasmonic metal nanoparticles. It is important to understand how enhanced fields around plasmonic metal nanoparticles can be used to enhance the local deposition of optical energy to a sub-diffraction region. This chapter first includes a discussion of how the plasmonic properties are affected by absorption in the embedding medium. For clarity, here we focus on analytical equations for spheres to avoid any uncertainty surrounding assumptions or approximations around the simulation asymmetrical metal nanoparticles. We expand our discussion of near-field absorption by introducing several new, field-based definitions for the three-dimensional extent of the near-field region. Subsequently, we present results showing the near-field deposition of energy in an aqueous medium with a dye. Finally, we extend our calculations to provide an estimate of the plasmonic-enhanced nonlinear near-field absorption in the medium surrounding a metal nanoparticle.

6.1: MOTIVATION

The extraordinary optical interaction of plasmonic metal nanoparticles has become a topic of great scientific interest. Recent advances in the scientific understanding of plasmonics has led to the application of plasmonic metal nanoparticles as a biomedical contrast agent for multiphoton imaging [46], for the targeted photothermal destruction of tissue [164], photodynamic therapy [165], optical data storage [131], solar cells [166], and photocatalysis [167]. Many proposed uses of plasmonic particles do not focus only on the interaction of light with nanoparticles, but also on the transfer of energy from the particle to the surrounding region, especially in the close vicinity called the near-field. Energy transfer can be through processes such as the redirection of optical energy flow through scattering, heating, enhanced electromagnetic fields, and complete ablation of the particle. Previous studies have examined the thermal energy transfer from a nanoparticle to the surrounding region [168,45]. Plech et al. showed that near-threshold ablation of plasmonic nanoparticles will preferentially occur near the poles of the particle, providing a link between experimental observations of ablation and calculated near-field properties [92]. Our group and others have also used ultrafast lasers to study plasmonic particle-mediated ablation patterns to create near-field enhancement ‘snapshots’ [152,93,43]. A primary goal in this research is to understand not only the plasmonic response of nanoparticle systems, but also to determine the mechanisms by which plasmonic particles interact with their surroundings. By understanding optical energy transfer, nanoparticles and techniques can be more effectively designed for advanced plasmonic applications in medical, sensor, and energy sectors.

Though plasmonic metal nanoparticles have become ubiquitous in studies ranging from photonics to biomedical engineering, many aspects of near-field enhancement remain relatively unexplored. For example, what is the contribution of scattered light to near-field intensity? What is the size and shape of the near-field region and what delimits the near-field boundary? What dictates the absorption of light in the near-field, and how does that affect the scattering and absorption of light by the particle? These questions are rarely posed, but can provide great insight into plasmonic enhancement [169]. It is difficult to design experiments to probe enhancement mechanisms because of the nanometer scale and ultrafast time scales of plasmonic near-field effects. Experimental results can often lead to ambiguity where several different physical mechanisms could be responsible for observed experimental phenomena, as in the case where arguments supporting both thermal and electromagnetic field mechanisms were proposed for ultrafast laser tip-assisted ablation of substrates [76]. To address questions about near-field energy transfer and to provide relevant theoretical examples, we examine enhanced absorption in the near-field region around plasmonic metal nanospheres.

One attractive candidate technology is plasmonic enhancement in thin film solar cells, where the efficiency can be limited by the thickness or corresponding optical absorption. One proposed approach involves the incorporation of the plasmonic nanoparticle directly within the absorber material [166]. In this example, both enhanced near-field absorption and increased path length due to scattering by the particle could lead to increased absorption by the semiconductor. However, it is unclear which mechanism will be dominant and what parameters will dictate the magnitude of each effect. The intensity and location of absorption can significantly influence the charge collection efficiency in thin film photovoltaics, so understanding the spatial dependence of absorption around integrated nanoparticles could enable more effective plasmonic design.

Other applications of plasmonic nanoparticles in absorbing media include their use as a photosensitizer to promote the absorption of dyes in photodynamic therapy, for the enhancement of fluorophores for molecular detection, the enhancement of chemical processes in photocatalysis, or the localization and enhancement of absorbed light in plasmonic photopolymerization. In these cases, the localization of the deposited light can be more important than the total optical interaction that is typically calculated from far-field extinction. Furthermore, intensity dependent effects such as saturation require the calculation of near-field optical absorption on a point-by-point basis. To date, there has been relatively little work in comparing the local or net near-field enhancement with increased absorption effects. Notable correlations have been observed [170], but further examinations of near-field optical absorption are necessary. To address these questions, we develop a mathematical framework to distinguish between near-field and far-field absorption in the medium.

This study focuses on the enhanced deposition of energy in the near-field of plasmonic nanospheres embedded in absorbing media. We begin with a presentation of the theory of plasmonic nanoparticles in absorbing media and an explanation of our computational approach. This description will be followed by example calculations presenting the effect on optical interaction due to absorption in the environment. Then, we develop the equations and assumptions for enhanced near-field energy deposition around plasmonic particles. Finally, the developed framework is used to quantify the total enhancement of optical deposition around plasmonic gold nanoparticles in absorbing aqueous media. The primary contribution of this work is in presenting and demonstrating a method for determining the point-by-point absorption in the near-field of a plasmonic nanoparticle.

6.2: THEORY AND METHODS

6.2.1: Calculation of the Optical Interaction of a Sphere

For an absorptive embedding medium ($Q_{inc} > 0$), on the other hand, the Mie theory equations should be re-derived to account for a complex refractive index in the medium [171,172]. Considering the discrepancies in published optical interaction efficiency equations for particles embedded in absorbing media, we redeveloped these expressions starting from the electric and magnetic field equations. We found that our derivations are equivalent to expressions presented in references [173,174]. In the interest of space, we refer the readers to these references for the expressions. As expected, these equations simplify to the standard Mie theory expressions when real arguments are provided for the refractive index of the medium.

6.2.3: Near-Field Absorption in the Medium around a Sphere

Calculation of the optical interactions of a nanoparticle is important for understanding its plasmonic interaction powers. However, when these particles are embedded in an absorbing media, the spatial distribution of enhanced fields outside a nanoparticle is of special interest in calculating absorption that depends nonlinearly on the local field intensity. These nonlinear effects may include multi-photon effects, photobleaching of dyes or absorptive materials and their saturation, or threshold effects. Therefore, we present a new point-by-point calculation method that allows for the calculation of the local absorption in the medium outside a plasmonic nanosphere.

Previous studies used spherical control volumes concentric on the scatterer to determine the total linear optical absorption within a shell region surrounding a plasmonic nanoparticle [175,176]. This method, however, can provide only limited information on the spatial distribution or contributing effects of the enhanced absorption. Since the region of near-field enhancement is not spherical, a concentric shell approach will include both enhanced and unenhanced regions in the particle near-field, resulting in a blurring of the actual enhancement volume. This averaged value of the enhancement will lead to incorrect solutions in the presence of nonlinear effects.

Recall that the flow and conservation of electromagnetic energy in optical fields can be expressed using the Poynting theorem [27]:

$$\oint_A \boldsymbol{S} \cdot \hat{n}\, dA = -½ \int_V \boldsymbol{J}^* \cdot \boldsymbol{E}\, dV - ½ \int_V \left(\boldsymbol{E} \cdot \frac{d\boldsymbol{D}}{dt} + \boldsymbol{H} \cdot \frac{d\boldsymbol{B}}{dt} \right) dV \tag{6.1}$$

One approach for determining the optical energy absorption in an absorbing medium at arbitrary locations can be found by simplifying the right hand side of Eq. (6.1) to a function of the $|\boldsymbol{E}|^2$ field only. Notably, Baffou *et al.* studied local heat generation in plasmonic nanoparticles using this method [177]. However, the presence of multiple interacting and significantly disrupted fields renders this approximation of uncertain accuracy in the region outside of a plasmonic nanoparticle.

Here, we propose directly solving the left side of Eq. (6.1)around a spherical particle in an absorbing medium to enable evaluating energy deposition at arbitrary points. To find the spatial distribution of enhanced field absorption, we replace the surface integral in Eq. (6.1) with a point-by-point volume integral according to the Divergence theorem:

$$\oint_A \boldsymbol{S} \cdot \hat{n} dA = \int_V \nabla \cdot \boldsymbol{S}\, dV \tag{6.2}$$

We can then find the local energy consumed at each point in space around the particle by expanding the divergence of the Poynting vector in terms of the electric and magnetic fields at each location around a sphere according to:

$$\nabla \cdot \boldsymbol{S} = ½[\boldsymbol{H}^* \cdot (\nabla \times \boldsymbol{E}) - \boldsymbol{E} \cdot (\nabla \times \boldsymbol{H}^*)] \tag{6.3}$$

The fields in an absorbing medium can be calculated using the expansion of fields in spherical vector harmonics similarly to standard Mie theory [7], but in this case, the wave number k, scattering coefficients, and Riccati-Bessel functions (ψ_n and ξ_n) are all complex. The energy absorbed at each point in space can be obtained by discretizing the near-field region and directly solving for the energy absorbed in each small volume unit according to:

$$\begin{aligned}(\nabla\times\boldsymbol{E})_r = \frac{\sin\phi}{r\sin\theta\, kr}\sum_{n=1}^{\infty} E_n\big((\pi_n-\tau_n\cos\theta-\sin\theta\,\tau_n')(\psi_n-b_n\xi_n)\\ + i(\tau_n-\pi_n\cos\theta-\pi_n'\sin\theta)(-\psi_n'+a_n\xi_n')\big)\end{aligned} \tag{6.4}$$

$$\begin{aligned}(\nabla\times\boldsymbol{E})_\theta = \frac{\sin\phi}{r}\sum_{n=1}^{\infty} E_n\Bigg(i\pi_n(-\psi_n''+a_n\xi_n'')+\tau_n(\psi_n'-b_n\xi_n')\\ + i\pi_n n(n+1)\left(\frac{\psi_n}{(kr)^2}-a_n\frac{\xi_n}{(kr)^2}\right)\Bigg)\end{aligned} \tag{6.5}$$

$$\begin{aligned}(\nabla\times\boldsymbol{E})_\phi = \frac{\cos\phi}{r}\sum_{n=1}^{\infty} E_n\Bigg(\pi_n(\psi_n'-b_n\xi_n')+i\tau_n(-\psi_n''+a_n\xi_n'')\\ + in(n+1)(\cos\theta\,\pi_n+\sin\theta\,\pi_n')\left(\frac{\psi_n}{(kr)^2}-a_n\frac{\xi_n}{(kr)^2}\right)\Bigg)\end{aligned} \tag{6.6}$$

Likewise, the vector components of curl of the magnetic field are given as:

$$\begin{aligned}(\nabla\times\boldsymbol{H})_r = -\frac{\cos\phi}{r\sin\theta\, kr}\frac{k}{\omega\mu}\sum_{n=1}^{\infty} E_n\big((\pi_n-\cos\theta\,\tau_n-\sin\theta\tau_n')(\psi_n-a_n\xi_n)\\ + i(\tau_n-\cos\theta\,\pi_n-\sin\theta\pi_n')(-\psi_n'+b_n\xi_n')\big)\end{aligned} \tag{6.7}$$

$$(\nabla \times \boldsymbol{H})_{\theta} = \frac{-\cos\phi}{r}\frac{k}{\omega\mu}\sum_{n=1}^{\infty} E_n \Bigg(\tau_n(\psi_n' - a_n\xi_n') + i\pi_n(-\psi_n'' + b_n\xi_n'') \\ + in(n+1)\pi_n\left(\frac{\psi_n}{(kr)^2} - b_n\frac{\xi_n}{(kr)^2}\right)\Bigg) \tag{6.8}$$

$$(\nabla \times \boldsymbol{H})_{\phi} = \frac{-\sin\phi}{r}\frac{k}{\omega\mu}\sum_{n=1}^{\infty} E_n \Bigg(\pi_n(-\psi_n' + a_n\xi_n') + i\tau_n(\psi_n'' - b_n\xi_n'') \\ + in(n+1)(\cos\theta\,\pi_n + \sin\theta\,\pi_n')\left(-\frac{\psi_n}{(kr)^2} + b_n\frac{\xi_n}{(kr)^2}\right)\Bigg) \tag{6.9}$$

The variable r in Eqs. (6.4)-(6.9) is the radius and k is the wave number of light in the medium surrounding the particle ($k = 2\pi m/\lambda$). The azimuthal angle is given by ϕ and the polar angle is denoted θ. The wavelength of light in a vacuum is given by λ and the refractive index of the surrounding medium is $m = \eta + i\kappa$. To calculate the curl of the fields, we need to find the values of the second derivatives of the Riccati-Bessel functions, ψ_n'' and ξ_n'' for each order n of the expansion. We derive these terms by taking the derivative of the recursion relationships:

$$\psi_n'' = \psi_{n-1}' - \frac{n\psi_n'}{kr} + \frac{n\psi_n}{(kr)^2} \tag{6.10}$$

$$\chi_n'' = \chi_{n-1}' - \frac{n\chi_n'}{kr} + \frac{n\chi_n}{(kr)^2} \tag{6.11}$$

$$\xi_n'' = \psi_n'' - \chi_n'' \tag{6.12}$$

The derivatives of the angular π_n and τ_n terms must also be calculated for each order of expansion from the suitable recursion relationships (Eqs. (6.13) and (6.14)). The initial conditions of the angular functions for the first few orders are shown in Eqs. (6.15) and (6.16). Subsequent terms can be determined using upward recursion relationships for increasing order n.

$$\pi'_{n+1} = \frac{2n-1}{n-1}(\cos\theta\,\pi'_n - \sin\theta\,\pi_n) - \frac{n}{n-1}\pi'_{n-1} \tag{6.13}$$

$$\tau'_{n+1} = n(\cos\theta\,\pi'_{n+1} - \sin\theta\,\pi_{n+1}) - (n+1)\pi'_n \tag{6.14}$$

$$\pi'_0 = 0, \pi'_1 = 0, \pi'_2 = -3\sin\theta \tag{6.15}$$

$$\tau'_0 = 0, \tau'_1 = \sin\theta\,, \tau'_2 = -12\sin\theta\cos\theta \tag{6.16}$$

Outside of the particle, three different sources contribute to near-field absorption in the medium: incident fields ($\nabla\cdot\boldsymbol{S}_{inc}$), scattered fields ($\nabla\cdot\boldsymbol{S}_{sca}$), and an interacting fields ($\nabla\cdot\boldsymbol{S}_{ext}$). The absorption in the medium due to the incident field ($\nabla\cdot\boldsymbol{S}_{inc}$) corresponds to the amount of energy absorbed in the volume occupied by the particle in the absence of a particle. The scattered and incident light contributions to the near-field absorption are always positive. The interaction term ($\nabla\cdot\boldsymbol{S}_{ext}$), which represents the effect of the interaction between the incoming and scattered light on the local absorption, can be positive or negative. The sign and magnitude will depend on whether the wave interference between the incident and scattered waves is constructive or destructive at that location. The 'extra' light absorbed in the near-field region is the sum of the scattered ($\nabla\cdot\boldsymbol{S}_{sca}$) and interaction ($\nabla\cdot\boldsymbol{S}_{ext}$) field contributions to absorption in the medium outside the particle.

6.2.4: Computational Methods

For all calculations, we use custom-written codes based on extended Mie theory and developed according to the discussion presented here and in the literature [7]. These codes are written with Matlab to calculate the electromagnetic fields (electric $\boldsymbol{E}$, magnetic $\boldsymbol{B}$, and Poynting vector $\boldsymbol{S}$) at any point in space inside or outside spherical particles in spherical coordinates. All fields are presented relative to the incident intensity of the non-enhanced fields of the incident light at that location in space. The refractive indices for water across the visible spectrum are calculated using a Sellmeier-type equation that fits experimental observations of the optical response [18]. The refractive indices of gold are at each wavelength are interpolated from tabulated experimental data [24]. In all cases, we assume that the beam is large in comparison with the particle, and that the plane wave approximation is valid. In our chosen geometry, the wave travels in the positive z direction, which implies that there is constant intensity for z planes, and that the light is linearly-polarized along the x-axis. Though we initially assume linear polarization of the incident light, the spherical symmetry of the all particles examined implies that these approximations are also valid for unpolarized incident light conditions.

6.2.5 Validation

We first verified our analytical expressions for the extended Mie theory interaction efficiencies that matched well with the published results of references [173,174] through various validation efforts and benchmark tests. 1) The equations for the scattering coefficients were verified for consistency using direct matrix inversion of the linear equations developed using the boundary conditions for the spherical geometry. 2) We checked the field calculations by determining the incident and scattered fields on a spherical shell control volume surrounding the particle. By numerically integrating the radial components of the various Poynting vector constituents across the area of a spherical shell, we could check the calculated efficiencies against the previously published series expansions for linearly absorbing media.

We then verified that our numerical simulations are valid. The numerical values could be calculated for any radius control volume shell for a non-absorbing medium, but should be checked at the sphere surface in absorbing media to examine the optical response at the particle. These tests yielded very satisfactory agreement with the series expansions, where the relative error decreased exponentially to less than 2.2 × 10^{-6} for $\mathrm{Q}_{\mathrm{sca}}Q_{sca,NP}$, $Q_{abs,NP}$, and $Q_{ext,NP}$ at an angular step of 0.5° at the sphere surface for a 50 nm gold sphere on resonance in a water-like medium with an imaginary refractive index of 0.2. The internal fields within the sphere could also be checked against the absorption efficiency by setting the shell radius vanishingly close to the sphere surface (arbitrarily chosen as 10^{-9} nm, in this case), resulting in similar accuracy.

The limiting behavior can also be used to verify that calculations match expected trends. As the radius became large, the absorption within a spherical control volume surrounding a particle approached the absorption of the medium, as expected. Additionally, optical fields and interaction efficiencies calculated using extended Mie theory expressions were found to yield identical results for non-absorbing media ($\kappa_M = 0$) and in the limit of the negligible absorption ($\kappa_M = 10^{-6}$) as standard Mie theory.

Subsequently, we studied the accuracy of our calculations for the chosen step sizes. The point-by-point divergence of the Poynting vector within the particle was numerically integrated to test the equations for energy absorption. We applied Eq. (6.2) to the volume of the particle to directly find the total absorption of energy by the particle using a volume integration approach. This expression is equivalent (albeit more computationally intensive) to the surface integral expression of the absorption efficiency. These results also agreed satisfactorily, reaching a relative error of 1.2 × 10^{-7} under the same conditions. We set the spatial discretization such that the chosen volume was small enough that the fields could be approximated as constant over the small discretized volume element. Specifically, we set the number of radial steps equal to the particle radius divided by the number of angular steps, but the calculations were relatively insensitive to radial step size.

Finally, we compared our new point-by-point volumetric calculations against spherical shell control volume calculations at various radii outside the particle in a linearly absorbing medium for multiple metals, wavelengths, shell radii, and imaginary refractive indices of the medium. Additionally, derivations for absorption within the shell of a coated sphere were also used to verify the energy absorption in a spherical shell region outside the particle if the shell material was set equal to the environment. Similar agreement ($\sim 10^{-6}$ relative error) was found between the coated sphere solutions, the control volume shell solutions, and point-by-point volume divergence values, verifying our presented calculation method.

6.3: OPTICAL PROPERTIES OF PLASMONIC NANOSPHERES IN ABSORBING MEDIA

Before determining the spatial distribution of absorption outside a plasmonic nanoparticle, we first examine the effects of absorption on the plasmonic response of metal nanoparticles using analytical expressions from extended Mie theory. Dielectric particles in absorbing media have been studied in some detail [171,172,173,174], but fewer studies have theoretically examined metallic particles in absorbing media [178,179]. To identify the effects of absorption within the medium on the plasmonic properties of a metal nanoparticle, we present results for a 50 nm gold sphere in water with an additional absorbing dye at various concentrations. Gold nanoparticles are often employed in aqueous environments because of the synthesis, stability, and biocompatibility of nanoparticles under these conditions. Here, the index of refraction of water is modified by adding an imaginary refractive index (κ_M = 0, 0.05, 0.1 and 0.2) component that is held constant across the calculated spectrum (λ = 400–800 nm), similar to solutions containing India ink, carbon black pigment, or black dye used in dye-sensitized solar cells. Note that an imaginary component of $\kappa_M = 0.2$ represents strong absorption corresponding to an absorption coefficient $\alpha_M \equiv 4\pi\kappa_M/\lambda = 5\ \mu\text{m}^{-1}$ at a wavelength of 500 nm. The chosen imaginary refractive index values encompass the typical values for thin-film photovoltaics at red to near-infrared wavelengths.

Here we will only present inherent optical interaction efficiencies, *i.e.* efficiencies calculated at the particle surface, to focus on the changing plasmonic behavior of the particle as a function of the medium [173]. For the calculation of efficiencies at the particle surface we do not need to take into account the changes in the relationship between the scattering and absorption efficiencies due to absorption by the medium that occurs as a function of distance from the nanoparticle surface. We will discuss the absorption efficiencies in the medium in the following sections.

The results for the extinction efficiency of the nanosphere ($Q_{ext,NP}$, Figure 6.1a) show a slight red-shifting resonance peak that diminishes in strength as the imaginary coefficient of refraction of the medium increases. This trend is also followed by the absorption efficiency ($Q_{abs,NP}$, Figure 6.1b), matching the findings of Quinten [178] among others. One unremarked aspect of the plasmonic response, however, is the dramatic increase in the scattering efficiency ($Q_{sca,NP}$) with increasing imaginary component of the medium, shown in Figure 6.1c. This effect is only apparent for particles with a large imaginary part of the refractive index such as metals, and is not observed for dielectric or weakly absorbing nanoparticles.

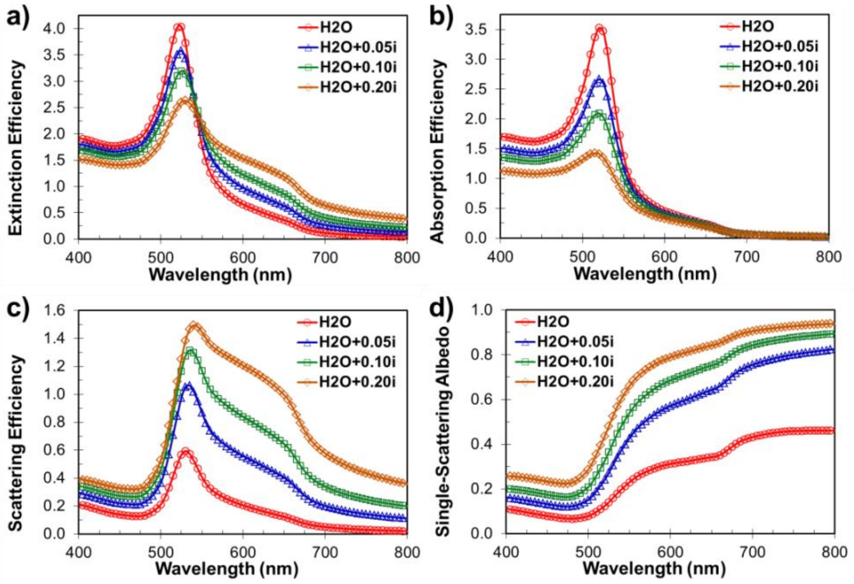

Figure 6.1: Shift and broadening of a plasmonic resonance in an absorbing medium. *Calculations are for a 50 gold nanoparticle in water with an added hypothetical dye with constant absorption constant over the entire simulated spectrum at various concentrations to yield constant imaginary refractive indices of* κ_M*= 0, 0.05, 0.1 and 0.2. The interaction efficiencies of the particle, calculated at the surface, are shown as a function of wavelength for a)* $\boldsymbol{Q_{ext,NP}}$*, extinction, b)* $\boldsymbol{Q_{abs,NP}}$*, absorption, c)* $\boldsymbol{Q_{sca,NP}}$*, scattering, and d) the fraction of scattered light in the total extinction (single-scattering albedo).*

For certain applications of plasmonic nanoparticles in absorbing media, scattering by the particle can promote near-field absorption in the medium surrounding the nanoparticle as a net gain, while the absorption by the particle can act as a parasitic loss of optical intensity. We thus calculate the single-scattering albedo, defined as the ratio of the scattering efficiency to the extinction efficiency $\left(Q_{sca,NP}/Q_{ext,NP}\right)$, which provides a scaled comparison of these terms. We find that as the embedding medium becomes more absorbing, the absorption efficiency of the particle decreases as the scattering efficiency increases, yielding a significantly increasing single-scattering albedo (Figure 6.1d). The single-scattering albedo also tends to increase with the wavelength. It can be seen that absorption is the dominant source of extinction for a 50 nm sphere in water, but that scattering is dominant for the same sphere in water with higher levels of added dye at wavelengths longer than 550 nm.

These results are useful in qualitatively understanding the role of the imaginary part of the refractive index on a plasmonic resonance. For example, we notice that even a relatively small absorption component can have a dramatic effect on the optical response. This phenomenon is an inherent property of the imaginary refractive index on the optical properties of the particle/environment plasmonic system. A comparison of a nanoparticle embedded in a pure dielectric medium with equivalent magnitude refractive index does not yield the same increase in the scattering efficiency. The increased scattering-to-absorption ratio for nanoparticles in an absorbing medium suggests that the plasmonic enhancement of absorption by the medium could be more promising than a familiarity with the optical properties of metal nanoparticles in an non-absorbing medium (as they are typically synthesized, measured, and evaluated) would suggest.

6.4: NEAR-FIELD ABSORPTION PROPERTIES OF THE MEDIUM

In this section, we expand our calculations to determine the amount of energy deposited in the near-field and the volume over which the energy is absorbed using our point-by-point method. This type of calculations is of crucial importance towards the use of plasmon-enhanced absorption in applications with threshold, saturation, or nonlinear effects.

6.4.1: Near-Field Boundary Criteria

To calculate how much total energy is absorbed in the near-field (*NF*), we first need to determine an effective boundary for the near-field region. Here, we propose a cutoff criterion approach for quantifying the energy deposited in the near-field and evaluate its potential as it is applied for different fields' strengths. We note that even in the immediate vicinity of the nanoparticle, some regions will absorb more energy, while other regions will actually absorb less than would be absorbed if the particle was not present.

Separating the near-field region from the far-field can help elucidate the different mechanisms and effects of near-field enhancement for plasmonic nanoparticles and determine an accurate volume over which enhanced absorption occurs. A large difference can be observed between the field properties in the near-field and the far-field. In the far-field, the electric and magnetic fields can be resolved into propagating waves with a defined relationship between the magnitude and phase. In the near-field of a plasmonic particle, however, this is not the case. In addition to the propagating waves, there is also an inhomogeneous wave component that will dissipate as a function of distance from the metal particle and will not reach the far field. This field can be utilized if near-field coupling can be achieved, as in near-field scanning optical microscopy, frustrated total internal reflection, or in the presence of an absorbing medium.

An appropriate definition of the near-field would encompass the region where the majority of the added near-field absorption occurs, while also providing a contiguous region around the particle. Furthermore, the criterion should satisfy the requirement that the absorption is dominated by the incident field component outside the defined near-field region, and that this region is thus unimportant for evaluating the effect of a plasmonic nanoparticle. Within the near-field region, the energy absorbed due to each component field can be used to identify contributions to the total absorption of energy in the surrounding region.

The simplest boundary for separating the near- and far-field regions is a sphere of $\lambda/2\pi$ in radius, introduced in the microwave antenna field [180]. This criterion is based on the point at which the contributions of a dipole (electric field) and loop (magnetic field) elements of a hypothetical antenna become equal. While this boundary provides a simple rule of thumb for near-field effects, it cannot provide an acceptable metric for either the shape or volume of the region of enhancement around a plasmonic nanoparticle, as the near-field region depends strongly on the material, size and shape of the nanoparticle scatterer.

Here we propose to define the near-field as the volume over which the electromagnetic fields are enhanced above a certain level of the incident optical fields, the cutoff level, f. This definition can be used to identify the region that is characterized by enhanced optical absorption over the background level. The near-field can be chosen to be the region over which the fields exceed the unaffected incident field magnitudes for the square of the electric field ($|\boldsymbol{E}|^2$), square of the magnetic field ($|\boldsymbol{B}|^2$), and Poynting vector magnitude ($|\boldsymbol{S}|$). While the electric field is commonly thought to dominate many optical interactions, both the magnetic field and enhanced Poynting vector are relevant parameters, as recent studies on laser-induced magnetization and plasmonic ultrafast laser nanoablation have demonstrated [181,43,182]

Figure 6.2 presents the near-field enhancement regions calculated with each of the proposed near-field criteria. The images show the near-field enhancement half-volumes, with the field values shown on a logarithmic color scale in the mid-plane of the particle in the plane described by the intersection of the polarization and propagation vectors. All calculations are for a 50 nm gold sphere in water with imaginary component of the refractive index $\kappa_M = 0.1$. The electromagnetic fields generally decay asymptotically as a function of distance from the particle to the background levels, so a cutoff level must be chosen to bound the near-field region. Each near-field is calculated from the particle surface out to a level where the field reaches the background plus a small margin of difference, chosen in this case as a cutoff $f = 1.25$ times the incident field at that point. This cutoff level provides a large enough margin to overcome nonlinear thresholds without creating bulk effects in the laser field [34].

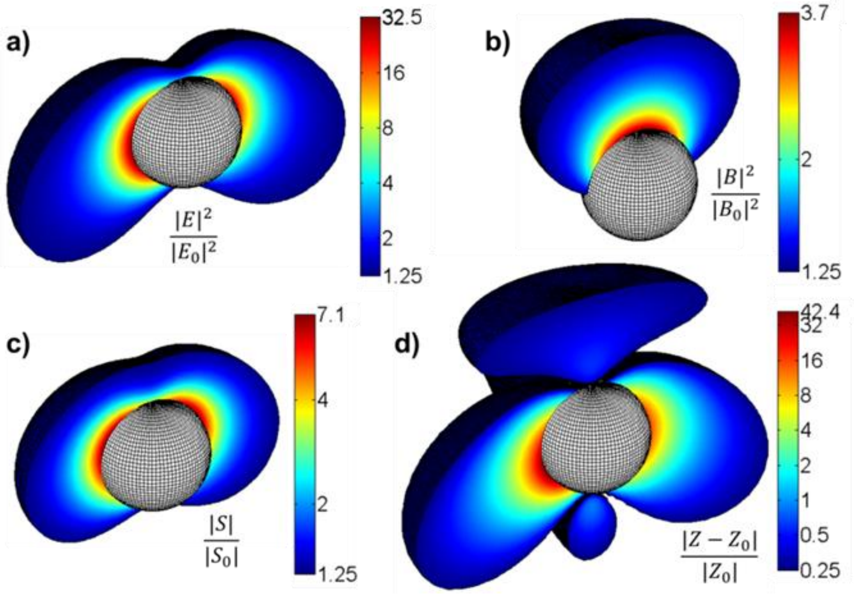

Figure 6.2: Plasmonic near-field enhancement regions calculated for different field-based criteria. *Calculations are for a 50 nm gold sphere in water with on resonance at an in vacuo wavelength of 535 nm. The particle is depicted with black grid lines. The different criteria are a)* $|E|^2/|E_0|^2 > f_E^2$, *b)* $|B|^2/|B_0|^2 > f_B^2$, *c)* $|S|/|S_0| > f_S$, *d)* $|Z-Z_0|/|Z_0| > f_Z-1$, *where all cutoff margins f are chosen to be 1.25.*

The magnitude of the local wave impedance, *Z*, can similarly be used to identify the near-field region around a nanoparticle. The concept of optical impedance was initially proposed in 1938 as a measure of the propagation characteristics of a medium [183] and defined as:

$$|\boldsymbol{Z}| = \frac{|\boldsymbol{E}|}{|\boldsymbol{B}|} \tag{6.17}$$

This ratio is nearly constant around dielectric spheres, but varies by orders of magnitude in the near-field of a plasmonic metal nanoparticle [182]. As the distance from a plasmonic nanoparticle increases, the wave impedance asymptotically approaches the characteristic impedance of the wave in the medium, given by the square root of the ratio of the permeability μ to the permittivity ε. The volume where the impedance deviates significantly from the characteristic impedance of the medium is indicative of the presence of an inhomogeneous wave component of the electromagnetic fields, even in a non-absorbing medium. Figure 6.2d shows the region over which the wave impedance deviates from the characteristic far-field optical impedance of the medium. This figure depicts the absolute value of the deviation. There are regions where the wave impedance is significantly larger and smaller than the background level, as can be predicted from a comparison of Figure 6.2a and Figure 6.2b.

6.4.2: Near-Field Volume and Average Absorption Enhancement

We calculate the volumes of the near-field through a point-by-point summation of discrete volume elements in spherical coordinates starting from the sphere surface. For each radial step, the total volume is incremented at each polar (θ) and azimuthal angle (ϕ)

pair where the chosen near-field criterion is satisfied. The size of a volume element, ΔV_j, depends on the position in spherical coordinates according to:

$$\Delta V_j = ⅓\Delta\phi(\cos(\theta - \Delta\theta) + \cos(\theta + \Delta\theta))((r + \Delta r)^3 - (r - \Delta r)^3), \qquad (6.18)$$

where r is the radius for the center of the volume element and $\Delta\theta\Delta\phi\Delta\theta$, $\Delta\phi$, and Δr are the step sizes. We continue incrementing the radius until no points in the spherical shell satisfy the near-field criterion. The total near-field volume, V_{NF}, can then be calculated by summing the discrete volume elements ΔV_j for all points, N, that exceed the chosen threshold.

Figure 6.3a presents the spectral dependence of the near field volume as calculated for each of the near-field criteria considered. This analysis provides several results. First, the volumes calculated for the $|E|^2$ and $|S|$ criteria show similar trends, but the $|S|$ volumes are significantly smaller over the whole spectrum. The $|B|^2$ criterion provides the smallest overall volume, while the impedance criterion $|Z|$ provides the largest volume because it includes both the electric and magnetic regions of enhancement. The near-field volumes depend strongly on both the chosen definition and the cutoff level. Therefore, it is crucial to choose an appropriate criterion that will represent correctly the dominating field for a given application whether this application is for enhancing absorption in thin film solar cells, or for laser-induced magnetization and plasmonic ultrafast laser nanoablation.

The average near-field absorption enhancement for each criterion can be evaluated by dividing the total near-field energy absorption by the amount of energy that would be absorbed over the same volume in the absence of the particle.

$$\bar{Q}_{enh,NF} = \frac{\sum_{j=1}^{N}(\nabla \cdot S_{scat} + \nabla \cdot S_{ext} + \nabla \cdot S_{inc})_j * \Delta V_j}{\sum_{j=1}^{N}(\nabla \cdot S_{inc})_j * \Delta V_j} \tag{6.19}$$

Figure 6.3b shows that the average enhancement (or relative enhanced deposition), is significantly higher for the region calculated for the $|S|$ criterion than for the other terms, primarily on account of the reduced near-field volume. The average enhancement depends strongly on the cutoff level chosen, starting initially at a high level and decaying monotonically as the distance from the particle surface increases.

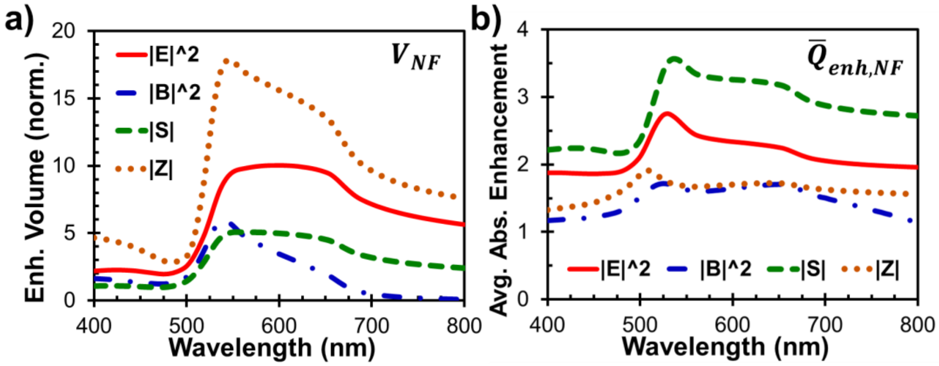

Figure 6.3: Near-field volume and absorption enhancement as a function of wavelength for different cutoff criteria. *The values are determined for the* $|E|^2/|E_0|^2 > f_E^2$, $|B|^2/|B_0|^2 > f_B^2$, $|S|/|S_0| > f_S$, *and* $|Z-Z_0|/|Z_0| > f_Z-1$ *terms. Plots correspond to a 50 nm gold sphere in a water medium with an imaginary refractive index coefficient* $\kappa_M = 0.1$ *and cutoff criterion of* $f=1.25$ *for each field. a) The volume of the near-field normalized by the volume of the naoparticle. b) The average enhancement, determined by dividing the energy absorbed in the near-field region relative to absorption over the same volume in the absence of a particle. The average absorption enhancement is shown for each of the defined near-field criteria.*

Figure 6.3 results indicate that significantly enhanced near-field absorption can also occur well off of the particle plasmon resonance and we evaluate plasmonic enhancement over a broad spectrum encompassing the plasmonic resonance. Off-resonance near-field enhancement around a metal nanoparticle can be described in terms of multiple different mechanisms: lightning rod, plasmonic, and field exclusion. 1) The ‘lightning rod’ effect, which is caused by a field confined near a metallic surface with a small radius of curvature, should be relatively constant as a function of wavelength for a given particle size. 2) The plasmonic effect enhances near-field electromagnetic fields as a result of the resonant oscillation of electrons drawing in light from an area much larger than the particle itself. 3) In the red to near-infrared region, far from the resonance for a small particle, we also observe near-field enhancement, but in this case, the increased complex refractive index magnitude leads to rejection of the optical fields near the particle boundary and increased electromagnetic densities immediately outside the particle (field exclusion effect) [184]. Our simulations take into account these enhancement mechanisms inherently.

6.4.3: Calculation of Near-Field Absorption Efficiency

One of the most interesting parameters that can be calculated using a point-by-point integration method is the net near-field enhanced absorption. With the volumes determined in the previous section, we can then account for extra energy deposition in those near-field volumes from plasmonic near-field enhancement. We define a new term called the enhanced near-field absorption efficiency, $Q_{abs,NF}$, to describe the enhanced near-field deposition of energy in the surrounding medium by summing the contributions of the scattered fields $\nabla \cdot \mathrm{S}_{\mathrm{scat}} (\nabla \cdot S_{scat})$ and the interaction term $\nabla \cdot \mathrm{S}_{\mathrm{ext}} (\nabla \cdot S_{ext})$:

$$Q_{abs,NF} = \frac{\sum_{j=1}^{N} (\nabla \cdot S_{scat} + \nabla \cdot S_{ext})_j * \Delta V_j}{I_0 A_{CS}} \tag{6.20}$$

We do not include the absorption due to the incident field ($\nabla \cdot S_{inc}$) here because that will occur regardless of the presence of a nanoparticle. We normalize this term according to the optical power incident on the particle, I_0A_{CS}, so that this term can be directly compared with the standard optical interaction efficiencies of the particle.

Figure 6.4a shows the absorption in each calculated near-field region. The most energy is deposited in the region defined using the $|E|^2$ criterion, although similar amounts are also deposited in the volumes found using the $|S|$ and $|Z|$ near-field criteria. Only a small amount of absorption occurs in the near-field region found using the magnetic field condition region ($|B|^2$), although this result may not hold for a magnetic embedding material. Finally, we note that the near-field absorption peaks are red-shifted from the far-field extinction, scattering and absorption efficiency peaks of the particle. The deviation between near-and far-field optical properties has been previously noted [185].

Figure 6.4b presents the contributions to near-field absorption from scattered and incident waves to near-field intensity enhancement using only the $|\boldsymbol{S}|$ near-field criterion as similar trends are also obtained using the $|\boldsymbol{E}|^2$ boundary criterion. These results enable us to evaluate what term is the main contributor to the total near-field absorption by the media. We observe that enhanced absorption in the near-field occurs mainly as a result of the enhanced scattered field. This result holds for even small metal nanoparticles well off the plasmonic resonance in nearly transparent media. The interaction term is found to provide an increasingly important contribution for long wavelengths off-resonance. This result implies that the interaction term is a good indication of the perturbation of the field, which is increased for larger particles or long wavelengths where field rejection effects increase.

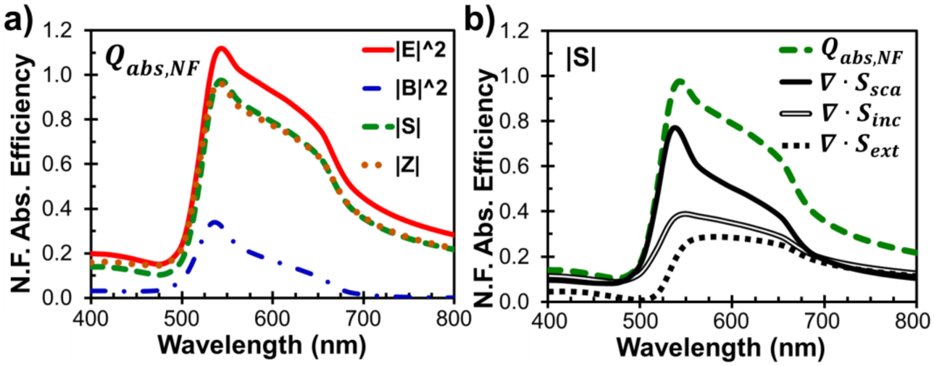

Figure 6.4: Near-field absorption efficiency plots in an absorbing medium. *Calculations are for a 50 nm gold sphere in a water medium with an imaginary refractive index coefficient* $\kappa_M = 0.1$ *for a set cutoff of* $f = 1.25$. *a) The near-field absorption efficiency calculated for each of the different criteria (*$|E|^2/|E_0|^2 > f_E^2$, $|B|^2/|B_0|^2 > f_B^2$, $|S|/|S_0| > f_S$, *and* $|Z-Z_0|/|Z_0| > f_Z-1$*). b) The contributions of each field component to the near-field absorption in the medium.*

6.4.4: Dependence of the Near-Field Absorption on the Cutoff

To test the effect of the cutoff on the calculated near-field absorption, we examine the near-field absorption as a function of cutoff value for each of the field criteria. Thus far, we have shown the calculated values for a single cutoff level (f = 1.25). Figure 6.5a shows the enhanced near-field absorption in the medium as the cutoff approaches the background, revealing an asymptotic trend in the extra near-field energy deposition. The chosen cutoff level of f =1.25 corresponds to more than 90% of the converged value for the extra near-field absorption for the $|\boldsymbol{S}|$ criterion.

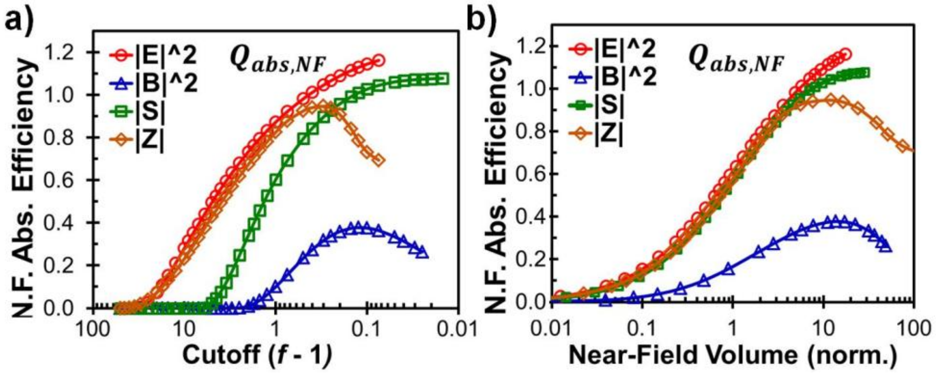

Figure 6.5: Convergence of the enhanced near-field absorption in an absorbing medium. *Calculations are for a 50 nm gold sphere on resonance in a water-dye mixture with* $\kappa_M = 0.1$ *for each of the different criteria* ($|E|^2/|E_0|^2 > f_E^2$, $|B|^2/|B_0|^2 > f_B^2$, $|S|/|S_0| > f_S$, *and* $|Z-Z_0|/|Z_0| > f_Z-1$)*. a) Convergence of the near-field absorption efficiency for each near-field criterion as a function of the cutoff. b) Convergence of the near-field absorption efficiency as a function of the near-field volume.*

The difference in the near-field absorption between the $|\boldsymbol{E}|^2$ and $|\boldsymbol{S}|$ conditions collapses when the data is plotted as a function of the calculated near-field volume determined for each condition (Figure 6.5b). This equivalence shows that the volumetric absorption enhancement density is nearly identical for these two criteria up to volumes ~10× greater than the nanoparticle volume. As the chosen cutoff level approaches unity, all criteria lead to the inclusion of detached enhancement regions that occur due to interference between the incident and scattered waves. These 'islands of enhancement', which are typically found more than five radii from the particle surface, are characterized by very low deposited energy densities, but their large volume causes the enhanced near-field absorption value calculated to diverge at cutoff levels of $f < 1.075$ for the $|\boldsymbol{E}|^2$ and $f < 1.015$ for the $|\boldsymbol{S}|$ conditions.

The near-field deposition accounts for a predominance of absorption around a plasmonic nanoparticle. Figure 6.6 presents the fraction of energy absorbed within the near-field region as compared to that absorbed in a total spherical volume. Considering the total absorption occurring in a spherical shell volume encompassing a gold nanoparticle (shown as a white dashed line in Figure 6.6a), 70% of the absorption occurs in the near-field region (as described within the outermost solid black line in Figure 6.6a), while the near-field region occupies only 30% of the total volume (Figure 6.6b). This peak in the absorption density occurs at a distance of ~2 radii from the center of the sphere. This result show that majority of the near-field absorption happens very close to the particle within 1 radius shell around the particle. This phenomenon becomes even more pronounced when considering nonlinear effects as we will be discussing in the section of nonlinear absorption.

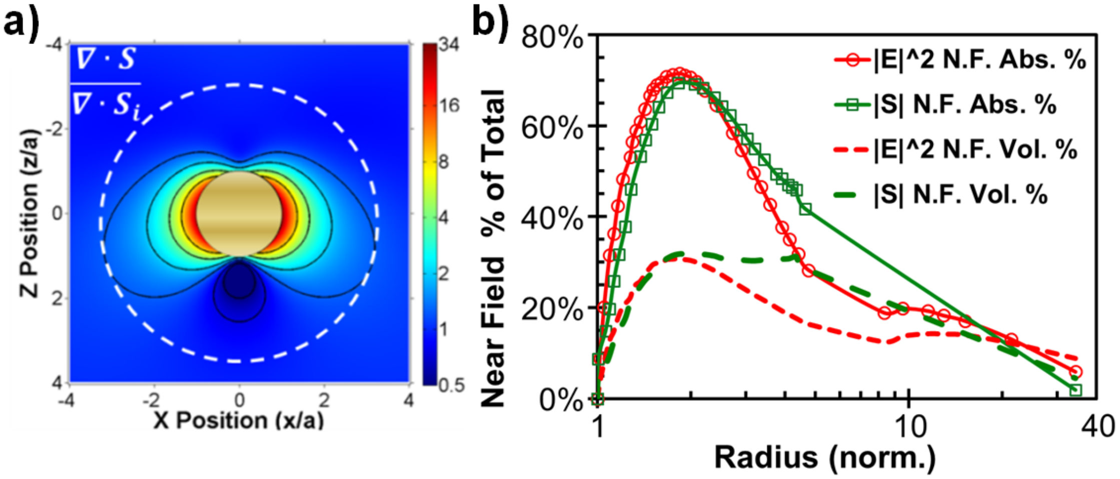

Figure 6.6: Fraction of absorption that occurs in the near-field as a function of radius for a 50 nm gold sphere. *a) Enhanced near-field absorption around a plasmonic nanoparticle near-field contours (black lines) at 8, 4, 2, 1.25, 0.75 and 0.5 × enhancement. The dashed white line represents a spherical volume encompassing the near-field volume at a cutoff of 1.25. Please note that there are region where the intensity drops below the background level – the regions of 0.75 and 0.5 × enhancement below the nanoparticle b) Near-field percentage of total absorption (symbols) and near-field percentage volume (dashed lines) as a fraction of absorption or volume for a spherical volume encompassing the near-field.*

6.4.5: Medium Absorption Properties as a Function of Distance

One of the main questions we posed in the beginning of this study was to understand what dictates the near-field absorption by the medium and how scattered light contributes to this absorption. To understand the net effect and extent over which the enhanced local absorption occurs, we calculate absorption by the medium starting from the nanosphere surface to the far-field. Specifically, we sum the total contribution for each field component, $\nabla \cdot \boldsymbol{S}_{sca}$ and $\nabla \cdot \boldsymbol{S}_{ext}$, as a function of radius for a spherical control volume on a point-by-point basis and normalize them by the total power incident on the particle, I_0A_{CS}, to obtain unitless efficiencies of the medium, $Q_{sca,M}$ and $Q_{ext,M}$, respectively.

$$Q_{sca,M} = \frac{\sum_{j=1}^{N}(\nabla \cdot S_{scat})_j * \Delta V_j}{I_0 A_{CS}} \tag{6.21}$$

$$Q_{ext,M} = \frac{\sum_{j=1}^{N}(\nabla \cdot S_{ext})_j * \Delta V_j}{I_0 A_{CS}} \tag{6.22}$$

Figure 6.7 presents the interaction efficiencies of the medium normalized by the optical interaction efficiencies of the particle. The efficiency of light absorbed by the medium from the scattered field ($Q_{sca,M}$, blue triangles), rapidly approaches the scattering efficiency of the nanoparticle, $Q_{sca,NP}$. As expected, the scattered light will be absorbed by the medium as it travels from the particle surface to the far-field. The interesting point is that much of the scattered light (~70%) is absorbed within one radius from the sphere surface (the two radii, *r/a*=2, from the center). This result is independent of the level of absorption in the medium. We hypothesize that this abnormally high absorption close to the particle occurs because of the disruption in the electric and magnetic fields in the near-field. Beyond this point, the absorption proceeds as expected with an exponential trend until all scattered light is absorbed, which can easily be shown as a linear trend on the log-scale plot of Figure 6.7.

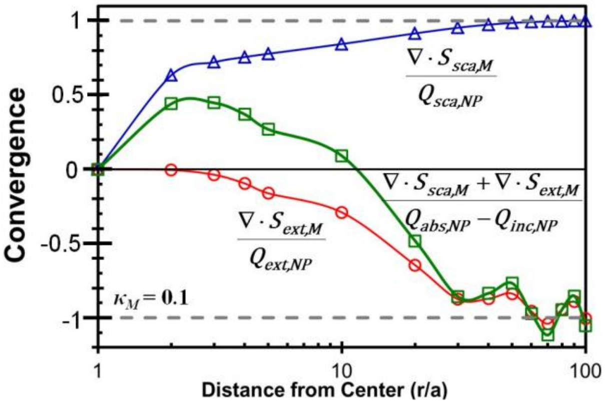

Figure 6.7: Convergence of the summed contributing terms to total absorption for a 50 nm gold sphere on resonance in a water-dye medium with κ_M = 0.1. *Each of the field components that contribute to absorption by the medium converge to final values related to the far-field optical properties of the nanoparticle as the distance from becomes large.*

Figure 6.7 also shows the extinction efficiency of absorption by the medium from the contribution of the interaction between the incident and scattered waves ($Q_{ext,M}$, red circles), as it converges to the negative of the extinction efficiency of the particle, $Q_{ext,NP}$. This result is an expression of the conservation of energy around a plasmonic particle. The light that is removed by the particle from the incident light field reduces the optical energy directly available for absorption by the medium. The total absorption by the medium around the particle is correspondingly reduced. As would be expected form a conservation of energy, near-field enhancement does not provide a net gain, but instead is an effect of a redistribution of optical energy. Thus, there is no extra absorption in total, but only enhanced absorption near a particle for linearly absorbing media. It should be noted that this result is only applicable for a semi-infinite around the particle. In applications where all light is not absorbed such as thin-film solar cells or where the magnitude of local absorption can have an effect, like in photodynamic therapy, the redistribution of light to enhance absorption near the particle can be beneficial.

The third curve in Figure 6.7 represents the summed extra absorption in the medium due to the presence of the particle ($\nabla \cdot \boldsymbol{S}_{sca,M} + \nabla \cdot \boldsymbol{S}_{ext,M}$, green squares). This curve also peaks at around two radii, showing that there are indeed regions of net increased absorption around a plasmonic nanoparticle. At larger distances from the particle, this term converges to a negative value of the net effect of the particle on absorption in the medium, which is given by the difference of the absorption by the particle, $Q_{abs,NP}$, and absorption of the medium that would occur in the same volume in the absence of a particle, $Q_{inc,NP}$. The net extra absorption converges by a distance of around 100 radii, or ~9λ. The long distance to converge to 1 shows the large extent of the disruptive effect that a metal nanoparticle has on the surrounding light field for even a moderate extinction efficiency of $Q_{ext,NP} = 3.3$. However, majority of the abosrption is concentrated within 1 radius away from the particle.

6.5: NONLINEAR ABSORPTION

To demonstrate additional advantages of our proposed method of calculations on a point-by-point basis, we estimate nonlinear absorption in a medium around a plasmonic nanoparticle. For nonlinear absorption by the medium, the local absorption coefficient will vary as a function of the intensity at that location. This analysis cannot be accomplished with a spherical control volume surface method, as the changing optical properties lead to non-physical negative values for the absorption by the medium. As discussed previously, no net far-field absorption gains can be achieved in a linear embedding medium. However, plasmonic nanoparticles can lead to net gains overall gains in nonlinearly absorbing material because the material properties at each point will depend on the local field intensity.

Specifically, we evaluate a two-photon absorption process in water with fluorescein at λ = 780 nm where most ultrafast lasers are typically available to initiate nonlinear processes. At this wavelength, linear absorption by fluorescein dye is negligible. We initially assume a constant incoming intensity, I_0, over a limited region surrounding the particle, which is plausible because of the small size of the nanoparticle relative to typical focal volumes. Though we demonstrate this method for a two-photon absorption process, it could theoretically be used for a combination of any order nonlinear or linear absorption process, provided the absorption can be expressed in terms of the refractive index.

We first calculate the electromagnetic fields at each point in space around the plasmonic nanoparticle assuming a uniform refractive index of the medium given by unenhanced intensity field, I_0. We then use the calculated fields to determine the local intensity ($|\boldsymbol{S}|$) at each point and use this value to adjust the local imaginary part of the refractive index. Finally, we calculate the energy absorption at each location with the updated refractive index. In this case, we neglect the effect of the updated local properties on the plasmonic behavior of the sphere, as this cannot be solved with a Mie theory-type approach. However, this effect is expected to be small because of the low probability of nonlinear absorption. Recent studies have shown that the effect of adjusting the local properties can be accomplished with a discrete dipole approach, but this approach is much more computationally intensive [186].

The two-photon absorption for a purely nonlinear absorber is given by:

$$\kappa_M = \frac{\beta\lambda}{4\pi} I \tag{6.23}$$

Here, the imaginary refractive index κ_M is dependent on the intensity I at each location and β is the two-photon absorption coefficient, which is expressed in terms of the number density of fluorophores, N_D, and the two-photon absorption cross-section, σ_{TPA} [187]:

$$\beta = \frac{N_D}{\hbar\omega}\sigma_{TPA} \tag{6.24}$$

Example calculations are shown in Figure 6.8. We use a previously reported $\sigma_{TPA} = 45$ GM value for fluorescein in an alkali environment [188]. The concentration and optical power are set to be consistent with our nonlinear fluorescence imaging experimental conditions [189]. Specifically, the fluorescein concentration is set at 25 µM ($N_D = 1.5 \times 10^{16}$ cm^{-3}), with an average optical power of 5mW, corresponding to a peak power of $I_0 = 4.8 \times 10^{10}$ W/cm^2 at the focus. These values yield an unenhanced nonlinear imaginary coefficient of refraction of $\kappa_{M,0} = 8 \times 10^{-9}$. We also present results for linear absorption for a uniform fixed refractive index at the same value.

The preliminary results presented in Figure 6.8a show a significantly strengthened response in the near-field for the nonlinear medium relative to unenhanced light, even though total absorption is much lower in the nonlinear medium. We find that the strongest response occurs for a radius R = 75 nm gold sphere (Figure 6.8a). Figure 6.8b expands on this data by focusing on a 150 nm sphere (R = 75 nm) and comparing the fraction of absorption and volume fraction for the near-field relative to a spherical shell. The peak is higher for the nonlinear absorption and the near-field absorbed fraction stays higher as a function of volume because a smaller amount of light will be absorbed out of the plasmon-focused region. Finally, we present the net amount of extra light absorbed due to the presence of the plasmonic particle as a function of distance from the particle.

The net gain for nonlinear absorption levels off a value close to 25× the amount of light absorbed in a volume equivalent to that occupied by the sphere, but the value for linear absorption peaks near 10 and afterwards begins to decay towards negative levels.

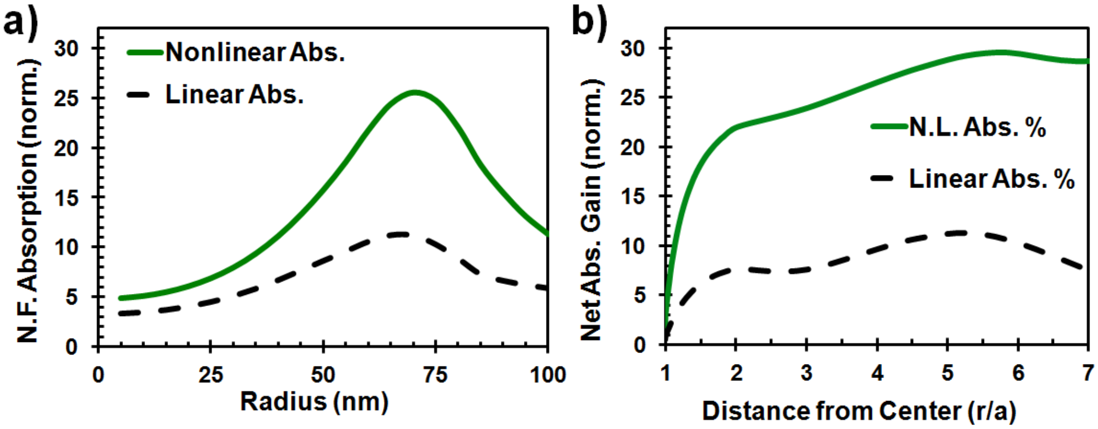

Figure 6.8: Comparison of absorption in a linear and nonlinear medium around a plasmonic nanosphere. *Nonlinear calculations are estimates for absorption in the medium surrounding a gold nanosphere in a water-like environment with* $\kappa_M = 8 \times 10^{-9}\, I/I_0$ *(nonlinear) and for the same index (linear) at a near-field cutoff* $f = 1.25$. *a) Near-field absorption, normalized by* $\boldsymbol{Q_{inc,NP}}$, *as a function of nanoparticle radius. b) Net absorption gain in linear and nonlinear media for a 150 nm gold sphere, normalized by* $\boldsymbol{Q_{inc,NP}}$.

6.6: CONCLUSION

In this chapter, we present calculations for determining absorption in the near-field around plasmonic metal nanoparticles. We show that the ratio of scattering-to-absorption increases for plasmonic metal nanoparticles in absorbing media. Several different criteria are presented for distinguishing the near-field region based on the calculated electromagnetic field magnitudes. We find that conditions based on the $|E|^2$ and $|S|$ enhancements yield the best descriptions of the near-field. We demonstrate the calculation of near-field enhanced absorption in the near-field based on the contribution of scattered, incident and interaction fields, showing that the scattered field is the strongest contributor to near-field enhanced absorption in the embedding medium. Finally, we showed how the calculation method can be used to estimate multiphoton absorption around a plasmonic nanosphere.

Chapter 7: Plasmonics for Enhanced Photovoltaic Absorption

Here, we present a study into the use of plasmonic particles for increasing the absorption in thin-film photovoltaic devices. The chapter is organized as follows. First, we describe the motivation for the project. Subsequently, we review thin film solar cells and plasmonics in solar cells. We then present our new results in this field, including numerical studies and a discussion of experimental results. This study builds on previous efforts in evaluating the far-field properties, absorption in the near-field around a plasmonic nanoparticle, nanoparticle synthesis, thin-film deposition, and nanoparticle self-assembly to target improvement in a specific application. Finally, we provide a set of conclusions based on these results.

7.1: INTRODUCTION

More than 120 petajoules (PJ, 1 PJ = 1 × 1015 J) of solar energy strike the Earth's surface every second. More solar energy reaches the Earth's surface in 90 minutes than is consumed by the entire world population in a year from all sources combined [190]. Given the bounty of solar energy, it has long been a dream to harness this clean and renewable energy source for useful purposes. The first practical solar cell was developed in 1954 [191], but the usage of solar cells was largely confined to 'off-grid' applications due to high costs and low efficiencies for the next few decades [192]. Steady decreases in the costs and increases in the efficiency of conventional silicon solar modules made impressive advances over the years [193], but photovoltaic power remained economically impractical in comparison with utility power from other sources. Furthermore, expanded competition with the computer semiconductor industry for silicon feedstock led to shortages and module price increases between 2004 and 2008 [194,195]. Though additional foundries have since come online, the issue that the most efficient solar cells are fabricated from the highest quality silicon remains a limiting factor. Over the years, many efforts have been made to reduce material usage as a means of cutting costs, but it was not until the disruptive commercial introduction in the early 2000's of low cost thin film solar cells that made compelling material cost reductions possible. Thin film solar cells are chemically deposited rather than sliced from a boule, which dramatically improves the economic viability of solar photovoltaics. They have significant advantages over standard 'thick' crystalline wafer-based silicon solar cells in fabrication cost, material usage, and energy payback, while maintaining a crucial advantage in the cost-to-power ratio (dollars per watt, \$/W) [196]. Other benefits of this type of cell include the ability to fabricate the cells on durable and flexible substrates, or to incorporate the solar cells into buildings (BIPV) [196,197]. Currently, thin film solar devices represent the fastest growing segment of a multi-billion dollar market that is doubling every 2 years, largely based on advantages in production volumes and cost efficiency advantages on a \$/Watt basis [196].

Despite all of these innovations and even including substantial government subsidies, solar energy is currently only cost-competitive with utility scale power in a few regions of the United States on a levelized cost of energy (LCOE) basis. One of these regions is California, which has both abundant solar resources and high cost electricity markets [198]. To achieve widespread use, however, solar costs need to reach true grid parity, for which significant new advances need to occur. Unfortunately, as thin film solar cell technology matures, the initial rapid gains in module efficiency, and the corresponding rate of improvement in solar cells, is beginning to stagnate for conventional solar cell device types. According to recent Department of Energy published goals [194,199], new ideas and approaches are needed to continue cost reductions to reach the ultimate goal of grid parity. Expanded availability of low cost solar photovoltaics could have tremendous implications worldwide for the environment, electricity production in third world nations, and health.

While thin film solar cells are superior on a $/W basis, they still trail in the overall efficiency of wafer-based silicon solar materials. This difference is largely based on the poor conversion efficiency of thin film solar cells in the red-NIR wavelength range, which carries almost half of the useful solar irradiation at the Earth's surface. Thin film solar cells are characterized by extremely low efficiencies at long wavelengths because of the absorption path length can be large relative to the film thickness [200]. Another cause of low absorption in thin-film devices is that existing light-trapping technologies used in conventional solar cells are not relevant for thin film solar devices. The poor absorption of these materials in the long wavelength portion of the solar spectrum is due to the trend in semiconductor devices of increasingly long absorption lengths as the wavelength increases [200]. As the cell thickness decreases, the longer absorption length of near-infrared light leads to the low conversion efficiency of light to useful energy in this range. Interestingly, this near-bandgap light is the most efficiently converted light, as only one bandgap of energy can be efficiently harvested from any photon, regardless of the incident energy. Together, these factors show that there is a problem to be solved and an attractive opportunity for boosting the conversion efficiency of long-wavelength light for thin film solar cells.

We propose a new method to improve the efficiency of thin film solar cells. We aim to implement plasmonic light trapping into low bandgap thin film solar cells to increases absorption of light in the red-NIR portion of the solar spectrum that is not efficiently absorbed in typical thin film cell. By focusing on plasmonic nanostructures that can be colloidally fabricated and deposited, we can gain the advantages of plasmonic light interactions without disrupting the crucial cost advantages of thin film solar cells in a practical manner. The method can be applied in standard environments and can be tuned for various semiconductor materials. Preliminary calculations show that relative efficiency gains exceeding 25% can be achieved if near-infrared light can be effectively captured in thin film solar cells.

Plasmonic solar enhancement is an emerging scientific field that makes use of the extraordinary optical properties of noble metallic nanoparticles to improve the efficiency of solar cells. Plasmonic nanoparticles have a resonant interaction with light that matches the plasmon frequency of the particle. At this frequency, the particle acts as a nanolens, gathering light from an area much larger than the particle itself and generating high intensities in the near-field. The plasmon frequency depends on the size, shape, material, and surrounding environment of the particle. These parameters can also be used to tune the way that the particle interacts with the incident light, shifting the ratio of scattering to absorption and the angular distribution of scattered light. The ability to modify the interaction behavior can be of the utmost importance when employing these particles for practical purposes. By increasing conversion efficiency at low added cost, we hope to provide significant benefit to promote cost efficiency of solar cells and provide a step towards the ultimate goal of widespread grid parity.

Multiple mechanisms have been proposed for the plasmonic enhancement of photovoltaic absorption in various solar cell types. The most probable mechanisms for absorption enhancement in commonly used semiconductor materials are near-field enhancement and high-angle scattering that redirects and traps light within cell. Through careful examination of simulations and experimental results, we determine the dominant mechanism and then work to design and synthesize plasmonic materials that will lead to the strong plasmonic absorption enhancement. By increasing conversion efficiency at low added cost, we aim to provide significant benefit to promote cost efficiency of solar cells and provide a step towards the ultimate goal of widespread grid parity.

7.2: BACKGROUND

Before a new step in the scientific field can be made, it is important to be aware of the research that has been pursued and published in the past. To that end, we review two topics of specific interest: thin film solar photovoltaics and plasmon-enhanced solar cells.

7.2.1: The Challenges of Thin Film Solar Cells

Thin film solar cells have significant advantages over conventional ‘thick’ solar cells, including: 1) decreased time to generate the energy used in fabrication (energy payback), 2) low-temperature fabrication resulting in less energy usage and reduced fabrication costs, 3) the possibility of using inexpensive substrates, 4) the possibility to integrate solar cells into flexible materials, 5) the ability to create semi-transparent solar cells, and 6) the ability to fabricate cells using high-throughput roll-to-roll processing [197]. Most thin film solar cell materials are characterized by significantly stronger absorption than conventional crystalline silicon, which allows the thin film structure to capture a significant portion of the incident light with reduced thickness. The material requirements and fabrications costs are lower for thinner cells, so there is an impetus towards using as thin of an absorber layer as practicable. While short wavelength light can still be absorbed efficiently in a thin film cell, the decreased thickness dictates that only a small amount of light is absorbed at longer wavelengths, where the absorption lengths remain long, as shown in Figure 7.1.

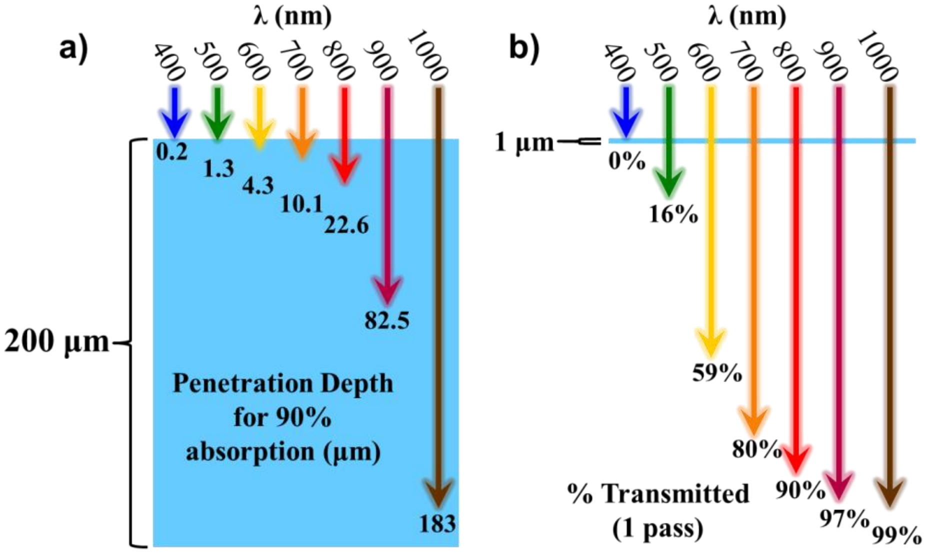

Figure 7.1: Effect of wavelength on the absorption of light for two different semiconductor thicknesses. *(a) A conventional 'thick' silicon cell (200 µm) is able to absorb most of the incident light across a wide spectral range. The arrows terminate at a depth where 90% of the light has been absorbed. (b) The effect of reducing the absorber thickness for a thin film microcrystalline silicon device (typical thickness ~1 µm). Most long wavelength light is not absorbed. All lines and boxes are to scale.*

Figure 7.2 presents the spectral dependence of the absorbed and converted light for two thicknesses of silicon as a function of the wavelength compared with the incident solar irradiance. Some light is lost due to reflection and inefficiencies, but most of the incident light is absorbed by the 200 μm thick cell. The 1 μm thick cell, however, has a peak in the absorbance spectrum in the short wavelength region on account of the absorption length relative to the cell thickness, and longer wavelength light is only weakly absorbed. While the difference in the absorption is significant, the calculated difference in the conversion of absorbed photons to electron-hole pairs is even more dramatic, as the conversion efficiency for an absorbed photon increases as the photon energy approaches the bandgap of the absorber material. A large margin for improvement, indicated with red slashes, can be seen in Figure 7.2, especially in the long-wavelength portion of the spectrum.

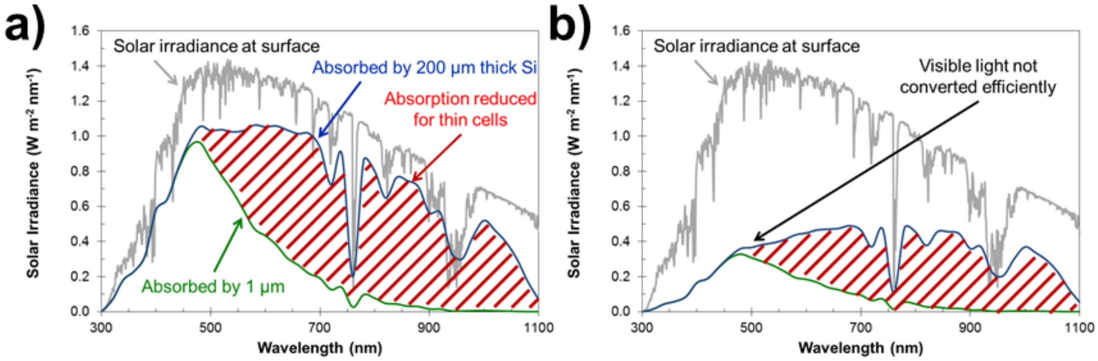

Figure 7.2 Simulated absorption spectra together with the conversion of the energy in incident photons to charge carriers for silicon solar cells of various thicknesses. *(a) The spectral dependence of absorption for two different thicknesses of a silicon solar cell as compared with the incident solar spectrum for North American locations, the NREL Air-Mass (AM) 1.5 spectrum. The thinner 1 μm cell exhibits very low absorption efficiencies for red-NIR wavelengths. (b) The spectral dependence of conversion for the two silicon thicknesses.*

The ‘thin film’ device structure also relaxes the material quality requirements with reduced dependence on diffusion for charge separation [200], enabling the use of thin film deposition techniques. Due to differences in device structure and charge collection, special designs are used with thin film solar cells, including features such as transparent conductive oxides for front contacts.

There are three primary commercially relevant semiconductor materials for thin film solar cells: amorphous silicon (a-Si), cadmium telluride (CdTe), and the copper indium gallium diselenide ($CuIn_{1-x}Ga_xSe_2$, CIGS) system [200]. Amorphous silicon, which was the first thin film material type commercialized, is limited by relatively low efficiencies and light-induced degradation, which is known as the Staebler-Wronski effect and results in a decrease in the cell efficiency with light soaking due to changes in the conductivity of the metastable structure. Amorphous silicon has found new use when integrated into 'micromorph' tandem cells with microcrystalline cells [196]. In the commercial solar sector, First Solar, a U.S. based manufacturer of CdTe cells that was founded in 1999 and started significant cell production in 2005, is now the world's largest manufacturer of solar cells with revenues exceeding $2.5 billion in 2010. First Solar produces photovoltaic cells with the lowest $/W, has been the fastest growing technology company in the U.S. and currently undergoing a two year doubling of their production capacity [200,201]. There are also several venture capital-backed CIGS start-ups in the United States.

In addition to the semiconductor-based thin film solar photovoltaic materials (a-Si, CdTe, and CIGS), there are a few other emerging thin film solar cell technologies that offer promising approaches to low-cost, wide-usage solar electric energy conversion. Two of the most interesting alternative ideas are organic solar cells and dye-sensitized solar cells (DSSC). Organic solar cells, which have made significant advances in the past ten years, seek to replace the absorber material with an organic semiconductor [202].

These devices have recently reached NREL-confirmed lab record efficiency of 7.9%, and have very promising potential for low-cost fabrication. DSSC's, also known as Grätzel cells after the inventor, offer a completely different approach: they consist of a solar absorber dye that is bound to a high-surface area titania (TiO_2) structure which serves as one of the two electrodes separated by an electrolyte [203]. These cells were originally designed to mimic the photosynthesis process. Although both of these solar cell types offer intriguing potential for very low cost-to-power ratios, more research is needed before these cell types are commercially competitive.

Thin film solar material systems are typically limited in two opposing ways. The charge collection is improved as the material thickness decreases, but the optical absorption decays dramatically. Additionally, the limited abundance of the rare elements indium and tellurium implies that the absorber layer should be reduced as much as possible to conserve resources and reduce costs. With the exception of expensive multiple junction gallium arsenide-based systems, the optical absorption of the material can be a limiting factor in the total optical conversion.

Compounding this problem, conventional light-trapping techniques that have been optimized for 'thick' silicon cells are not relevant for thin film materials. Light trapping is the ability of a cell to retain the light that is incident on the cell by reducing reflections and increasing light. One of the most successful light trapping strategies for conventional 200 μm thick silicon cells is the selective etching of the cell to create a surface texture of pyramids or inverse pyramids [204], usually with a height of ~3 μm. This dimension is much larger than the total thickness of most thin film cells. Significant effort has been directed into depositing thin film solar cells onto natural or designed rough surfaces

[205]. This is a promising approach, but this approach can lead to ‘shorting’ and may be challenging or expensive to attain over large areas. The light trapping requirements are much more stringent for thin film cells than ‘thick’ cells because of the increased number of interactions with the material boundaries before absorption, especially in the red and near-infrared regions.

Though thin film solar cells have seen remarkable growth and success in the past decade, only a miniscule fraction of total electricity production in the United States comes from solar power (0.03%). The limited market penetration is largely due to the persistent issue of cost competition with other energy sources. Additionally, the dramatic growth in the solar industry is still largely contingent on significant government incentives and subsidies, many of which are due to expire in 2016 [194,198]. The shift of governments away from solar incentives and subsidies means that cost-to-power ratio reductions must continue to render photovoltaic technologies cost-competitive in the future. Furthermore, since thin film cells are generally lower efficiency than crystalline silicon, the relative balance of system costs and area requirements are significantly higher for thin film cells. Improving the light collection and conversion efficiency has the potential to significantly enhance the performance of all types of thin solar cells. Thin film solar cells have enormous potential for world energy production, but increasing the light collection efficiency is the best path forward for continuing reductions in solar cell costs for increased solar energy generation.

7.2.2: Plasmon-enhanced Photovoltaics

Plasmonics is one attractive candidate technology for enhancing the optical absorption for thin film solar cells. Thin film solar cells have significant advantages over conventional ‘thick’ crystalline silicon cells in terms of the cost to power ratio ($/W), but thin film cells still lag in terms of overall efficiency and improvements are still needed for limited area applications. The thickness of thin-film solar cells is often limited by poor charge carrier transport, and long wavelength light, which is the most efficiently converted to useful current, is not absorbed. By integrating plasmonic particles tuned to selectively interact with this long wavelength light, the overall absorption and conversion of thin film solar cells can be enhanced. Conversely, fabrication costs and material demands can be reduced if the absorber thickness can be reduced with plasmonic enhancement at the same efficiency level.

In a pioneering work, Stuart and Hill showed in 1998 that the efficiency of photodetectors could be enhanced at long wavelengths by employing the plasmonic resonance of specially prepared vacuum-sputtered incomplete metal film island nanostructures [206]. This idea caught the interest of solar researchers and the first use of the plasmonic effect for solar photovoltaic applications was published in early 2000 [207]. This approach is often used with thermal annealing after deposition to aggregate and grow the ‘island’ structures to shift the resonance of the nanostructures to longer wavelengths. Unfortunately, the high-temperature tuning of this structure is energy intensive, and limited in the achievable wavelength range. While larger islands shift the resonance towards the red-NIR, they will also result in increased reflectivity in the visible and decreased active solar surface area that together reduce the overall light collection efficiency. Though some interesting work has been done with these structures, most notably by Pillai *et al.*, the concept is of fundamentally restricted in its use because of the limitations associated with this technique [208].

Other researchers have studied arrays of metal structures, such as grating structures, cylinders, hemispheres, that can be fabricated using e-beam lithography [209,210,166]. Precisely spaced arrays of different shapes can be created using lithographic methods, which makes this technique extremely interesting for studying plasmonic properties for solar applications [209]. However, this method is extremely low throughput, expensive, and energy intensive, and not applicable to large-scale commercial solar cell fabrication. The goal of solar cell cost-to-power ratio reduction cannot be met with this technique. A related approach uses lithographical techniques to create a hard master copy that can be pressed into soft materials, in a process known as imprint lithography, to create nanoscale features [205]. This approach has great promise, but remains in the research stage.

Overcoming the fabrication limitations of lithography techniques, the colloidal synthesis and application of plasmonic nanoparticles represents an opportunity as a feasible and applicable method for creating useful nanostructures. The synthesis techniques for colloidal particles have the potential to create liters of metal nanoparticle solution for little more than the cost of the precursor chemicals. The use of colloidally prepared and deposited plasmonic particles for enhancing solar energy conversion was first demonstrated using gold nanospheres on a silicon *pn* junction by Schaadt *et al.* in 2005 [211]. Since then, plasmonic nanospheres (silver or gold) have been studied for the enhancement of various types of solar cells, including demonstrated improvements, albeit modest, in the optical response for thin film amorphous silicon solar cells [212], DSSCs [213], and organic photovoltaics [214].

There are several fundamental reasons for the modest gains observed to date with the use of plasmonic nanoparticles to improve the efficiency of thin film solar cells. First, the resonance for spheres is mainly limited to visible wavelengths. Since the main improvement needs are in the red-NIR, large spheres must be employed. However, side-scattering is reduced for large spheres, which scatter most of the light in forward and reverse directions and result in limited contribution to the overall improvement of the thin film solar cells. The resonance of spheres can be red-shifted by incorporation into high refractive index semiconductor materials [166] and several groups have theoretically proposed or computationally studied the potential of integrating plasmonic spheres directly into the semiconductor materials. Unfortunately, this approach could cause parasitic losses in the charge collection efficiency, as metal surfaces within a semiconductor material could act as charge trapping locations. The magnitude of this effect has not yet been considered, but this effect could be mitigated through the use of dielectric-coated metal nanoparticles. Dielectric coating can have a profound effect on the plasmonic response, indicating the need for an in-depth study of the governing effects. Plasmonic enhanced cells utilizing this principle have not been fabricated thus far.

Non-spherical plasmonic particles have the potential to overcome some of difficulties with spherical particles by decoupling the plasmon resonance from the overall nanoparticle size. The applied research performed to date for the use of non-spherical plasmonic particles for solar applications has been unable to correctly match plasmonic properties to thin film solar materials. Two of the most relevant studies include Lee *et al.*, who employed gold nanorods, and Kulkarni *et al.*, who used triangular silver nanoprisms [215,216]. Both of these studies were unsuccessful in significantly enhancing solar absorption with non-spherical particles. There are a few fundamental reasons that limited the ability of these two studies to show improvement in the efficiency of solar cells. First and foremost, the plasmonic resonance was beyond the bandgap of the materials tested, which implies that the plasmonic effect cannot contribute to the material response. Second, after finding no useful enhancement with gold nanorods, Lee *et al.* actually reshaped the nanorods into spherical particles. Though Lee *et al*. was able to change the plasmonic resonance into a useful range for their situation, they missed the most crucial aspect of using non-spherical particles to improve efficiency in longer wavelengths. Mendes *et al.* computationally studied the possibility of using ellipsoidal particles, but no description of repeatable synthesis or solar cell integration methods were given [217].

For successful implementation of plasmonics in solar cells, there is a need for a complete understanding of both plasmonics and semiconductor device performance. To achieve this goal, we investigate novel designs to enhance the performance of thin film solar cells. The plasmon resonance of nanoparticles can be tuned to selectively and resonantly scatter light to promote the absorption of light in wavelengths that are typically poorly absorbed in thin film solar cells, but care must be taken to ensure that the enhancement occurs in a useful region and is not counteracted by losses. We target the highest conversion efficiency region where absorption is particularly weak (the red-NIR wavelengths) using low-cost, scalable techniques (colloidal particle synthesis and application).

7.3: OVERVIEW OF PLASMONIC-ENHANCED PHOTOVOLTAICS

Alternative light trapping techniques must be developed for thin film photovoltaics because conventional methods are not applicable to thin film applications.

Plasmonics offers a potential solution for enhancing the optical absorption for thin film solar cells. Thin film solar cells have significant advantages over conventional ‘thick’ crystalline silicon cells in terms of the manufacturability and cost-to-power ratio, but thin film cells still lag in terms of overall efficiency. By integrating plasmonic particles tuned to selectively interact with weakly absorbed long wavelength light, the overall absorption and conversion of thin film solar cells can be enhanced. Conversely, fabrication costs and material demands can be reduced if the absorber thickness can be reduced at the same efficiency level.

Plasmonic particles have great, untapped potential for enhancing the efficiency of solar energy conversion. Our previous research has focused on understanding energy flows around plasmonic nanoparticles, including the effect of nanoparticle morphology on the absorption, scattering and near-field enhancement of incident light. Electromagnetic simulations are used to evaluate the efficacy of plasmonic nanoparticles for light management in thin film solar cells. Simulations can be used to test many more plasmonic and optical designs than could be achieved experimentally. Furthermore, our efforts in nanoparticle synthesis and nanoparticle self-assembly make it possible to fabricate and deposit the custom-designed particles that simulations have identified as promising for photovoltaic applications. Here we present our calculations and experimental results for various configurations of plasmonic solar cells.

The mechanism of absorption enhancement is usually given as light scattering and coupling into guided modes within the solar material (eg. [166]), leading to an increase in the effective light path length within the active medium of the solar cell. However, alternate mechanisms for plasmonic solar interaction have been proposed, including direct near-field enhancement [217,218], absorption by the particle itself [219], and anti-reflective capabilities [220]. While we believe high-angle scattering and internal reflection is the most reasonable and dominant plasmonic enhancement effect, we investigate the enhancement mechanism and estimate contributions of different effects as part of this research. In subsequent sections, we use our capabilities for electromagnetic simulation to predict the capacity of plasmonic nanoparticles for enhancing the absorption of solar cells, followed by experimental efforts to observe these enhancements.

Various geometries have been proposed for integrating plasmonic nanostructures in thin film solar cells [166], and each rely on different effects to promote optical absorption. One approach involves placing the nanoparticles on top of the semiconductor or embedding the nanoparticles in the dielectric layer on top of the solar cell [Westphalen 2001]. This method can lead to gains, especially in the long wavelength region, but can also have losses in the visible region due to absorption by the particle. Furthermore, this approach cannot benefit from the enhanced near-fields around plasmonic nanoparticles. A second approach involves locating nanoparticles at the back surface of the solar cell (back reflector). This approach can also improve scattering at long wavelengths and does not have the disadvantage of increased losses, but only backscattered light will contribute to enhancement. Additionally, the enhanced fields near the particle are unlikely to lead to significant gains, because back surface recombination can be significant in thin film solar cells. Interface effects can lead to dramatic shifts in the plasmonic response, especially in drawing the field enhancement pattern towards the interface. A third method involves the incorporation of the plasmonic nanoparticle directly within the absorber material. This approach has the advantages of full usage of the near-field enhancement and that all scattering will result in increased path lengths within the absorber. Furthermore, high angle scattering can lead to coupling into guided modes within the semiconductor layer, leading to nearly complete absorption. An added benefit is that the charge carrier collection efficiency is higher in this region than in the areas near the interfaces due to high separation fields and decreased diffusion or drift distances, resulting in reduced recombination. We examine these different mechanisms and locations for plasmonic nanoparticle-enhanced solar cells through simulation and experiment.

7.4: SIMULATIONS FOR GOLD NANORODS IN THE TOP LAYER OF A SOLAR CELL

One of the most common approaches for plasmonic enhancement of semiconductor thin film solar cells is in integrate nanoparticles within or on top of the front 'window' layer of the cell. This is because the nanoparticles can be deposited after the semiconductor, making this configuration the easiest to fabricate. For this geometry, asymmetrical or very large particles need to be used to shift the resonance into the red or near-infrared regions where absorption enhancement in the solar cell is necessary. We first consider gold nanorods embedded in a glass layer on top of the ITO layer for a 1 µm thick microcrystalline silicon solar cell.

We hypothesize that the large interaction efficiency and near-infrared plasmon peak of gold nanorods could be promising for enhancing the poor long wavelength performance of a thin microcrystalline silicon cell. Gold nanorods are characterized by a much stronger plasmonic resonance than spherical particles, implying that a low coverage fraction could be sufficient to enhance NIR performance. This approach allows for minimal visible losses due to absorption by the plasmonic particles, which is lost to heat.

When metal nanoparticles are outside of the absorber material, near-field enhancement cannot contribute to enhanced absorption, and thus the only applicable enhancement mechanism is an increased optical path length within the solar cell through scattering by the particle.

7.4.1: Calculation of Solar Enhancement using Plasmonic Interaction Efficiencies

Our first efforts examined the wavelength-dependent effect of optical path length increases within the silicon absorber layer according to the redirection of light into horizontal directions. Once the light is within the absorber material, most light is coupled into guided modes, and very little light escapes as the internal reflection increases with incidence angle (Figure 7.3a). By scattering light into horizontal directions, the effective path length can be increased, because the lateral dimensions *D* are much larger than the thickness of the thin film *L*. The nanorods are assumed to be randomly oriented and spaced in a hexagonal pattern such that the optical interaction regions do not overlap for any wavelength (Figure 7.3b). The plasmonic interaction areas vary dramatically as a function of wavelength as shown in the green and red circles, which indicate the extinction cross-sections for light at 480 and 880 nm, respectively. This disparity is an important effect, as the particle scattered fraction, which can contribute to enhanced absorption in the solar cell, is 25% at 480 nm but 75% at 880 nm. The net effect of the plasmonic nanoparticles is determined by summing the extra absorption from path length increase due to scattering and the loss due to absorption by the plasmonic particle, where the magnitude of each effect is scaled by the interaction efficiency and surface coverage.

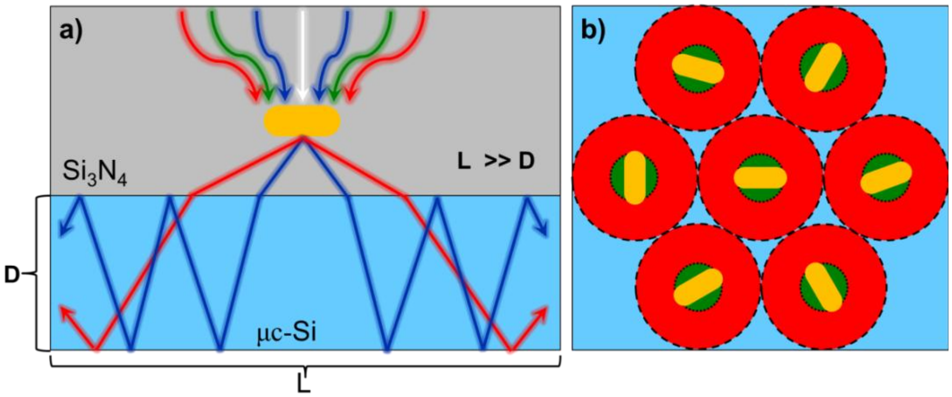

Figure 7.3: Enhancement mechanism and simulation schematic for plasmonic enhancement with gold nanorods embedded in the top layer. *This figure shows the drawing in of light over a region that is larger than the particle. a) The optical path length is within the absorber is increased by scattering by a plasmonic nanoparticle. b) A scale representation of the light that interacts with the plasmonic nanoparticle on resonance (red circles) and the cross-section off resonance in the visible (green circles).*

We use the previously benchmarked DDA technique to calculate the scattering and absorption cross-sections, which are then multiplied by a path length enhancement factor. The absorption is calculated using the optical path length and the absorption coefficient at each wavelength. The fraction of absorbed optical energy converted to useful charge-hole pairs is found for each wavelength by dividing the photon energy by the band gap of the solar cell. The losses due to reflection at the interfaces (air-glass, glass-silicon) and the cell resistance are also taken into account. We use shell (Linux) or batch (Windows) file processing to rapidly estimate the plasmonic absorption enhancement for many difference particle sizes and shapes using DDA across whole spectral ranges. We simulate gold nanorods with a constant diameter of 50 nm, but varying aspect ratio from 1 to 4. We use silicon nitride as a window layer because the plasmonic response is stronger and the scattered fraction is higher in this medium than silicon oxide (silica). In these simulations, unpolarized light is incident on the solar cell at each wavelength according to the intensity present in the measured solar spectra.

Figure 7.4 shows simulated results for 50 nm diameter gold nanorods with an aspect ratio of two embedded in a silicon nitride top layer. We estimate 9% losses in the UV and visible wavelengths up to 550 nm, but strong 68% gains over the 550 to 1100 nm wavelength range of the solar spectrum. These results that lead to promising 21% gains in the overall conversion efficiency.

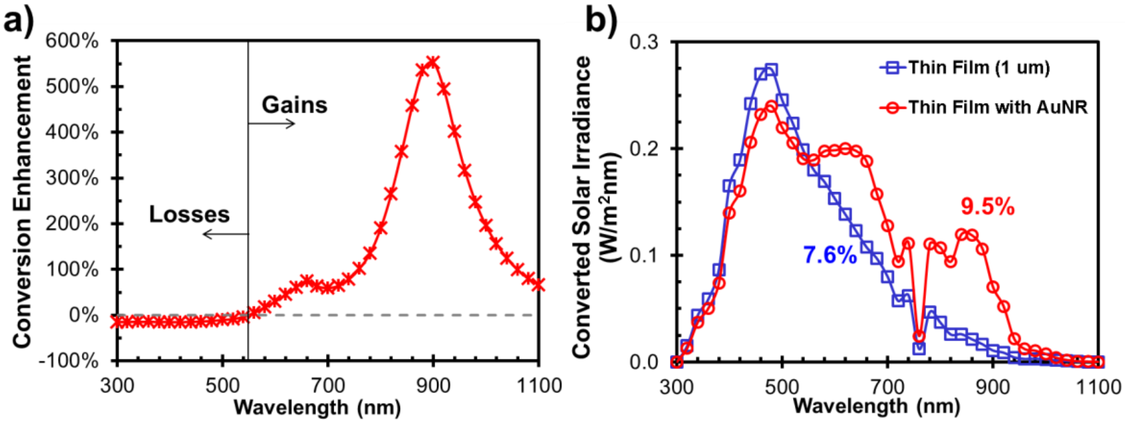

Figure 7.4: Simulated absorption spectra for silicon solar cells with the effect of integrated plasmonic particles. *a) The conversion enhancement as a function of wavelength follows the plasmonic resonance for a 50 × 100 nm gold nanorod embedded in* Si_3N_4 *in a microcrystalline silicon device. b) The total effect of the nanorods on the conversion response including the incident light intensity. The numbers indicate the estimated overall conversion efficiency of the simulated cell.*

The results show the spectrally-resolved differences in the absorption that can be obtained by applying nanorods to thin film solar cells and the potential of plasmonics for enhancing the absorption of red-NIR light. Additional improvements can be obtained by incorporating nanorods with two different complementary sizes to effectively target a wider portion of the spectrum. Two narrow size distribution nanoparticle sets are preferable over one wide distribution sample because the spacing can be reduced while avoiding interaction overlap because of the separated plasmon peak wavelengths.

Simulations with the microcrystalline silicon system also showed that thinner cells benefit from plasmonic light enhancement proportionally more than thicker cells. While the overall efficiency is expected to decline with decreasing cell thickness, thinner cells will reap much stronger relative gains from plasmonic enhancement. Specifically, for the same scattering length enhancements, a 1 μm thick mc-Si cell can improve by 21%, whereas a 150 nm cell could improve by more than 30% over the unenhanced value.

7.4.2: Angle-Resolved Calculation of Plasmonic Enhancement

The previous calculations show the promise of plasmonic enhancement, but they rely on one plausible but unproven assumption: that the scattering by a particle embedded in the glass window layer results in an increase in the optical path length in an absorber material. To test this principle, we need to extend our analysis of optical path length enhancement for a calculated angular distribution of scattered light from a plasmonic particle across the entire solar spectrum. We extend our DDA calculations to find the scattered intensity as a function of polar angle only, as the path length enhancement can be assumed to be independent of the azimuthal angle for unpolarized light if the expanse of the cell is large compared to its thickness. We then derive and implement calculation of the complex indices of refraction on the Fresnel equations at non-normal angles of incidence as a function of wavelength using aluminum as a back contact and reflector. These equations are coupled with the solar absorption model to extend the previously shown results by following each scattered ray from the particle surface to the interface and determining the absorption within the material and the losses at the boundaries.

This analysis revealed several key points of interest. First, we observe that high angles of incidence, corresponding to scattering in the lateral directions, yielded significant increases in the reflected light at the interface. This result indicates that once the light is within the absorber material, almost all of the light will be absorbed by the semiconductor as the light is guided through nearly complete reflection at each interface, as we had initially hypothesized. However, the unintended but unavoidable consequence of scattering by a particle in the glass layer was increased reflection at the glass-silicon interface, which drastically reduced the benefit of this approach. The 21% gains predicted by an optical interaction cross-section based simulation are reduced to only 6% when using a more rigorous angle-dependent analysis.

7.4.3: Conclusions for Plasmonic Nanoparticles Embedded in the Top Glass Layer

Together, the results presented in this section show that though plasmonic nanoparticles are very effective at the wavelength-selective redirection of light for solar applications, we conclude that embedding nanoparticles in the top glass layer is not a viable approach. We find two major sources of losses in this configuration: absorption by the particle, and an increased reflectivity that decreases optical coupling into the solar absorber. Silver nanorods could be used in place of gold to reduce the effect of absorption, but the approach of embedding plasmonic nanoparticles in a glass layer itself is primarily limited because high angle scattering from the nanoparticles also leads to increased reflection at the dielectric-semiconductor interface. However, this analysis was useful in the introduction and development of concepts such as the wavelength dependent interaction cross-sections, nanoparticle coverage density, scattering to absorption ratio, increase in path length within a simulated solar cell, angle-dependent scattering, and complex refractive index Fresnel equations for oblique incidence reflectivity. Furthermore, we found that the plasmonic particles performed as hypothesized, where dramatic increase in the absorption could be obtained for a thin film solar cell by increased path lengths through high angle scattering from the particle, if the light could be coupled into the material. Thus, we remain convinced of the potential for plasmonic nanoparticles for enhancing the absorption of thin film solar cells, especially for very thin absorber layers, but need to investigate other configurations for their effective use.

7.5: PLASMONIC ENHANCEMENT IN THE CIGS SYSTEM

One attractive target for plasmonic enhancement is the copper (indium, gallium) diselenide system. The Korgel group at the University of Texas at Austin has recently developed printable nanocrystalline CIS cells that are fabricated at room-temperature with efficiencies up to 3.1% [221]. Importantly, fabrication of these cells does not require energy-intensive vacuum deposition or high-temperature annealing processes. Low-temperature synthesis represents an attractive avenue for significant decreases in fabrication costs for solar cells, while also enabling the use of low cost flexible plastic substrates. These CIS cells are an especially interesting target for plasmonic enhancement because there is a great need for improvement in the absorption efficiency. Due to inefficient charge separation and collection properties, the cells must be extremely thin (ideal CIS thickness $\leq$ 150 nm) [221]. Consequently, they absorb only a small fraction of incident solar light. Most of the light absorbed by the cells is in the visible wavelength region of the solar spectrum, but the internal quantum efficiency (the fraction of photogenerated carriers actually extracted) remains high over the entire red-NIR portion of the solar spectrum [221]. Therefore, the application of plasmonic nanoparticle in the red-NIR regime has the potential to significantly enhance the performance of these cells if light trapping can be used to increase absorption in the long wavelength region. This result, coupled with the high internal quantum efficiency at long wavelengths [221], show that the Dr. Korgel group's ultrathin nanoprinted cells are an attractive target for plasmonic enhancement.

Working with students in the Korgel group, we tested the spray-deposited CIS system to test the potential of plasmonic light management for improving the efficiency of thin film solar cells, specifically focusing on the long wavelength portion of the solar spectrum using targeted non-spherical plasmonic particles (gold nanorods). Plasmonic nanoparticles were integrated at the back surface in the fabricated devices to avoid the disadvantages described in the previous section. The electrical performance of the fabricated cells were characterized with the electrical performance of the fabricated cells for open circuit voltage, short circuit current, fill factor, and overall efficiency.

Initial results with this system were inconclusive. The fabrication process was challenging, and it could be difficult to specifically identify the cause of specific changes in the complicated system until the final cell was fabricated. A steep learning curve in fabrication was observed, where senior students could make excellent cells, but we had a tough time with consistency. This technique and the application of plasmonics to spray-deposited thin film CIGS cells is still regarded as very promising, but significant efforts would need to be expended for ultimate success with plasmonic enhancement. Thus, further study was confined to simpler semiconductor systems to isolate individual variables in the system.

7.6: SIMULATIONS FOR NANOPARTICLES EMBEDDED IN THE ACTIVE ABSORBER LAYER

Our next implementation considered nanoparticles embedded in the active absorber layer. In this case, plasmonic nanoparticles can improve the absorption efficiency in several ways. First, the particle absorption loss is mitigated by the strong absorption of short wavelength light in a very thin region at the top of the cell, which results in very little short wavelength light reaching the nanoparticle. This is an important effect, because the parasitic losses are much higher for these wavelengths. Furthermore, both back-scattering and forward scattering will be beneficial for improving absorption within the semiconductor layer. Lastly, near-field enhancement may contribute to a localization of absorbed energy within the cell.

However, in this case, several additional factors must be considered to study plasmonic nanoparticles in absorbing media. Current simulation methods are insufficient for calculating plasmonic contributions to optical absorption. For example, screening many configurations with finite-difference time-domain codes is impractical. Finite discretization of rounded particles with cubic domains can also lead to errors in the enhancement, optical response and scattering behavior in the near-field. Furthermore, discrete dipole solutions for metal nanoparticles in absorbing media are unavailable at the time of writing. Therefore, there is a need for an exact analytical method to simulate the optical absorption around a plasmonic structure embedded in an absorbing material.

The optical properties of typical solar thin film photovoltaic absorber materials result in a strong red shift in the plasmonic peak, with the result that silver spheres can provide a strong peak in the red-NIR wavelength region. Thus, we focus on silver spheres, whose optical interaction can be solved analytically with previously introduced extended Mie theory. Additionally, one must also consider the potential adverse effects that could occur due to integrating foreign materials in the absorber layer. One such effect is the potential for charge carrier trapping by a metal surface present within the semiconductor layer. In this case, the exposed nanoparticle surface could act as 'traps' and decrease the charge collection efficiency. This possibility could be mitigated by the presence of thin dielectric shells to insulate the metal surface. This will require a further extension in the theory to compute the fields and absorption around a core-shell plasmonic/dielectric particle embedded in an absorbing medium.

7.6.1: Simulation Parameters

For all calculations, we use custom-written codes based on Mie theory based codes developed following the discussion presented in Bohren and Huffman [7]. These codes are written with Matlab to calculate the electromagnetic fields (electric E, magnetic B, and Poynting vector S) at any point in space inside or outside the coated spherical particles in Cartesian or spherical coordinates. All fields are presented relative to the incident intensity of the non-enhanced fields of the incident light at that location in space. We also used the mathematical expressions and codes developed in the previous chapter for optical deposition in the near-field outside the particle.

The refractive indices for the dielectric materials water and amorphous silicon dioxide (silica) are calculated using Sellmeier-type fits to experimental observations. All other material refractive indices are interpolated from tabulated experimental data, including metals [24], cadmium telluride [24], copper (indium, gallium) diselenide

(CIGS) [222], and silicon [223]. The optical properties of crystalline silicon are used here to represent the optical properties of micro-crystalline silicon, as relatively small differences are observed in the useful portion of the solar spectrum (400–1100 nm). We use a typical indium to gallium ratio of 0.3:0.7 for the CIGS material. The AM 1.5 solar spectrum is used for the distribution of solar intensity as a function of wavelength [NREL 2003].

7.6.2: Nanoparticle Optical Properties in Solar Absorber Materials

Figure 7.5 shows the effects of an absorbing media on the resonance of plasmonic nanoparticles. There is a large red-shift in the plasmonic resonance when changing from water to solid materials, and a strengthening of the resonance. As shown before for a dyed water medium, we also observe a dramatic increase in the scattered fraction of the particle in the two absorbing solar materials (CdTe and μc-Si) compared with two non-absorbing dielectric media (H_2O and SiN_x). This is a very important result for the use of plasmonics for solar cells, as absorption by the particle represents a parasitic loss and scattering is desirable for promoting absorption in long-wavelength regions where the absorption length is larger than the thickness for thin film materials. These results expand on previous results for plasmonic enhancement in absorbing materials and demonstrate the promise of plasmonics embedded in real solar absorber materials.

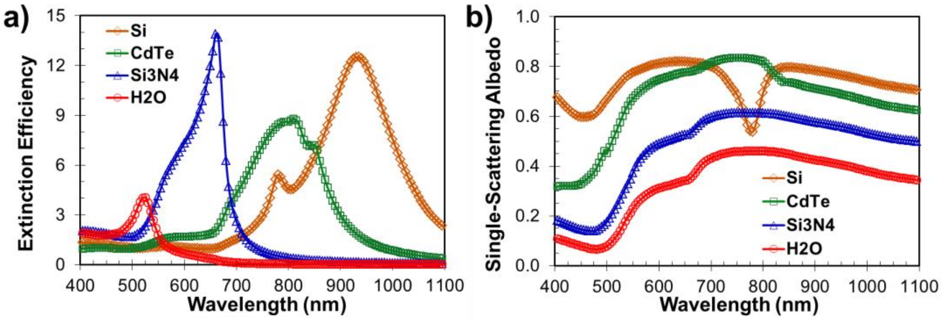

Figure 7.5: Changes in plasmonic properties for a 50 nm gold sphere embedded in various media. *a) Plasmon resonance shift and b) single-scattering albedo for gold in water, silicon nitride, cadmium telluride and microcrystalline silicon.*

7.6.3: Dielectric-Coated Plasmonic Nanoparticles

A complete treatment of the use of plasmonic nanoparticles embedded in the active absorber material for solar applications should also address potential charge-carrier losses at the metal sphere surface. Metal surfaces within a solar cell could act as trapping locations, resulting in decreases in the ability to separate charges and the corresponding efficiency of a photovoltaic cell. Thin dielectric layers can have dramatic effects on electronic properties at an interface, so we here consider the presence of a thin dielectric shell around metal nanoparticles in an effort to mitigate the effect of trapping.

Exposed metal surfaces within the active layer could drastically reduce charge collection efficiencies, so silica shells on metal nanoparticles are proposed to mitigate charge trapping at the metal surface. However, it is necessary to keep the silica shell as thin as possible to avoid damping the plasmonic response and avoid losing near-field enhancement that could otherwise be used to enhance solar absorption by the medium.

To estimate the shell thicknesses necessary to effectively insulate the silver surface from the surrounding medium and prevent charge carrier trapping, we look to the measurements of leakage current in a metal-oxide-semiconductor field effect transistor

(MOSFET) as a function of silicon dioxide thickness. Hou *et al*. showed that an increase in the oxide layer thickness of approximately 1 nm was sufficient to reduce the leakage current at the gate by ~5 orders of magnitude at a voltage of 1 V, which is estimated be similar to the conditions within the solar cell [224]. Similarly, Zhao *et al*. found that a native oxide layer, usually around 2.1 nm thick, on silicon increased the sheet resistance by more than two orders of magnitude in an electrode/oxide/semiconductor testing configuration of silicon nanomembranes [225]. These results indicate that an oxide thickness of ~2 nm should be sufficient to effectively insulate a metal surface. Previously, we showed that thin silica shells can be fabricated on silver cores during synthesis, which we will study here for enhancing thin-film photovoltaic absorption.

7.6.4: Theory of Coated Spheres in an Absorbing Medium

We extend Mie theory equations for the electromagnetic fields at all points inside and around a coated sphere in an absorbing medium, building on our previous work for nanoparticles in absorptive embedding media and previously published solutions for coated spheres [5]. The spherical harmonic coefficients can be solved for using direct matrix inversion of the coated sphere boundary conditions. The fields can then be obtained using the same equations as an uncoated sphere in an absorbing medium.

The calculation of spheres coated with concentric layers can also be solved analytically [14]. This solution has become relevant for plasmonics as nanoparticle synthesis methods for creating spherical shell coatings have recently been developed for metal core/dielectric shell, dielectric core/metal shell, bimetallic shell structures and multilayer concentric structures. Coated sphere calculations follow the same spherical harmonic solution method as Mie theory, but new scattering coefficients must be found using the boundary conditions at each of the interfaces. Once the updated electric and magnetic field coefficients are obtained, the fields inside the core and outside the shell can be solved using the same equations as for an uncoated sphere. Coated sphere (shell) calculations were verified by setting the core and shell to be the same material or by setting the core and environment to be the same material and comparing the results with extended Mie theory calculations. Coated sphere calculations were tested two ways: first, a direct derivation following previously published work [7], and second, direct solution of the system of linear equations set up using the boundary conditions through matrix inversion.

7.6.5: Effect of a Silica Shell on the Plasmonic Resonance

The optical effect of a shell between a metal and a semiconductor can be quite dramatic. Large blueshifts in the plasmon resonance wavelength are observed for Ag@SiO_2 nanoparticles in silicon, although they are not observed for Ag@SiO_2 particles in water. This blueshift is especially important for plasmonic solar applications, Silica coatings also allow for larger particles (and correspondingly higher scattering-to-absorption ratios) than would be normally feasible for a given material bandgap, because the red-shift that comes with increasing particle size can be counteracted by the blue-shift that occurs due to the silica shell.

Figure 7.6 shows the effect of a thin silica shell and an absorbing medium on the plasmonic response of a silver nanoparticle. We present the scattering efficiency (solid lines) and the scattering-to-extinction ratio (dotted lines, right axis). The configurations include a 50 nm Ag nanoparticles in: water, water with a 2 nm SiO2 shell, microcrystalline silicon (μc-Si) medium, and μc-Si medium with 2 nm SiO2 shell.

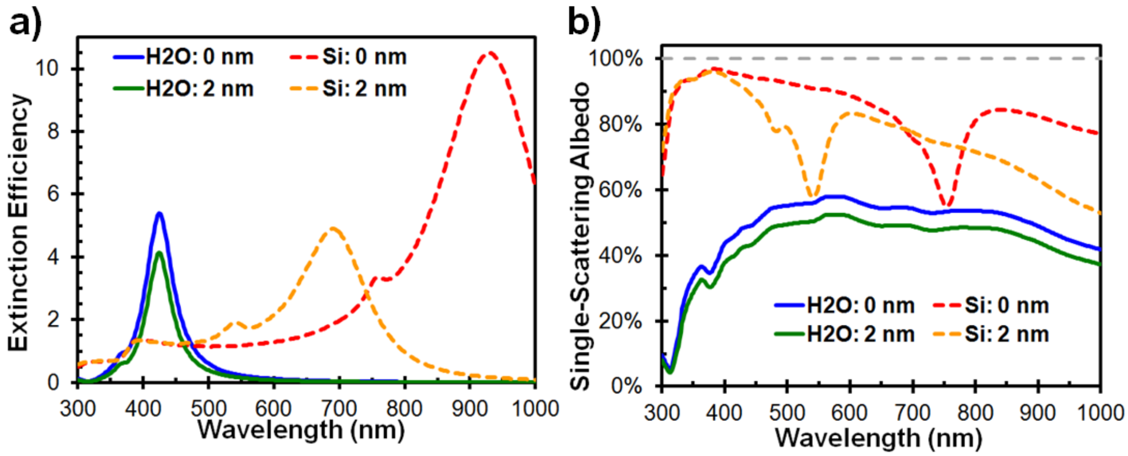

Figure 7.6: Plasmonic response of a 50 nm Ag sphere in different conditions.

These results reveal a few points of interest. First, the silica shell results in only a slight red-shift in a water medium. For a μc-Si medium, however, a thin silica shell results in a dramatic blue-shift in the resonance. This behavior occurs because of the relative difference between the optical properties of the silver sphere and the shell relative to the surrounding medium. Interestingly, the presence of an absorbing medium still results in a significantly enhanced scattering-to-extinction ratio.

7.6.6: Plasmonic Enhancement Mechanisms

For plasmonic nanoparticles embedded in an absorbing medium, both enhanced near-field absorption and increased path length due to scattering by the particle will lead to increased absorption by the semiconductor. However, it is unclear which mechanism will be dominant and which parameters dictate the magnitude of each effect. These two mechanisms are not generally maximized for the same size and shape. An understanding of the dominant mechanism of enhanced energy deposition is extremely important for the effective design of plasmonic particles for solar applications. Here, we evaluate both contributions to the enhanced optical absorption in thin film photovoltaics.

The near-field absorption can be calculated according to the method described in the previous chapter. Briefly, we examine the extra light absorbed in the near-field around a plasmonic nanoparticle using a point-by-point method using the divergence of the Poynting vector at each location. The loss from absorption by the particle and the displacement by the particle are considered for determining the net effect of the particle.

To determine the total amount of extra energy deposited in a medium due to a plasmonic particle, one must also examine the scattered light in addition to enhanced near-field energy deposition. Scattering in the perpendicular directions will provide a net gain in absorption within the cell for photons with energies greater than the bandgap, as the lateral dimensions of thin film solar cells are typically much larger than the thickness. This effect can also be considered in terms of the coupling of incident light into guided modes, where the absorption path length can be much larger than the thickness of the cell.

We find the angular distribution of energy scattered outside the near-field region to determine the increase in absorption within the medium on account of plasmonic scattering. Plasmonic particles are of significant interest for increased scattering in solar cells because of their strong high-angle scattering relative to dielectric particles, which scatter light primarily in the forward direction. The light that scatters from the particle (outside of the near-field region) is ray-traced to the interface, reflection is calculated, and then the reflected ray is traced to the opposite surface. The total amount absorbed on each path is calculated from the reflection losses at each surface. We follow each ray until it reaches 0.1% of its initial intensity. The enhanced path length and corresponding absorption is calculated with ray tracing and using complex Fresnel equations to determine reflection at the cell boundaries. This rigorous approach builds on an initial estimate that can be obtained by determining the percentage of light scattered in the lateral (x and y) directions. By calculating the scattered light outside of the near-field region, we avoid 'double counting' any absorption while still being able to account for all sources of absorption. The total gain in absorption by the semiconductor layer from scattering is calculated for each wavelength by integrating the angular contributions for each polar angle.

Figure 7.7 shows each of the mechanisms that contribute to enhanced plasmonic absorption in photovoltaic semiconductor materials. Two materials are shown: μc-Si, which is an indirect (weak) absorber (Figure 7.7a), and CIGS, which is a direct (strong) absorber. In this figure, the path length enhancement through scattering from the particle is denoted 'light trapping', while the plasmon-enhanced absorption around the nanoparticle is shown as the' near-field'. The two loss mechanisms are displacement of absorber material by the particle and absorption by the nanoparticle. The sum of all these values is shown as the net gain, which is positive for most of the solar spectrum but is negative for short wavelengths.

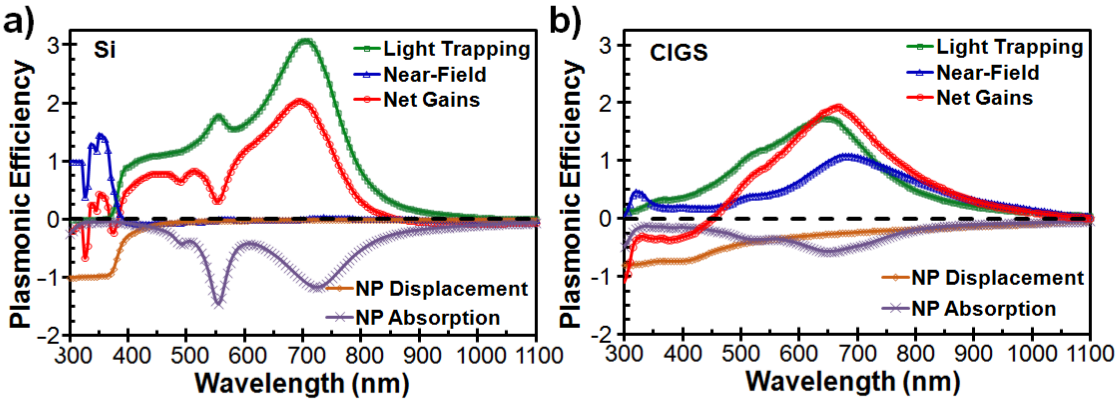

Figure 7.7: A comparison of plasmonic effects for a 54 nm Ag@SiO$_2$ nanoparticle embedded in photovoltaic semiconductors. Wavelength-dependent interaction efficiencies are shown for each of the gain and loss mechanisms for plasmonic nanoparticles in a) μc-Si, and b) CIGS.

Several points can be drawn from these results. First, the peak plasmonic gains are similar for both of these materials, but the contributing terms are different. We distinguish between near-field and scattering effects for energy absorption, which was previously unavailable. Enhanced light trapping through scattering is completely dominant for weak absorbers, such as μc-Si, but the near-field absorption is important for strong absorbers, becoming the major source of enhancement for CIGS at long wavelengths. The loss due to displaced absorber is found to be a correspondingly weak effect for μc-Si, but is significant for CIGS. These results imply that a back surface location for plasmonic elements may be more advantageous for strong absorbers. Though we show semiconductor displacement as a loss mechanism, it could also be argued no displacement loss will be physically observed in most thin film systems. Most thin films deposition methods will follow the morphology of the surface. We also find that the absorption by the particle is stronger for the weakly absorbing μc-Si, consistent with our findings on the scattering fraction in the previous chapter.

We also notice anomalous, negative effects in the short wavelength region, where the imaginary part of the refractive index is larger for the semiconductor than for the metal. In this case, the plasmonic nanoparticle acts more like a void than a metal. All of these results are for a unit intensity at each wavelength, however, which is useful for comparing the magnitude of effects, but not physically relevant for solar irradiation incident on a nanoparticle embedded within a semiconductor layer.

7.6.7: Effect of Depth in Plasmon-Enhanced Thin Film Absorption

Plasmonics for solar cell applications can most effectively be used by placing plasmonic particles some distance into the material, thus mitigating the effect of wavelength regions where the particle has a negative effect. This works because the absorption lengths for short wavelengths are very small, meaning that this light will all be absorbed by the depth of the particle. While the incident spectrum at the surface well-known, the depth of the particle in the solar cell has a large effect on the spectrum present at the particle. Here we examine particles embedded at the midpoint of the solar absorber medium. We first determine the wavelength-dependent light intensity at the particle location (Figure 7.8a), which is significantly modified from the incident solar spectrum. Specifically, the short wavelength light is absorbed while long wavelength light mostly passes. This wavelength-dependent attenuation must be considered for each depth and system chosen, and it is an important effect for the use of embedded nanoparticles, as significantly reduced fractions of light reach the particle in the short wavelength portion of the spectrum where the plasmonic gain is low. Figure 7.8b shows the convolution of the intensity distribution of the solar spectrum with the previously calculated net wavelength-dependent gain from the presence of particle. In this case, we see that though there are regions where the nanoparticle would have a negative effect, placing the particles well within the absorber medium results in a net gain at all wavelengths.

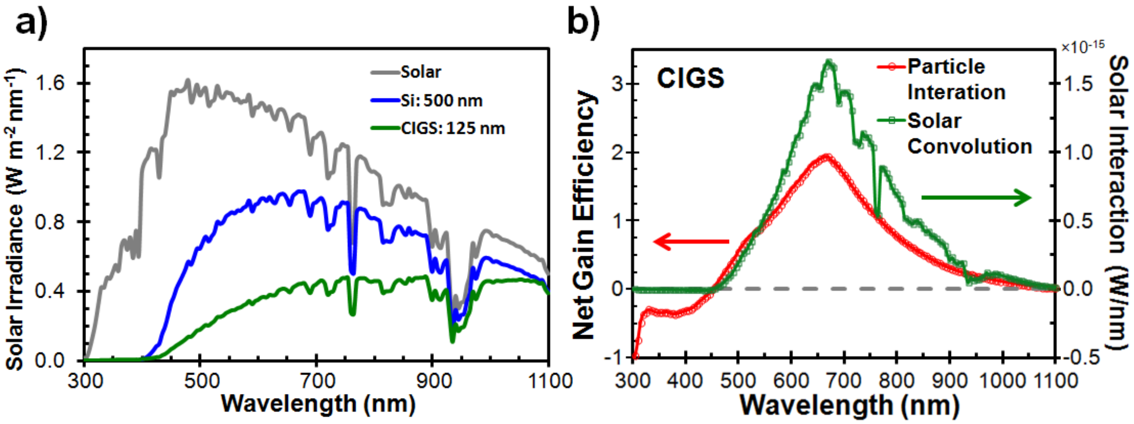

Figure 7.8: Intensity dependence of intensity and particle interaction for a 50 nm silver sphere with a 2 nm silica shell in semiconductors. a) The modified solar spectrum at the particle depth in silicon and CIGS. b) The net potential particle interaction, given as $(Q_{abs} - Q_{abs} - Q_{inc})_{NP}$, and the convolved intensity interacting with a single particle within a CIGS medium at a depth of 125 nm. The convolved intensity is the net potential particle interaction multiplied by the particle area and incident solar intensity at that location.

7.6.8 Embedded Ag@SiO$_2$ Nanoparticles for Enhanced Solar Absorption in Thin Film Photovoltaics

Silver nanoparticles coated with a thin silica shell (Ag@SiO$_2$) are considered for photovoltaic applications. Silver nanoparticles are used for this application because of the cost, strong, blue-shifted plasmonic response and improved scattering to absorption ratio relative to gold spheres. Here we consider silver core nanoparticles coated with a thin silica shell (Ag@SiO$_2$) for enhanced photovoltaic applications. Thus, we consider a 2 nm SiO$_2$ coating on a 25 nm silver core to yield a 54 nm overall particle size.

We consider a silica glass superstrate configuration, with an aluminum back surface. We include the effects of reflection from the air-to-glass and glass-to-silicon interfaces, but neglect the effect of the presence of a thin conducting oxide on the front layer, which is expected to have minor effects because of the small thickness and similarities to glass in optical properties. We similarly neglect the optical effect of a thin cadmium sulfide *p*-type layer for CIGS or CdTe or any differences between *p,* intrinsic, and *n* type layers in the microcrystalline silicon. The total efficiency gain is determined by numerically integrating over the chosen spectra for net gain from scattering and near-field absorption minus the loss mechanisms.

In the simulations, the particles are spaced in a hexagonal close-packed pattern such that the extinction and near-field areas at the plasmon peak will not overlap. Thinner cells yield higher performance gains, but the goal of producing higher overall efficiency cells requires a balance between absorption and plasmonic enhancement. We here make a minimum absorber thickness of 10 times the nanoparticle core radius to minimize the effect of interfaces and to ensure that 'bulk' environment conditions apply.

We analytically determine the contribution of plasmonic nanospheres embedded in absorbing media to total optical absorption. We calculate the overall gain as a function of wavelength in terms of the absorption and conversion to useful electrical energy. Figure 7.9 shows the solar spectrum, calculated optical power absorbed and optical power converted for both plasmon-enhanced and unenhanced μc-Si solar cell. The displacement between the red and blue lines represents the differences induced by the plasmonic nanospheres incorporated into the cell. A pronounced increase in the absorption is observed near the peak of the nanoparticle plasmonic response for the net gain.

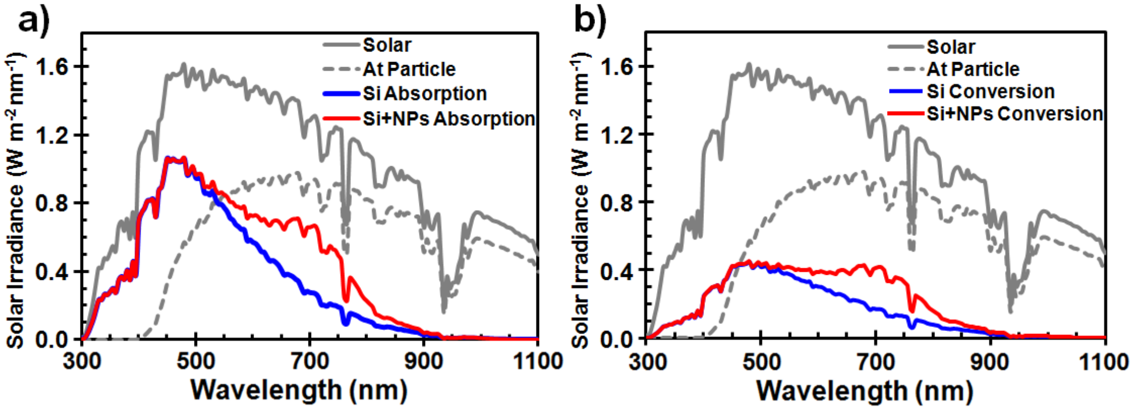

Figure 7.9: Plasmonic enhancement of absorption and conversion using embedded Ag@SiO2 nanoparticles in μc-Si. The enhanced absorption (a) and the enhanced conversion (b) are shown for 50 nm silver spheres with a 2 nm thick silica shell embedded at the center of a 1 μm thick μc-Si semiconductor layer.

We completed a similar analysis for CdTe and CIGS absorber layers. The μc-Si cell in the previous example is 1000 nm thick, but here we consider 250 nm thick CIGS and CdTe absorber layers because of their strong absorption. We also determine the effect of increasing the nanoparticle size for the thicker μc-Si cell. These data are presented in Table 7.1.

The results shown in compiled in Table 7.1 demonstrate some interesting trends. First, we note that significant enhancement is found for μc-Si, while weaker gains are found for CdTe and CIGS thin films. The nanoparticle enhancement effects are observed to be limited by the reduced intensity at the particle in strongly absorbing materials such as CIGS, while the relatively high bandgap energy of CdTe limits the potential of long wavelength plasmonic absorption enhancement in CdTe solar cells.

Table 7.1: Comparison of the predicted enhancements for Ag@SiO$_2$ nanoparticles embedded in various thin film solar absorber materials. The SiO$_2$ shell thickness is 2 nm for all cases.

	μc-Si	**μc-Si**	**CdTe**	**CIGS**
Absorber Thickness (nm)	1000	1000	250	250
Ag Core Diameter (nm)	100	50	50	50
Estimated Absorption Without NP's (W/m^2)	210	210	393	553
Gain from Perpendicular Scattering (W/m^2)	126	77	49	32
Gain From N.F. Absorption (W/m^2)	3	2	22	28
Loss due to Displaced Absorber (W/m^2)	-2	-1	-5	-9
Loss due to Particle Extinction (W/m^2)	-30	-22	-42	-42
Net Gain in Absorption (W/m^2)	94	56	52	10
Estimated Total Absorption (W/m^2)	306	266	445	563
Estimated Total Conversion (W/m^2)	118	97	137	154
Estimated Absorption Gain with NP's	46 %	27 %	6.0 %	1.7 %
Estimated Conversion Gain with NP's	65 %	36 %	7.7 %	2.5 %

The strong plasmonic enhancement for μc-Si could be very useful. Increasing the absorption of μc-Si cell in a tandem geometry, where a amorphous silicon cell is placed on top of and in series with a μc-Si cell, could yield multiplied benefits, because then the amorphous Si cell could be thickened to absorb additional light, based on current matching conditions. Though we observe that the overall enhancement is relatively weak in CdTe or CIGS, plasmonic enhancement could still be attractive. If absorption can be increased with plasmonics, then the absorber thickness can be decreased to capture the same amount of light, which can serve to decrease material demands and fabrication costs while increasing charge separation and collection. Charge collection can be a problem for lower quality deposited materials and thus plasmonics could potentially increase the fill factor, a factor which we do not address in these simulations. In general, we find that the total plasmonic enhancement benefit is strongest when optical absorption is a limiting factor, such as weak absorbers and extremely thin solar cells. We note that the effect is even stronger for thinner cells, although the overall absorption is reduced.

Our simulated results clearly show that nanoparticles can be used to increase absorption, locally and through scattering, for thin film solar materials. We hypothesize here that silica coating on metal nanoparticles can mitigate the effects of charge carrier trapping, provided that crystalline quality can be maintained in the surrounding medium. It remains to be seen whether any additional adverse effects will be seen. Experiments will be used to test these conclusions.

7.7: EXPERIMENTAL EVALUATION FOR NANOPARTICLES EMBEDDED IN THE ACTIVE ABSORBER LAYER

The initial goal of this research will be to observe changes in the spectral response near the plasmonic resonance of the metal nanoparticles, while later efforts will focus on improving the overall efficiency of the cells. We target significant gains (>50%) in the near-resonance region in the red-NIR wavelength range and 20% overall efficiency gains. It will be of significant interest to try to gain the advantages of plasmonic enhancement while mitigating or avoiding any adverse effects due to integrating metal nanoparticles into the solar cell structure.

To meet these goals, we present several benchmarks along the way. First, we show the repeatable deposition of silicon thin films. We next show the embedding of self-assembled sub-monolayers of plasmonic metal nanoparticles in PE-CVD deposited materials. Then, we show the effect of a dielectric shell on the plasmonic resonance of a metal nanoparticle in an absorbing material. These results also show the increased absorbance in the red-NIR on account of scattering by the nanoparticles. Finally, we embed Ag@SiO_2 nanoparticles in silicon sandwiched between two electrodes. By applying a voltage across these terminals, we can finally evaluate the photocurrent response due to increased absorption within the medium.

7.7.1: Thin Film Deposition and Characterization

We use plasma-enhanced chemical vapor deposition (PE-CVD, Oxford Plasmalab 80+) for the deposition of amorphous silicon, silicon dioxide, silicon nitride, and for mixed amorphous-microcrystalline silicon. In PE-CVD, constituent gases are flowed into the deposition chamber at a near-vacuum, and then ignited into a plasma through the deposition of radio-frequency excitation (13.56 MHz). In a typical deposition, 250 nm of silicon was deposited onto a 3 × 3 array of pre-cleaned polished glass or indium tin oxide (ITO) coated slides, where the thickness was confirmed by surface profilometry. Figure 7.10 shows the consistency and optical properties of the deposited thin films through optical absorbance and ellipsometry measurements.

These results show that the deposition is consistent across the deposition window and that the deposited films are primarily amorphous in nature, although some microcrystallinity or void content can be deduced from the somewhat reduced imaginary refractive index component.

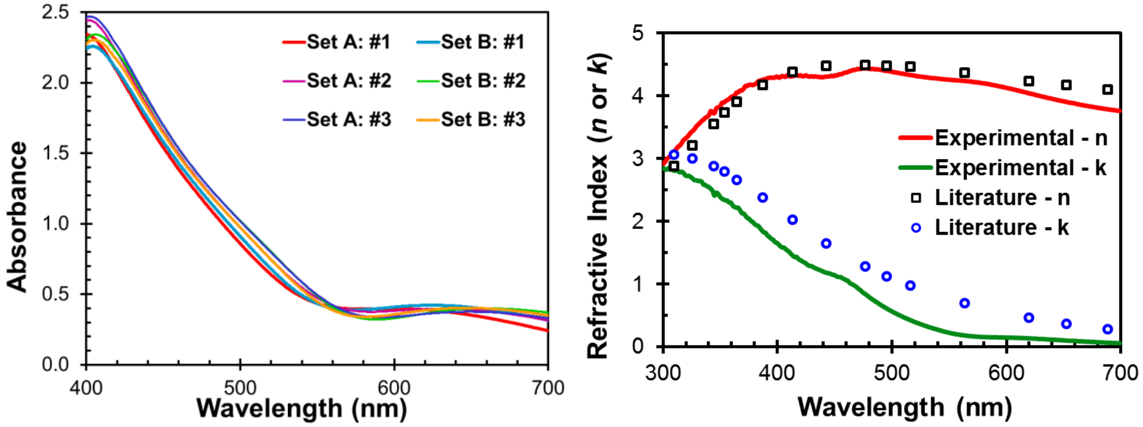

Figure 7.10: Measurements of thin silicon films deposited with PE-CVD. a) Optical absorbance of deposited amorphous silicon thin films showing the intra- and inter-batch film consistency. b) Optical constants of deposited amorphous silicon layers deposited via PECVD. The plot shows the experimentally obtained values from ellipsometry measurements along with reference values for amorphous silicon from [24].

Nearly pure microcrystalline silicon can be deposited using PE-CVD if hydrogen or helium feed gases are available. Alternatively, high pressures, radio frequencies, temperatures or plasma powers can also be used to promote the formation of microcrystalline silicon. Additionally, small amounts of impurity gases such as phosphine (PH_3) or diborane (B_2H_6) can be used to directly create doped layers for the fabrication of complete solar cells. Though these capabilities were unavailable at the facilities we had access to, they are commonly used with PE-CVD systems. Thus, results that we find here should be applicable for full solar cells fabricated with PE-CVD.

7.7.2: Nanoparticles Embedded in Plasma-Deposited Materials

A new method must be applied for the implementation of plasmonic particles for thin-film photovoltaic applications. Electron beam lithography is too expensive and slow for practical use, and it is limited in terms of shapes and morphology that can be farbicated. Furthermore, we have shown that rapid and inexpensive wet-chemistry synthesis methods can provide the controllable shape, size and desired shell configurations necessary for effective use in photovoltaics. Here we apply our designed and fabricated core-shell particles to thin-film semiconductor absorber layers to create well-distributed sub-monolayers using self-assembly.

We create sub-monolayers following the procedure described in the Nanoparticle Synthesis chapter. In short, we immerse freshly-cleaned substrates into a 1% (v/v) ethanolic solution of aminopropyltriethoxysilane (APTES), wash with copious ethanol, dry briefly at 80 °C, then place into a nanoparticle solution. We showed previously that this procedure was leads to extremely homogenously layers across expanses of 1” × 1” using gold and silver nanoparticles.

An open question for the use of plasmonic nanoparticle monolayers is whether they can be integrated into thin-film photovoltaic materials with standard fabrication techniques. We test premise this by sandwiching plasmonic nanoparticle monolayers between thin film dielectric layers fabricated with PE-CVD, which is often used industrially for the deposition of thin silicon films. We examine the absorbance of the plasmonic nanoparticles on the substrate before and after the top layer deposition to check that the nanoparticles remain on the surface, *i.e.* that they are not removed during the plasma deposition step, and to test the expected plasmonic shift for a nanoparticle embedded in a solid material.

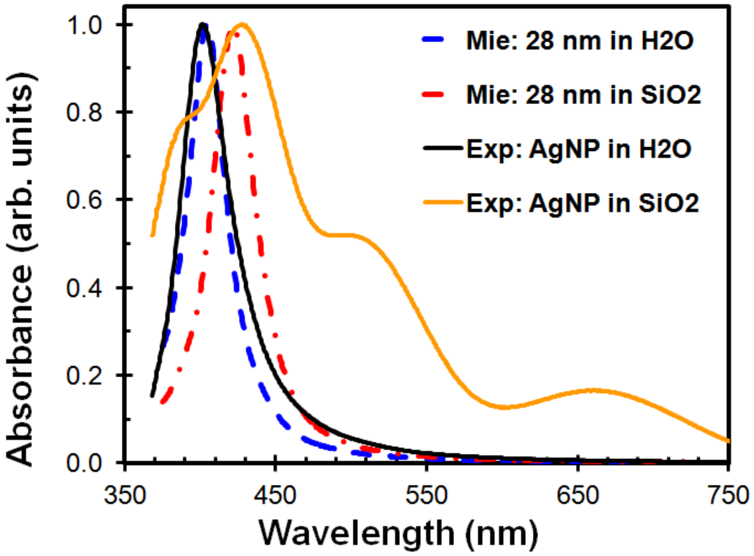

Figure 7.11: Comparison of optical properties of silver nanoparticles in different media using simulations and experimental observations. *The silver nanoparticles are first measured in a colloidal solution. These nanoparticles were then self-assembled on a clean glass slide and a 1 μm SiO_2 layer was deposited on top with PE-CVD.*

The results show the expected trends, where the plasmonic peak red-shifts when the surrounding medium is silica rather than water. The discrepancies observed between simulation and experimental results for nanoparticles embedded in the glass can be explained because of the assumption of the glass slide and plasma-deposited thin film consisted of glassy silica, where in both cases the optical properties differ slightly. The broad peaks at 520 and 670 nm are most probably the result of agglomeration on the surface. The observation of a strong plasmonic peak resulting from nanoparticles monolayers embedded in the glass layer is a very promising proof-of-concept showing the feasibility of our approach.

For effective use in solar applications, we must also be able to control the surface density and spacing of the particles embedded in the absorber material. We initally attempted to control the surface density of particles by varying the substrate immersion time in the nanoparticle solution, but this yielded inconsistent results and reduced the homogeneity of the deposited layer across the substrate surface. Adjusting the concentration of the nanoparticle solution, however, was found to provide the desired level of control. Figure 7.12 shows the spacing of gold nanoparticles on a glass substrate for three different colloidal concentrations.

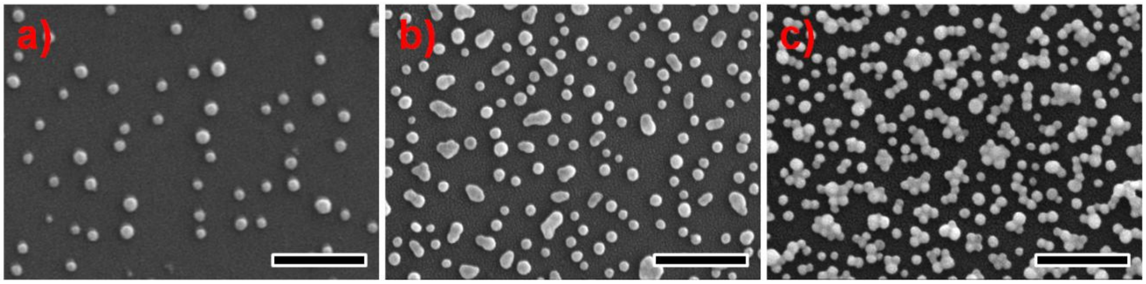

Figure 7.12: The spacing in self-assembled sub-monolayers can be controlled with the concentration of the metal nanoparticle colloid. The concentration is a) 25%, b) 50%, and c) 100% of the initial solution. The scale bar represents 250 nm.

In Figure 7.12, we observe that the spacing increases as the concentration decreases. We also see that the higher concentrations lead to agglomeration of the nanoparticle, which will broaden and red-shift the well-defined plasmonic response of isolated metal nanoparticles. We use a typical dilution ratio of 33% for all further photovoltaic monolayer work to avoid agglomeration and achieve sufficient coverage. We were also able to demonstrate evenly distributed sub-monolayers of Ag@SiO_2 nanoparticles on both glass and silicon substrates. It was necessary to centrifuge and resuspend Ag@SiO_2 in water before the self-assembly step, as no nanoparticles would attach to the surface while the nanoparticles were suspended in the ethanol-water mixture that the shells are grown in, which we attribute to surface charge effects. Formation of

$Ag@SiO_2$ sub-monolayers on a substrate enabled the testing of the conditions identified in the simulation section for the enhancement of absorption in thin silicon films.

7.7.3: Effect of Dielectric Shell on a Plasmonic Particle in an Absorbing Medium

Our simulations showing the dramatic effect of a thin dielectric shell on a metal nanoparticle embedded in an absorbing medium reveal an intriguing, undiscussed effect of great importance for plasmonics in photovoltaic materials. It is of great interest to try to experimentally validate this conclusion. We test this optical behavior by first fabricating a set of different thickness silica shells on a single set of silver nanoparticle cores by varying the concentration of TEOS for a defined nanoparticle concentration. The peak shift of these different shells can be used to determine their thickness. The silver nanoparticles used in this study have a diameter of 60 ± 7 nm. These core-shell nanoparticles are organized into sub-monolayers embedded within 800 nm thin film of silicon on polished glass substrates. For this test, to more closely approximate simulations, we use increased plasma power and pressure in the PE-CVD fabrication stage to obtain thin films with a higher degree of microcrystallinity. These substrates, along with control samples that were fabricated without any integrated nanoparticles, were then tested with UV-Vis-NIR spectrometry to determine the wavelength-dependent absorbance of the $Ag@SiO_2$-Si composites.

There is a slight variation in the thickness of the thin films deposited with the PE-CVD, leading to some thin film interference effects even in the first deposited layer before the nanoparticles are deposited. At least six samples were measured for each silica shell thickness, plus seven control samples in total. We also observe sharply increasing absorption of light below a wavelength of ~600 nm. Thus, we consider the integrated absorbance over the range of 600 – 1000 nm as a measure of the effectiveness of plasmonic enhancement. The optical properties of Ag@SiO$_2$ nanoparticles with various shell thicknesses can improve absorption when embedded in silicon thin films. The initial nanoparticle core had a diameter of 36 nm and a plasmonic peak width of 64 nm (FWHM). The results of these studies are presented in Figure 7.13.

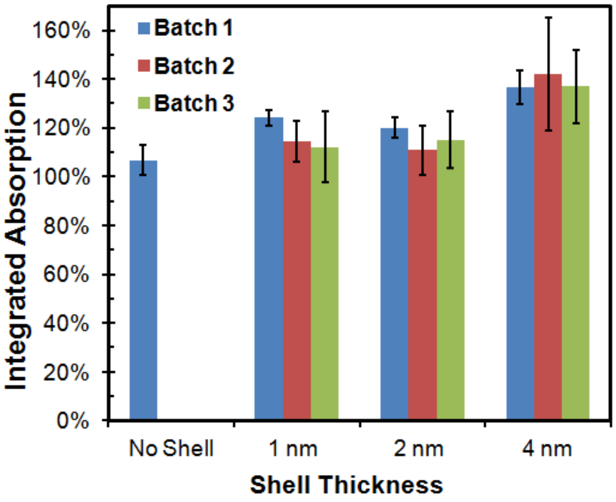

Figure 7.13: Absorption enhancement for silicon thin films on account of plasmonic Ag@SiO$_2$ nanoparticles. *The averaged gains over all batches are 7±6%, 17 ±8%, 15±6%, and 39±11% for the no shell, 1, 2 and 4 nm cases, respectively.*

Figure 7.13 demonstrates the importance of the thickness of the silica shell on the absorption of the structure. We found that all of the test samples resulted in a higher absorbance than the control, and that the measured absorbance was highly dependent on the shell thickness. The strongest enhancement is observed for the ~4 nm thick shell. This was unexpected, but upon further study with electron microscopy, we found that thinner shells did not result in complete shell coverage. We noticed some variation between the samples tested for each Ag@SiO$_2$ shell thickness, indicating that some improvement in the consistency should be possible. We also observed that there was some broadening in the peak during the centrifugation procedure, so this process could be optimized. However, these results are very promising in terms of directly showing strongly increased absorption by plasmonic nanoparticles embedded in a semiconductor.

7.7.4: Increased Absorbance in Plasmonic Thin Semiconductor Composites

There are two possible effects that could lead to the observed enhanced absorption effect. First, the primary enhancement mechanism could be plasmonic scattering and near-field absorption, as we have predicted through simulations. However, another beneficial mechanism that could also be occurring is the surface roughening. We believe this is a minor effect, especially in the long wavelength region where we see increased absorbance, as all four particle types tested were very similar in overall size. The mechanism could be further tested by replacing the plasmonic nanoparticles with a dielectric pure scatterer, which serves primarily as a source of surface roughness. We have been able to demonstrate monolayer fabrication of our synthesized silica nanoparticles on glass surfaces, but an optimization of the nanoparticle size and surface density would need to be performed to match conditions between the two tests. Furthermore, complete monolayers of SiO_2 nanoparticles form relatively easily, which could result in misleading data. Silica nanoparticles will primarily scatter in the forward direction, however, and our calculations show a reduced effect for silica nanoparticles relative to the plasmonic particles, so we believe our current hypothesis to be correct regarding the mechanism of absorption enhancement. Furthermore, our results from the previous section show that though surface roughness may play a role in enhancement, plasmonic enhancement will most likely have a stronger effect. We make this conclusion because all of the tested particles had similar outer diameters and we expect that the surface roughness to be similar for these cases. Thus, plasmonic enhancement of absorption is demonstrated with Ag@SiO$_2$ nanoparticles embedded in thin-film silicon.

7.7.5: Plasmon-Enhanced Thin Film Photodetector

We also fabricated thin film silicon photoconductive optical detectors as a final verification of the use of embedded plasmonic nanoparticles for the enhancement of red-NIR absorption within the semiconductor. The previous results proved that the absorbance increases for the semiconductor and metal nanoparticle composite relative to a semiconductor layer alone, but it could be ambiguous whether this light is absorbed by the nanoparticles or the medium. We can use simulations to predict the magnitude of absorption by the particle and we have shown that scattering should be a much stronger effect in semiconductor materials, so we have reason to believe that enhanced absorption occurs in the silicon. It is worthwhile, however, to investigate a more direct measure of the absorption by the material. Thus, we embed Ag@SiO$_2$ nanoparticles in a silicon matrix surrounded by two electrodes.

To fabricate these devices, we start with indium tin oxide (ITO) coated polished glass superstrates. These provide both an electrode and an optically transparent window for coupling in incident light. We then mask the edges to avoid delamination of the silicon layer and also to provide surface area for the front contact. Subsequently, we deposit a thin silicon top layer (400 nm) using PE-CVD. This is used as the substrate for self-assembly of a sub-monolayer of Ag@SiO$_2$ particles following the previously described procedures. Then, another layer of silicon is deposited, sandwiching the nanoparticles in the silicon. Finally, a thin film silver back electrode is fabricated with thermal deposition. A set of four completed devices are shown in Figure 7.14. Clear differences in the optical response are immediately apparent for the substrates with embedded plasmonic particles. In this case, the substrates are viewed from the backside, and the bright white reflection indicates higher surface roughness for the silver contact on account of the successfully integrated plasmonic nanoshell structures (bottom left and top right).

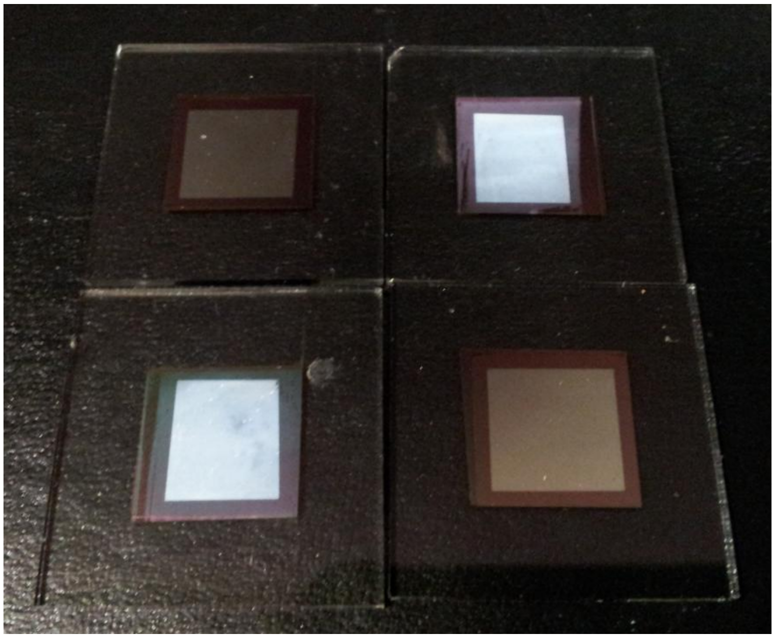

Figure 7.14: Photograph of plasmon-enhanced photodetectors fabricated on ITO-coated glass slides. All four substrates are coated with a silver top electrode. The top left and bottom right substrates are controls (no nanoparticles), while the bottom left and top right semiconductor layers have Ag@SiO$_2$ nanoparticles embedded in the Si layer.

Before the back electrode was deposited, we performed UV-Vis-NIR on each of the cells. Two sets of samples were prepared, with control and test samples in each set. In the first case, the control is kept pristine, while in the second set, it is coated with an APTES monolayer, but no nanoparticles, to test absorption. We find that the two control samples had similar integrated absorbances, even including the thin APTES layer. The two plasmon-enhanced cells, however, each had significant improvement in the absorption in the 600-1200 long wavelength region (38% and 45%).

These devices were tested by applying a voltage across the electrodes to provide a mechanism for separating photogenerated electron-hole pairs. Alternatively, the resistance was measured as a function of incident optical power for a white light source. Initial results indicate an improved photoconductive response that shows the presence of a plasmonic effect in this case, and not simply the surface roughness, resulting in increased absorption by the semiconductor. Our proof-of-concept experiments demonstrate plasmonic enhancement using a Ag@SiO_2 nanoparticle system driven by the use of simulations to predict successful configurations. This promising approach has identified an attractive possibility for use in full solar cell configurations.

7.8: CONCLUSIONS

In this chapter, we evaluate plasmonic nanoparticles for the enhancement of absorption in thin film solar cells. We first review the literature and identify some of the limitations of earlier approaches and indicate the challenges of successful plasmonic integration. Investigations of nanoparticles embedded in the glass layer of a thin film solar cell showed that this top layer configuration is not a viable candidate for plasmonic enhancement. Our second approach, with nanoparticles supported on the back contact of a CIGS solar cell, was inconclusive. However, we found strong simulated gains for nanoparticles embedded in a μc-Si absorber layer, in the range of 20 – 70% depending on the material thickness. These calculations showed that the primary contribution is through scattering for plasmonic particles in a weak absorber, but that near-field absorption is stronger source of enhancement in strong absorbing materials. For this application, we originate the idea of dielectric shells on plasmonic particles to insulate the nanoparticle and to allow for more efficient plasmonic scattering for a given particle size within a semiconductor absorber layer. We also develop the use of self-assembled sub-monolayers of plasmonic nanoparticles embedded within two semiconductor layers for solar applications. Finally, we demonstrate the promise of this approach through proof-of-concept experiments showing the increased absorption through scattering and improved photocurrent generation from plasmonic-enhanced thin film silicon photodiodes.

Chapter 8: Conclusion and Future Directions

In this dissertation, we have shown a range of work on the applications of near- and far-field properties of plasmonic metal nanoparticles. These efforts have centered on proof-of-concept studies. Over the course of this work, several additional avenues opened up that were beyond the scope of the project that we were unable to pursue. Some of these vistas could lead to rich areas that enable deeper physical understanding into plasmonic mechanisms or improved use of plasmonics for practical purposes. Here we identify these promising areas and highlight some potential approaches for each of the subjects we have dealt with in this dissertation. Finally, we conclude with a set of findings that we have arrived at through these studies.

8.1: FUTURE DIRECTIONS IN THE SIMULATION OF PLASMONIC PROPERTIES

Several possibilities exist for the future development of the work presented here to advance the field of computational electrodynamics for plasmonic nanoparticle studies. One promising area is the calculation of polydispersity in a real nanoparticle solution by assuming a Gaussian distribution in the particle size and determining the standard deviation in the particle size required to reproduce the peak shape. This is an example of the calculation-intensive inverse scattering problem, but computational powers of desktop computers are currently sufficient to accomplish this goal using analytic solutions (*ie.* spheres) and this could also be feasible for DDA solutions of non-spherical particles in the near future. The discrete dipole approximation method could be extended in several ways for future studies that we here accomplished using extended analytical solutions for spheres. For example, it seems possible that DDA could be extended to allow for the simulation of particles in absorbing media, which is not possible on any of the currently available DDA code packages. We also found that the filtered coupled dipole (FCD) method provided worse results for near-field calculations when using the standard Green's function based dipole interaction terms to calculate the electric and magnetic fields from the converged dipole polarizations. A new derivation of the induced fields could be derived to achieve more accurate values. This would be of great benefit to the computational plasmonics community, as FCD provides hugely reduced simulation times and could provide significantly improved accuracy for noble metals in the near-infrared. Finally, we also remain exceedingly interested in the possibility of plasmonics in non-traditional materials, environments, and wavelength ranges. We believe that there is a great deal of promise in investigating these areas in greater detail.

8.2: FUTURE DIRECTIONS IN PLASMONIC NEAR-FIELD ABLATION

There are also some attractive possibilities for future study of plasmonic near-field ablation using ultrafast lasers. We have found that water, vacuum, and other embedding media can have a large effect on plasmonic response and the ablation of materials. It could be of great interest to control for the effect of the medium to further study the energy transfer process that occurs in plasmon-enhanced ultrafast laser nanoablation. For example, the pressure of the environment could have an effect on the expansion of the laser-induced plasma, which could provide a finer degree of control for plasmonic near-field ablation. Plasmonic nanoablation can provide the localization to extremely small scales, and the limit has not been yet reached. It would be interesting to probe the potential of plasmonics for the creation of features on the single nanometer scale. Another possibility is the use of optical trapping of plasmonic nanoparticles for localized nanoablation. We briefly studied this possibility and remain interested in its potential development. With plasmonics, the placement of the particle is a key factor in the ablation process, and optically controlled positioning could be an attractive feature.

Throughout this dissertation, we have performed our experiments considering the possible extension of plasmonic nanoablation of biological tissues, a subject previously studied in the Ben-Yakar group. This area has enormous promise, and remains an area of active study. The time domain simulation of optical breakdown with plasmonic enhancement and the potential role of the ejection of electrons as mechanism of breakdown could yield a better understanding of the use of plasmonics for ultrafast laser imaging and nanosurgery applications. On-the-fly optical trapping could also be used in biological tissues for enhanced imaging and treatment using asymmetric metal nanoparticles. Ultrafast laser nanoablation is both an attractive means of characterizing the plasmonic response as well as a promising method for creating nanoscale damage in targeted locations.

8.3: FUTURE DIRECTIONS IN NANOPARTICLE SYNTHESIS

The field of nanoparticle synthesis has made great strides in recent years, but there remains great promise for intelligently designing and synthesizing novel metal nanoparticle structures for specific applications. We have specifically identified several potential directions for future research in nanoparticle synthesis. First, additional studies into the optimization of silica coating on silver nanorods should be further investigated. This effect could be addressed by coating the particles with a dielectric shell, which has recently been demonstrated for gold nanorods [226].

Initial results, shown in Figure 5.8, demonstrate the feasibility of this idea, but care must be taken in two directions. First, the strong binding of CTAB on the surface must be overcome, presumably through polyethylene glycol (PEG) replacement followed by a modified Stöber process to grow the silica shell. However, we often observed a small fraction of silver nanorod formation even for citrate-mediated syntheses, indicating that it is possible to create silver nanorods in the absence of CTAB. These efforts could lead to a nanoparticle with a very strong NIR resonance that are thermally stable, biocompatible, luminescent and highly scattering.

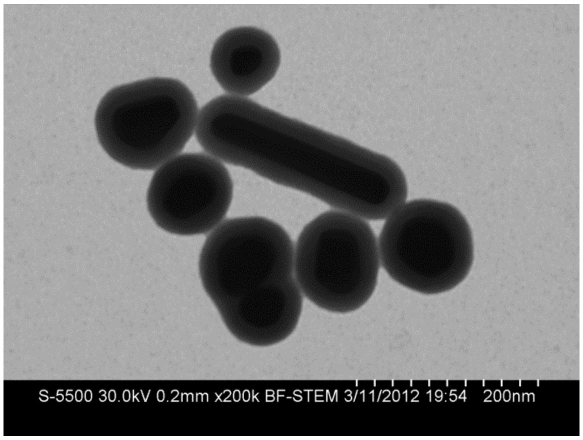

Figure 8.1: Evidence of homogenous silica coating on rod-shaped silver particles from an early synthesis attempt.

Aluminum nanoparticles could be extremely interesting for plasmonic solar applications. In addition, several simulation groups have identified electron-beam lithography fabricated cylindrical aluminum disc structures as strong contenders for plasmonic solar enhancement. Although several research studies have identified aluminum nanostructures as attractive in this application using simulations or e-beam lithography, no research on the colloidal synthesis of aluminum nanoparticles has yet been presented. Aluminum nanoparticles are attractive for several reasons. First, the strong plasmonic response with relatively high scattering to absorption could lead to gains with limited parasitic losses. Second, the resonance is blue-shifted from silver into the ultraviolet. This can be useful, because then nanoparticles embedded in high-index absorbed materials can be have their plasmonic peak shifted into visible regions of high solar irradiance. Finally, aluminum nanoparticles could have a native oxide 'shell' on the surface, which could reduce adverse metal charge-trapping effects. Another interesting possibility is the potential for using soft templates to grow non-spherical aluminum nanoparticles is very interesting. Similar chemical reactions and reagents can be used to synthesize various metals in anisotropic shapes, including gold, silver and copper. Aluminum also exhibits a face-centered cubic crystal structure, and it may be possible to grow anisotropic shapes using similar wet-chemical approaches. Developing triangular aluminum nanoprisms, discs and nanorods could be attractive because the strong resonance of aluminum could be shifted into visible wavelengths in aqueous media, and possibly towards near-infrared wavelengths when embedded in absorbing materials.

Additionally, the synthesis of alloy nanoparticles for plasmonic tuning represents an intriguing possibility. Very little work has been done in this area for plasmonic purposes, but alloy nanoparticle synthesis for catalyst fabrication has investigated this area in detail.

Another interesting approach for solar applications would be the possibility of synthesizing titania (TiO_2) shells on metal nanostructures. Titania has long been used as an electrode material for dye-sensitized solar cells, and has recently been identified as a potential candidate for an intermediate band element for solar cells. Titania has a large refractive index, which leads to a higher scattering intensity and scattering fraction when coated on metal nanoparticles. Several published studies have described procedures for synthesizing titania shells, notably using titanium isopropoxide as a precursor. More effort is needed, however, to obtain smooth homogenous shell structures. Silicon nitride would also be a very interesting coating material that is as yet unexplored.

Finally, microwave synthesis has recently been shown to be a viable method for creating nanosized particles with non-equilibrium, metastable phase materials that would normally require long reaction times, high temperature furnace treatments. Metals are known to strongly absorb microwaves, potentially leading to favorable local growth conditions while avoiding any particulate formation in the solvent. It may be of interest to investigate microwave synthesis techniques for growing various kinds of shells on metallic nanoparticles.

One other recent development in plasmonic particles on a substrate has been the growth of asymmetric particles directly on a substrate of interest. This technique has been demonstrated for spheres and silver nanorods. This could vastly decrease the effort involved with synthesis and SAM fabrication, and could prove to be significantly more cost-effective or industrially-friendly than the currently described methods.

Although nanoparticle synthesis has been explored for more than a century, it remains a rich scientific area with a great deal of potential. We believe that further efforts in characterizing, simulating and designing new particle shapes, sizes, and materials will continue to provide improved performance in applied plasmonics.

8.4: FUTURE DIRECTIONS IN SOLAR PLASMONIC EFFORTS

A final goal of this research would be evaluating full plasmonic-enhanced solar cells. We were able to show enhanced photocurrent generation in a plasmonic thin film photodetector, proving the concept, but the enhancement of a thin-film silicon solar cell would further demonstrate the potential of our proposed method. We did not have the facilities available to readily accomplish this goal, but several alternate approaches could potentially be used to create *p* and *n* doped regions in deposited thin film silicon layers, such as thermal thin film deposition of doped silicon using e-beam heating or rapid thermal annealing of a spin-coated boron or phosphorous compound on a silicon layer. If any of these efforts were successful, then the even more dramatic improvement of a micromorph silicon solar cell could also be attempted.

Another area of interest is the investigation of scale-up and the integration of plasmonics into semiconductor materials on the industrial scale. Silica-coated nanoparticles are resistant to high temperatures, so it could be possible to even use them in processes with sintering steps. We considered this during our fabrication development, and our dip processing method for nanoparticle self-assembly seems like it could be favorably scaled up for mass production, but more research is necessary.

We also note that further optimization of nanoparticle size, shape, and material could be used to obtain plasmonic absorption enhancement gains beyond the levels indicated here. Non-spherical particles, which are typically characterized by stronger plasmonic resonances and near-field enhancements, could lead to additional improvements, especially if coated with high-index dielectric coatings. Additionally, multiple particles could be tuned to enhance separate portions of the solar spectrum, acting as a spatial wavelength filter. In this case, narrow size distribution nanoparticles are crucial to space the nanoparticles as close as possible without spectral overlap. The ability of a particle to scatter light in the horizontal direction may also prove interesting when coupled with quantum dot solar cells, which can preferentially absorb light propagating in specific directions. Particle shaping efforts will need to be evaluated to ensure that loss mechanisms do not arise upon integration in thin film solar cells.

8.5: CONCLUDING REMARKS

In this dissertation, we have investigated plasmonic enhancement using simulations and targeted experiments to determine the mechanisms, magnitude and potential of plasmonic nanoparticles for advanced applications. We studied and compared both near-field and far-field effects, with a focus on determining the spatial extent of plasmonic effects. In our characterization of physical plasmonic nanoparticle samples, we found that simulations could only be used to accurately predict the optical response of nanoparticles if the true shapes and size distributions are simulated. Idealized nanoparticle shapes, which are commonly used for simulations, do not provide a result that can be usefully compared with experimental observations. We use our far-field optical interaction calculations with heat transfer models to determine experimental limits for plasmon-enhanced multiphoton imaging with asymmetric gold nanoparticles. We find maximum optical power before nanoparticle melting can be found for a single pulse, implying that long term imaging can be accomplished without signal degradation. We also directly demonstrate the near-field nanoablation of silicon substrates using plasmonic enhancement from gold nanorods. These experiments were used to identify the near-field enhancement and mechanism of plasmon-assisted ablation. The experimentally observed shape of the ablation region and reduction of the ablation threshold are compared with simulations to show the importance of the enhanced electromagnetic fields in near-field nanoablation with plasmonic nanoparticles. Specifically, we find that the Poynting vector magnitude crossing the surface is a better predictor of the effective plasmonic enhancement than the more commonly used squared electric field. This implies that the deposition of energy is an important parameter in near-field nanoablation.

Applications of plasmonic nanoparticles often benefit from narrow size distribution colloids because the plasmonic effect is dictated by the number of particles enhanced at a specific wavelength. Wide size distributions result in a blurring and weakening of the optical response. Here, we presented a new synthesis method for the seeded-growth of nearly monodisperse metal nanoparticles ranging from 10 to 100 nm in diameter, both with and without dielectric shells of controlled thickness. Our nanoparticle samples have significantly smaller peak widths than previously reported samples. Here we report nanoparticle peak widths as small as 34 nm, as opposed to typical values at ~70 nm FWHM peak widths. This represents a significant improvement in monodispersity. Our seeded growth method is used to acquire fine control over the position and width of the plasmonic peak response. We also demonstrated self-assembled sub-monolayers of these particles with controllable concentrations for use in surface and layered geometries. Our developed techniques can be used with a 'design, synthesize, and test' approach to plasmonic enhancement in various applications

We developed a new method for determining the spatial distribution of absorption around plasmonic nanoparticles, including distinguishing near-field and far-field regions. We find the point-by-point enhanced absorption in a medium around a plasmonic nanoparticle. We demonstrate the utility of these equations in the study of plasmon-enhanced optical absorption for thin-film photovoltaic cells. We find that the redirection of light within a thin film is the dominant mechanisms for enhancement for weak absorbers, but that direct near-field enhanced absorption an important mechanism for strong absorbers. Plasmonic nanoparticle systems are identified using simulations and then we synthesize and test these systems using proof-of-concept experiments to demonstrate the potential of this approach. We show an improvement of the absorbance within plasmonic nanoparticle sandwiched in semiconductor thin films. This is shown to result from increased absorption by the semiconductor material through photocurrent measurements, showing that plasmonics can be designed to enhance absorption in the long wavelength region for thin-film photovoltaic applications.

Appendices

A1: SILVER NANOSPHERE SYNTHESIS

Protocol

1. **Thoroughly clean glassware to remove all surfactants, oils, and organic materials.**
    a. Wash all beakers and stir bars with copious amounts of soap and water.
    b. Dry beakers and stir bars at ~105 °C. Mix a fresh batch of *aqua regia*, which is a 3:1 mixture of pure hydrochloric acid to pure nitric acid. **CAUTION! Aqua regia is extremely corrosive and should be treated with great care. Store aqua regia waste in a separate waste container that can vent to atmosphere.*
    c. Fill a 100 mL beaker with the *aqua regia* and use a magnetic stir bar to stir for 15 minutes. The *aqua regia* will change color to a yellow to a deep orange-red.
    d. Triple rinse the beaker with distilled water.
    e. Triple rinse the beaker with ultrapure water.
    f. Dry beakers and stir bars at ~105 °C, then allow to cool to room temperature.

2. **Synthesize silver nanoseeds using sodium borohydride as a reducing agent.**
    a. Add 47 mL of ultrapure water to a freshly cleaned beaker.
    b. Add 0.5 mL of 100 mM $AgNO_3$ in ultrapure water to the beaker.
    c. Begin stirring solution in beaker.
    d. Cool 40 mL of ultrapure water in a glass vial (A) for 15 minutes on ice (not an ice pack).
    e. Place half of the ice-cold ultrapure water in another capped glass vial (B).
    f. Weigh out 76 mg of $NaBH_4$ into a plastic weighing dish.
    g. Rapidly add the $NaBH_4$ to the water in (B).
    h. Rapidly rinse the weighing dish with the remaining ice-cold water from (A), and add to the capped glass vial (B) to ensure all traces of $NaBH_4$ powder is in solution (B).
    i. Seal vial (B) and shake until all powder is dissolved (a few seconds).
    j. Rapidly add 2 mL of $NaBH_4$ solution to $AgNO_3$ solution under stirring. Nanoparticles will form immediately, evidenced by a rapid color change from clear to yellow.
    k. Stir solution at moderate speed for overnight.

l. Place all of the solution in a centrifuge tube and age for three days before use.
m. Measure on a spectrometer. A good synthesis results in a strong plasmonic peak at ~395 nm with a full width half max of ~35 nm.

3. **Seeded growth of silver nanoparticles over a range of sizes**
    a. Add 110 mL of ultrapure water to a freshly cleaned 250 mL glass beaker.
    b. Add 5 mL of freshly prepared 100 mM Na Citrate in ultrapure water solution.
    c. Add 35 mL of previously prepared silver seeds
    d. Heat under stirring to precisely 90 ºC, approaching from below, and continue to monitor the temperature throughout the synthesis. Maintain 90 ºC. Do not allow to boil or even exceed 95 ºC. Cover with foil.
    e. Heat up a 500 mL glass water container full of ultrapure water up to 90 ºC.
    f. Add 100 µL of 100 mM $AgNO_3$ solution to the 250 mL beaker.
    g. Maintain at 90 ºC for 20 minutes
    h. Repeat the $AgNO_3$ addition and waiting 2 more times.
    i. Remove 50 mL of solution (AgNP sample #1) and quench the reaction on ice immediately. Keep in ice cold water for at least 15 minutes.
    j. Add 50 mL of pre-heated ultrapure water to the nanoparticle solution.
    k. Add 2 mL of 100 mM Na Citrate solution.
    l. Repeat addition and maintenance 3×. Remove next nanoparticle batch (AgNP #2). Add water and sodium citrate solution.
    m. Repeat this process as many times as necessary to reach the desired size. The color and opacity should shift as the steps increase.
    n. Age for at least 3 days, then measure on the spectrometer.

A2: SYNTHESIS OF GOLD NANORODS

<u>Step 1: Setup</u>

1. Clean all glassware and stir bars thoroughly, first with soap and water, then *aqua regia* (3:1 HCl to HNO_3), rinse three times with distilled water and finally rinse three times with ultrapure water (R > 18 MΩ/cm).

2. Mix a 12.5 mM [Au] solution using a chloroauric acid solution ($HAuCl_4 \times 3H_2O$) mixed with ultrapure water (18 MΩ).

3. Mix a 50 mM [Ag] solution using $AgNO_3$ and ultrapure water.

4. Mix an 80 mM solution of cetyl-trimethyl-ammonum bromide (CTAB) in ultrapure water. CTAB is also known as hexadecyltrimethylammonium bromide or centrimonium bromide. Depending on the CTAB, this may require ~1 hour of vigorous stirring and mild heating (~40ºC) to obtain full dissolution of the CTAB powder.

5. Mix ultrapure water with the CTAB and gold solutions to end up with a final solution with an 80-100 mM CTAB concentration and a 0.5 mM gold concentration. This will be called the ‘growth’ solution.

Step 2: Gold Seed Synthesis

1. Make a 50 mM sodium borohydride ($NaBH_4$) solution with ultrapure water. Cool the water in an ice bath before adding the boric acid. Keep this solution on ice until use. This solution evolves hydrogen, so this should be used within 30 minutes of mixing.

2. Begin stirring 10 mL of the growth solution in a small beaker at moderate speed. The solution should have a clear yellow coloration.
   a. Add 24 mL of 100 mM CTAB solution. Mix CTAB solution at slightly elevated temperatures (~40°C) with stirring to dissolve CTAB until completely transparent without any suspended particulates.
   b. Add 1 ml of 12.5 mM [Au] solution

3. Add 200 μL of 50 mM $NaBH_4$ to the growth solution. The solution should change color immediately upon addition of the borohydride solution (yellow to brown). A slow color change to pale pink/brown may be observed after 30 minutes.
   a. Add 1 mL of fresh, ice-cold 48 mM Sodium Borohydride (NaBH4) solution while stirring moderately

4. Set aside seeds to age for two hours. This allows for the evolution of hydrogen from the solution and reduces the probability of new seed reduction in the growth solution due to remaining borohydride ions in solution.
   a. Allow to stir for 10 minutes
   b. Age for at least two hours before use.

5. Resulting seeds are spherical and 3 - 5 nm in diameter.
   a. Prepared nanosphere seeds are 3 – 5 nm in diameter, well-dispersed, with an extinction peak at TEST nm.

Step 3: Gold Nanorod Growth

1. Make a 10 mM ascorbic acid (AA) solution with ultrapure water (18 MΩ). This solution should be made right before nanorod growth, but it is not as time-sensitive as the borohydride solution.

2. Begin stirring 50 mL of the Au/CTAB solution in a small beaker. The solution should have a clear yellow coloration.

3. Add 300 µL of the AA solution to the beaker under stirring.

4. Add 300 µL of the $AgNO_3$ solution to the beaker under stirring.

5. Finally, add 50 µL of the previously prepared gold seed to the beaker under stirring.

6. A gradual color change to blue, purple or pink will be observed over about 1 hour. Gold nanorods will be present in this solution.

A3: SELF-ASSEMBLED MONOLAYERS OF METAL NANOPARTICLES ON A SUBSTRATE

Protocol

1. **Thoroughly clean substrates to remove all dust, oils, and organic material.**
   a. Immerse substrates in a 3:1 mixture of sulfuric acid to hydrogen peroxide (Piranha solution). **CAUTION!: Piranha solution is extremely reactive and should be treated with great care. DO NOT MIX ORGANIC SOLVENTS WITH PIRANHA SOLUTION!*
   b. Wash substrates individually with copious ultrapure water and blow dry. Though time consuming, washing substrates individually is crucial for obtaining consistent results by reducing residual contamination.
   c. Wash substrates individually with ethanol and blow dry.

2. **Functionalize substrate surface with charged monolayer**.
   a. Mix a solution of 1 wt. % APTES in ethanol in a disposable plastic petri dish.
   b. Immerse substrate in APTES solution for ~12 hours.

   c. Remove substrate from solution and wash with copious ethanol and blow dry.
   d. Heat substrates for 1 minute at 100 °C.

3. **Attach nanoparticles to the substrate surface.**
   a. Immerse functionalized substrates in a nanoparticle solution bath**.**
   b. Leave samples in the bath for ~6 hours.
   c. Remove samples from nanoparticle solution and immediately wash with ultrapure water.
   d. Gently blow dry colored substrates with clean dry air.

References

1 I. Freestone, N. Meeks, M. Sax and C. Higgitt. The Lycurgus Cup - A Roman Nanotechnology. *Gold Bulletin*, 40 (2007).

2 Yguerabide, J. Yguerabide and E.E. Light-Scattering Submicroscopic Particles as Highly Fluorescent Analogs and Their Use as Tracer Labels in Clinical and Biological Applications. *Analytical Biochemistry*, 262 (1998).

3 P.K. JAIN, K.S. LEE, I.H. EL-SAYED, AND M.A. EL-SAYED. Calculated Absorption and Scattering Properties of Gold Nanoparticles of Different Size, Shape, and Composition: Applications in Biological Imaging and Biomedicine. *Journal of Physical Chemistry B*, 110 (2006).

4 V. Sharma, K. Park and M. Srinivasarao. Colloidal dispersion of gold nanorods: Historical background, optical properties, seed-mediated synthesis, shape separation and self-assembly. *Materials Science and Engineering R*, 65 (2009).

5 C.J. Murphy, A.M. Gole, S.E. Hunyadi and C.J. Orendorff. One-Dimensional Colloidal Gold and Silver Nanostructures. *Inorganic Chemistry*, 45 (2006).

6 Mie, G. Beiträge zur Optik trüber Medien, speziell kolloidaler Metallosungen. *Annalen der Physik*, 25 (1908). The title translates to 'Contributions to the optics of cloudy media, especially colloidal metal solutions'.

7 Huffman, C.F. Bohren and D.R. *Absorption and Scattering of Light by Small Particles*. Wiley-VCH, Weinheim, Germany, 2004.

8 Chumanov, D.D. Evanoff Jr. and G. Synthesis and Optical Properties of Silver Nanoparticles and Arrays. *ChemPhysChem*, 6, 10.1002/cphc.200500113 (2005), 1221-1231.

9 H. Kuwata, H. Tamaru, K. Esumi, and K. Miyano. Resonant light scattering from metal nanoparticles: Practical analysis beyond Rayleigh approximation. *Applied Physics Letters*, 83 (2003).

10 Barnes, W.A. Murray and W.L. Plasmonic Materials. *Advanced Materials*, 19 (2007).

11 S. Tokonami, Y. Yamamoto, H. Shiigi and T. Nagaoka. Synthesis and bioanalytical applications of specific-shaped metallic nanostructures: A review. *Analytica Chimica Acta*, 718 (2011).

12 http://www.scattport.org/index.php/programs-menu. Accessed 4/1/2012.

13 Vlieger, P.A. Bobbert and J. Light scattering by a sphere on a substrate. *Physica A*, 137 (1986).

14 Kerker, A.L. Aden and M. Scattering of Electromagnetic Waves from Two Concentric Spheres. *Journal of Applied Physics*, 22 (1951), 1242-1246.

15 M.I. Mishchenko, L.D. Travis, and D.W. Mackowski. T-matrix computations of light

scattering by nonspherical particles: A review. *Journal of Quantitative Spectroscopy and Radiative Transfer*, 55, dx.doi.org/10.1016/0022-4073(96)00002-7 (1996), 535-575.

16 M.H. Chowdhury, S.K. Gray, J. Pond, C.D. Geddes, K. Aslan, and J.R. Lakowicz. Computational study of fluorescence scattering by silver nanoparticles. *M. H. Chowdhury, S. K. Gray, J. Pond, C. D. Geddes, K. Aslan, and J. R. Lakowicz, "ComputJournal of the Optical Society of America B*, 24 (2007), 2259-2267.

17 Sellmeier, W. Zur Erklärung der abnormen Farbenfolge im Spectrum einiger Substanzen. *Annalen der Physik und Chemie*, 219 (1871), 272-282.

18 Masumura, M. Daimon and A. Measurement of the refractive index of distilled water from the near-infrared region to the ultraviolet region. *Applied Optics*, 46 (2007), 3811-3820.

19 Brixner, B. Refractive-Index Interpolation for Fused Silica. *Journal of the Optical Society of America*, 57 (1967), 674-676.

20 A.H. Harvey, J.S. Gallagher, and J.M.H.L. Sengers. Revised Formulation for the Refractive Index of Water and Steam as a Function of Wavelength, Temperature and Density. *Journal of Physical Chemistry Reference Data*, 27 (1998), 761-774.

21 C.M. Herzinger, B. Johs, W.A. McGahan, J.A. Woollam, and W. Paulson. Ellipsometric determination of optical constants for silicon and thermally grown silicon dioxide via a multi-sample, multi-wavelength, multi-angle investigation. *Journal of Applied Physics*, 83 (1998), 3323-3336.

22 P.G. Etchegoin, E.C. Le Ru, and M. Meyer. An analytic model for the optical properties of gold. *Journal of Chemical Physics*, 125, DOI: 10.1063/1.2360270 (2006), 164705.

23 Christy, P.B. Johnson and R.W. Optical Constants of the Noble Metals. *Physical Review B*, 6 (1972), 4370-4379.

24 Palik, E.D., ed. *Handbook of Optical Constants of Solids*. Academic Press, New York, U.S.A. , 1985.

25 Tocho, L.B. Scaffardi and J.O. Size dependence of refractive index of gold nanoparticles. *Nanotechnology*, 17 (2006).

26 Schatz, E.A. Coronado and G.C. Surface plasmon broadening for arbitrary shape nanoparticles: A geometrical probability approach. *Journal of Chemical Physics*, 119 (2003).

27 Jackson, J.D. *Classical Electrodynamics*. Wiley, New York, U.S.A., 1975.

28 Draine, B.T. The discrete-dipole approximation and its application to interstellar graphite grains. *Astrophysical Journal*, 333 (1988).

29 A. Penttilä, E. Zubko, K. Lumme, K. Muinonen, M. A. Yurkin, B. Draine, J. Rahola, A. G. Hoekstra, and Y. Shkuratov. A. Penttilä, E. Zubko, K. Lumme, K. Muinonen,

M. A. YurkinComparison between discrete dipole implementations and exact techniques. *Journal of Quantitative Spectroscopy and Radiative Transfer*, 106 (2007).

30 K.L. Kelly, E. Coronado, L. L. Zhao and G. C. Schatz. The Optical Properties of Metal Nanoparticles: The Influence of Size, Shape, and Dielectric Environment. *Journal of Physical Chemistry B*, 107 (2003).

31 Weingartner, B.T. Draine and J.C. Radiative torques on interstellar grains. I. Superthermal spin-up. *Astrophysical Journal*, 470 (1996).

32 Pennypacker, E.M. Purcell and C.R. Scattering and absorption of light by nonspherical dielectric grains. *Astrophysical Journal*, 186 (1972).

33 Flatau, B.T. Draine and P.J. Discrete-dipole approximation for scattering calculations. *Journal of the Optical Society of America A*, 11 (1994).

34 M.A. Yurkin, V.P. Maltsev and A.G. Hoekstra. The discrete dipole approximation for simulation of light scattering by particles much larger than the wavelength. *Journal of Quantitative Spectroscopy and Radiative Transfer*, 106 (2007).

35 Hoekstra, M.A. Yurkin and A.G. THe discrete dipole approximation: An overview and recent developments. *Journal of Quantitative Spectroscopy and Radiative Transfer*, 106 (2007).

36 Hoekstra, M.A. Yurkin and A.G. The discrete-dipole-approximation code ADDA: Capabilities and known limitations. *Journal of Quantitative Spectroscopy and Radiative Transfer*, 112 (2011).

37 Hoekstra, M.A. Yurkin and A.G. The discrete dipole approximation: an overview and recent developments. *Journal of Quantitative Spectroscopy and Radiative Transfer*, 106 (2007).

38 M.A. Yurkin, V.P. Maltsev and A.G. Hoekstra. Convergence of the discrete dipole approximation II. An extrapolation technique to increase the accuracy. *Journal of the Optical Society of America A*, 23 (2006).

39 M.A. Yurkin, D. de Kanter, and A.G. Hoekstra. Accuracy of the discrete dipole approximation for simulation of optical properties of gold nanoparticles. *Journal of Nanophotonics*, 4 (2010).

40 Chumanov, D.D. Evanoff Jr. and G. Size-Controlled Synthesis of Nanoparticles. 2. Measurement of Extinction, Scattering, and. *Journal of Physical Chemistry B*, 108, 10.1021/jp0475640 (2004), 13957-13962.

41 Mulvaney, S.W. Prescott and P. Gold nanorod extinction spectra. *Journal of Applied Physics*, 99 (2006).

42 C. Ungureanu, R.G. Rayavarapu, S. Manohar, and T.G. van Leeuwen. Discrete dipole approximation simulations of gold nanorod optical properties: Choice of input parameters and comparison with experiment. *Journal of Applied Physics*, 105 (2009).

43 Ben-Yakar, R.K. Harrison and A. R.K. HarrRole of Near-Field Enhancement in Plasmonic Laser Nanoablation using Gold Nanorods on a Silicon Substrate. *Optics Express*, 18 (2010), 22556-22571.

44 V. Kotaidis, C. Dahmen, G. von Plessen, F. Springer and A. Plech. Excitation of nanoscale vapor bubbles at the surface of gold nanoparticles in water. *Journal of Chemical Physics*, 124 (2006).

45 O. Ekici, R.K. Harrison, N.J. Durr, D.S. Eversole, M. Lee and A. Ben-Yakar. Thermal analysis of gold nanorods heated with femtosecond laser pulses. *Journal of Physics D*, 41 (2008).

46 N.J. Durr, T. Larson, D.K. Smith, B.A. Korgel, K. Sokolov, and A. Ben-Yakar. 21. N. J. Durr, T. LarTwo-photon luminescence imaging of cancer cells using molecularly targeted gold nanorods. *Nano Letters*, 7 (2007).

47 I. Ayranci, R. Vaillon and N. Selcuk. Performance of discrete dipole approximation for prediction of amplitude and phase of electromagnetic scattering by particles. *Journal of Quantitative Spectroscopy and Radiative Transfer*, 103 (2007).

48 S. Link, C. Burda, B. Nikoobakht and A.M. El-Sayed. Laser-induced shape changes of colloidal gold nanorods using femtosecond and nanosecond laser pulses. *Journal of Physical Chemistry B*, 104 (2000).

49 El-Sayed, S. Link and M.A. Spectroscopic determination of the melting energy of a gold nanorod. *Journal of Chemical Physics* , 114 (2001), 2362-2368.

50 M. Hu, X. Wang, G.V. Hartland, P. Mulvaney, J.P. Juste, and J.E. Sader. Vibrational Response of Nanorods to Ultrafast Laser Induced Heating: Theoretical and Experimental Analysis. *Journal of the American Chemistry Society*, 125 (2003), 14925-14933.

51 S.J.Peppernick, A.G. Joly, K.M. Beck, and W.P. Hess. Plasmonic field enhancement of individual nanoparticles by correlated scanning and photoemission spectroscopy. *Journal of Chemical Physics* , 134 (2011), 034507.

52 Durr, N.J. Nonlinear Imaging with Endogenous Fluorescence Contrast and Plasmonic Contrast Agents. *Ph.D. Dissertation*, University of Texas at Austin (August 2010).

53 H.J. Münzer, M. Mosbacher, M. Bertsch, O. Dubbers, F. Burmeister, A. Pack, R. Wannemacher, B. U. Runge, D. Bäuerle, J. Boneberg, and P. Leiderer. Optical near field effects in surface nanostructuring and laser cleaning. *Proceedings of SPIE*, 4426 (2002).

54 A. Luft, U. Franz, A. Emsermann, and J. Kaspar. A study of thermal and mechanical effects on materials induced by pulsed laser drilling. *Applied Physics A*, 63 (1996), 93-101.

55 Gower, M.C. Industrial applications of laser micromachining. *Optics Express*, 7

(2000), 56-67.

56 Chichkov, B.N., Momma, C., Nolte, S., Alvensleben, F. van, and Tuennermann, A. Femtosecond, picosecond and nanosecond laser ablation of solids. *Applied Physics A*, 63 (1996), 109-115.

57 Phipps, C.R. *Laser Ablation and its Applications*. Springer, Santa Fe, 2007.

58 W. Watanabe, N. Arakawa, S. Matsunage, T. Higashi, K. Fukui, K. Isobe, and K. Itoh. Femtosecond laser disruption of subcellular organelles in a living cell. *Optics Express*, 12 (2004), 4203-4213.

59 B. Girard, D. Yu, M.R. Armstrong, B.C. Wilson, C.M.L. Clokie, and R.J.D. Miller. Effects of Femtosecond Laser Irradiation on Osseous Tissues. *Lasers in Surgery and Medicine*, 39 (2007), 273-285.

60 S.I. Anisimov, V.V. Zhakhovskii, N.A. Inogamov, K. Nishihara, Y.V. Petrov, and V.A. Khokhlov. Ablated Matter Expansion and Crater Formation under the Action of Ultrashort Laser Pulse. *Journal of Experimental and Theoretical Physics*, 103 (2006), 183-197.

61 A.P. Joglekar, H. Liu, E. Meyhöfer, G. Mourou, and A.J. Hunt. Optics at critical intensity: Applications to nanomorphing. *Proceedings of the National Academy of Sciences*, 101 (2004).

62 A. Vogel, J. Noack, G. Hüttman and G. Paltauf. Mechanisms of femtosecond laser nanosurgery of cells and tissues. *Applied Physics B*, 81, 10.1007/s00340-005-2036-6 (2005), 1015-1047.

63 A. Ben-Yakar, A. Harkin, J. Ashmore, R. L. Byer, and H. A. Stone. Thermal and fluid processes of a thin melt zone during femtosecond laser ablation of glass: the formation of rims by single laser pulses. *Journal of Physics D*, 40 (2007).

64 J. Koch, F. Korte, C. Fallnich, A. Ostendorf, and B.N. Chichkov. Direct-write subwavelength structuring with femtosecond laser pulses. *Optical Engineering*, 44 (2005), 051103.

65 A. Rodriguez, Mikel Echeverría, M. Ellman, N. Perez, Y.K. Verevkin, C.S. Peng, T. Berthou, Z. Wang, I. Ayerdi, J. Savall, and S.M. Olaizola. Laser interference lithography for nanoscale structuring of materials: From laboratory to industry. *Microelectronic Engineering*, 86, 10.1016/j.mee.2008.12.043 (2009), 937-940.

66 K. Kawamura, T. Ogawa, N. Sarukura, M.Hirano, and H. Hosono. Fabrication of surface relief gratings on transparent dielectric materials by two-beamholographicmethod using infrared femtosecond laser pulses. *Applied Physics B*, 71, 10.1007/s003400000335 (2000), 119-121.

67 B. Tan, N.R. Sivakumar, and K. Venkatakrishnan. Direct grating writing using femtosecond laser interference fringes formed at the focal point. *Journal of Optics A*, 7, 10.1088/1464-4258/7/4/003 (2005), 169-174.

68 C. Tan, C.S. Peng, J. Pakarinen, M. Pessa, V.N. Petryakov, Y.K. Verevkin, J. Zhang, Z. Wang, S.M. Olaizola, T. Berthou, and S. Tisserand. Ordered nanostructures written directly by laser interference. *Nanotechnology* , 20 (2009).

69 A. Chimmalgi, T.Y. Choi, C.P. Grigoropoulos, and K. Komvopoulos. Femtosecond laser aperturless near-field nanomachining of metals assisted by scanning probe microscopy. *Applied Physics Letters*, 82 (2003).

70 J. Serbin, A. Egbert, A. Ostendorf, B.N. Chichkov, R. Houbertz, G. Domann, J. Schulz, C. Cronauer, L. Fröhlich, and M. Popall. Femtosecond laser-induced two-photon polymerization of inorganic organic hybrid materials for applications in photonics. *Optics Letters*, 28 (2003).

71 M.B. Mohamed, V. Volkov, S. Link, and M.A. El-Sayed. The ‘lightning’ gold nanorods: fluorescence enhancement of over a million compared to the gold metal. *Chemical Physics Letters*, 317 (2000), 517-523.

72 Synge, E.H. A suggested method for extending the microscopic resolution into the ultramicroscopic region. *Philisophical Magazine*, 6 (1928), 326.

73 D.W. Pohl, W. Denk, and M. Lanz. Optical stethoscopy: Image recording with resolution λ/20. *Applied Physics Letters*, 44, 10.1063/1.94865 (1984), 651-653.

74 D.J. Hwang, A. Chimmalgi, and C.P. Grigoropoulos. Ablation of thin metal films by short-pulsed lasers coupled through near-field scanning optical microscopy probes. *Journal of Applied Physics*, 99, 10.1063/1.2172723 (2006), 044905.

75 S. Nolte, B. N. Chichkov, H. Welling, Y. Shani, K. Lieberman, and H. Terkel. Nanostructuring with spatially localized femtosecond laser pulses. *Optics Letters*, 24 (1999), 914-916.

76 A. Chimmalgi, C.P. Grigoropoulos, and K. Komvopoulos. Surface nanostructuring by nano-/femtosecond laser-assisted scanning force microscopy. *Journal of Applied Physics*, 97, 10.1063/1.1899245 (2005), 104319.

77 Michel, D. Cleveland R.G. A Review of Near-Field Laser Ablation for High-Resolution Nanoscale Surface Analysis. *Applied Spectroscopy Reviews*, 43, 10.1080/05704920701829084 (2008), 93-110.

78 A.A. Milner, K. Zhang, and Y. Prior. Floating Tip Nanolithography. *Nano Letters*, 8, 10.1021/nl801203c (2008), 2017-2022.

79 N. Murphy-DuBay, L. Wang, and X. Xu. Nanolithography using high transmission nanoscale ridge aperture probe. *Applied Physics A*, 93, 10.1007/s00339-008-4752-3 (2008), 881-884.

80 T.H. Taminiau, R.J. Moerland, F.B. Segerink, L. Kuipers, and N.F. van Hulst. λ/4 Resonance of an Optical Monopole Antenna Probed by Single Molecule Fluorescence. *Nano Letters*, 7, 10.1021/nl061726h (2007), 28–33.

81 M.R. Beversluis, A. Bouhelier, and L. Novotny. Continuum generation from single

gold nanostructures through near-field mediated interband transitions. *Physical Review B*, 68, 10.1103/PhysRevB.68.115433 (2003), 115433.

82 E. ul Haq, Z. Liu, Y. Zhang, S.A. Alang Ahmad, L.-S. Wong, S.P. Armes, J.K. Hobbs, G.J.Leggett, J. Micklefield, C.J. Roberts and J.M.R. Weaver. Parallel Scanning Near-Field Photolithography: The Snomipede. *Nano Letters*, 10 (2010).

83 B.S. Luk'yanchuk, Y.W. Zheng, and Y.F. Lu. Laser cleaning of solid surface: Optical resonance and near-field effects. *Proceedings of SPIE*, 4065 (2000), 576-587.

84 D. Brodoceanu, L. Landström, and D. Bäuerle. Laser-induced nanopatterning of silicon with colloidal monolayers. *Applied Physics A*, 86 (2006).

85 N.N. Nedyalkov, P.A. Atanasov, and M. Obara. 7. N. N. Nedyalkov, Near field properties of a gold nanoparticle array excited by a femtosecond laser. *Nanotechnology*, 18 (2007).

86 Piestun, W. Cai and R. Patterning of silica microsphere monolayers with focused femtosecond laser pulses. *Applied Physics Letters*, 88 (2006), 111112.

87 Arnold, E. Mcleod and C.B. Subwavelength direct-write nanopatterning using optically trapped microspheres. *Nature Nanotechnology*, 3, dx.doi.org/10.1038/nnano.2008.150 (2008), 413-417.

88 Ashkin, A. Acceleration and Trapping of Particles by Radiation Pressure. *Physical Review Letters*, 24, dx.doi.org/10.1103/PhysRevLett.24.156 (1970), 156–159.

89 Arnold, E. McLeod and C.B. Array-based optical nanolithography using optically trapped microlenses. *Optics Express*, 17, dx.doi.org/10.1364/OE.17.003640 (2009), 3640-3650.

90 B.J. Messinger, K. Ulrich von Raben, R.K. Chang, and P.W. Barber. Local fields at the surface of noble-metal microspheres. *Physical Review B*, 24, dx.doi.org/10.1103/PhysRevB.24.649 (1981), 649-657.

91 Quinten, M. Local fields and Poynting vectors in the vicinity of the surface of small spherical particles. *Zeitschrift fuer Physik D*, 35, dx.doi.org/10.1007/BF01437071 (1995), 217-224.

92 A. Plech, V. Kotaidis, M. Lorenc, and J. Boneberg. Femtosecond laser near-field ablation from gold nanoparticles. *Nature Physics*, 2 (2005).

93 D. Eversole, B. Luk’yanchuk, and A. Ben-yakar. Plasmonic laser nanoablation of silicon by the scattering of femtosecond pulses near gold nanospheres. *Applied Physics A*, 89 (2007).

94 K.B. Crozier, A. Sundaramurthy, G.S. Kino, and C.F. Quate. Optical antennas: Resonators for local field enhancement. *Journal of Applied Physics*, 94, dx.doi.org/10.1063/1.1602956 (2003), 4632-4642.

95 M. Zhang, D. Bullen, S.-W. Chung, S. Hong, K.S. Ryu, Z. Fan, C.A. Mirkin, and C. Liu. A MEMS nanoplotter with high-density parallel dip-pen nanolithography probe

arrays. *Nanotechnology*, 13, dx.doi.org/10.1088/0957-4484/13/2/315 (2002), 212-217.

96 J. Chung, S. Ko, C.P. Grigoropoulos, N.R. Bieri, C. Dockendorf, and D. Poulikakos. Damage-Free Low Temperature Pulsed Laser Printing of Gold Nanoinks On Polymers. *Journal of Heat Transfer*, 127, dx.doi.org/10.1115/1.1924627 (2005), 724-732.

97 T. Kraus, L. Malaquin, H. Schmid, W. Riess, N.D. Spencer, and H. Wolf. Nanoparticle printing with single-particle resolution. *Nature Nanotechnology*, 2, dx.doi.org/10.1038/nnano.2007.262 (2007), 570-576.

98 T. Kaji, S. Ito, H. Miyasaka, Y. Hosokawa, H. Masuhara, C. Shukunami, and Y. Hiraki. Nondestructive micropatterning of living animal cells using focused femtosecond laser-induced impulsive force. *Applied Physics Letters*, 91, dx.doi.org/10.1063/1.2753103 (2007), 023904.

99 D.P. Banks, C. Grivas, J.D. Mills, R.W. Eason, and I. Zergioti. Nanodroplets deposited in microarrays by femtosecond Ti:sapphire laser-induced forward transfer. *Applied Physics Letters*, 89, dx.doi.org/10.1063/1.2386921 (2006), 193107.

100 M. F. Yanik, H. Cinar, H.N. Cinar, A. D. Chisholm, Y. Jin, and A. Ben-Yakar. Functional regeneration after laser axotomy. *Nature*, 432 (2004), 822.

101 S.X. Guo, F. Bourgeois, T. Chokshi, N.J. Durr, M.A. Hilliard, N. Chronis, and A. Ben-Yakar. Femtosecond laser nanoaxotomy lab-on-a-chip for in vivo nerve regeneration studies. *Nature Methods* , 5, 6 (June 2008), 531-533.

102 N. Shen, D. Datta, C.B. Schaffer, P. LeDuc, D.E. Ingber, and E. Mazur. Ablation of cytoskeletal filaments and mitochondria in live cells using a femtosecond laser nanoscissor. *Mechanics and Chemistry of Biosystems*, 2 (2005), 17-25.

103 K. Koenig, I. Riemann, F. Stracke, and R. Le Harzic. Nanoprocessing with nanojoule near-infrared femtosecond laser pulses. *Medical Laser Application*, 20 (2005), 169-184.

104 A. Lewis, H. Taha, A. Strinkovski, A. Manevitch, A. Khatchatouriants, R. Dekhter, and E. Ammann. Near-field optics: from subwavelength illumination to nanometric shadowing. *Nature Biotechnology*, 11 (2003), 1378-1386.

105 Deckert, A. Rasmussen and V. New dimension in nano-imaging: breaking through the diffraction limit with scanning near-field optical microscopy. *Analytical and Bioanalytical Chemistry*, 381 (2005), 165-172.

106 M.W. Berns, R.S. Olson, and D.E. Rounds. In vitro Production of Chrmosomal Lesions with an Argon Laser Microbeam. *Nature*, 221, dx.doi.org/10.1038/221074a0 (1969), 74-75.

107 Berns, M.W. Partial Cell Irradiation with a Tunable Organic Dye Laser. *Nature*, 240, dx.doi.org/10.1038/240483a0 (1972), 483-485.

108 Parrish, R.R. Anderson and J.A. Selective Photothemolysis: Precise Microsurgery by Selective Absorption of Pulsed Radiation. *Science*, 220 (1983), 524-527.

109 C.P. Lin, M.W. Kelly, S.A.B Sibayan, M.A. Latina, and R.R. Anderson. Selective Cell Killing by Microparticle Absorption of Pulsed Laser Radiation. *IEEE Journal of Selected Topics in Quantum Electronics*, 5 (1999), 963-968.

110 N. Lewinski, V. Colvin, and R. Drezek. Cytotoxicity of Nanoparticles. *Small*, 4, dx.doi.org/10.1002/smll.20700595 (2008), 26-49.

111 I.H. El-Sayed, X. Huang, and M.A. El-Sayed. Surface Plasmon Resonance Scattering and Absorption of anti-EGFRAntibody Conjugated Gold Nanoparticles in Cancer Diagnostics: Applications in Oral Cancer. *Nano Letters*, 5 (2005), 829-834.

112 O.C. Faokhzad, S. Jon, A. Khademhosseini, T.-N.T. Tran, D.A. LaVan, and R. Langer. Nanoparticle-aptamer Bioconjugates: A New Approach for Targeting Prostate Cancer. *Cancer Research*, 64 (2004), 7668-7672.

113 K. Sokolov, D. Nida, M. Descour, A. Lacy, M. Levy, B. Hall, S. Dharmawardhane, A. Ellington, B. Korgel, and R. Richards-Kortum. Molecular Optical Imaging of Therapeutic Targets of Cancer. *Advances in Cancer Research*, 96, dx.doi.org/10.1016/S0065-230X(06)96011-4 (2007), 299-344.

114 H. Takahashi, T. Niidome, A. Nariai, Y. Niidome, and S. Yamada. Photothermal reshaping of gold nanorods prevents further cell death. *Nanotechnology*, 17, dx.doi.org/10.1088/0957-4484/17/17/024 (2006), 4431-4435.

115 A. Ben-Yakar, D. Eversole and O. Ekici. Spherical and Anisotropic Metal Nanomaterials in Laser-Based Cancer Therapy. In Kumar, Challa, ed., *Non-Magnetic Metallic Nanomaterials for Life Sciences*. Wiley-VCH, Weinheim, Germany, 2008.

116 D. Pissuwan, S.M. Valenzuela, C.M. Miller, and M. B. Cortie. A Golden Bullet? Selective Targeting of Toxoplasma gondii Tachyzoites Using Antibody-Functionalized Gold Nanorods. *Nano Letters*, 7, dx.doi.org/10.1021/nl072377+ (2007), 3808-3812.

117 D. Pissuwan, S.M. Valenzuela, M.C. Killingsworth, X. Xu, and M.B. Cortie. Targeted destruction of murine macrophage cells with bioconjugated gold nanorods. *Journal of Nanoparticle Research*, 9, dx.doi.org/10.1007/s11051-007-9212-z (2007), 1109-1124.

118 L. Tong, Y. Zhao, T.B. Huff, M.N.Hansen, A. Wei, and J.-X. Cheng. Gold Nanorods Mediate Tumor Cell Death by Compromising Membrane Integrity. *Advanced Materials*, 19, dx.doi.org/10.1002/adma.200701974 (2007), 3136-3141.

119 P.K. Jain, I.H. El-Sayed, and M.A. El-Sayed. Au nanoparticles target cancer. *Nano Today*, 2 (2007), 18-29.

120 V.P. Zharov, K.E. Mercer, E.N. Galitovskaya, and M.S. Smeltzer. Photothermal Nanotherapeutics and Nanodiagnostics for Selectice Killing of Bacteria Targeted

with Gold Nanoparticles. *Biophysical Journal*, 90, dx.doi.org/10.1529/biophysj.105.061895 (2006), 619-627.

121 D. lapotko, E. Lukianova, M. Potapnev, O. Aleinikova, and A. Oraevsky. Method of laser activated nano-thermolysis for elimination of tumor cells. *Cancer Letters*, 239, dx.doi.org/10.1016/j.canlet.2005.07.031 (2006), 36-45.

122 C.M. Pitsillides, E.K. Joe, X. Wei, R.R. Anderson, and C.P. Lin. Selective Cell Targeting with Light-Absorbing Microparticles and Nanoparticles. *Biophysical Journal* , 84 (2003), 4023-4032.

123 M. Schomaker, J. Baumgart, D. Motekaitis, D. Heinemann, J. Krawinkel, M. Pangalos, W. Bintig, E. Boulais, R. Lachaine, B. St.-Louis Lalonde, A. Ngezahayo, M. Meuneir, and A. Heisterkamp. Mechanisms of gold nanoparticle mediated ultrashort laser cell membrane perforation. *Proceedings of SPIE*, 7925 (2011), 79250F.

124 Eversole, D.S. Plasmonic Laser Nanosurgery. *Ph.D. Dissertation*, University of Texas at Austin (August 2011).

125 C.L. Hoy, N.J. Durr, P.Chen, W. Piyawattanametha, H. Ra, O. Solgaard, and A. Ben-Yakar. Minaturized probe for femtosecond laser microsurgery and two-photon imaging. *Optics Express*, 16, dx.doi.org/10.1364/OE.16.009996 (2008), 9996-10005.

126 C.L. Hoy, O. Ferhanoglu, M. Yildirim, W. Piyawattanametha, H. Ra, O. Solgaard, and A. Ben-Yakar. Optical design and image performance testing of a 9.6-mm diameter femtosecond laser microsurgery probe. *Optics Express*, 19, dx.doi.org/10.1364/OE.19.010536 (2011), 10536-10552.

127 H. Wang, Y. Wu, B. Lassiter, C.L. Nehl, J.H. Hafner, P. Nordlander and N.J. Halas. 20. H. Wang, Y. Wu, B. Lassiter, C. L. Nehl, J. H. Hafner, P. NSymmetry breaking in individual plasmonic nanoparticles. *Proceedings of the National Academy of Sciences*, 103 (2006).

128 C. Sönnichsen, T. Franzl, T. Wilk, G. von Plessen, and J. Feldmann. Drastic Reduction of Plasmon Damping in Gold Nanorods. *Physical Review Letters*, 88 (2002).

129 T.R. Jensen, M.D. Malinsky, C.L. Haynes, and R.P. Van Duyne. Nanosphere Lithography: Tunable Localized Surface Plasmon Resonance Spectra of Silver Nanoparticles. *Journal of Physical Chemistry B*, 104 (2000).

130 A. Oldenburg, M.N. Hansen, D.A. Zweifel, A. Wei, and S.A. Boppart. Plasmon-resonant gold nanorods as low backscattering albedo contrast agents for optical coherence tomography. *Optics Express*, 14 (2006).

131 P. Zijlstra, J.W.M. Chon and M. Gu. Five-dimensional optical recording mediated by surface plasmons in gold nanorods. *Nature*, 459 (2009).

132 Arnold, N. Influence of the substrate, metal overlayer and lattice neighbors on the

focusing properties of colloidal microspheres. *Applied Physics A*, 92 (2008).

133 T. Sakai, T. Miyanishi, N. Nedyalkov, Y. Nishizawa, and M. Obara. Nano-dimple processing of silicon surfaces by femtosecond laser irradiation with dielectric particle templates in the Mie scattering domain. *Journal of Physics D*, 42 (2009).

134 B.S. Luk'yanchuk, N. Arnold, S.M. Huang, Z.B. Wang, and M.H. Hong. Three-dimensional effects in dry laser cleaning. *Applied Physics A*, 77 (2003).

135 J.H. Kim, S.H. Ehrman, G.W. Mulholland, and T.A. Germer. Polarized light scattering by dielectric and metallic spheres on silicon wafers. *Applied Optics* , 41 (2002).

136 J.H. Kim, S.H. Ehrman, G.W. Mulholland, and T.A. Germer. 44. J. H. Kim, S. H. Polarized light scattering by dielectric and metallic spheres on silicon wafers. *Applied Optics*, 41 (2002).

137 Knox, S.R.G. Hall and S.D. Traceable measurements for beam propagation ratio M^2. *Journal of Physics: Conference Series*, 85, dx.doi.org/10.1088/1742-6596/85/1/012014 (2007), 012014.

138 Byer, A. Ben-Yakar and R.L. Femtosecond laser ablation properties of borosilicate glass. *Journal of Applied Physics*, 96 (2004).

139 P.P. Pronko, P.A. VanRompay, C. Horvath, F. Loesel, T. Juhasz, X. Liu, and G. Mourou. Avalanche ionization and dielectric breakdown in silicon with ultrafast laser pulses. *Physical Review B*, 58 (1998).

140 Besner, S. Surface modifications during femtosecond laser ablation in vacuum, air, and water. *Proceedings of SPIE*, 5578 (2004).

141 D. Giguère, G. Olivié, F. Vidal, S. Toetsch, G. Girard, T. Ozaki, J.C. Kieffer, O. Nada, and I. Brunette. Laser ablation threshold dependence on pulse duration for fused silica and corneal tissues: experiments and modeling. *Journal of the Optical Society of America A* , 24 (2007).

142 I. Chowdhury, A. Wu, X. Xu, and A. Weiner. Ultra-fast laser absorption and ablation dynamics in wide-band-gap dielectrics. *Applied Physics A*, 2008 (92).

143 Y. Wang, X. Xu, and L. Zheng. Molecular dynamics simulation of ultrafast laser ablation of fused silica film. *Applied Physics A*, 92 (2008).

144 S.E. Kirkwood, M.R. Shadnam, A. Amirfazli, and R. Fedosejevs. Mechanism for femtosecond laser pulse patterning of self-assembled monolayers on gold-coated substrates. *Journal of Physics Conference Series*, 59 (2007).

145 X. Ni, C. Wang, L. Yang, J. Li, L. Chai, W. Jia, R. Zhang, and Z. Zhang. Parametric study on femtosecond laser pulse ablation of Au fil. *Applied Surface Science*, 253 (2006).

146 S. Amoruso, X. Wang, C. Altucci, C. De Lisio, M. Armenante, R. Bruzzese, N. Spinelli, and R. Velotta. Double-peak distribution of electron and ion emission

profile during femtosecond laser ablation of metals. *Applied Surface Science*, 186 (2002).

147 S. Wellershoff, J. Hohlfeld, J. Güdde, and E. Matthias. 30. S. Wellershoff, J. Hohlfeld, J. The role of electron–phonon coupling in femtosecond laser damage of metals. *Applied Physics A*, 69 (1999).

148 Urey, H. H. Urey, "Spot size, depth-of-focus, and diffraction ring intensity formulas for truncated Gaussian beams. *Applied Optics*, 43 (2004).

149 E. Cappelli, S. Orlando, D. Sciti, M. Montozzi, and L. Pandolfi. 48. E. Cappelli, S. OrCeramic surface modifications induced by pulsed laser treatment. *Applied Surface Science*, 154 (2000).

150 K. Sokolowski-Tinten, J. Bialkowski, A. Cavalleri, D. von der Linde, A. Oparin, J. Meyer-ter-Vehn, and S.I. Anisimov. Transient states of matter during short pulse laser ablation. *Physical Review Letters*, 81 (1998).

151 S. Link, C. Burda, B. Nikoobakht, M. A. El-Sayed. How long does it take to melt a gold nanorod? A femtosecond pump-probe absorption spectroscopic study. *Chemical Physics Letters*, 315 (1999).

152 P. Leiderer, C. Bartels, J. König-Birk, M. Mosbacher and J. Boneberg. Imaging optical near-fields of nanostructures. *Applied Physics Letters*, 85 (2004).

153 J. Turkevich, P.C. Stevenson and J. Hillier. A study of the nucleation and growth processes in the synthesis of colloidal gold. *Discussions of the Faraday Society*, 55 (1951).

154 Pileni, M.P. Nanosized Particles made in Colloidal Assemblies. *Langmuir*, 13 (1997).

155 N.G. Bastus, J. Comenge and V. Puntes. Kinetically Controlled Seeded Growth Synthesis of Citrate-Stabilized Gold Nanoparticles of up to 200 nm: Size Focusing versus Ostwald Ripening. *Langmuir* , 27 (2011).

156 Khlebtsov, N.G. Determination of Size and Concentration of Gold Nanoparticles from Extinction Spectra. *Analytical Chemistry*, 80 (2008).

157 Y. Kobayashi, H. Katakami, E. Mine, D. Nagao, M. Konno, and L.M. Liz-Marzan. Silica coating of silver nanoparticles using a modified Stoeber method. *Journal of Colloid and Interface Science*, 283, dx.doi.org/10.1016/j.jcis.2004.08.184 (2005), 392-396.

158 D. Mongin, V. Juve, P. Maioli, A. Crut, N. Del Fatti, F. Vallee, A. Sanchez-Iglesias, I. Pastoriza-Santos, and L.M. Liz-Marzan. Acoustic Vibrations of Metal-Dielectric Core-Shell Nanoparticles. *Nano Letters*, 11 (2011), 3016-3021.

159 L.M. Liz-Marzan, M. Giersig, and P. Mulvaney. Synthesis of Nanosized Gold-Silica Core-Shell Particles. *Langmuir*, 12 (1996), 4329-4335.

160 G. Chumanov, K. Sokolov, B.W. Gregory, and T.M. Cotton. Colloidal Metal Films

as a Substrate for Surface-Enhanced Spectroscopy. *Journal of Physical Chemistry*, 99 (1995), 9466-9471.

161 S. Malynych, I. Luzinov, and G. Chumanov. Poly(Vinyl Pyridine) as a Universal Surface Modifier for Immobilization of Nanoparticles. *Journal of Physical Chemistry B*, 106 (2002), 1280-1285.

162 W. Stoeber, A. Fink, and E. Bohn. Controlled Growth of Monodisperse Silica Spheres in the Micron Size Range. *Journal of Colloid and Interface Science*, 26 (1968), 62-69.

163 D. Aherne, D.M. Ledwith, M. Gara, and J.M. Kelly. Optical Properties and Growth Aspects of Silver Nanoprisms Produced by a Highly Reproducible and Rapid Synthesis at Room Temperature. *Advanced Functional Materials*, 18, dx.doi.org/10.1002/adfm.200800233 (2008), 2005-2016.

164 L.R. Hirsch, R.J. Stafford, J.A. Bankson, S.R. Sershen, B. Rivera, R.E. Prive, J.D. Hazle, N.J. Halas, and J.L. West. Nanoshell-mediated near-infrared thermal therapy of tumors under magnetic resonance guidance. *Proceedings of the National Academy of Sciences*, 100 (2003), 13549-13554.

165 D.C. Hone, P.I. Walker, R. Evans-Gowing, S. FitzGerald, A. Beeby, I. Chambrier, M.J. Cook, and D.A. Russell. Generation of Cytotoxic Singlet Oxygen via Phthalocyanine-Stabilized Gold Nanoparticles: A Potential Delivery Vehicle for Photodynamic Therapy. *Langmuir*, 18 (2002), 2985-2987.

166 H.A. Atwater and A. Polman. Plasmonics for improved photovoltaic devices. *Nature Materials*, 9 (2010).

167 J.-J. Chen, J.C.S. Wu, P.C. Wu, and D.P. Tsai. Plasmonic Photocatalyst for H2 Evolution in Photocatalytic Water Splitting. *Journal of Physical Chemistry C*, 115 (2011), 210-216.

168 Hartland, M. Hu and G.V. Heat Dissipation for Au Particles in Aqueous Solution: Relaxation Time versus Size. *Journal of Physical Chemistry B*, 106 (2002), 7029-7033.

169 Kurokawa, H.T. Miyazaki and Y. How Can a Resonant Nanogap Enhance Optical Fields by Many Orders of Magnitude?. *IEEE Journal of Selected Topics in Quantum Electronics*, 14 (2008), 1565-1576.

170 Gao, S., Ueno, K., and Misawa, and H. Plasmonic Antenna Effects on Photochemical Reactions. *Accounts of Chemical Research*, 44 (2011), 251-260.

171 W.C. Mundy, J.A. Roux, and A.M. Smith. Mie scattering by spheres in an absorbing medium. *Journal of the Optical Society of America*, 64 (1974), 1593-1597.

172 Chylek, P. Light scattering by small particles in an absorbing medium. *Journal of the Optical Society of America*, 67 (1977), 561-563.

173 Chylek, I.W. Sudiarta and P. Mie-scattering formalism for spherical particles

embedded in an absorbing medium. *Journal of the Optical Society of America A*, 18 (2001), 1275-1278.

174 Sun, Q. Fu and W. Mie theory for light scattering by a spherical particle in an absorbing medium. *Applied Optics*, 40 (2001), 1354-1361.

175 Dynich, R.A. Utilization efficiency of spherical metal nanoparticles that increase light absorption in absorbing media. *Journal of the Optical Society of America A*, 28 (2011), 222-228.

176 Peumans, J.-Y. Lee and P. The origin of enhanced optical absorption with metal nanoparticles embedded in the active layer. *Optics Express*, 18 (2010), 10078-10087.

177 G. Baffou, R. Quidant, and C. Girard. Heat Generation in plasmonic nanostructures. *Applied Physics Letters*, 94 (2009), 153109.

178 Quinten, M. *Optical Properties of Nanoparticle Systems*. Wiley-VCH, Weinheim, Germany, 2011.

179 R.A. Dynich, A.N. Ponyavina, and V.V. Filippov. Local Field Enhancement near Spherical Nanoparticles in Absorbing Media. *Journal of Applied Spectroscopy*, 76 (2009), 705-710.

180 Capps, C. Near field or far field? *EDN* (August 16 2001), 95-102.

181 C.D. Stanciu, F. Hansteen, A.V. Kimel, A. Kirilyuk, A. Tsukamoto, A. Itoh, and T. Rasing. All-Optical Magnetic Recording with Circularly Polarized Light. *Physical Review Letters*, 99 (2007), 047601.

182 Harrison, R.K. and Ben-Yakar, and A. Role of near-field enhancement in plasmonic nanoablation using gold nanorods on a silicon substrate: reply. *Optics Express*, 19 (2011), 6179-6181.

183 Schelkunoff, S.A. The Impedance Concept and its Application to Problems of Reflection, Refraction, Shielding and Power Absorption. *Bell Systems Technological Journal*, 17 (1938), 17-48.

184 Xu, H. Electromagnetic energy flow near nanoparticles - I: single spheres. *Journal of Quantitative Spectroscopy and Radiative Transfer*, 87 (2004), 53-67.

185 Nordlander, J. Zuloaga and P. On the Energy Shift between Near-Field and Far-Field Peak Intensities in Localized Plasmon Systems. *Nano Letters*, 11 (2011), 1280-1283.

186 N.K. Balla, P.T.C. So, and C.J.R. Sheppard. Second harmonic scattering from small particles using the Discrete Dipole Approximation. *Optics Express*, 18 (2010), 21603-21611.

187 G.O. Clay, C.B. Schaffer, and D. Kleinfeld. Large two-photon absorptivity of hemoglobin in the infrared rande of 780-880 nm. *Journal of Chemical Physics*, 126 (2007), 025102.

188 N.S. Makarov, M. Drobizhev, and A. Rebane. Two-photon absorption standards in the 550 - 1600 nm excitation wavelength range. *Optics Express*, 16 (2008), 4029-

4047.

189 N.J. Durr, C.T. Weisspfennig, B.A. Holfeld, and A. Ben-Yakar. Maximum imaging depth of two-photon autofluorescence microscopy in epithelial tissues. *Journal of Biomedical Optics*, 16 (2011), 026008.

190 Agency, International Energy. 2010 Key World Energy Statistics. *Annual Report* (2010).

191 Perlin, J. The Silicon Solar Cell Turns 50. *NREL Report*, BR-520-33947 (2004).

192 Margolis, S. Price and R. 2008 Solar Technologies Market Report. *NREL Report*, GO-102010-2867, Energy Efficiency and Renewable Energy Program (2010).

193 Chu, Secretary of Energy S. Is it time for a 'sun shot'?. *Presentation at the $1/Watt Workshop*, Washington, D.C. (August 2010).

194 R. Wiser, G. Barbose, C. Peterman and N. Darghouth. Tracking the Sun II: The Installed Cost of Photovoltaics in the U.S. from 1998–2008. *LBNL Report*, 2674E, Energy Efficiency and Renewable Energy Program (2009).

195 http://www.solarbuzz.com, Statistics section of.

196 Mehta, S. Thin Film 2010: Market Outlook to 2015. *Greentech Media Research* , Executive Summary (2010).

197 M. Pagliaro, G. Palmisano and R. Ciriminna. *Flexible Solar Cells*. Wiley VCH, Weinheim, Germany, 2008.

198 P. Denholm, R.M. Margolis, S. Ong and B. Roberts. Break-Even Cost for Residential Photovoltaics in the United States: Key Drivers and Sensitivites. *NREL Report*, TP-6A2-46909 (2009).

199 Lewis, N.S. Basic Research Needs for Solar Energy Utilization. *Report of the Basic Sciences Workshop on Solar Energy Utilization* (April 2005).

200 Nelson, J. *The Physics of Solar Cells*. Imperial College Press, London, UK, 2010.

201 http://www.firstsolar.com.

202 M. Helgesen, R. Sondergaard and F.C. Krebs. Advanced materials and processes for polymer solar cell devices. *Journal of Materials Chemistry*, 20 (2010).

203 Grätzel, Brian O'Regan and Michael. A low-cost, high-efficiency solar cell based on dye-sensitized colloidal TiO2 films. *Nature*, 353 (1991).

204 J. Zhao, A. Wang, P. Altermatt, and M. A. Green. Twenty-four percent efficient silicon solar cells with double layer antireflection coatings and reduced resistance loss. *Applied Physics Letters*, 66, dx.doi.org/10.1063/1.114124 (1995), 3636-3638.

205 V.E. Ferry, M.A. Verschuuren, H.B.T. Li, E. Verhagen, R.J. Walters, R.E.I. Schropp, H.A. Atwater, and A. Polman. Light trapping in ultrathin plasmonic solar cells. *Optics Express*, 18, dx.doi.org/10.1364/OE.18.00A237 (2010), A237-A245.

206 H.R. Stuart and D.G. Hall. Island size effects in nanoparticle enhanced photo-

detectors. *Applied Physics Letters*, 73 (1998).

207 M. Westphalen, U. Kreibig, J. Rostalski, H. Lüth and D. Meissner. Metal cluster enhanced organic solar cells. *Solar Energy Materials and Solar Cells*, 61 (2000).

208 S. Pillai, K.R. Catchpole, T. Trupke and M.A. Green. Surface plasmon enhanced silicon solar cells. *Journal of Applied Physics*, 101 (2007).

209 C. Hägglund, Michael Zäch and Bengt Kasemo. Enhanced charge carrier generation in dye sensitized solar cells by nanoparticle plasmons. *Applied Physics Letters*, 92 (2008).

210 R.A. Pala, J. White, E. Barnard, J. Liu and M.L. Brongersma. Design of Plasmonic Thin-Film Solar Cells with Broadband Absorption Enhancements. *Advanced Materials*, 21 (2009).

211 D.M. Schaadt, B. Feng and E.T. Yu. Enhanced semiconductor optical absorption via surface plasmon excitation in metal nanoparticles. *Applied Physics Letters*, 86 (2005).

212 D. Derkacs, S.H. Lim, P. Matheu, W. Mar and E.T. Yu. Improved performance of amorphous silicon solar cells via scattering from surface plasmon polaritons in nearby metal nanoparticles. *Applied Physics Letters*, 89 (2006).

213 S.D. Standridge, G.C. Schatz and J.T. Hupp. Distance Dependence of Plasmon-Enhanced Photocurrent in Dye-Sensitized Solar Cells. *Journal of the American Chemical Society*, 131 (2009).

214 D. Duche, P. Torchio, L. Escoubas, F. Monestier, J.-J. Simon, F. Flory and G. Mathian. Improving light absorption in organic solar cells by plasmonic contribution. *Solar Enegry Materials and Solar Cells*, 93 (2009).

215 J.H. Lee, J.H. Park, J.S. Kim, D.Y. Lee and K. Cho. High efficiency polymer solar cells with wet deposited plasmonic gold nanodots. *Organic Electronics*, 10 (2009).

216 A.P. Kulkarni, K.M. Noone, K. Munechika, S.R. Guyer and D.S. Ginger. Plasmon-Enhanced Charge Carrier Generation in Organic Photovoltaic Films using Silver Nanoprisms. *Nano Letters*, 10 (2010).

217 M.J. Mendes, A. Luque, I. Tobias and A. Marti. Plasmonic light enhancement in the near-field of metallic nanospheroids for application in intermediate band solar cells. *Applied Physics Letters*, 95 (2009).

218 M. Kirkengen, J. Bergli and Y.M. Galperin. Direct generation of charge carriers in c-Si solar cells due to embedded nanoparticles. *Journal of Applied Physics*, 102 (2007).

219 Halas, J.R. Cole and N.J. Optimized plasmonic nanoparticle distributions for solar spectrum harvesting. *Applied Physics Letters*, 89 (2006).

220 D. Wan, H. Chen, T. Tseng, C. Fang, Y. Lai and F. Yeh. Antireflective Nanoparticle Arrays Enhance the Efficiency of Silicon Solar Cells. *Advanced Functional Materials*, 20 (2010).

221 V.A. Akhavan, M.G. Panthani, B.W. Goodfellow, D.K. Reid and B.A. Korgel. Thickness-limited performance of CuInSe2 nanocrystal photovoltaic devices. *Optics Express*, 18 (2010).

222 P.D. Paulson, R.W. Birkmire, and W.N. Shafarman. Optical characterization of CuIn1-xGaxSe2 alloy thin films by spectroscopic ellipsometry. *Journal of Applied Physics* , 94, dx.doi.org/10.1063/1.1581345 (2003), 879-888.

223 Green, M.A. Self-consistent optical parameters of intrinsic silicon at 300 K including temperature coefficients. *Solar Energy Materials and Solar Cells*, 92, dx.doi.org/10.1016/j.solmat.2008.06.009 (2008), 1305-1310.

224 Y.T. Hou, M.F. Li, Y. Jin, and W.H. Lai. Direct tunneling hole currents through ultrathin gate oxides in metal-oxide-semiconductor devices. *Journal of Applied Physics*, 91 (2002), 258-264.

225 X. Zhao, S.A.Scott, M. Huang, W. Peng, A.M. Kiefer, F.S. Flack, D.E. Savage, and M.G. Lagally. Influence of surface properties on the electrical conductivity of silicon nanomembranes. *Nanoscale Research Letters*, 6 (2011), 402.

226 Y.-S. Chen, W. Frey, S. Kim, K. Homan, P. Kruizinga, K. Sokolov and S. Emilianov. Enhanced thermal stability of silica-coated gold nanorods for photoacoustic imaging and image-guided therapy. *Optics Express*, 18 (2010).

Vita

Richard K. Harrison was born in Southern California in 1982. In 2000, he graduated from high school in Spokane, Washington. Richard attended the University of California San Diego. In 2005, Richard obtained his B.A. in German Studies and B. S. in Mechanical Engineering from the University of California San Diego. Richard married his wife, Katharine, in 2005. Also in 2005, Richard began his graduate studies at the University of Texas at Austin. Richard completed his Master of Science in Engineering in 2007 for work on nuclear characterizations of fuel cell catalyst nanoalloys under the guidance of Dr. Sheldon Landsberger and Dr. Arumugam Manthiram. Subsequently, Richard started his doctoral studies in the lab of Dr. Adela Ben-Yakar, where he was introduced to ultrafast lasers and plasmonics.

Permanent address: P.O. Box 31240, Spokane, WA 99223

This dissertation was typed by the author.